TOTAL AND COMPONENT FRICTION IN A MOTORED AND FIRING ENGINE

Riaz Ahmad Mufti

Submitted in accordance with the requirements for the degree of Doctor of Philosophy

The University of Leeds
School of Mechanical Engineering

January, 2004

The candidate confirms that the work submitted is his own and that appropriate credit has been given where reference has been made to the work of others.

ACKNOWLEDGEMENTS

First and foremost, I would like to express my sincerest thanks to my supervisor Professor Martin Priest, for his invaluable support, advice and encouragement throughout this study. It has been a great pleasure and honour to work under the supervision of such a distinguished scholar.

I would like to thank the Engineering and Physical Sciences Research Council (UK), Federal Mogul Corporation, Ford Motor Company, Jaguar Cars Limited and Shell Global Solutions for their financial and technical support of this research. In particular, the very helpful discussions with Dr. R.I. Taylor of Shell Global Solutions (Chester, UK) on the theoretical and experimental results presented herein and the provision of the test lubricants by Shell Global Solutions are gratefully acknowledged. Bob Gartside of Federal Mogul Corporation also kindly provided the grasshopper linkage and the thermistor signal conditioning unit used in the experiments, for which I am very grateful.

I would also like to thank Professor Chris Taylor for the guidance during the initial period of this study and Professor R.C. Coy for his expert opinions on the experimental and predicted results throughout the project. Thanks also go to Dr Richard Chittenden for very kindly analysing the Ricardo Hydra piston skirt motion to generate input data for the friction analysis.

Throughout this study members of technical staff have helped me and I would especially like to thank Paul Banks. Particular mention must also be given to Dr. David Barrell for his time and patience spent going through the draft of this thesis.

Finally I wish to thank my parents and my wife for their love, support and encouragement. I hope the completion of this research work will in some form repay them for the many sacrifices they have made.

ABSTRACT

Engine developers and lubricant formulators are constantly improving the performance of internal combustions engines by reducing the power losses and emissions. The majority of the mechanical frictional losses generated in an engine can be attributed to the main tribological components of an engine, the valve train, piston assembly and engine bearings. However no single method has been developed to measure the friction loss contribution of each component simultaneously in a firing engine. Such results would be invaluable to the automotive/lubricant industries, research institutions and for validating predictive mathematical models for engine friction.

The main focus of the research reported in this thesis was to validate an engine friction mathematical model called FLAME, developed in a separate study at Leeds. The validation was achieved by experimentally characterising the frictional losses generated from the major tribological components of a single cylinder gasoline engine.

A novel experimental system was developed to evaluate experimentally, frictional losses in all the three main tribological components of an engine under fired conditions. A specially designed pulley torque transducer was used to measure valve train friction whereas improved IMEP method was adopted to measure piston assembly friction. For the very first time bearing friction was determined experimentally in a fired engine indirectly by measuring total engine friction.

The FLAME engine friction model predicted valve train friction of the same order as the experimental data at engine speeds of 1500rpm and above. However, there was a much-reduced sensitivity to engine speed and temperature in the predictions. The piston assembly predicted results correlated very well with the measured data especially at lubricant inlet temperature of 80°C whereas for the bearing friction, the predicted results obtained with the short bearing approximation for the π film case were very close to the measured values. Overall the predicted total engine power loss results showed a good correlation with the experimental data especially at high lubricant inlet temperatures and engine speeds. It was concluded that the predicted results were in good agreement with the experimental results and the comparison validated the FLAME, engine friction model.

CONTENTS

LIST OF FIGURES

LIST OF SYMBOLS

MATHEMATICAL SYMBOLS AND VARIABLES

ENGINE VALVE TRAIN

b	Hertzian contact half-width
E'	equivalent elastic modulus
F	frictional force
G	dimensionless materials parameter, $\alpha E'$
H	average cam/follower frictional power loss
h_{cen}	central lubricant film thickness
h_{min}	minimum lubricant film thickness
I	inertia force
I_f	valve lift
k	valve spring stiffness
L	cam lobe width
M	equivalent reciprocating mass of the valve system
p	pressure
p_{max}	maximum Hertzian pressure
R	equivalent radius of curvature
r	perpendicular distance from the cam centre of rotation to the frictional force vector

r_b	base circle radius of cam
U	dimensionless speed parameter, $\frac{\eta_o V_C}{E'R}$
V_C	velocity of the point of contact relative to the cam
V_e	mean entrainment velocity, $\frac{1}{2}(V_C + V_f)$
V_f	velocity of the point of contact relative to the follower
V_s	sliding velocity, $(V_C - V_f)$
W	load
W'	dimensionless load parameter, $\frac{\mathrm{W}}{\mathrm{E'RL}}$
α	pressure-viscosity coefficient
θ	cam angular position
ω	camshaft angular velocity
δ	initial compression of valve spring
η	dynamic viscosity
η_o	dynamic viscosity at ambient pressure
τ	shear stress
μ_{lim}	limiting coefficient of friction

PISTON ASSEMBLY

A	cross section area
A_c	connecting rod cross section area
a_c	acceleration of any point on the connecting rod section 'B'
a_o	piston assembly acceleration
b	piston ring width
B_x, B_y	forces acting at big-end bearing centre
BDC	bottom dead centre
C_1-C_3	constants
C_x, C_y	forces acting at small-end bearing centre
c_p	specific heat at constant pressure
c_v	specific heat at constant volume
D	cylinder liner diameter
f	piston assembly friction
F_c	forces acting along the connecting rod axis
F_r	viscous traction force
F_s	piston side force
F_{STG}	forces measured by connecting rod strain gauges
F_x	hydrodynamic pressure force in 'x' direction
F_z	hydrodynamic force
g	gravitational acceleration
H	enthalpy

H_r	average friction power loss
K_c	discharge coefficient
L	connecting rod length
m_B	mass of connecting rod section 'B'
m_p	piston assembly mass
M_{sound}	Mach number
$\dot{m}$	mass flow rate
p	pressure
P_1	cylinder pressure
P_2	crankcase pressure
p_a	oil film pressure in inlet region of piston ring
p_b	oil film pressure in outlet region of piston ring
p_t	stagnation pressure
Q	volume flow rate per unit width
q	heat energy
$r_{o/c}$	distance between two points 'o' and 'c' on the connecting rod
R	gas constant
R_a	crank radius
R_r	effective radius of curvature
S	piston displacement
T	temperature
T_e	piston ring elastic tension

T_t	stagnation temperature
u	internal energy
U_r	velocity of piston ring
U_l	velocity of liner
v	velocity of flow
ν_p	poisson's ratio
w	work done
w_o	fluid flow velocity in
w_h	fluid flow velocity out
z	height
ρ	density of gas
γ	$\frac{c_p}{c_v}$
θ	crank angle
η	viscosity
ω	angular velocity

ENGINE BEARING

A	area
a_o	piston acceleration
b	bearing length
D	cylinder liner diameter
d	bearing diameter
C	out of balance load
c	bearing radial clearance
e	eccentricity
F	bearing load
F_B	big-end bearing load
F_m	main bearing load
F_G	gas force
F_{rec}	reciprocating inertia force
F_{rot}	rotating inertia force
F_T	side thrust force
H	bearing friction power loss
h	film thickness
m_c	connecting rod mass
m_p	piston assembly mass
$M^{\varepsilon}, M^{\phi}$	Mobility components
M^{ξ}, M^{μ}	Mobility components
p	pressure
r	bearing journal radius

R_a	crank radius
S	piston displacement
V	journal centre velocity
w_b	bearing bush angular velocity
w_l	bearing load angular velocity
w_j	bearing journal angular velocity
Z, W	Cartesian co-ordinates
θ	crank angle
ω	angular velocity
ψ	angle between connecting rod axis and cylinder liner axis
η	dynamic viscosity
α	angle measured form h_{max} in the direction of rotation
ε	eccentricity ratio
ϕ	attitude angle
ξ, μ	rectangular co-ordinates
β	angle between $\vec{V}$ and $\vec{F}$
λ	crank length / connecting rod length

ABBREVIATIONS

BDC	bottom dead centre
FM	friction modifier
NI	National Instruments
SAE	Society of Automotive Engineers
TDC	top dead centre

Chapter One

INTRODUCTION

1.1 INTRODUCTION

Engineers are constantly challenged to innovate advanced products to meet more demanding emissions and fuel economy targets. In the past 20 years the automotive industry has greatly improved vehicle fuel efficiency. This has been achieved by detail engine component design improvement and formulating compatible lubricants. A decrease in automotive engine friction gives the manufacturer the opportunity to increase engine output power and decrease the specific fuel consumption, especially at light loads, the region where most passenger vehicles run.

It is known (Parker et al [1989]) that out of the total energy released in the combustion chamber about 30% is lost to the exhaust gases and 30% as heat transfer to the engine/atmosphere. Of the remaining 40%, 6% is lost to engine pumping and a further 12% to engine friction, leaving 22% as engine brake power. Such figures are indicative and will vary with engine type and operating conditions. Although the 12% attributable to engine friction is small, according to Monaghan [1987], reducing the friction of a gasoline engine by 10% can give a fuel economy gain of 5%. According to international statistics HMSO [1995], there were a total of 494 million road vehicles in Europe, America and Japan in 1993, with the number increasing every year. With such a large number of reciprocating engines in service even a slight improvement in fuel economy can make a big difference.

Before 1876 when the Otto cycle was introduced the emphasis was entirely on the operating cycle of the engine and efficiency was dominated by the shape of the combustion and gas exchange cycles of the engine. The engine thermal efficiency was determined by comparing its indicator diagram with the ideal cycle efficiency. This was a reasonable approach as the early engines were designed to run at full load and had very low operating speeds so their mechanical efficiency was usually around 80%. At

that time they had more room for improvement in the engine cycle through higher compression ratios, better breathing, improved charge preparation and ignition conditions. The introduction of the internal combustion engine into vehicles made it necessary to look at friction more closely since operating speeds increased thereby increasing frictional power loss.

The regimes of lubrication associated with the main components of an internal combustion engine piston assembly, cam/follower and engine bearing are shown in the modified Stribeck curve Yang [1992], figure 1.1. Their performance depends upon the modes of lubrication and some components may enjoy more than one form of lubrication during a single cycle. This clearly reflects the challenges that face the engine component designers and lubricant formulators in improving operational characteristics in response to the strict legal pressures on emissions control and energy efficiency.

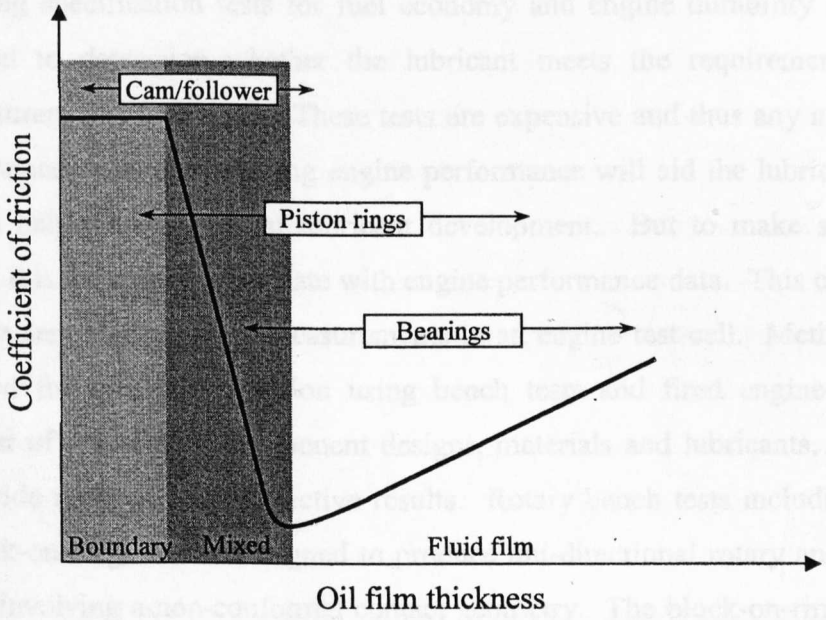

Figure 1.1. The Stribeck curve

The piston rings are subject to large, rapid variations of load, speed, temperature and lubricant availability. During a single stroke of the piston, the piston ring experiences all three modes of lubrication boundary, mixed and fluid film. Elastohydrodynamic

lubrication of piston rings is possible on the highly loaded expansion stroke, Rycroft et al [1997]. The lubrication of the overhead cam/follower has proved to be inherently poor. In the last twenty-five years most automotive manufactures have experienced operating problems with cam and follower lubrication and the engineering science background to this has been widely studied. The cam/follower interface is mostly lubricated under boundary, mixed and elastohydrodynamic regimes.

Engine bearings have smooth conforming surfaces that are relatively low stressed. Designers employ different configurations of oil feed holes and grooves to ensure the presence of fluid film between the bearing and shaft throughout the engine operation. Although the engine bearings mainly operate in the hydrodynamic lubrication regime, during engine start and stop conditions boundary lubrication may also play a role.

One way of improving engine efficiency and fuel economy is to reduce the energy losses generated by friction between the mechanical components. Detailed and demanding specification tests for fuel economy and engine durability are now being developed to determine whether the lubricant meets the requirements of the car manufacturers and legislators. These tests are expensive and thus any information that can be gained through modelling engine performance will aid the lubricant formulator and thus help cut the cost of lubricant development. But to make such modelling effective it is important to validate with engine performance data. This can be achieved through a series of tests and measurements in an engine test cell. Methods have been developed for measuring friction using bench tests and fired engines to study the behaviour of new engine component designs, materials and lubricants. Bench testing can provide rapid and cost effective results. Rotary bench tests including pin-on-disc and block-on-ring, can be designed to produce uni-directional rotary and reciprocating motion, involving a non-conformal contact geometry. The block-on-ring test has been used in laboratories for the evaluation of piston rings, liners, and cams/followers. However the main disadvantage of rotary bench test methods is that real engine components cannot be tested. One of the most widely used tribometers to analyse friction and wear is the Cameron-Plint TE-77. This provides reciprocating motion which makes it suitable for simulating piston/cylinder liner dynamics and a modified version is used to simulate piston liner movement using real engine specimens to evaluate cylinder bore coatings and different lubricants. The main advantage of this

bench test is that real engine components can be tested. Bench tests are also used to assess the tribological properties of energy conserving lubricants, including studies of base stock formulation, viscosity index improver and friction modifier.

As the engine environment cannot be completely simulated in bench tests, engine tests are often needed to verify and validate the findings. A number of different techniques have been used throughout the world to measure total or component engine friction. One of the techniques to measure total engine friction is to determine the difference between the engine indicated power and brake power. The indicated power is measured using the PV diagram and is dependent on the accurate measurement of cylinder pressure. The brake torque is measured by an engine dynamometer. Subtracting the above parameters results in total engine friction loss provided all the auxiliaries are independently driven. This method was not popular in the early stages, as the accuracy of cylinder pressure measurement and the procedure to determine the top dead centre was not very accurate.

In the motoring break down method, the engine is electrically motored and the power required to drive the engine taken as the friction power loss, Monaghan [1987]. Progressive strip down of the engine was used to give an idea of the contribution of different components. The method is still widely used today and is certainly a good way of monitoring the mechanical losses in the engine during a development program. But the results can be very misleading as the lubricant and metal temperatures and the cycle pressures are unavoidably different from those in the real fired engine. Also removing components can damage the operating environment of those remaining and so the change in motored torque is not a reliable measure of the friction of that component. For example removing second piston ring will change the oil flow in the whole ring pack. Thus this method cannot give a real picture of the frictional contribution of the tribological components in the engine.

The Morse test is carried out on multi-cylinder engines by measuring brake power produced by the engine, Monaghan [1987]. In this test one cylinder is cut out and the drop in measured torque at constant speed is used to deduce the frictional and pumping loss of one cylinder. Again this method suffers from inaccuracies due to changes in temperature and with many engines the action of cutting one cylinder will disturb the

fuel supply and the gas exchange process, which can severely effect the operations of other units.

The Run-out test is also used to measure total engine friction, Yang [1992]. In this test the engine is allowed to run under constant (stable) conditions and then the fuel injection is suddenly stopped for a few engine revolutions. The fuel injection is then started again to regain the same previous stable engine operating condition. The drop in engine velocity during the fuel injection interruption is measured and friction torque is then calculated.

In the Willans Line test method the fuel consumption is measured at a number of engine brake outputs at a constant engine speed, Yang [1992]. A graph is then plotted of fuel consumption against the engine BMEP (brake mean effective pressure) and extrapolated back to zero fuel consumption to determine engine friction mean effective pressure, read off from intercept with the BMEP axis. This technique relies on close control of the engine at very light loads.

After the mid 1980's, with the advancement in sensor technologies, experiments started on the tribological components directly under firing conditions. Measurements have been carried out on the friction contribution of piston assembly and valve train individually but until now no attempt has been made to measure the friction losses in all the main tribological components of the engine under firing conditions at the same time. Thus the exact percentage of the relative friction losses in the various engine components under firing conditions was not known.

It is generally accepted (Dowson et al [1987]) that friction losses associated with the piston assembly, engine bearings, and valve train account for typically 80% of the total mechanical losses. Further, the piston assemblies are recognized to be responsible for 50 percent or even more of the frictional power consumption. These figures depend on many factors including engine type and operating conditions. The valve train may have lower frictional losses than the other tribological components but has proven to be the most difficult to design and lubricate. To reduce engine friction, an accurate method of assessing friction levels through engine concept, design and development is paramount.

To understand the interaction between surfaces and lubricating oil and to validate any predictive friction model, very accurate friction force data is required, and to obtain this, sophisticated experiments need to be carried out. Truly representative results can only be obtained if experiments are undertaken on a real fired engine and the friction loss in each component is recorded.

1.2 OBJECTIVES OF THE RESEARCH PROJECT

The main aim of this research project was to validate an engine friction mathematical model called FLAME, over a range of load, engine speeds and lubricant temperatures, with a series of engine lubricants. The model was developed in a separate study by Yang [1992], later modified by Dickenson [2000] and comprises three parts, addressing each of the main tribological components (piston assembly, valve train and engine bearings). The validation was to be achieved by characterising the frictional losses generated from the major tribological components of a real fired engine by developing experimental techniques to determine simultaneously the power loss in each component of a single cylinder, four valve, Ricardo Hydra gasoline engine under fired conditions.

Specific aspects of the research programme to address the above were,

- Develop an experimental technique to measure average and instantaneous camshaft friction torque under fired conditions over a range of engine speeds, loads and lubricant temperatures. This technique was to be applied to the Hydra engine with minimum engine modification and the findings to be used to validate the FLAME engine valve train friction model.

- Experimentally measurement of piston assembly instantaneous friction using the IMEP (indicated mean effective pressure) method with an advanced data acquisition system. This method was to be applied with very little engine crankcase modification and by integrating the friction force over the complete engine cycle, allowing average piston assembly friction to be calculated. The experimental results then to be used to validate the FLAME piston assembly friction model.

- Determine engine-bearing friction indirectly from measuring the friction contribution from the other main tribological components. Total output torque was to be determined by the engine dynamometer and by measuring the cylinder pressures, the PV (pressure volume) diagram obtained, thus determining total engine friction. Knowing the piston assembly friction, valve train friction and total engine friction, the engine bearing friction is deduced, as the crankshaft does not drive the auxiliaries. The experimental result then to be used to validate the FLAME engine bearing friction model.

- Instrument the engine with a number of sensors to determine the parameters required to validate the FLAME engine friction model.

- Develop an advanced data acquisition system to measure and record data from a number of transducers, allowing simultaneous measurement of friction from major engine tribological components.

1.3 STRUCTURE OF THE THESIS

CHAPTER 1

This chapter looks into the engine friction tests carried out to monitor the friction losses in the engine using bench tests and also real fired engines, thus giving a short introduction of tests available or carried out in the last 2-3 decades. More detailed reviews are given in chapters three, six and nine for engine valve train, piston assembly and bearing friction respectively. The chapter also describes the structure of this research thesis.

CHAPTER 2

The first part of this thesis addresses the engine valve train friction loss and comprises three chapters (chapter two, three and four). Chapter two describes the existing FLAME engine valve train friction model to estimate the friction and the associated power loss generated between the cam and the flat-faced follower. The chapter

describes in detail the parameters required for the prediction of the central and minimum film thickness at the cam/follower interface. The model also predicts the friction power losses generated by the camshaft bearings (using the Short Bearing Mobility Method), the follower/guide and the valve/guide.

CHAPTER 3

In chapter three a number of experimental studies undertaken in the last three decades to study the friction losses at the cam/follower interface are described. Also explained in this chapter is a new experimental method allowing detailed analysis of single-cylinder engine valve-train friction. The technique allows instantaneous as well as average friction measurements to be carried out under both motored and fired conditions at any engine speed.

CHAPTER 4

The engine valve-train friction experimental results measured by using the technique described above and the predicted results obtained from the FLAME valve-train friction model outlined in chapter two are compared in chapter four. The effect of four different lubricants: SAE 0W20 with and without friction modifier; SAE 10W40 and SAE 5W30 with friction modifier, on engine valve-train friction loss is described in this chapter.

CHAPTER 5

The second part of this thesis addresses the friction contribution from the engine piston assembly. This part also comprises three chapters (chapters five, six and seven). Chapter five describes the mathematical model of friction loss generated by the compression rings by analysing hydrodynamic lubrication of a single ring and then applying the technique to the rest of the ring pack (excluding oil control ring). The chapter also describes in detail the friction model of the oil control ring/cylinder liner interaction and also the piston skirt/cylinder liner friction using a complex analysis that involves piston secondary motion.

CHAPTER 6

To validate the FLAME piston assembly friction model outlined in chapter five, the IMEP (indicated mean effective pressure) method was used to measure friction experimentally and is explained in this chapter. This experimental technique measures

instantaneous and average piston assembly friction with no major engine modification required, giving a true picture of piston assembly friction loss in a real fired engine. The instrumentation required and the commissioning of this experimental technique is described in detail in this chapter.

CHAPTER 7

The experimental results for piston assembly friction loss measured on a single cylinder Hydra gasoline engine using the IMEP method are described in chapter seven. The measured data are compared with the predicted results using the FLAME piston assembly friction model and the Leeds Piston Skirt Lubrication and Dynamics Analysis model, Chittenden and Priest [1993]. Also explained in this chapter are the effects of different lubricants, oil temperatures and engine speeds on the piston assembly friction loss.

CHAPTER 8

The third part of this research thesis addresses the frictional losses generated from engine crankshaft bearings and comprises two chapters (chapter eight and nine). Chapter eight explains the FLAME engine bearing friction model and presents the lubrication and frictional analysis of both the big-end and main bearings using the Short Bearing Mobility Method and the Finite Width Method.

CHAPTER 9

Chapter nine explains an indirect way of measuring engine bearing friction loss and the required instrumentation. The comparison of experimental and predicted results using the FLAME bearing friction model are also described in detail in this chapter.

CHAPTER 10

The final part of this thesis also comprises two chapters (chapters ten and eleven). In chapter ten the influence of lubricant temperature and engine speed on the engine component friction and also on the total engine friction has been analysed in detail, looking at the benefit of low and high viscosity lubricants. In this chapter the effect of two different lubricants on the engine component friction has been studied experimentally and the percentage contribution from each tribological component is described in detail.

CHAPTER 11

All the instrumentation and data acquisition system required to perform this research project, to measure simultaneously friction losses from the main tribological components of an engine is explained in great detail in chapter eleven.

CHAPTER 12

Finally the conclusions arising from this research work are listed in chapter twelve, along with suggestions for further development of techniques to measure power loss from other parts of the engine and refinement of the FLAME engine friction model.

All the Appendixes are given in the end of the thesis including copies of two published papers and two presentations (Appendix VI) given below,

Published:

- Mufti, R.A. and Priest, M, "Experimental and theoretical study of instantaneous engine valve train friction", Jour. Tribology, ASME 2003, vol 125(3), pp 628-637.

- Mufti, R.A. and Priest, M, "Experimental evaluation of engine valve train friction under motored and fired conditions", Tribological research and design for engineering systems, Proc. 29th Leeds-Lyon Symposium on Tribology 2002, Elsevier, Tribology series 41, pp 767-778.

Presentations:

- R.A. Mufti, "Experimental investigation of piston assembly, valve train and crankshaft bearing friction in a firing gasoline engine", Mission of Tribology Research 11, Institution of Mechanical Engineers, London, December 2002.

- R.A. Mufti, M. Priest and R.J. Chittenden, "Experimental and theoretical study of piston assembly friction in a fired gasoline engine", STLE annual meeting,

New York, April 2003. (The contents of this presentation to be submitted as a journal paper):

This thesis is divided into parts due to the complexity of this research project addressing the frictional losses in all the main tribological components of an internal combustion engine and for easy of understanding. To aid clarity three separate nomenclatures are tabled for each of the valve train, piston assembly and engine bearing friction parts.

PART I

ENGINE VALVE TRAIN FRICTION

Chapter two

ENGINE VALVE TRAIN FRICTION MODEL

2.1 INTRODUCTION

Yang [1992] developed an engine friction analysis, later modified by Dickenson [2000] called FLAME (Friction and Lubrication Analysis Model for Engines). It addresses friction losses in the three main tribological components: piston assembly, bearing and valve train. The valve train friction model presents the lubrication and friction for either the tapered cam and domed follower arrangement or the cam and flat faced follower system. It also addresses the contribution of power losses from the camshaft bearings, the follower/guide and the valve/guide interfaces. The model evaluates the component loading, film thickness, Hertzian stress, frictional torque and power losses at every instance around the complete engine cycle.

This chapter describes existing lubrication theories to estimate the friction and the associated power loss generated between the cam and the flat faced follower. The chapter covers the kinematics of the direct acting overhead cam mechanism, cam/follower loading, cylindrical Hertzian stress calculations and EHL (elastohydrodynamic lubrication) analysis for the prediction of the central and minimum film thickness. The model also predicts the power losses generated by the camshaft bearings using the Short Bearing Mobility Method described in Part III (engine bearing friction part), the follower/guide friction accounting for both boundary lubrication and full film lubrication and the valve/guide friction assuming it is generated by the shear of the lubricant between concentric working surfaces. Experiments were conducted on a Ricardo Hydra Gasoline Engine, a four-valve single cylinder research engine. Each camshaft is carried in three plain bearings. The inlet camshaft is slightly longer than the exhaust as it accommodates a rotating disk at the non-driven end used as a trigger for the ignition timing system.

2.2 KINEMATICS

The analysis of the kinematics of cams acting against domed and a flat faced follower systems can be found in Dyson and Naylor [1960]. Although the software is structured to analyse nearly all type of cam/follower arrangements, discussion here is confined to the direct acting cam and flat faced follower used in the engine under study and illustrated in the free body diagram figure 2.1.

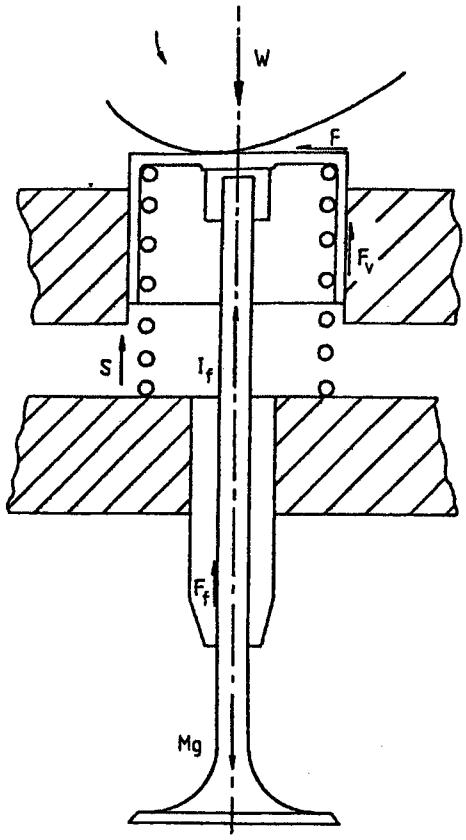

Figure 2.1. Overhead cam acting against a flat faced follower, Ball [1988].

Figure 2.2 shows the contact between a cam and flat faced follower. The cam is designated component number one and the follower component number two. In this study it is assumed that the follower does not rotate about 'Z' axis. The cam rotates about its centre O and O' is the instantaneous centre of the radius of curvature of the cam surface at the point of contact with the follower. The velocity of the follower in the 'Z' direction is given by

$$v = \frac{dI_f}{dt} = e\omega \qquad 2.1$$

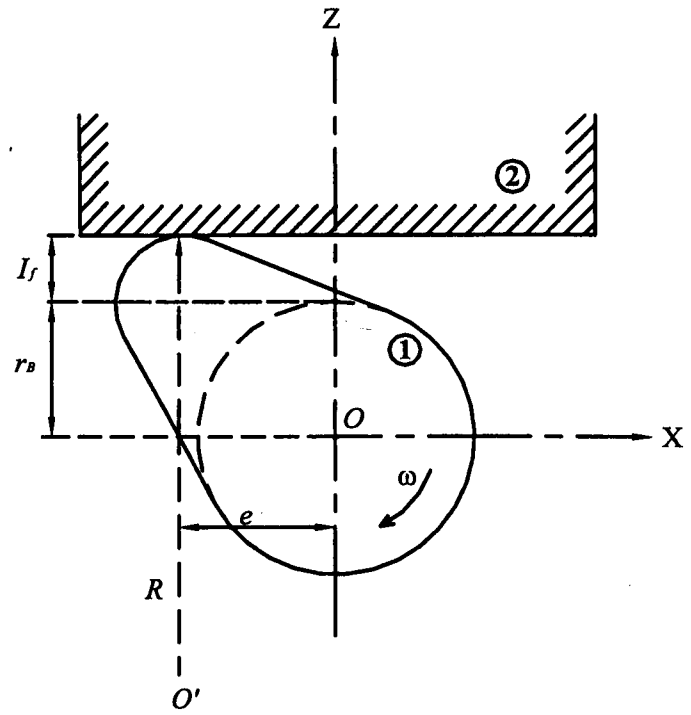

Figure 2.2. View of the cam and follower contact.

The follower can only move along the 'Z' axis, thus its velocity along the 'X' axis is zero. The acceleration can be similarly calculated as

$$a = \frac{d^2 I_f}{dt^2} = \omega \frac{de}{dt} \qquad 2.2$$

where e = eccentricity and I_f = cam lift

The entraining velocity of the lubricant is defined as the mean of the two surface velocities and is expressed as,.

$$V_e = \frac{1}{2}\left((u_1 - u) + (u_2 - u)\right)$$

or

$$V_e = \frac{1}{2}\left(V_C + V_f\right) \qquad 2.3$$

where

u is the velocity of the contact expressed as $\frac{-de}{dt}$. The negative sign indicates a decrease in distance 'e' as the point moves in the X direction, figure 2.2.

u_1 is the velocity of the cam at the point of contact and is given by,

$$u_1 = (r_b + I_f)\omega$$

u_2 is the velocity of the follower at the point of contact, which in this case is zero.

Thus the velocity of contact point with respect to the follower in X direction ,

$$V_f = u_2 - u = \frac{de}{dt} = \frac{a}{\omega} = \omega \frac{d^2 I_f}{d\theta^2} \qquad 2.4$$

Also the velocity of contact point with respect to cam in X direction,

$$V_C = u_1 - u = (r_b + I_f)\omega + \frac{de}{dt}$$

or $$V_C = \left[(r_b + I_f) + \frac{de}{d\theta}\right]\omega \qquad 2.5$$

As

$$\frac{de}{dt} = \frac{de}{d\theta}\frac{d\theta}{dt} = \frac{de}{d\theta}\omega \qquad 2.6$$

From equation 2.4 and 2.6

$$\frac{de}{d\theta} = \frac{d^2 I_f}{d\theta^2}$$

Hence equation 2.5 becomes

$$V_C = \left[r_b + I_f + \frac{d^2 I_f}{d\theta^2}\right]\omega \qquad 2.7$$

For flat faced follower the instantaneous radius of curvature is given by

$$R = \frac{V_C}{\omega}$$

Substituting equation 2.7 in the above equation, the instantaneous radius of curvature of a point moving along the cam is given by,

$$R = \frac{d^2 I_f}{d\theta^2} + I_f + r_B \qquad 2.8$$

The sliding velocity can be calculated as,

$$V_s = V_C - V_f$$

2.3 DYNAMIC ANALYSIS

To undertake lubrication and stress analysis for a cam/follower interface, the load at the contact needs to be determined. The forces associated with the operation of the valve mechanism are inertia force, spring force, forces due to dynamic deflection and damping of the components and friction between the moving parts. It is assumed that the valve train is rigid and therefore the dynamic deflections and damping characteristics of the system are neglected. The inertia force '*I*' is equal to the product of the equivalent mass of the reciprocating parts and the acceleration of these parts. The equivalent mass of the system is assumed to be the sum of the mass of the moving parts and one third of the spring mass. The inertia force is thus given by,

$$I = \left(M + \frac{1}{3}m \right) a$$

The spring force *S*, is equal to the product of the spring stiffness and the deflection of the spring from its free length;

$$S = k\left(I_f + \delta\right)$$

where δ is the initial displacement of the spring.

Summing loads in the vertical direction, neglecting component weight and friction

$$W = S + I$$

$$W = k\left(I_f + \delta\right) + \left(M + \frac{1}{3}m \right) \omega^2 \frac{d^2 I_f}{d\theta^2} \qquad 2.9$$

Where '*W*' is the applied load at the cam/follower interface. Full details of the analysis can be found in Ball [1988].

The valve train system considered has a hydraulic lash adjuster arrangement, keeping the cam and the follower in contact throughout the operating cycle. Thus over the cam base circle the resultant load will depend upon the lash adjuster fluid pressure, the plunger area and the check valve spring compression force. This has been estimated by multiplying the plunger area (153mm^2) by the cam inlet lubricant pressure (4bar), assuming the effect of check valve spring force is negligible.

2.4 CONTACT PRESSURE

Once the contact loading at the cam/tappet interface has been determined, the maximum Hertzian contact pressure and the dimensions of the contact area can be predicted according to the Hertz theory of elastic contact Hertz [1882], given the shape of the components. It can be shown that the contact between a cam and a flat-faced follower is geometrically equivalent to the contact of a cylinder of length (L) and radius (R) against a plane. Figure 2.3, shows a line contact between a cylinder and a plane with a Hertzian contact patch.

According to the assumptions of the Hertzian theory of elastic contact, that is;

- The bodies are elastic in accordance with Hooke's Law.
- The contact area is small with respect to the radius of curvature of the undeformed cylinder.
- Only normal pressures are considered.

It can be shown that the pressure distribution between the bodies, for a line contact is semi-elliptical, figure 2.4, and is given by;

$$p = p_{\max}\left[1-\frac{x^2}{b^2}\right]^{\frac{1}{2}} \qquad 2.20$$

Where b, is the contact half width;

$$b=\left[\frac{8WR}{\pi LE'}\right]^{\frac{1}{2}} \qquad 2.21$$

The equivalent radius of curvature R is expressed as,

$$\frac{1}{R}=\frac{1}{r_c}+\frac{1}{r_f}$$

As the follower radius of curvature r_f for a flat faced follower is infinity, the term ($1/r_f$) tends to zero. Maximum direct stress at the surface occurs at the centre of the rectangular boundary p_{max} and is expressed as,

$$p_{\max}=\frac{2W}{\pi Lb} \qquad 2.22$$

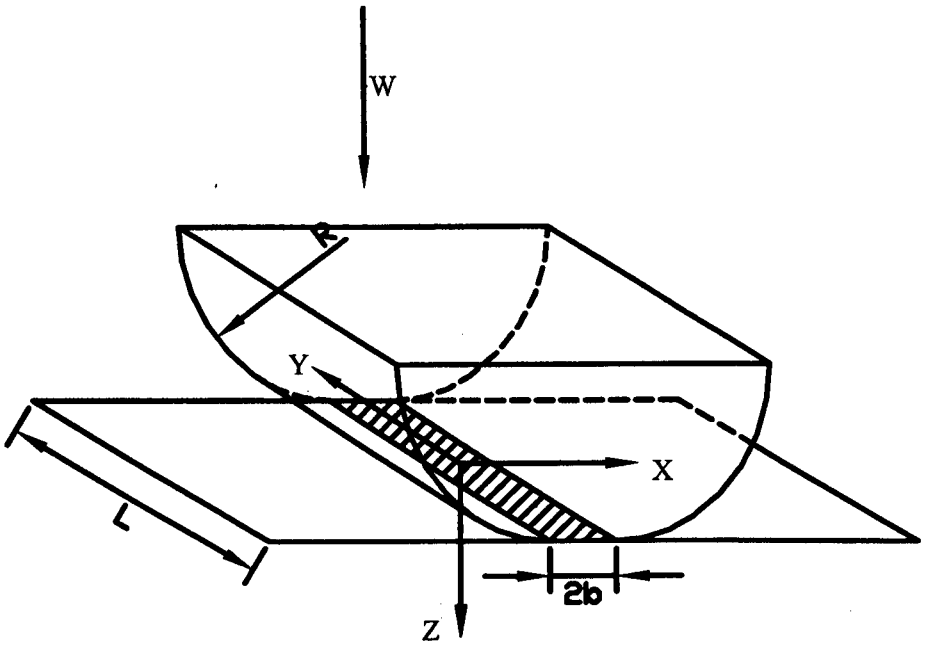

Figure 2.3. Contact between a cylinder and a plane with Hertzian contact patch

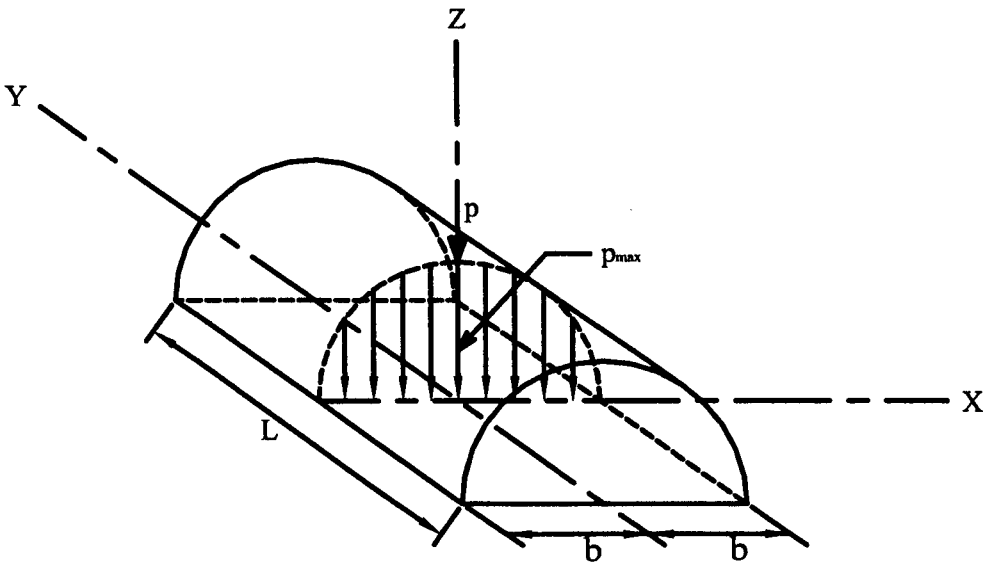

Figure 2.4. Semi-elliptical pressure distribution for a line contact

2.5 LUBRICANT FILM THICKNESS

The classical theory of hydrodynamic lubrication assumes that the surfaces are smooth and rigid and the lubricant is isoviscous. Applying this theory to the contact between a cam nose and follower results in the prediction of a very small minimum film thickness compared with the surface roughness of the cam and follower. The long service life of such heavily loaded components revealed that a different type of lubrication mechanism acts as a form of protection. This mechanism is called EHL (elastohydrodynamic lubrication). EHL takes place between non-conformal surfaces when very high pressures are generated at the interface resulting in elastic deformation of the contacting bodies. The pressure generated in the lubricant within the interface may be of the order of hundreds of mega-Pascals or even GPa, resulting in dramatic changes in the lubricant properties. At very extreme pressures the viscosity of the lubricant increases rapidly and the lubricant exhibits almost solid like characteristics.

The operating conditions at the cam/follower interface are very severe. Assuming that an adequate supply of oil reaches the contact, full separation of the contact is not guaranteed even with favourable elastohydrodynamic behaviour. The lubrication regime ranges from elastohydrodynamic through mixed lubrication to full boundary lubrication. Lubricant film thickness may be sensibly predicted in the first instance using elastohydrodynamic lubrication theory Taylor [1991].

Dowson and Higginson [1977] developed a formula for the minimum lubricant film thickness between two perfectly smooth cylinders in line contact

$$\frac{h_{min}}{R} = 2.65U^{0.70}G^{0.54}W'^{-0.13} \qquad 2.23$$

A similar formula was presented by Dowson and Toyoda [1979] for the film thickness at the centre of the contact,

$$\frac{h_{cen}}{R} = 3.06U^{0.69}G^{0.56}W'^{-0.10} \qquad 2.24$$

These formulae are not strictly accurate for the situation developed between the cam and follower interface as under such conditions squeeze film lubrication may also play a role. It has been recognised that squeeze film lubrication is very important around the parts of the cam cycle where the entrainment of the lubricant is small. However they,

are felt to be adequate for quasi-steady state analysis used in the qualitative analysis of engine valve train design.

Around the nose of the cam where the entrainment velocity is modest and loads high, some element of boundary lubrication may be anticipated. Boundary lubrication occurs when surface contact takes place over an area comparable to the area developed in dry contact. In such cases the friction is determined by the physical and chemical properties of the solids and lubricant at the common interface. Thus under such conditions the law of dry friction is often applied since the coefficient of friction is independent of load, viscosity, speed and contact area.

2.6 FRICTION FORCE AND POWER LOSS

Friction force between the cam and the follower is determined assuming an elastohydrodynamic lubricant film separates the surfaces and the interface is isothermal at any given instant. The elastic deformation between the cam and follower is large compared with the lubricant film thickness and therefore the contact pressures and dimensions can be approximated by a dry Hertzian contact. As the viscous friction force is proportional to the velocity gradient at the solid boundaries, by approximating the lubricant contact region between the cam and follower as a region of constant film thickness (h_{cen}), in the manner of classical elastohydrodynamic theory, and neglecting the contribution of any rolling friction, the sliding friction force may be predicted.

It is apparent that a change in pressure changes the lubricant viscosity. The relationship between pressure and viscosity is described well by Barus equation,

$$\eta = \eta_0 . e^{\alpha p} \qquad 2.25$$

where η = viscosity at pressure 'p'

η_0 = viscosity at atmospheric pressure and lubricant temperature.

α = pressure-viscosity coefficient.

Substituting the Barus relationship equation 2.25, for dynamic viscosity at elevated pressure and the assumed contact geometry we obtain for the friction force

$$F = \int_{-b}^{+b} \frac{\eta_0 V_s e^{\alpha p}}{h_{cen}} dx \qquad 2.26$$

Substituting equation 2.20, Hertzian pressure distribution across the contact in the above equation;

$$F = \frac{\eta_0 V_s e^{\alpha p_{max}}}{h_{cen}} \int_{-b}^{+b} e^{\left(1-x^2/b^2\right)^{\frac{1}{2}}} dx \qquad 2.27$$

In the Barus relationship the viscosity varies exponentially with pressure and thus at high pressures the viscosity term can become extremely large, predicting very high friction forces on the basis of equation 2.27. Lubricant analysts have indicated the existence of a limiting coefficient in highly loaded conformal contacts. This limiting coefficient of friction depends on the presence and type of friction modifier in the oil and the lubricant analysts carryout tests to estimate the maximum coefficient of friction that can reach under dry contact condition. Therefore at the cam/follower interface the friction coefficient cannot exceed the limiting valve and for this reason the model calculates the instantaneous coefficient of friction at each cam angle interval and compares this with a limiting value (μ_{lim}). If at any instance the coefficient of friction produced from this process is found to be greater than the pre- determined limiting value, the model calculates friction using the limiting value and boundary lubrication is assumed

$$F = \mu_{lim} W \qquad 2.28$$

The instantaneous power loss due to friction is simply the product of friction torque and cam angular speed. It can be integrated around cam cycle to give an average power loss,

$$H = \frac{1}{2\pi} \int_{0}^{2\pi} Fr\omega . d\theta \qquad 2.29$$

Where (r) is the perpendicular distance from the cam centre of rotation to the line of action of the friction vector.

2.7 CAMSHAFT BEARING PERFORMANCE

The Ricardo Hydra single cylinder gasoline engine has two camshafts, one for intake and one for exhaust. Each camshaft has two cams and is supported by three plain bearings and driven by a toothed belt via a pulley located at one end of the camshaft figure 2.5.

The camshaft bearing loads arise from the reaction and friction forces at the cam/follower interfaces and the pulley loading from the drive belt. Full calculation of these loads is a statically indeterminate problem which can be very complicated and time consuming to solve. Simplified assumptions are therefore often adopted, treating the camshaft as a series of separate, statically determinate rigid beams. The bearing loads can then be estimated assuming the only forces acting on the bearing are those present between neighbouring bearings. The pulley load on the camshaft bearings was estimated using a torque and force balance method, neglecting camshaft bearing friction torque Dickenson [2000]. This method underestimates the pulley load but this has negligible influence on the overall calculations, only introducing a small error in the loading of the camshaft bearing closest to the pulley.

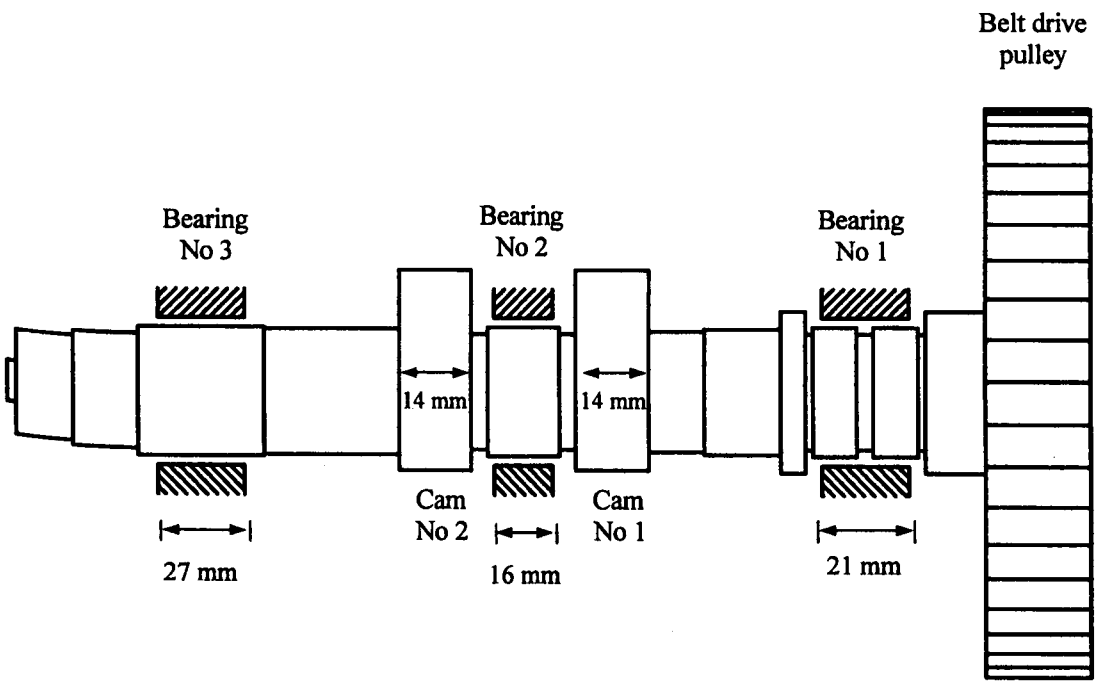

Figure 2.5. Ricardo Hydra Gasoline Engine camshaft layout

The camshaft bearings are subject to rapidly changing loads and are thus treated as dynamically loaded bearings using the short bearing mobility method, the length to diameter ratio being well within the limit of 0.7 for the application of the short bearing approximation. The bearing analysis does not take account of thermal and elastic deformation.

When predicting friction, the model has the option of considering a (π) or (2π) lubricant film. It has been shown Dickenson [2000], that the frictional power loss computed on the basis of viscous shearing of a complete (2π) film with a dynamically loaded bearing gives a fair approximation to the frictional power loss observed experimentally. A complete (2π) film was therefore used for the camshaft bearing losses in this study.

2.8 FOLLOWER/GUIDE INTERFACE FRICTION

The follower/guide friction may be modelled using either boundary or full fluid film lubrication analyses. This is dictated by the user and is strongly related to the lubrication and working conditions of the engine being studied.

The friction forces generated under boundary lubrication model are determined from a static balance of the forces acting on the follower, which is permitted to tilt in its guide. Full fluid film lubrication assumes that the follower and guide remain concentric and the clearance space filled with lubricant, figure 2.6. Friction is then determined from the simple shear of the lubricant film in a manner similar to the well known Petroff friction calculation for rotating plain journal bearings, the main difference here being that the motion is reciprocating rather than rotating. Figure 2.6, shows the schematic diagram of such a model.

The friction force due to the viscous shearing of the lubricant is simply given by;

Friction force = (Shear stress) (Shear area)

$$= \left(\eta \frac{V}{c}\right)(\pi d L) \qquad 2.30$$

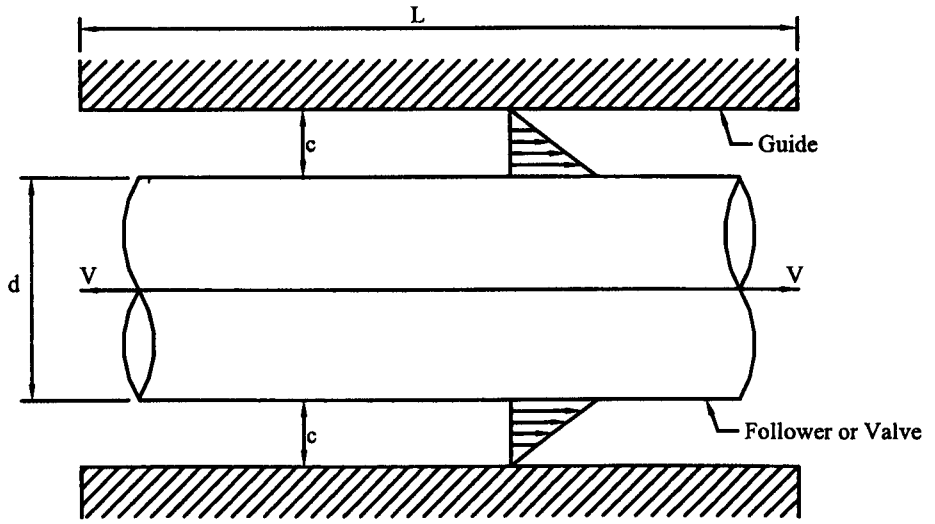

Figure 2.6. Schematic diagram of follower/guide or valve/guide friction by viscous shearing

Once the instantaneous friction force is known, the frictional power loss can easily be calculated. The average power loss over the cycle can be obtained by integrating the frictional power loss with respect to cam angle over one complete cycle and dividing the result by 2π radians.

2.9 VALVE/GUIDE INTERFACE FRICTION

The contribution of the friction loss generated by the valve stem/guide interface is normally very small compared with that of the rest of the valve train, but is included to complete the valve train friction model. It is assumed that the valve stem remains concentric in its guide and the only friction force generated is from the viscous shear and can be calculated in a similar way to the follower/guide friction.

2.10 COMPUTER PROGRAM

Computer aided analysis is regarded as a very effective and efficient tool in optimizing the design and thus the performance of the engineering components. Based on the theory of the valve train friction described above, a computer program has been

developed Dickenson [2000]. Some minor changes have been carried out to this code to suit the present case study. The code is designed to analyse the kinematics and tribological performance of a cam and flat faced follower mechanism and a tapered cam and domed follower system. It also addresses the performance of the camshaft bearing, follower/guide friction and the valve/guide friction.

Figure 2.7, shows the flow chart of the valve train friction model computer program. The computer program comprises of four main parts;

- The cam and follower lubrication analysis.
- Camshaft bearing performance analysis.
- Follower/guide and valve/guide friction modelling.
- Parametric study of a given design of cam/follower.

All input data is read through an input data file and the values are in SI units unless requested otherwise. An example of the FLAME valve train friction model input data is given in Appendix I. For the kinematic analysis the valve lift and its first and second derivatives are required. For the present study the valve lift data for the Ricardo Hydra Engine is given as discrete points with zero degree cam angle at the highest valve lift. The required derivatives were obtained by numerically differentiating the discrete cam lift data points with respect to cam angle and then digitally filtered using a Butterworth filter to remove any noise induced by the numerical process.

The program is designed to deal with cam and flat faced follower and tapered cam and the domed follower systems. The user can select any system when running the program. The program calculates all the parameters required to determine cam/follower friction using the theory described above. It also predicts the friction torque arising from the contact and the related power loss. Camshaft bearing performance analysis is carried out using the same program developed for the analysis of main bearings. Thus for the camshaft bearing calculation the software redefines the cam angle as from 0° to 360° for one revolution of the camshaft when it rotates clockwise starting from the maximum lift position. Camshaft bearing loads are calculated at 1° interval of camshaft rotation. The bearing frictional power loss against cam angle is calculated and to obtain average power loss integration is carried out through the complete cam cycle.

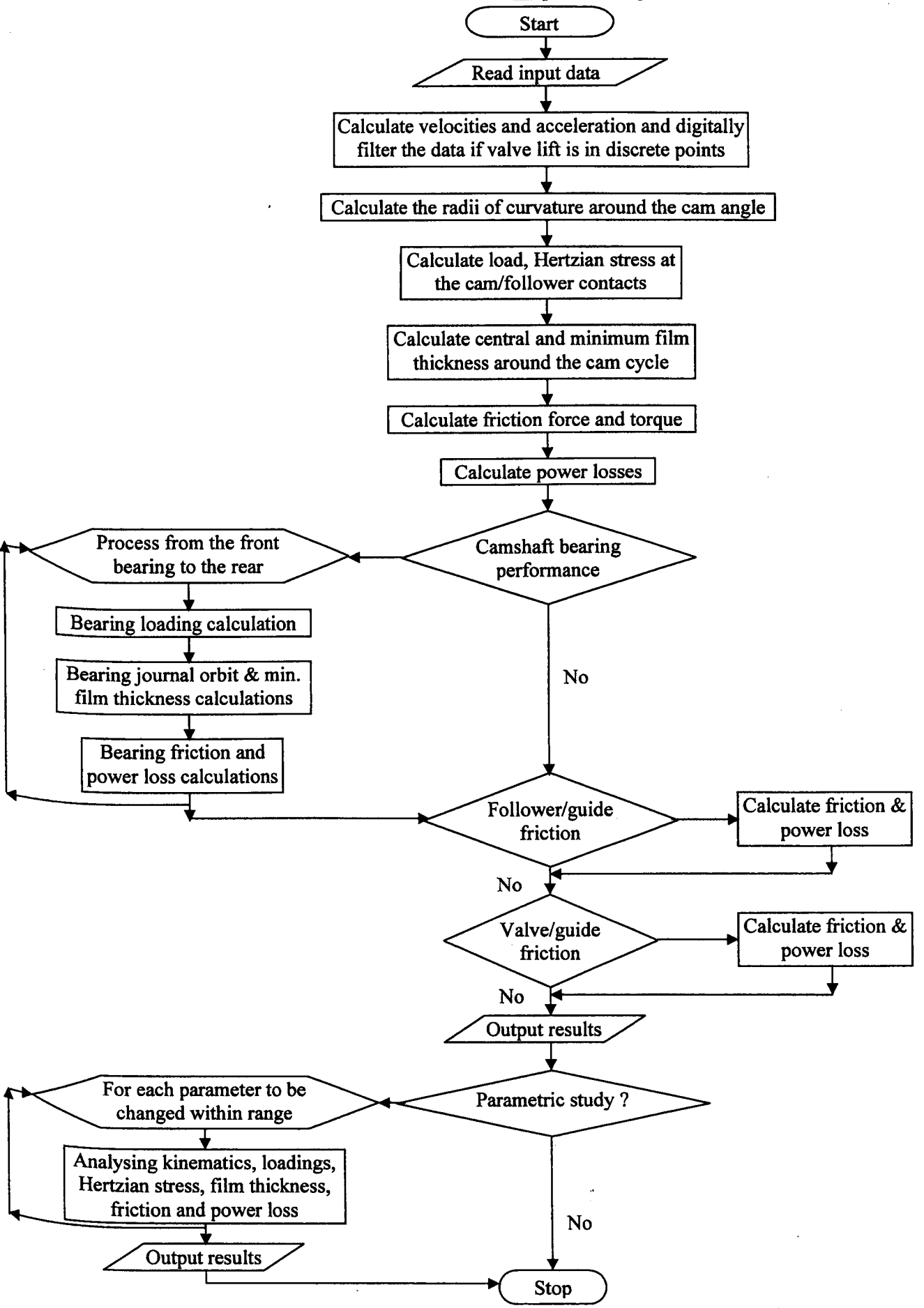

Figure 2.7. Valve train friction model computer program flow chart

For the friction and power loss analysis of the follower/guide interface, an option is given to the user for the selection of the method to calculate using either the boundary lubrication or the full film lubrication model.

The software also allows a parametric study to be carried out. The performance analysis of the valve train can be investigated by changing design parameters. These design parameters include the follower radius of curvature, the camshaft speed, the lubricant properties, the spring stiffness, the equivalent mass at the valve, the cam base circle radius and the cam width.

2.11 SUMMARY

A lubrication and power loss analysis of a cam and flat faced follower has been presented. It has also been demonstrated how the contact loading, Hertzian stress, EHL film thickness and the friction force can be calculated. A method for the prediction of the friction generated in the camshaft bearings using the dynamically loaded journal bearing lubrication analysis has also been outlined. The bearing friction loss was predicted using a complete film shearing approximation. The follower/guide and valve/guide interface friction have also been modelled.

For the validation of this FLAME engine valve train friction model, experiments were carried out on a real fired engine using a novel experimental technique explained in detail in the next chapter.

Chapter three

EXPERIMENTAL METHOD OF MEASURING ENGINE VALVE TRAIN FRICTION

3.1 INTRODUCTION

Internal combustion engine designers and lubricant analysis heavily rely on the computer based analytical tools. The sophistication and other complexity of these tools are growing rapidly. It is therefore important that the models, on which these techniques are based, are validated and continually improved by experimental techniques.

This chapter describes the development of a new experimental method used to investigate directly valve train friction as a function of crank angle with the help of a specially designed torque transducer. Also given in this chapter is the calibration of the apparatus and the instrumentation required for measuring the camshaft lubricant temperature. The details of the computer based data acquisition system and relevant software can be found in chapter eleven.

A number of experimental studies have been undertaken in the last three decades to study the friction losses at the cam/follower interface and the effect of lubricant properties and additives with regard to the failure of cams and followers.

Dyson and Naylor [1960] were possibly the first to report upon attempts to measure the friction at the cam/follower interface. Their apparatus incorporated a single flat-faced follower and cam arrangement. The follower was placed in a pair of instrumented flat springs and the deflection of this spring was used to measure the friction force, figure 3.1. It was reported that the arrangement was unsatisfactory due to the vibration of the flat spring.

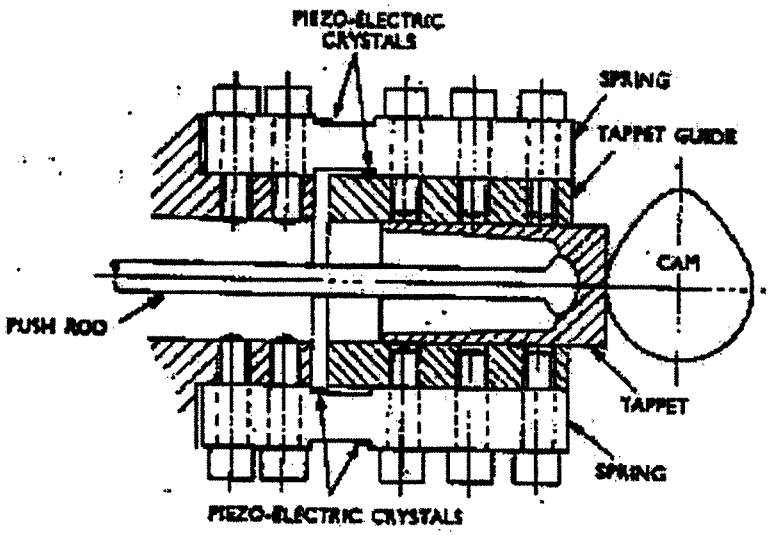

Figure 3.1. Arrangement for friction measurement of Dyson and Naylor [1960].

Armstrong and Buck [1981] measured the drive torque and power requirements of various types of valve train using a motored cylinder head with an in-line torque transducer. The power loss associated with the cam journal was evaluated by running the camshaft without the followers and no attempt was made to separate the friction torque from the geometric drive torque. Staron and Willermet [1983] used two different valve train arrangements to quantify the level of frictional loss in a 1.6 litre engine valve train and to assess the influence of lubricant viscosity and friction reducing additives on overall valve train friction. The cylinder head was driven via an electrical motor using an in-line torque transducer between the drive and the head. It was revealed that at lower speeds the camshaft bearing friction contributed significantly, friction losses in the valve train can be reduced by reducing spring tension and the use of friction reducing engine oil additives reduces friction substantially but oil viscosity has only a limited effect.

Ito, Yang and Negishi [1998] used a push rod cam/follower rig to simulate cam/follower operation. The cam/follower interface friction force was measured using an instrumented shaft that held the follower. The thrust force applied on the guide by the camshaft friction resulted in deformation of the housing shaft and thus the friction was measured directly, figure 3.2. It was reported that bending of the housing shaft and

the push rod could induce error in measuring the friction force. The results showed that the lubrication between the cam and tappet is predominantly in the mixed and boundary lubrication regimes and that abnormal wear is strongly connected to oil deterioration and high oil supply temperature.

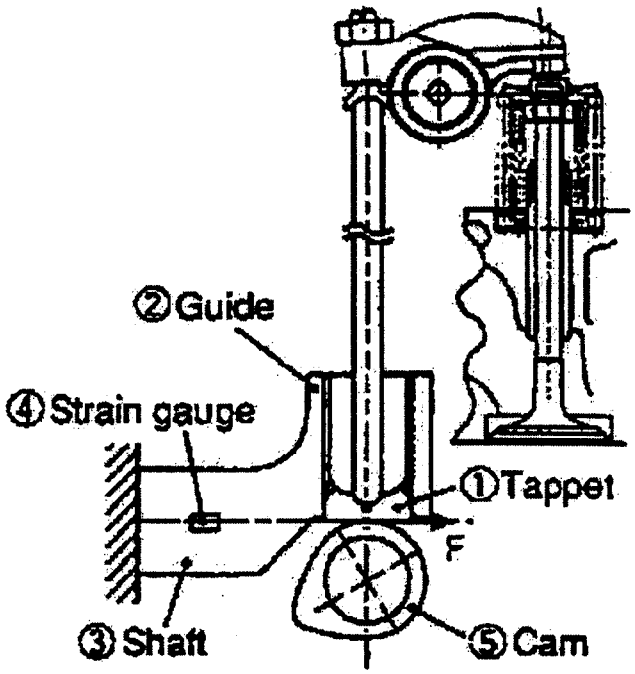

Figure 3.2. Friction measurement apparatus of Ito, Yang and Negishi [1998].

Ball et al [1986] compared the measurement of instantaneous and mean camshaft drive torque and auxiliary drive torque as a function of crank angle of a 1.6 litre four valve automotive gasoline and diesel engines using an instrumented belt drive pulley. It was shown that the camshaft instantaneous drive torque had peak amplitudes several times the mean level and that the belt tension had an adverse effect on the torque transducer output signal. Baniasad and Emes [1998] used a very similar procedure, demonstrating a new method of directly measuring average camshaft friction with exceptional accuracy and unprecedented convenience. The advantage of this method over previous techniques was that it could be run simultaneously with other engine development tests on either motored or fired engines, with little effort. The method used strain-gauged cam pulley spokes to measure the camshaft drive torque running at constant speed. It

was suitable for average friction torque measurement but not for instantaneous torque because of the adverse effect of belt tension on the instrumented pulley.

Dowson and co-workers [1989] measured the friction and power loss of a single cam and bucket follower and associated components in a motored rig. Instantaneous and average friction torque was measured using an in-line torque transducer. The thickness of the oil film between the contact was also monitored using electrical resistivity measurement between the cam and follower contact. This involved electrically isolating the camshaft using mica mounts. Experiments were carried out relating the influence of bulk temperature and camshaft rotational frequency with friction torque and power loss. The results were then compared with the predictions of a theoretical model. Pieprzak, Willermet and Dailey [1990] used a similar apparatus to measure the tappet/bore friction and camshaft drive torque for a direct acting bucket tappet. Tappet/bore and cam/tappet friction torque and friction coefficient as a function of cam angle were derived from the measurements. The camshaft drive torque was measured using an in-line torque transducer between the motor and the flywheel. The tappet/bore friction force was measured directly using a floating bore, consisting of an outer hardened steel sleeve supported by a linear bearing and an inner cast high silicon aluminium liner. A strain-gauge force sensor was installed to the steel sleeve by a quill, which restricted translatory motion to measure the friction force directly. It was concluded that the tappet/bore friction contributed significantly at low speed but diminished as the speed increased.

Crane and Meyer [1990] also studied the mechanical losses of two different gasoline engine valve trains. The first of these was a two valve per cylinder, single overhead camshaft engine with hydraulic direct acting followers. The other engine featured three valves per cylinder actuated from a single, overhead camshaft and rocker arms. The cylinder heads of these engines were removed and securely fastened to a test stand. A motor then drove the camshaft with an in-line torque transducer to measure the drive torque. This is a quick and relatively easy procedure to investigate valve train mechanical losses.

Monteil et al [1987] used the resistivity technique to measure the film thickness at the cam/follower interface. The electromotive force induced by the interaction of the cam

and follower surfaces was monitored. Thus small film thickness allowed more asperity contact resulting in large electromotive force to be induced. Base oil without any additives were used in the experiments to prevent the formation of reaction layers, which could change the resistivity across the contact.

Wakuri et al [1995] developed a rig to study the friction generated at the cam/follower interface, figure 3.3. A follower specimen was in contact with a cam specimen that was driven by an electric motor. The follower was held at the end of a rod supported with a spherical joint and loaded against the cam with valve springs through a needle roller bearing. A strain gauge sensor on the follower holder-rod detected the friction between the cam/follower contact.

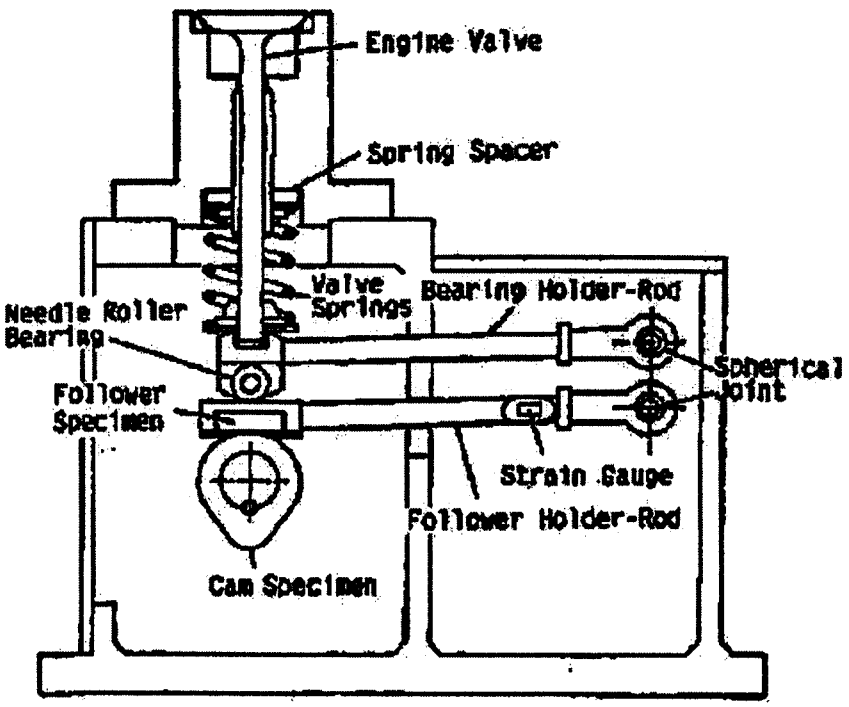

Figure 3.3. Cam/follower friction measurement apparatus of Wakuri et al [1995].

Teodorescu et al [2002] carried out experiments to analyse the friction in the push rod valve train of an internal combustion engine trying to separate the contribution of the different components to total friction losses in the valve train. The measurements were performed on a running engine. The engine valve train was instrumented with strain

gauge bridges on the rocker arm, the push rod and the camshaft to measure the forces and moments acting on these components, figure 3.4. It was concluded that the friction in the rocker arm bearing never reached hydrodynamic conditions and that the friction at the cam/tappet interface reduced with an increase in engine speed.

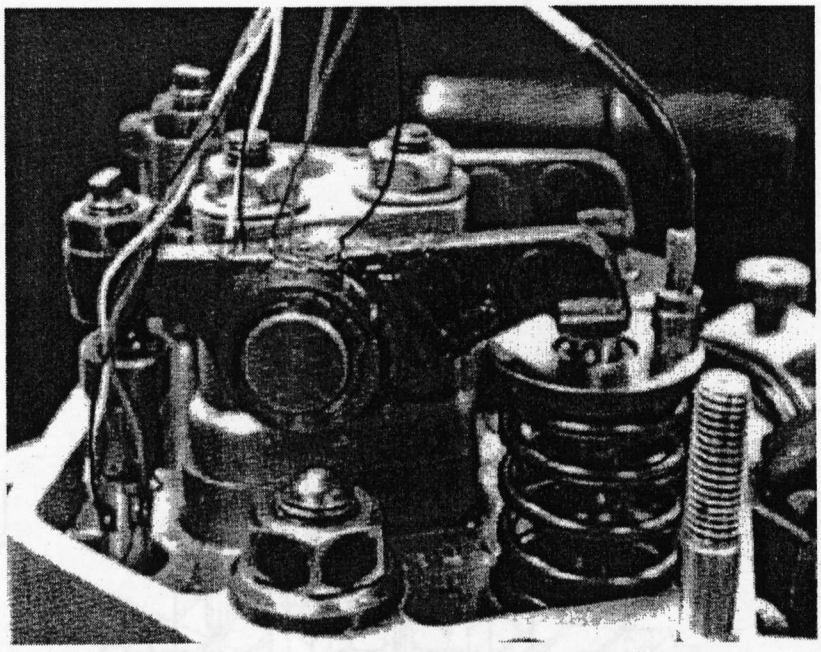

Figure 3.4. Instrumentation of the cylinder head of a diesel engine, Teodorescu et al [2002].

Harrison [1985] and van Helden el al [1985] independently developed similar apparatus in which the torque required to drive a single cam operating against a flat faced follower was measured using an in-line torque transducer. Van Helden and his co-workers calculated the theoretical geometric torque to give, by subtraction, the friction torque at the cam/follower interface. Zhu [1988] utilized a similar technique in an extensive study that employed an improved version of apparatus developed by Harrison [1985], figure 3.5.

Most of the experiments reported were carried out on test rigs under motored conditions. A new experimental method is described in this chapter, allowing detailed analysis of single-cylinder engine valve train friction. As the technique was implemented on a single cylinder engine, an in-depth study of valve train friction during

valve opening and closing was possible as the events are clearly differentiated. This technique allows instantaneous as well as average friction measurements to be carried out in both motored and fired conditions at any engine speed.

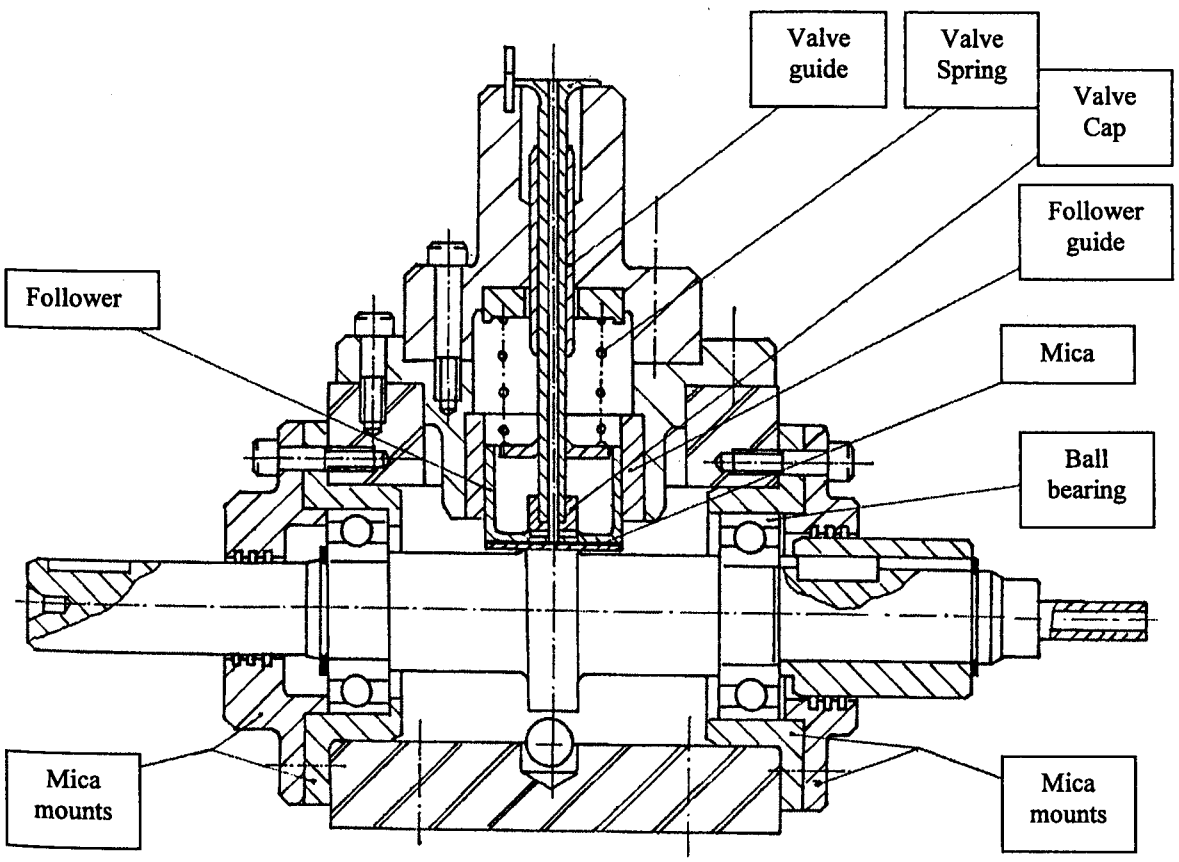

Figure 3.5. Test cell used by Zhu [1988] for measuring cam/follower friction.

3.2 ENGINE

The engine chosen for the experiments was a single-cylinder, four-valve Ricardo Hydra gasoline research engine derived from a standard production, four-cylinder, GM 2.0 litre engine. The engine has direct-acting overhead camshafts acting on flat-faced, hydraulic lash adjusted bucket followers driven by a toothed timing belt. The camshafts are short in length and both the cams are in phase, figure 3.6. An external, electrically driven pump supplies oil to the camshaft bearings and follower hydraulic lash adjusters. Full details of the engine and valve train can be found in Appendix I.

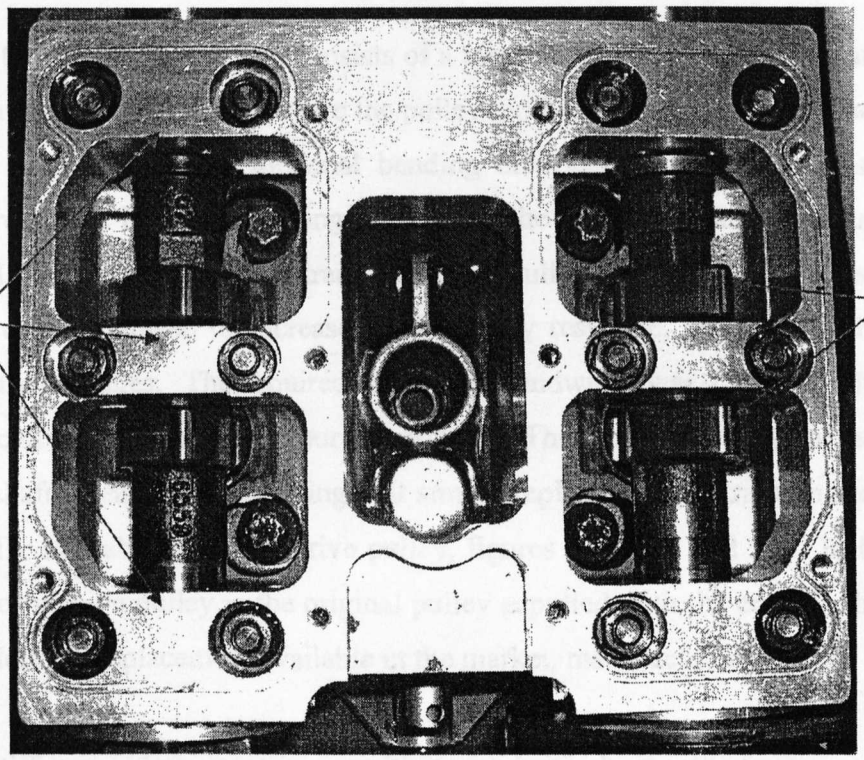

Figure 3.6. Ricardo Hydra single cylinder gasoline engine, cylinder head having two camshafts with cams in phase on each shaft.

3.3 CAMSHAFT TORQUE TRANSDUCERS

The torque sensing system was specially designed to integrate seamlessly into the original engine drive train arrangement and to be capable of evaluating both inlet and exhaust camshafts independently. The torque transducer model T311-111, was manufactured by Amber Instruments Limited (Dunston house, Dunston road,

Chesterfield, S41 9QD). The manufacturer was provided with complete details of the original valve train design and sketches of the required transducer design. The calculated Hydra engine valve train drive torque graph was also provided, obtained from the FLAME model, required to adjust transducer sensitivity and rigidity. The torque transducer is a two-part construction, with an instrumented central hub and a toothed pulley gear, figures 3.7(a) and 3.7(b). The transducer is designed in such a way that it can be fitted to almost any engine camshaft system. The torque transducer is fastened to the belt driving gear through elongated slots for cam timing adjustment. The belt drive gear is commercially available in different sizes for different engines.

The torque transducer central hub consists of a number of radial beams emanating from the drive hub to the outer flange where the pulley toothed gear is mounted. These radial beams are strain-gauged for torsional bending only. The multiple beams provide rigidity to resist the high side loading induced by the drive belt but with sensitivity to the applied torque in the drive train inducing pulley rotation. The mass of the transducer was minimised to increase its frequency response, resulting in the use of miniature strain gauges. The required transducer bandwidth was 15 Hz to 130 Hz and the manufacturers designed the sensor accordingly. The transducer does not require any additional shafts, bearings or couplings. It simply replaces the central hub section of a commercially available camshaft drive pulley, figures 3.7(a)(b) and 3.8. In figure 3.8 right-hand cam drive pulley is the original pulley supplied with the engine whereas the one on the left is a replacement available in the market, manufactured by Piper Cams.

Torsional stiffness and strain gauge sensitivity are critical aspects of torque transducer design. Bearing in mind that camshaft peak torque is considerably higher than the mean, the design requirement of the transducer was to be sensitive but also have high torsional rigidity to minimise undesirable torsional vibrations. A compromise was therefore required between sensitivity and rigidity. However the engine chosen to evaluate the technique is a single-cylinder gasoline engine with short inlet and exhaust camshafts, each having two cams in phase. Hence few torsional vibration problems were anticipated. Transducers were fitted to both shafts to simultaneously evaluate the frictional behavior of inlet and exhaust camshafts.

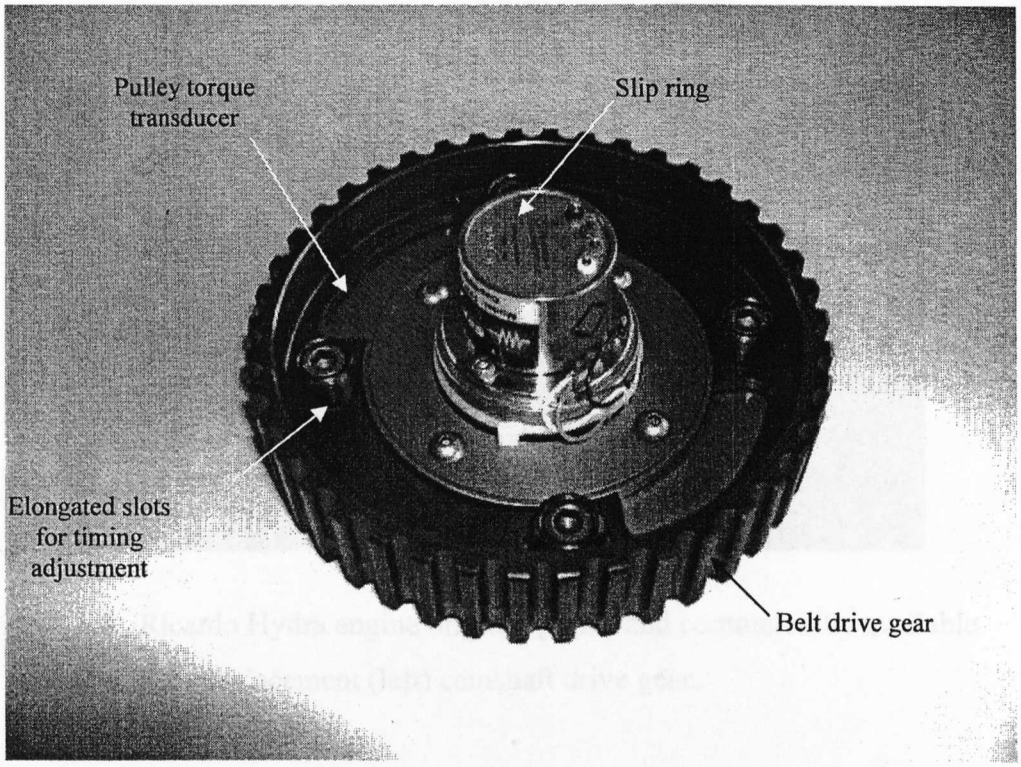

(a)

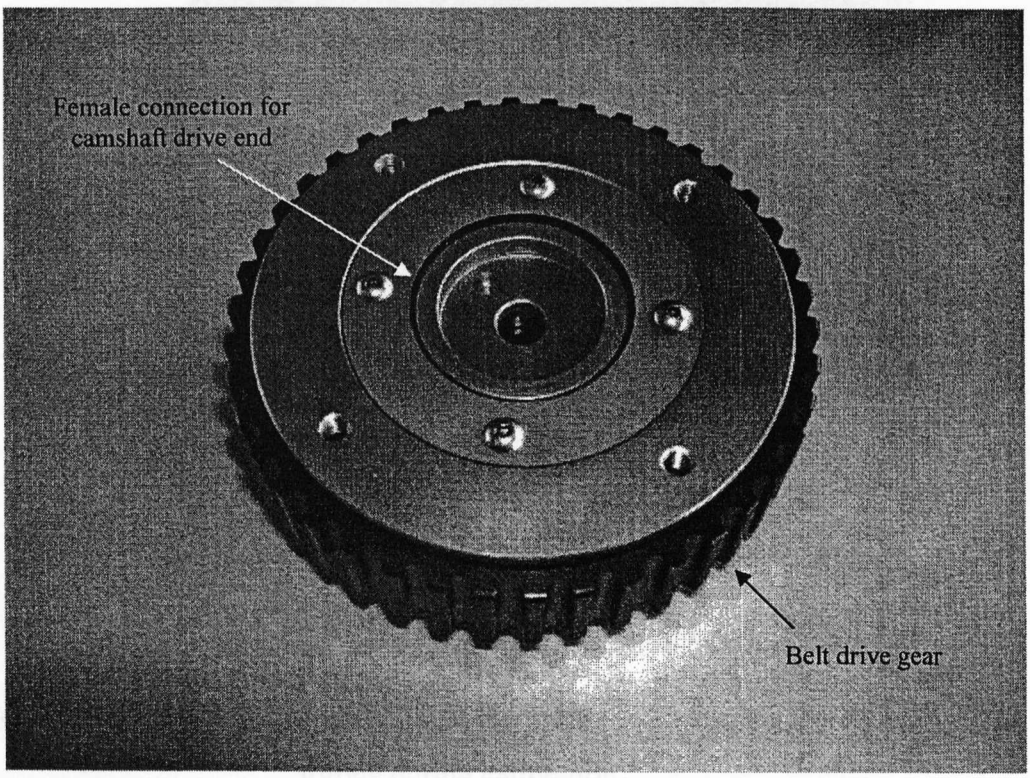

(b)

Figure 3.7. (a)(b). Camshaft pulley torque transducer attached to the belt drive gear.

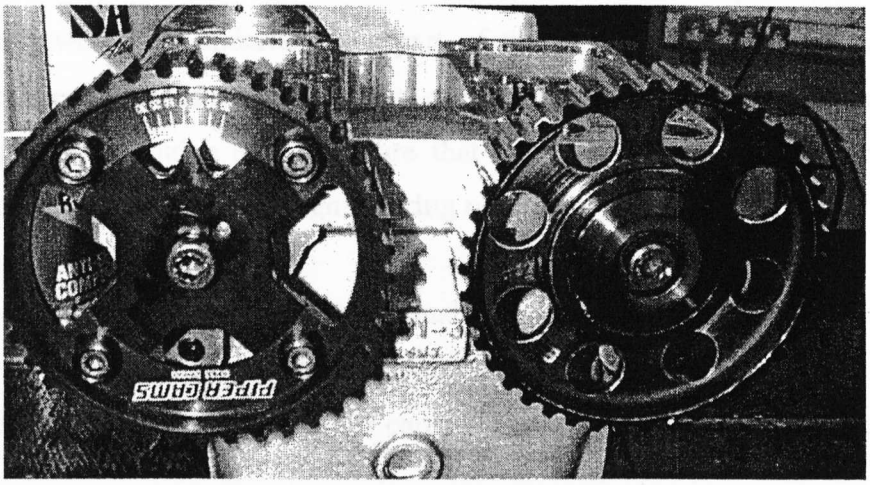

Figure 3.8. Ricardo Hydra engine original (right) and commercially available replacement (left) camshaft drive gear.

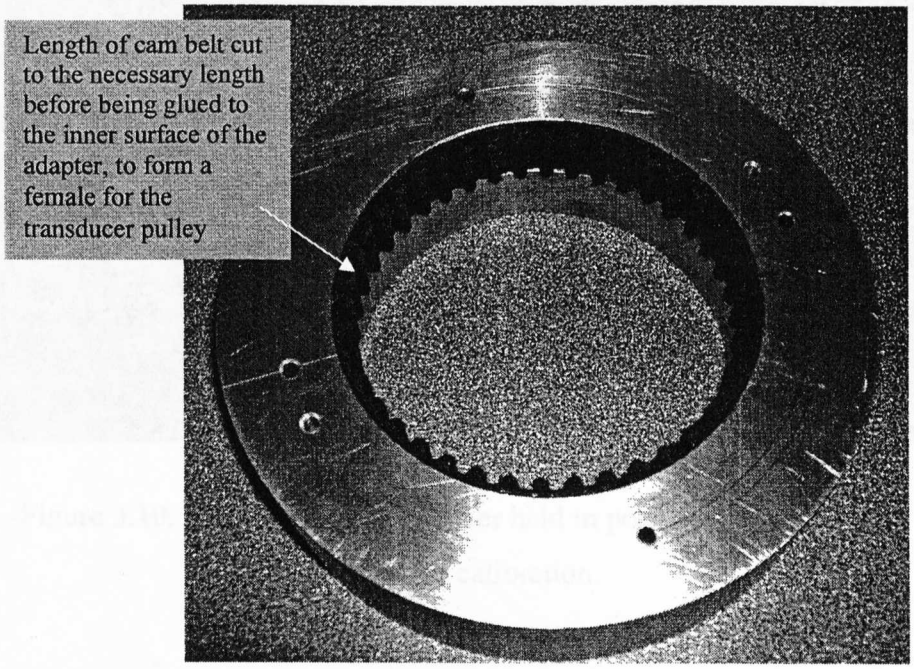

Figure 3.9. Female adapter designed to hold the pulley torque transducer to ensure pure torque during calibration.

3.4 PULLEY TORQUE TRANSDUCER CALIBRATION

The torque transducers were calibrated by the manufacturer prior to delivery. Additional tests were also undertaken as part of this research to establish accurate correlation between torque and output voltage over the range of applied torque expected in the Ricardo Hydra engine and to ensure that external factors such as drive belt tension did not influence the output signal during running.

Temperature effects were overcome conventionally through the use of a full Wheatstone bridge and temperature compensated strain gauges. The transducers were designed to be insensitive to belt loading through the careful arrangement of strain gauges in the bridge.

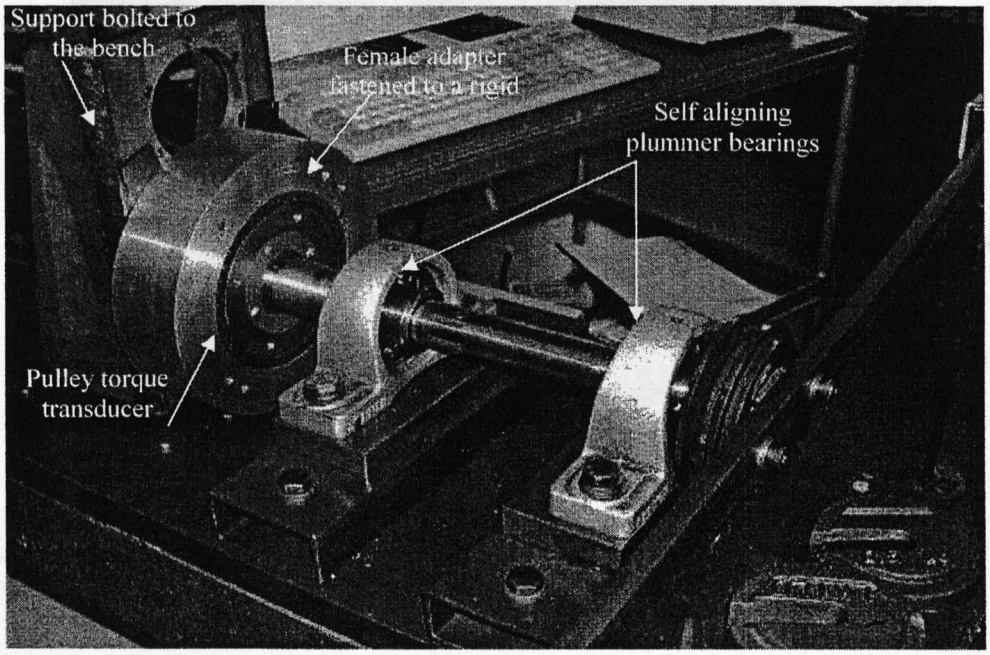

Figure 3.10. Pulley torque transducer held in position by the female adapter for calibration.

The transducers were statically calibrated by applying torque to the transducer hub, which was held steady in a specially designed female adapter, figure 3.9, resulting in pure torque being applied to the sprocket. As shown in figure 3.10 and 3.11, one end of a shaft was attached to the transducer hub whilst a torque was applied to the other end using a simple bar and weight hanging arrangement. The shaft was supported by two

ball bearings in plummer block mounts. The calibration was carried out in ten steps in both clockwise and anti-clockwise directions over a torque range of ±20Nm, figure 3.12. By measuring the output voltage on the amplifier for each applied torque, a relationship was established between torque and the output voltage. The average of three calibration readings were taken and the slope of the linear regression line, equation 3.1, through the data points, was calculated relating the output voltage to the camshaft drive torque, equation 3.2 and 3.3. The friction torque of the ball bearings was assumed to be negligible in comparison to the applied torque.

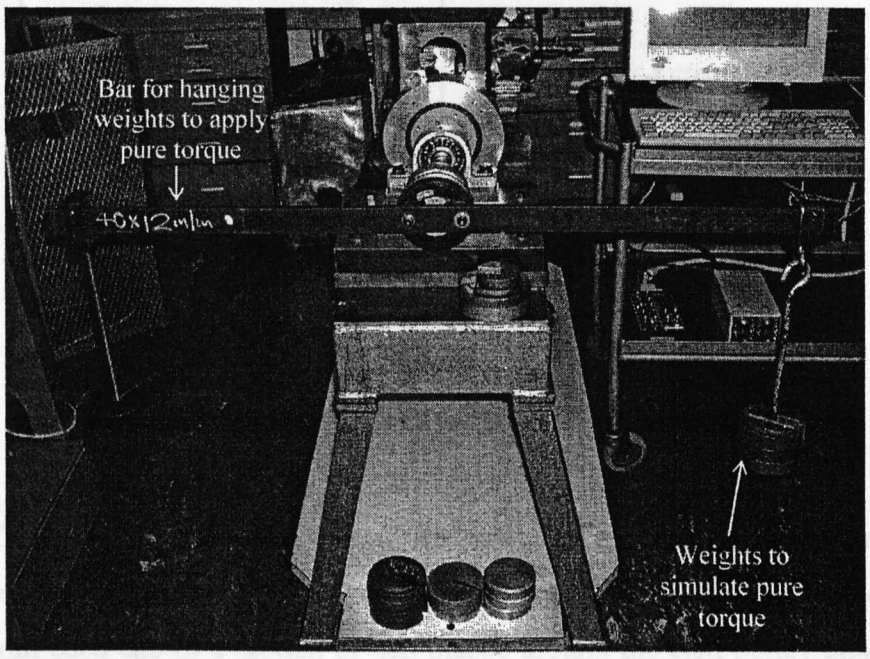

Figure 3.11. Pure torque applied to the pulley torque transducer by hanging weights for calibration.

$$\text{Slope} = \frac{n\Sigma xy - (\Sigma x)(\Sigma y)}{n\Sigma x^2 - (\Sigma x)^2} \qquad 3.1$$

The resulting equations relating the transducer output voltage to the applied torque are given by:

Inlet camshaft drive torque = 2.041× Output voltage 3.2

Exhaust camshaft drive torque = 2.032× Output voltage 3.3

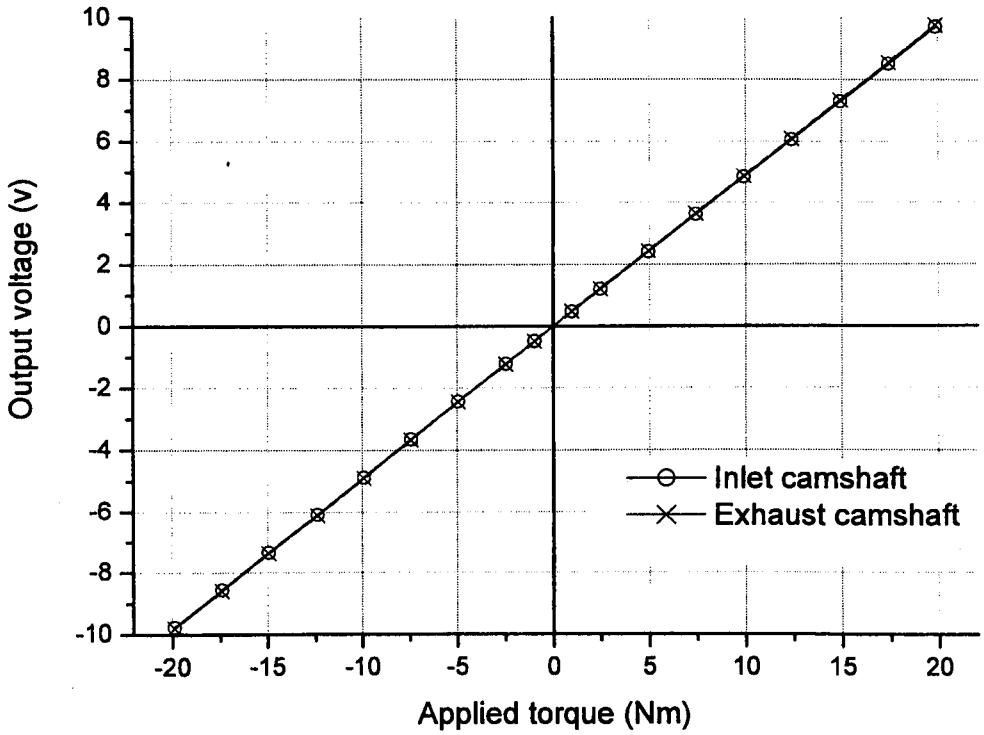

Figure 3.12. Pulley torque transducer static calibration

The effect of belt loading on the transducer was evaluated by applying a simulated belt tension as shown in figure 3.13. A mass of 5kg, equivalent to the cam belt tension, was suspended from each end of a section of belt placed around the cam pulley attached to the transducer hub. There was no applied torque and thus the desired outcome was a zero torque signal from the transducers. Readings were taken at 45° intervals of transducer rotation with many repeats. The results are shown in figure 3.14. Clearly belt loading does not have a significant effect on the output reading of either transducer, with an absolute torque error of less than 0.06Nm for instantaneous drive torque and 0.03Nm error for cyclic average drive torque. Whereas the relative torque error is much less than these values, 0.03Nm for instantaneous and less than 0.02Nm for average, determined by the test repeatability.

The engine drive train layout with the torque transducers in-situ is shown in figure 3.15. The drive belt safety guard, not shown, was used to prevent the slip ring units from rotating.

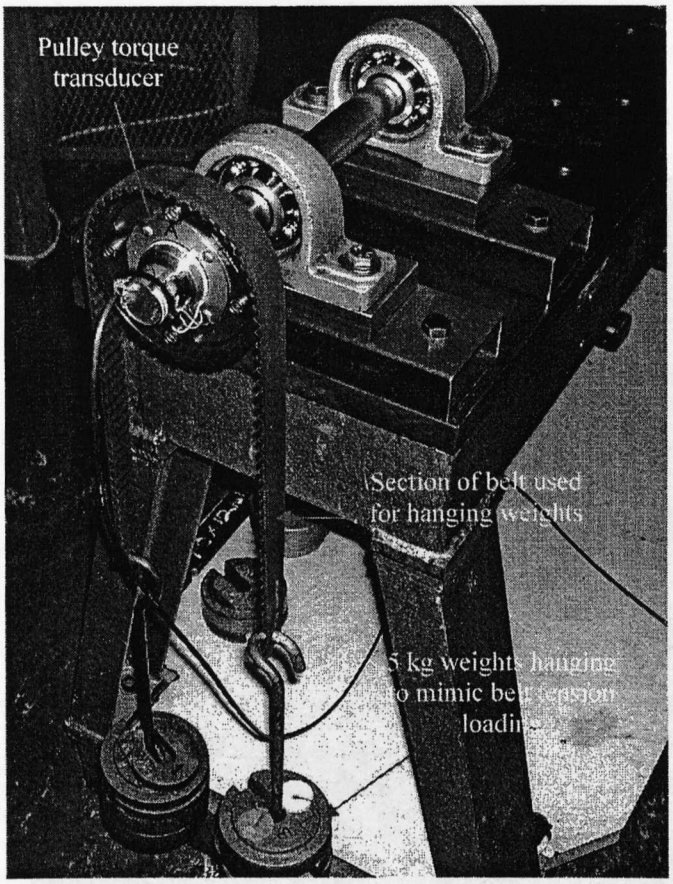

Figure 3.13. Mass suspended from pulley torque transducer to simulate belt loading

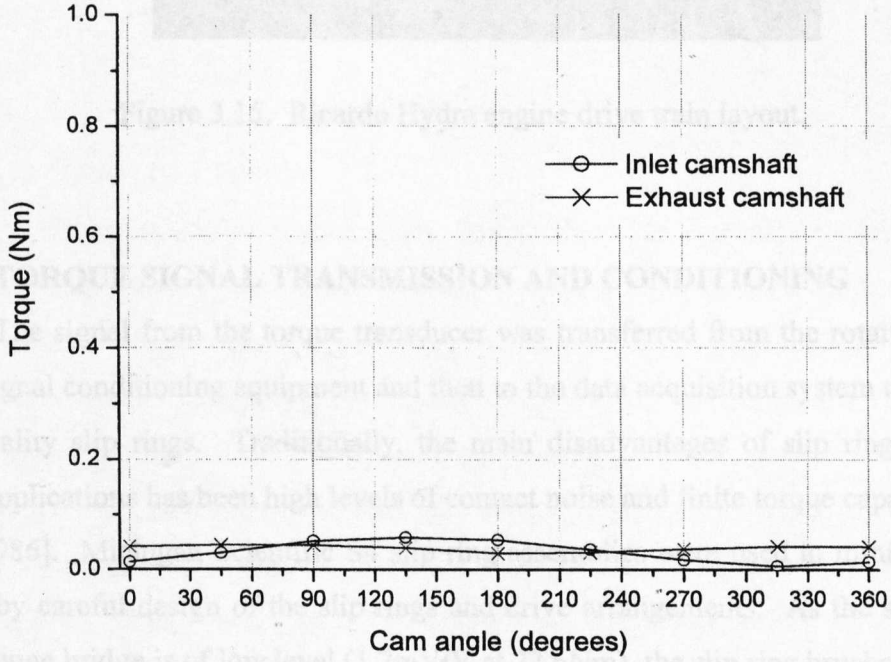

Figure 3.14. Variation of transducer output with pulley orientation under belt loading

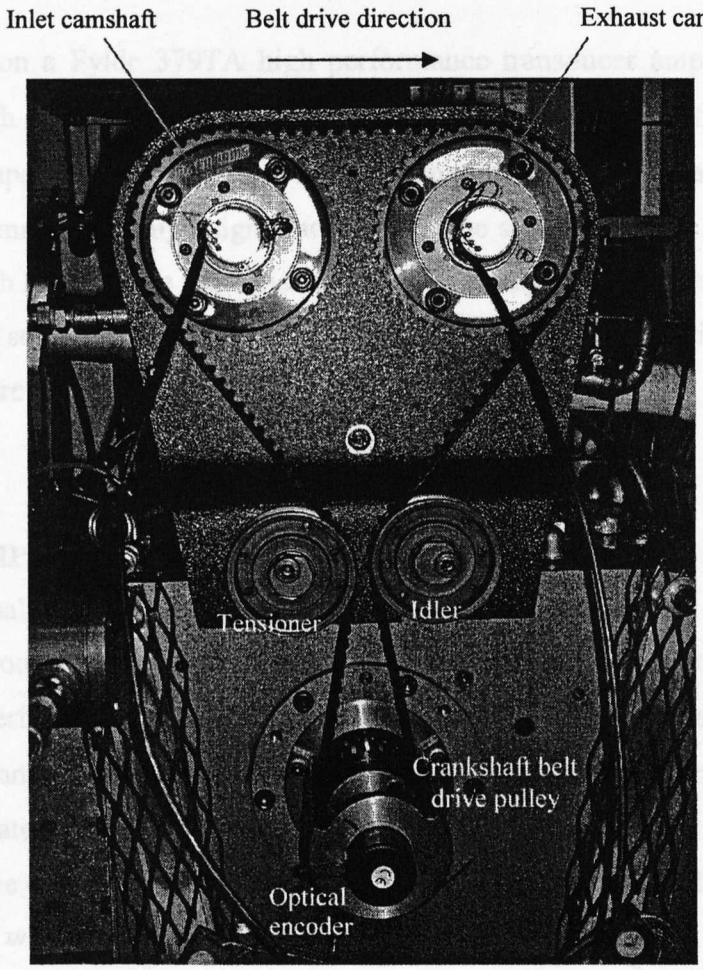

Figure 3.15. Ricardo Hydra engine drive train layout.

3.5 TORQUE SIGNAL TRANSMISSION AND CONDITIONING

The signal from the torque transducer was transferred from the rotating system to the signal conditioning equipment and then to the data acquisition system through the high quality slip rings. Traditionally, the main disadvantages of slip rings in strain gauge applications has been high levels of contact noise and finite torque capability Ball et al [1986]. Michigan Scientific S4 slip ring assemblies were used to minimise these effects by careful design of the slip rings and drive arrangements. As the signal from strain gauge bridge is of low level (1.2mV/V at 22.6Nm), the slip ring brushes and rings are made of precious metals that minimise noise, thus enabling the assemblies to be used for low level instrumentation signals. In addition, a high-grade stainless steel case ,

provides protection from dust and other contaminants and permanently lubricated low friction bearings are used to eliminate the need for routine cleaning and maintenance.

For this application a Fylde 379TA high performance transducer amplifier was used because of its high signal/noise ratio, high frequency response, low drift with time and high frequency capability. To use the complete range of the 12-bit analogue to digital converter and to maintain a high signal/noise ratio, the signal from the transducer was amplified to a high level before transmission to the data acquisition system. The gain of the amplifier was set to 900 and a 30-minute warm up period was specified before any measurements were taken.

3.6 OIL TEMPERATURE MEASUREMENT

An external heating and cooling system was used to control the engine oil temperature. In order to closely monitor and control the oil inlet temperature to the cam/follower interface, specially designed feed nozzles were used to supply small amount of lubricant directly from the oil heater to each cam/follower interface bath. Lubricant temperature was monitored at two separate locations, at inlet to the camshaft bearings and at the centre of the tip of the oil feed nozzle to the cam/follower interface. The temperatures were measured using 'K' type thermocouples.

3.7 OPTICAL ENCODER

A 755 series optical encoder from British Encoders was used to determine the cam/crank angle and to act as an external sampling clock for the data acquisition system. This particular encoder gives high accuracy, $\pm$ 0.017°, and 720 incremental pulses per revolution triggering data capture at every 0.5° crank angle. The encoder also produces an index TTL signal, once per revolution at the engine TDC position. The encoder was fitted on the forward end of the crankshaft through a flexible nickel bellows coupling. The advantage of this type of bellows coupling is that it can simultaneously compensate for parallel and angular shaft offsets. As parallel misalignment is accommodated by lateral displacement, the bellows coupling can handle severe alignment errors.

3.7.1 OPTICAL ENCODER INSTALLATION AND ENGINE TDC POSITION

The encoder is used to determine cam/crank angle not only for camshaft friction measurement but also for bearing and piston assembly friction. The accuracy of the measurement of piston assembly friction, using IMEP (indicated mean effective pressure) method explained in chapter six, greatly depends on how accurate the encoder is fitted. It has been reported in previous work Brown [1967] that for measuring engine IMEP resolutions greater than 1.0 degree could be adopted without serious loss of accuracy. The phasing sensitivity and the accuracy of measuring IMEP and PMEP (pumping mean effective pressure) largely depends on the calculation and shape of the engine pressure-volume diagram. Engines with low to moderate rates of pressure rise are more tolerant of pressure-volume phase errors than those with extreme rates of pressure rise. For diesel engines Brown [1967] showed that phase accuracy of the order of 0.1° crank angle was required to keep IMEP errors less than 1%. The tolerance can be relaxed to 0.2° to 0.3° crank angle for data taken from most spark-ignition engines, Lancaster et al [1975].

For the above mentioned reasons it was deemed necessary to adjust the encoder incremental and index mark signals with the engine TDC position to within 0.1° crank angle. A method widely used and described by Lancaster, Krieger and Lienesch [1975] was adopted to determine engine TDC position.

To determine the engine TDC position accurately, a dial gauge having a resolution of 0.001 mm was used to monitor the vertical position of the engine piston crown. An initial estimate of TDC was made using the dial indicator to locate the highest point of piston travel and aligning the encoder index and incremental pulse at this position. As the piston position changes very slowly with crank angle near TDC, marking the exact point of TDC position is very difficult, thus the dial gauge reading gave the initial TDC position within an estimated accuracy of ±0.4° crank angle. The encoder shaft and the crankshaft were locked at this point. More accurate location of engine TDC was determined by taking the dial indicator reading at a crank position where the piston position changes rapidly with crank angle, around 60° crank angle before and after TDC. Reading the encoder incremental pulse, the engine was rotated by hand to 100° crank angle BTDC and then moved back towards TDC, stopping at 60° BTDC. The

dial reading was recorded at this position. The engine was then rotated to 100° ATDC and moved back towards TDC again stopping at 60° ATDC. The dial gauge reading was recorded again. Measurement of the piston position was performed on both sides of TDC in order to reduce any systematic error Eriksson [1998]. The engine TDC offset was thus the midpoint between the two dial gauge readings. Releasing the encoder coupling and preventing the encoder shaft from moving, the engine was rotated via a 1.5metre long torque bar to remove the dial offset reading. The bar along with the dial gauge allowed movement of the engine with a resolution of nearly 0.01° crank angle. After removing the offset the encoder shaft and the crankshaft were locked together ensuring the encoder index and related incremental TDC signal corresponding with the engine TDC position, figure 3.16. This method was repeated a few times and the engine and encoder TDC position were adjusted to within ±0.03° crank angle.

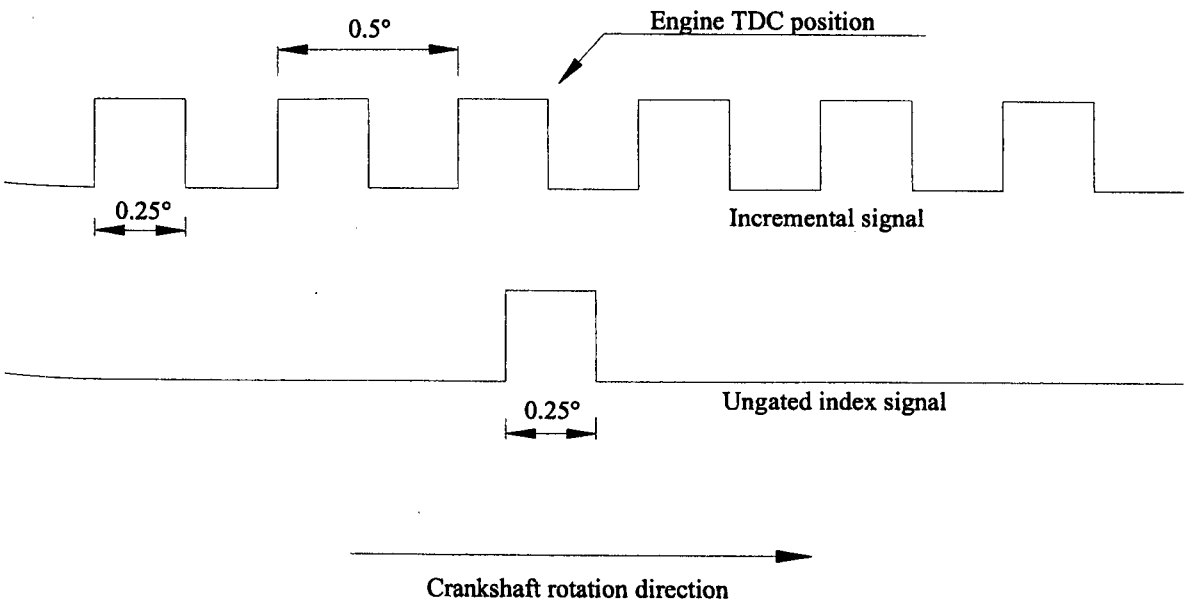

Figure 3.16. Encoder Index and related incremental mark aligned with the engine TDC position.

3.8 CAMSHAFT MASS MOMENT OF INERTIA

As the Ricardo Hydra engine is a single cylinder engine it was important to take into consideration the speed variation of the camshaft throughout the complete engine cycle. Under motored conditions the camshaft angular velocity is nearly constant and the camshaft pulley torque transducer measures a drive torque consisting of cam/follower valve frictions, geometric torque and camshaft bearing friction. But under fired conditions, with variable camshaft angular velocity, the camshaft inertial torque effect also influences the pulley transducer measured drive torque signal.

To accurately determine the cam/follower friction under fired conditions, it was vital to establish the inertial torque. This was carried out by calculating the camshaft assembly mass moment of inertia and measuring the angular speed of the camshaft throughout each experiment.

The mass inertia of the camshaft assembly is the mass inertia of camshaft and everything connected to it. Thus the assembly consists of the camshaft and that part of the pulley torque transducer drive arrangement inboard of the strain gauges, i.e. transducer female adapter where the camshaft is connected, the radial beams where the strain gauges are installed and the slip ring drive. The inlet camshaft is slightly different to the exhaust camshaft in that it is slightly longer as it drives an optical disk unit for engine ignition timing. The disk is connected to the rear end of the camshaft and its inertia was also included in the overall camshaft assembly inertia. The mass inertia of the camshaft assembly was calculated using a solid modeling package, AutoCAD 2000, figure 3.17(a) and 3.17(b).

Inlet camshaft assembly inertia:
2.113×10^{-5}(optical disk) + 1.317×10^{-4} (camshaft) + 0.185×10^{-3} (part of pulley torque transducer) = 3.382×10^{-4} kg-m^2

Exhaust camshaft assembly inertia:
1.255×10^{-4} (camshaft) + 0.185×10^{-3} (part of pulley torque transducer) = 3.108×10^{-4} kg-m^2

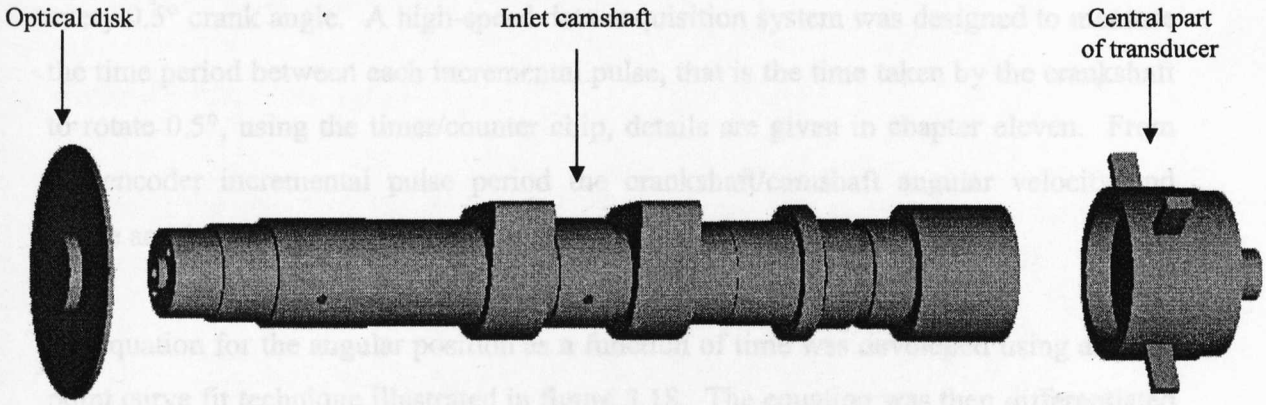

Figure 3.17(a). Inlet camshaft assembly, not to scale, (Optical disk + camshaft + central part of pulley torque transducer).

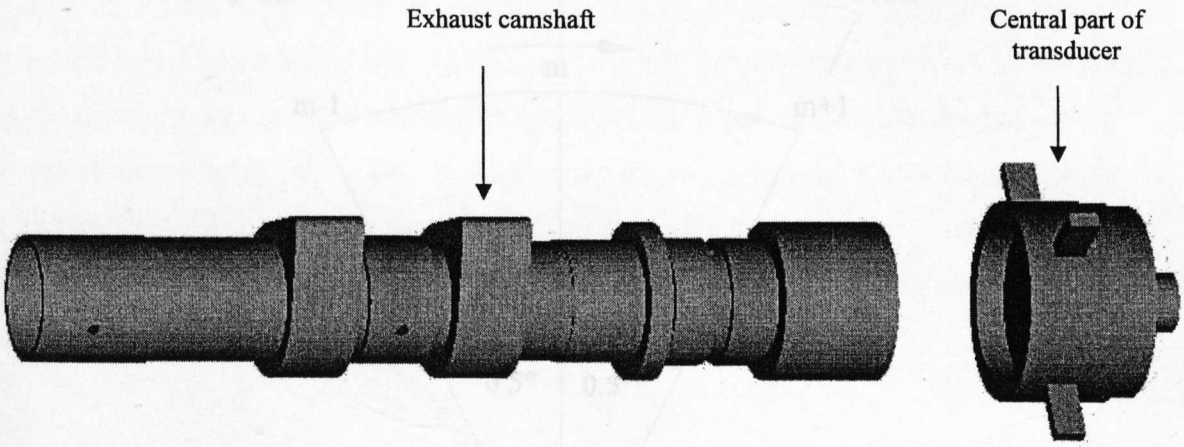

Figure 3.17(b). Exhaust camshaft assembly, not to scale, (camshaft + central part of pulley torque transducer).

3.8.1 CRANKSHAFT/CAMSHAFT ANGULAR POSITION, VELOCITY AND ACCELERATION

The encoder index pulse was used to determine engine TDC crank angular position whereas the incremental pulse was used to sample the analogue channels at every 0.5° crank angle. A high-speed data acquisition system was designed to measure the time period between each incremental pulse, that is the time taken by the crankshaft to rotate 0.5°, using the timer/counter chip, details are given in chapter eleven. From the encoder incremental pulse period the crankshaft/camshaft angular velocity and hence acceleration was calculated.

An equation for the angular position as a function of time was developed using a three-point curve fit technique illustrated in figure 3.18. The equation was then differentiated with respect to time to calculate and crank angular velocity equation 3.4, and acceleration equation 3.5. The time period of each incremental pulse was measured using a 20MHz clock on one of the data acquisition boards. The camshaft angular velocity and acceleration are half that of crankshaft because of the 1:2 speed ratio of the timing belt drive.

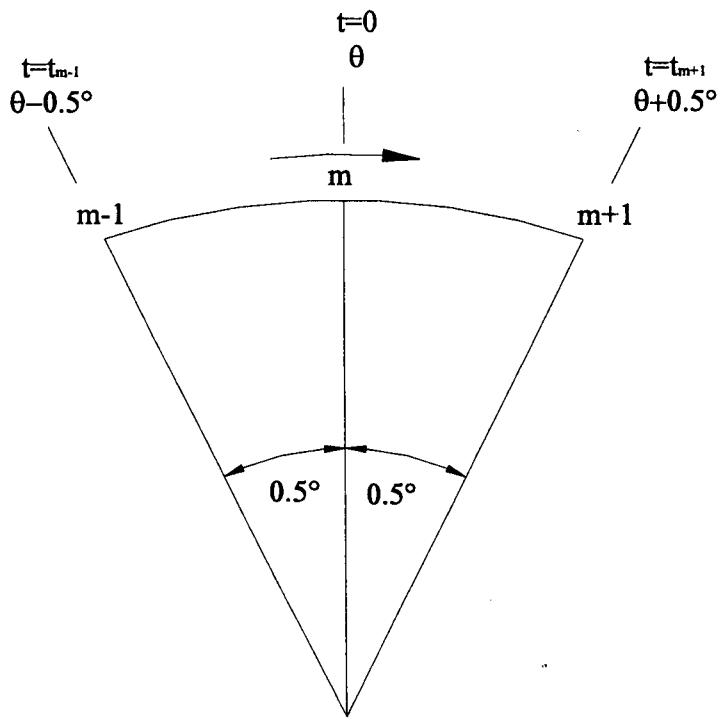

Figure 3.18. Three point curve fit technique used for calculating angular velocity and acceleration

Crankshaft angular velocity: $\frac{-\delta\theta\left(t_{m+1}^2 + t_{m-1}^2\right)}{t_{m+1}t_{m-1}\left(t_{m+1} - t_{m-1}\right)}$ 3.4

Crankshaft angular acceleration: $\frac{2\delta\theta\left(t_{m+1} + t_{m-1}\right)}{t_{m+1}t_{m-1}\left(t_{m+1} - t_{m-1}\right)}$ 3.5

Where $\delta\theta = 0.5^{\circ} crankangle$

The complete detail of the design and programming of the engine data acquisition system is given in chapter eleven.

3.9 SUMMARY

A new technique to measure instantaneous and mean camshaft drive torque in a running engine, without modification of the drive torque has been developed. The calibration of specially designed pulley torque transducers and the effect of belt loading on the transducers output have been demonstrated and found to have no detrimental effect on the transducer output signal.

The adjustment of an optical encoder index pulse with engine TDC position has been described. As the experiments are carried out on a single cylinder engine, the effect of camshaft speed variation throughout one engine cycle cannot be ignored. A technique has been described to measure camshaft speed variation and to calculate inertial effects of the camshaft assembly. The camshaft friction was measured using the technique mentioned in this chapter and the predicted camshaft friction was determined using the FLAME engine valve train friction model, explained in the previous chapter. The results are given in the next chapter.

Chapter four

EXPERIMENTAL AND THEORETICAL EVALUATION OF ENGINE VALVE TRAIN FRICTION

4.1 INTRODUCTION

This chapter describes the engine valve train friction experimental results using the technique detailed in the previous chapter. In the first section of this chapter experimental results are compared with the theoretical results obtained from the FLAME valve train model outlined in Chapter two. As the valve train model is insensitive to cylinder gas pressure, the experimental results under motored conditions were compared with the friction model. The effect of four different lubricants: SAE 0W20 with and without friction modifier; SAE 10W40 and SAE 5W30 with friction modifier, on engine valve train friction loss is described in the second half of this chapter whereas the last section reports the difference in valve train friction loss under motored and fired conditions. The experiments were carried out on a 4-valve single cylinder Ricardo Hydra gasoline engine.

4.2 EXPERIMENTAL PROCEDURE

In order to measure valve train friction under both motored and fired conditions and to validate the engine valve train friction model the following information was logged,

- Instantaneous camshaft drive torque.
- Cam/follower interface lubricant bath inlet temperature.
- Camshaft bearing lubricant inlet temperature.
- Cylinder pressure.
- Engine speed.
- Crankshaft/camshaft acceleration.
- Camshaft assembly mass inertia.
- Camshaft angular position.

Initial work to commission the system revealed that a clear simultaneous and instantaneous torque signal could be obtained with no significant errors from belt loading. However, the results indicated that the signal levels at zero torque could drift with temperature, despite the use of compensated strain gauges. This troublesome effect has been noted by other researchers, Ball et al [1986]. A test procedure was therefore developed to minimise the effect of this zero drift. This involved regular zeroing of the torque transducers at stabilised running temperatures before starting the experiment and then measuring any drift from zero torque immediately after the experiment by removing the belt. This method gave high repeatability thereby justifying the somewhat laborious procedure. Belt tension was kept constant by regular adjustment at the required running conditions.

To achieve oil inlet temperatures to the cam/follower interface above 90°C in motored conditions it proved necessary to install an additional electrically driven pump to supply a small proportion of the lubricant flow directly to the cam/follower interface via the feed nozzle mentioned in section 3.6 of chapter three. Cylinder head oil temperature was controlled by an external heating system integrated into an oil reservoir, effectively forming an external sump. Thus two completely independent lubricant circuits, each having its own electrically driven gear pump, heating system and sump were used, one for valve train and the other for the engine crankcase lubrication.

4.3 POST PROCESSING

The data collected from the torque transducers had a characteristic waveform with a frequency proportional to engine speed. As the experiments for the model validation, were carried out under motored conditions the shape of the trace remained constant, demonstrating high transducer repeatability. A snapshot of the transducer output voltage is shown in figure 4.1. Due to the rigidity of the camshaft system vibration levels were quite low at engine speeds up to 2000rpm. The vibration of the camshaft was studied by carrying out a frequency spectrum analysis and the data was digitally filtered using a Butterworth filter with special attention paid to potential phase shifts. The cut-off frequency was set to 200 Hz. Figure 4.2 shows a typical result of digital filtering of the outputs from both transducers at an engine speed of 2500rpm.

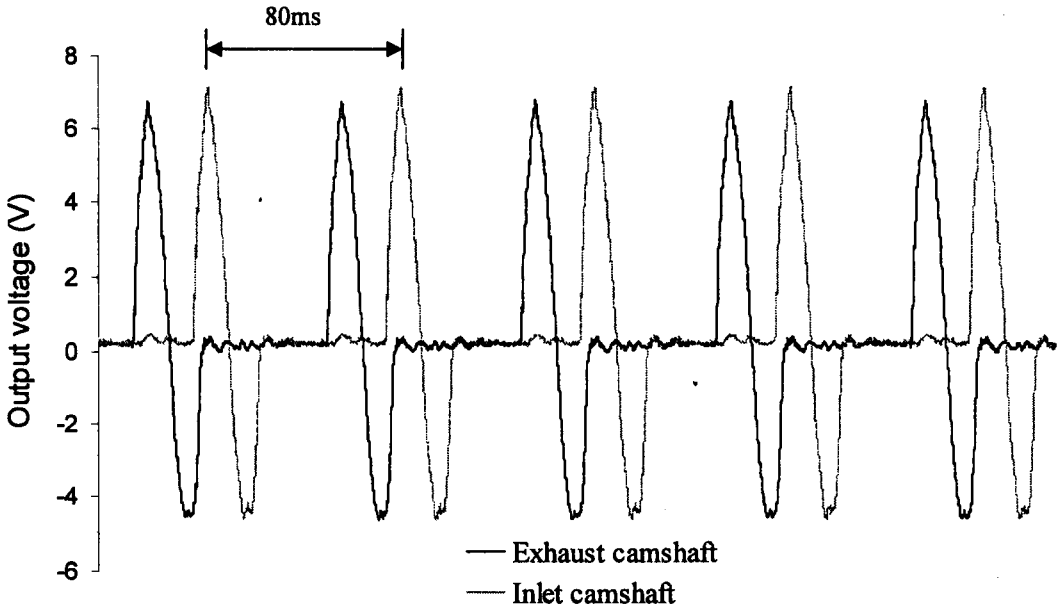

Figure 4.1. Typical torque transducer output voltages, engine speed 1500rpm.

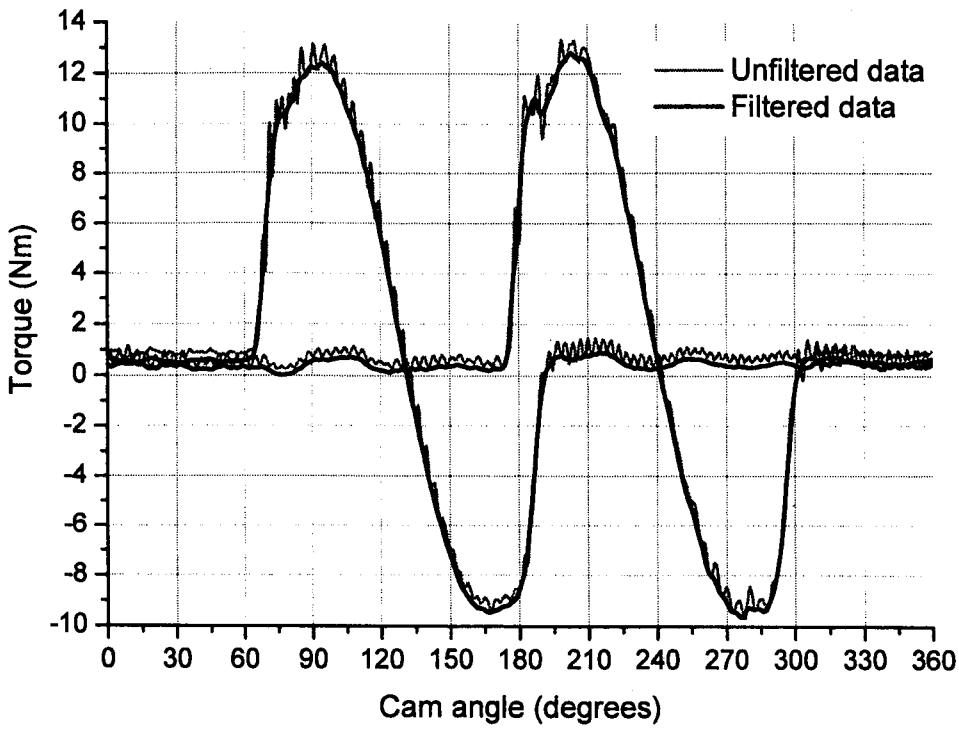

Figure 4.2. Effect of digital filter (Butterworths) on raw data recorded at engine speed 2500rpm, lubricant temperature 40°C.

4.4 COMPARISON OF EXPERIMENTAL AND THEORETICAL RESULTS

The motored experiments on the Ricardo Hydra engine were carried out at valve train oil inlet temperatures of 40°C, 60°C, 80°C and 95°C, the upper limit being defined by the capabilities of the torque transducers. The valve train drive torque was measured at engine speeds of 800rpm, 1500rpm, 2000rpm and 2500rpm for each temperature. Two different lubricants were used for the validation of the friction model: SAE 0W20 without friction modifier and SAE 0W20 with an organic friction modifier. Data characterising the lubricants is listed in Appendix II.

During the experiments, the required oil inlet temperature was maintained and torque measurements for the complete speed range were taken. Thus the experiments were carried out in four sets, obtaining measurements at four different speeds at each temperature and for each lubricant.

4.4.1 FILM THICKNESS AND ENTRAINMENT PREDICTIONS

Figure 4.3(a) shows a typical variation of the predicted minimum and central film thickness in the cam/follower contact, zero degrees cam angle corresponding to the cam nose. The cam flanks enjoy a large thickness of lubricant even though the load over this region is relatively high. At around ±40° the entraining velocity is very low, figure 4.3(b), and severe lubrication conditions prevail with a dramatic fall in lubricant film thickness. At this point squeeze film lubrication plays a vital role. Around the cam nose region, boundary lubrication is dominant.

4.4.2 TORQUE AND FRICTION

When analysing torque acting on a camshaft, care must be taken to appreciate the constituent parts. The total torque measured by the torque transducer is known as the drive torque and under motored conditions this is composed of friction torque, which is a function of tribological performance, and geometric torque. Geometric torque arises from the force required to open the valve against the resistance of the valve spring, the energy from which is stored in the valve spring and returned to the camshaft as torque in the opposite rotational direction as the valve closes, figure 4.4. In

all the drive torque figures, the first sine wave represents the exhaust camshaft drive torque whereas the second is the inlet camshaft drive torque.

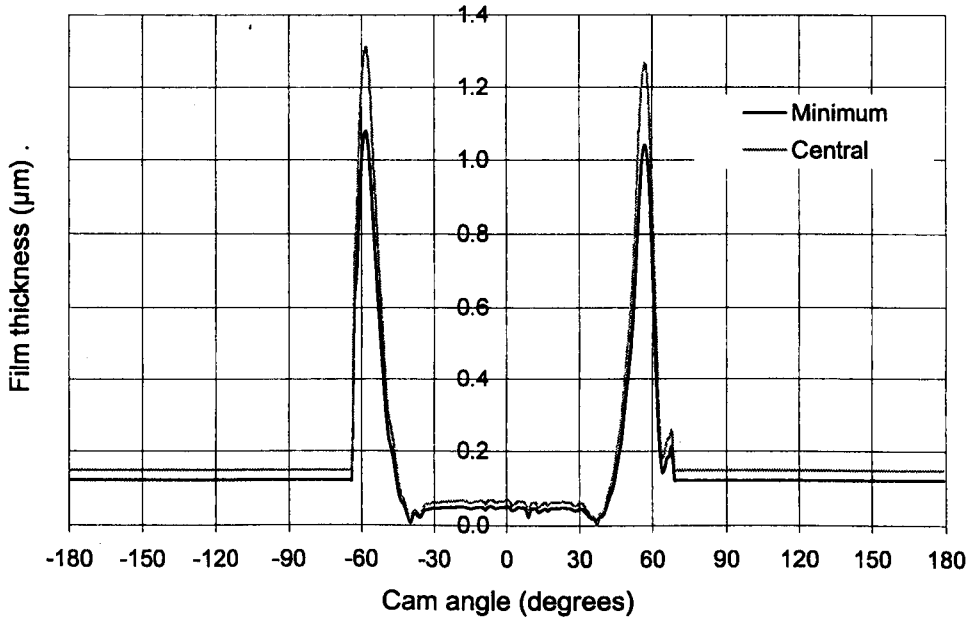

(a)

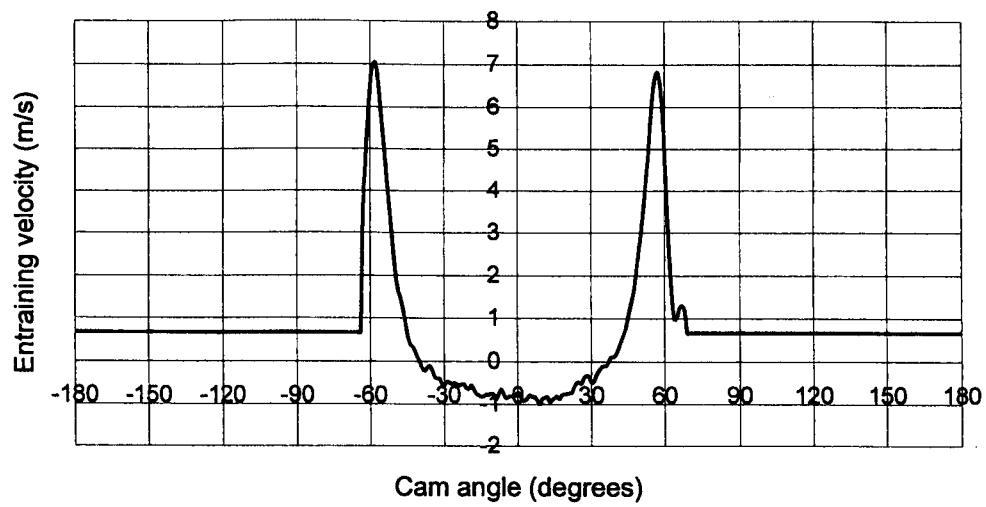

(b)

Figure 4.3(a)(b). Predicted minimum and central film thickness in the cam/follower interface and entraining velocity.

(Oil temperature 80°C, engine speed 1500rpm, SAE 0W20 without friction modifier)

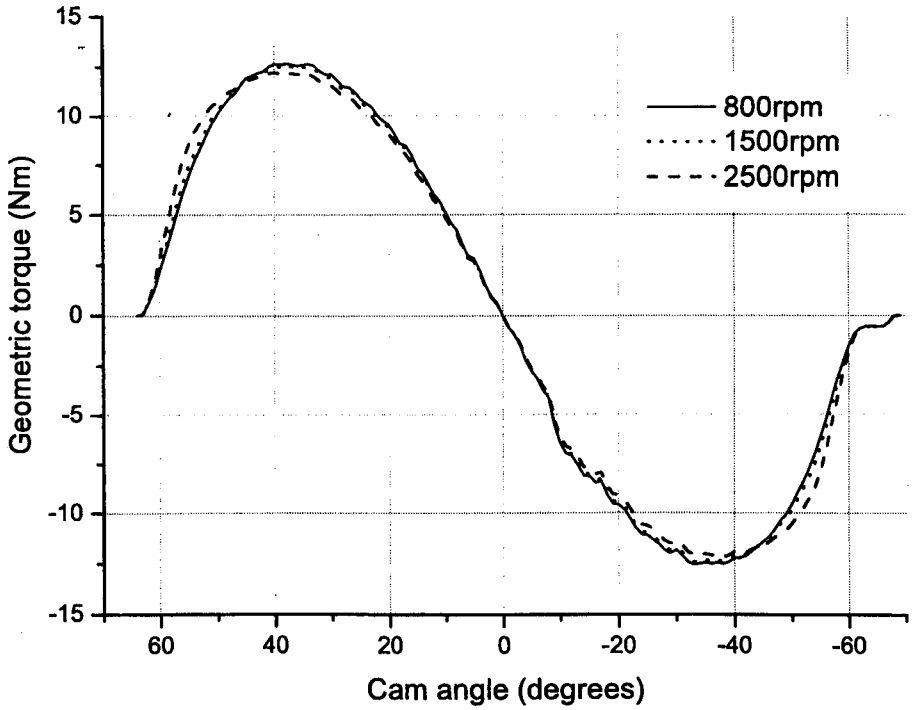

Figure 4.4. Computed inlet camshaft geometric torque at different engine speeds.

In the conventions used in this thesis, during valve opening the geometric torque is positive and when closing it is negative. Friction torque is positive throughout so that during valve opening, more friction gives more positive values of total torque. Conversely, during valve closing more friction diminishes, makes more positive, the negative torque. Taking the mean of the drive torque over the cam event effectively removes the geometric torque contribution, which ideally has equal positive and negative parts, and yields an average cyclic friction torque. This assumes that there is no energy loss in the geometric torque during valve opening and closing, which for a hydraulic follower may not be entirely true. It has been reported by Zhu and Taylor [2001] that a small amount of oil leakage can occur in the hydraulic element which can alter the geometric torque by decreasing valve spring compression. Any such leakage would be greatest at low speeds with high oil temperatures. This complicating factor was borne in mind when analysing the results of the experiments. The geometric torque in figure 4.4 is according to the inlet valve lift curve figure 4.5.

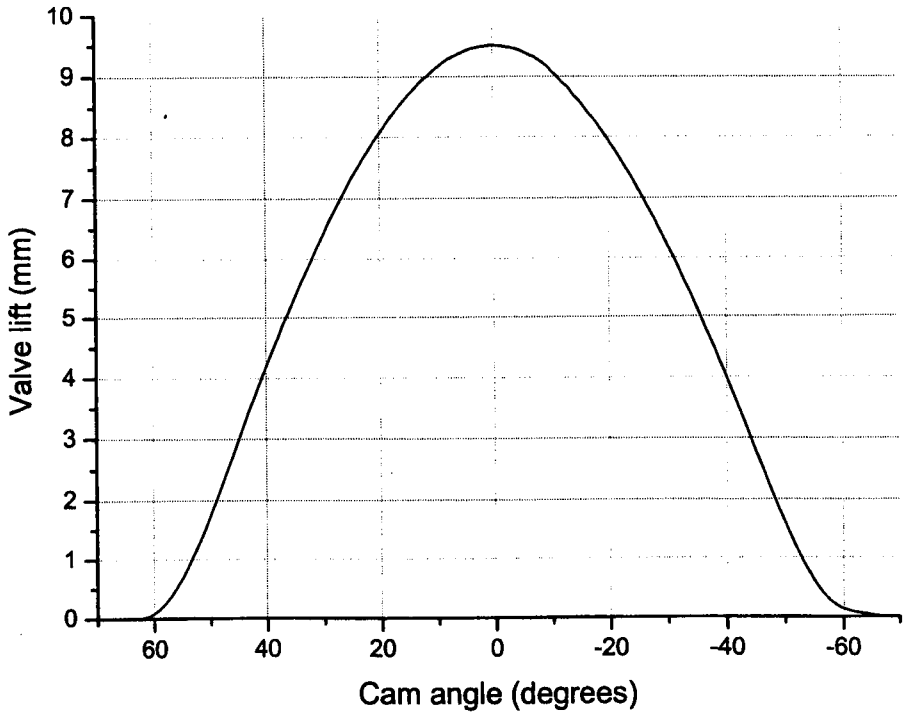

Figure 4.5. Ricardo Hydra inlet valve lift curve, symmetrical at 0° cam nose.

The experimental variations of average cyclic friction torque over the cam event only and over the complete cam cycle, with engine speed are presented in figures 4.6(a)(b) and 4.7(a)(b) for two different lubricants: SAE 0W20 without and with friction modifier. The data presented are the average of twenty engine cycles and are for the inlet camshaft only. The inlet and the exhaust cams are nearly the same shape and in motored conditions very little difference was observed between their torque measurements. Thus for the purposes of engine valve train friction model validation, only the inlet camshaft results are presented.

It can be seen for both the lubricants figures 4.6 and 4.7, that as the camshaft rotational frequency increases the average measured friction torque decreases due to improved lubrication conditions at higher frequencies arising from increased lubricant entrainment and reduced cam load at the nose. At relatively low engine speeds, the cam load is dominated by valve-spring compression, resulting in high friction around the cam nose.

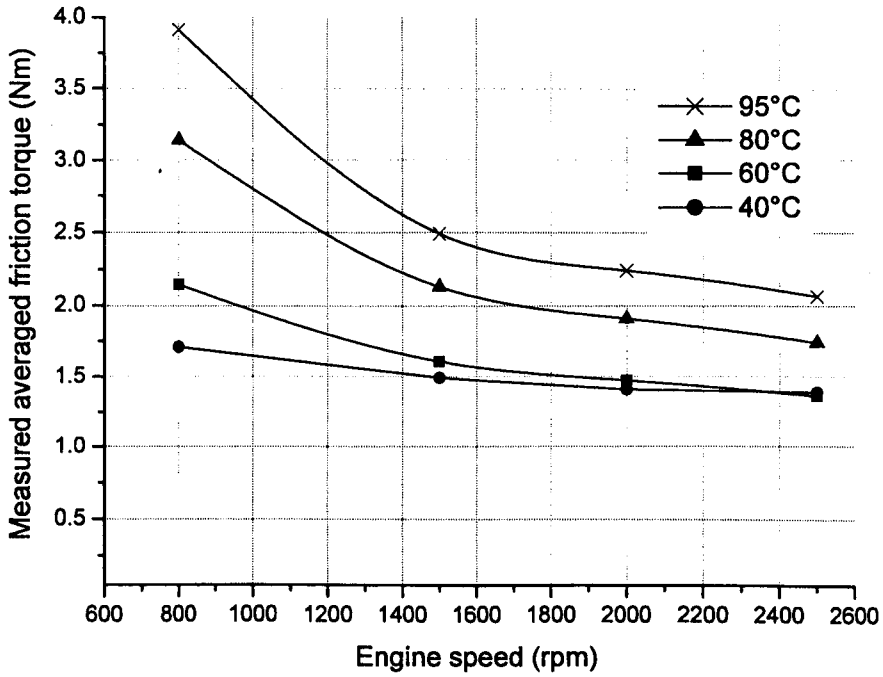

(a). Averaged over cam event

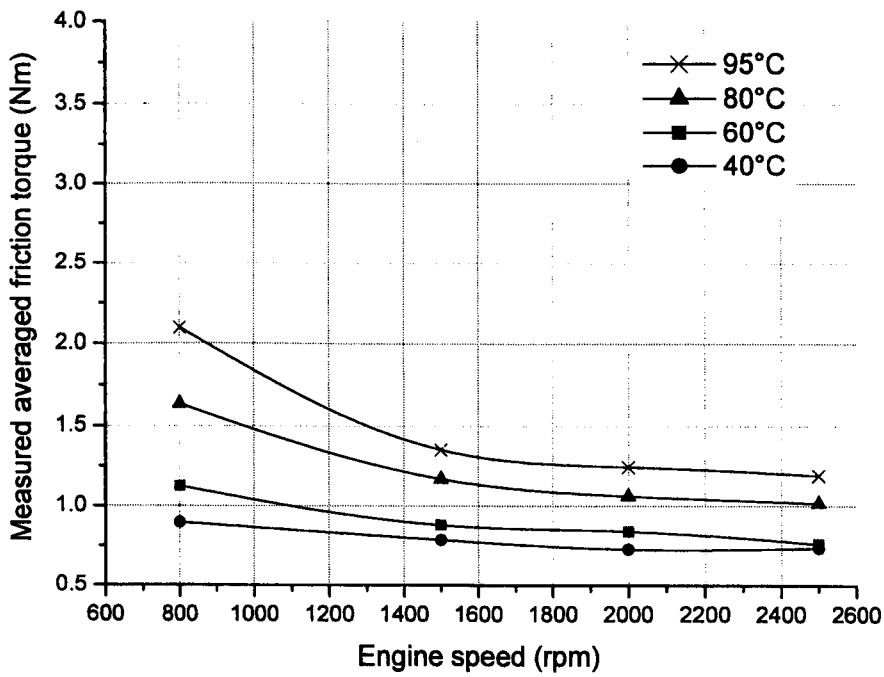

(b). Averaged over complete cam cycle

Figure 4.6(a)(b). Experimental inlet camshaft friction torque averaged over the cam event only and over the complete cam cycle, SAE 0W20 without friction modifier.

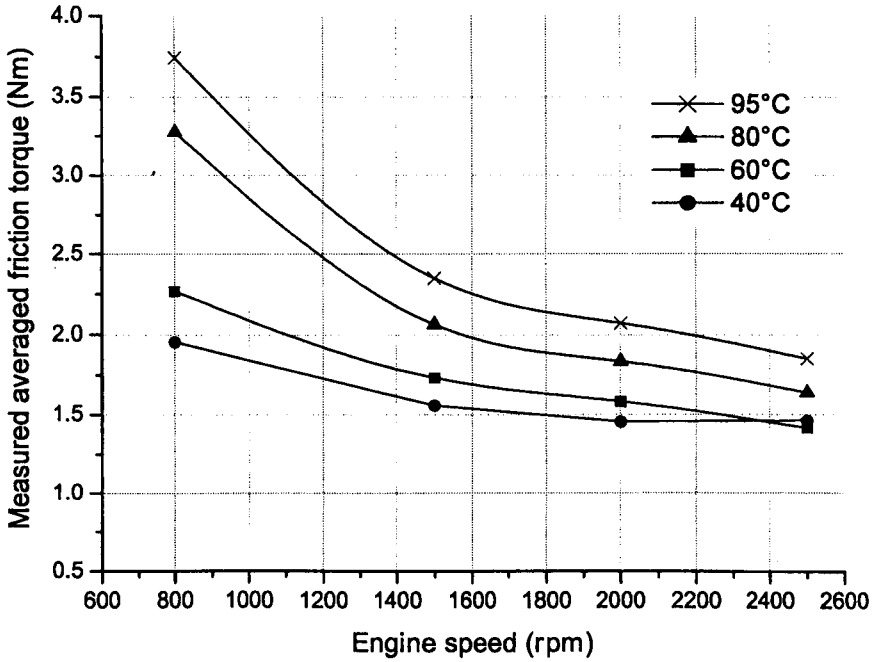

(a). Averaged over cam event

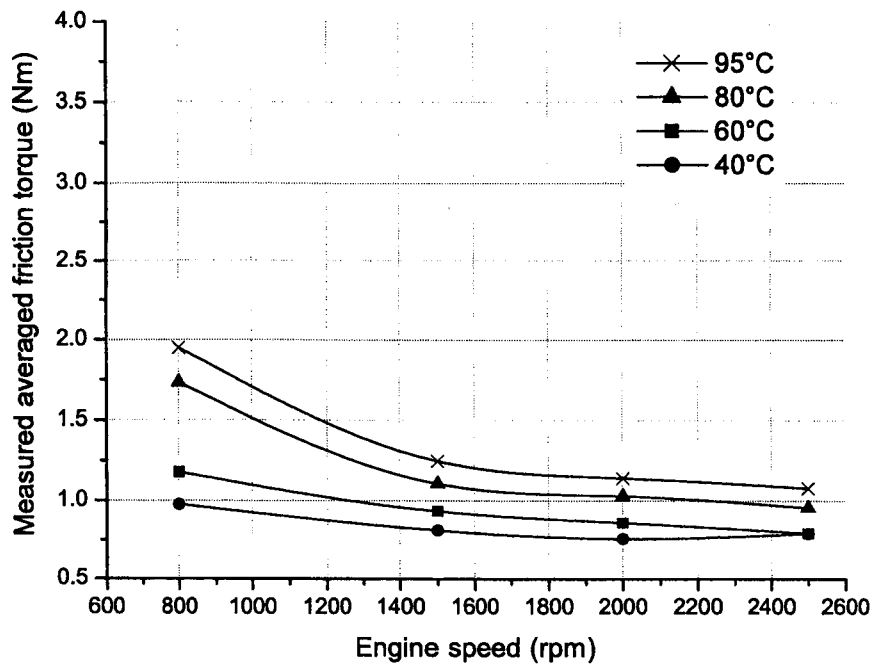

(b). Averaged over complete cam cycle

Figure 4.7(a)(b). Experimental inlet camshaft friction torque averaged over the cam event only and over the complete cam cycle, SAE 0W20 with friction modifier

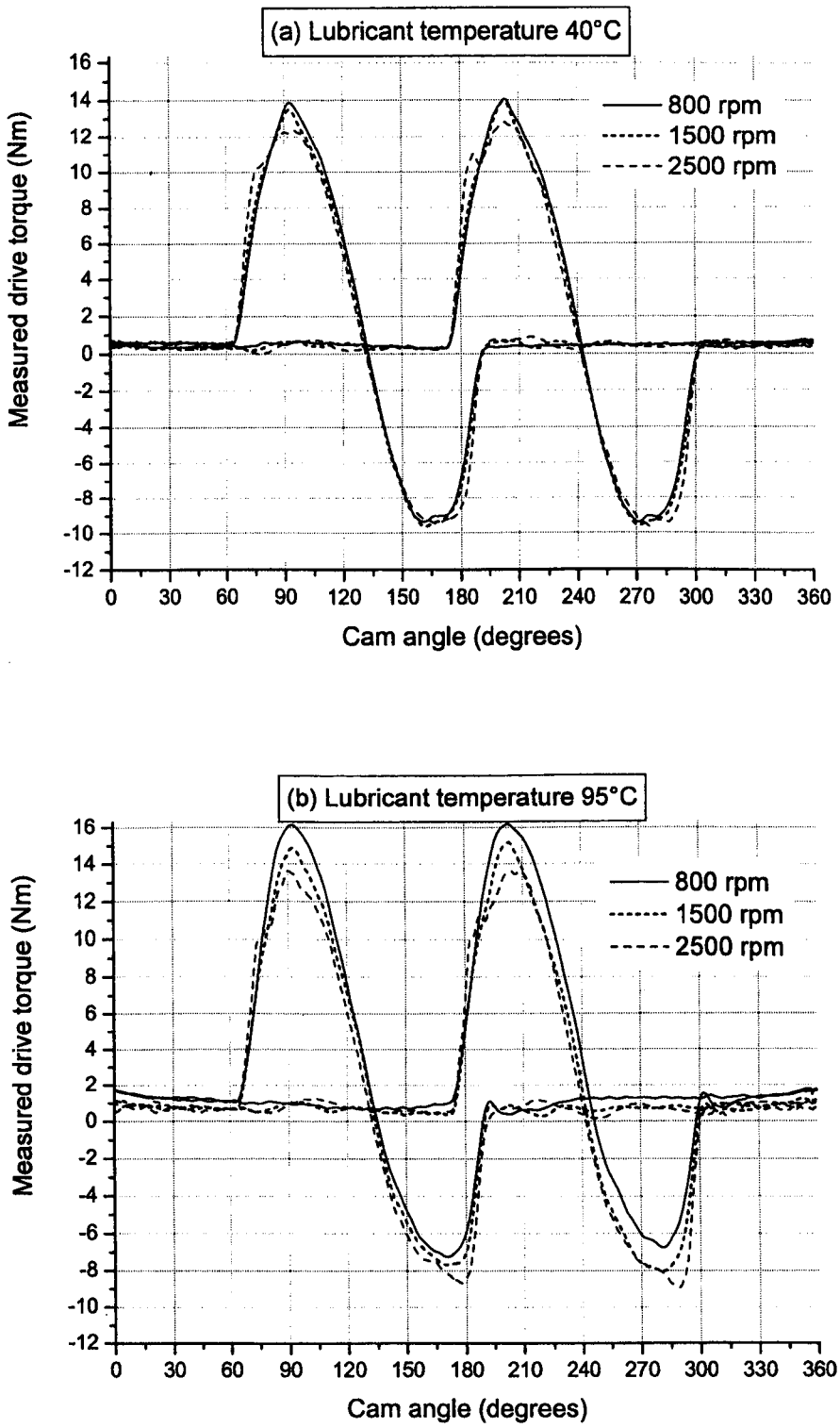

Figure 4.8(a)(b). Instantaneous measured exhaust and inlet camshaft drive torque under motored conditions, using SAE 0W20 without friction modifier

At high speeds, however, inertia plays a major role as the acceleration of the tappet has a negative value around the cam nose and it becomes more negative as engine speed increases resulting in a decrease in load around the cam nose, as shown in figure 4.4. This is consistent with the experiments reported by Baniasad and Emes [1998]. There is a sharper decrease in average torque with increasing speed at higher oil temperatures. Figure 4.6(a), at lubricant temperature 95°C, for an engine speed increase of 1700rpm there is a decrease of 46% friction losses that is from 3.9Nm at 800rpm to 2.1Nm at 2500rpm whereas at 40°C lubricant temperature, for the same engine speed increase results in 18% decrease of friction losses, that is from 1.7Nm to 1.4Nm for the cam event only. A similar picture can be seen for the friction losses over the complete cam cycle, figure 4.6(b). This is explored further in the instantaneous drive torque data of figure 4.8(a) and 4.8(b) for oil temperatures of 40°C and 95°C respectively. At higher temperature, the reduction in lubricant viscosity increases the tendency towards mixed and boundary lubrication at lower engine speeds but as the rotational frequency increases fluid film lubrication plays a greater role. The shape of the curves in figures 4.6(a) and 4.6(b) are nearly identical indicating that the friction losses over the cam event plays a major role in the overall camshaft friction losses.

Similar trends were observed with the SAE 0W20 lubricant containing an organic friction modifier, see figure 4.7(a) and 4.7(b). Comparing the behaviour of both the lubricants, it can be seen that the average experimental torque is relatively similar at low temperatures but at high temperatures the average friction torque decreases with the friction modified oil as expected for a temperature sensitive additive. At 95°C lubricant temperature and engine speed of 2500rpm the friction torques for SAE 0W20 without friction modifier were 2.1Nm and 1.13Nm over the cam event only and over the complete cam cycle respectively, whereas for the same conditions for SAE 0W20 having friction modifier the friction torques decreases to 1.85Nm and 1.06Nm for the cam event only and over the complete cam cycle, a decrease of 12% and 6% friction losses respectively are observed.

Comparative results were also obtained from the theoretical model under the operating conditions of the experiments, also shown in figure 4.9 for the cam event only.

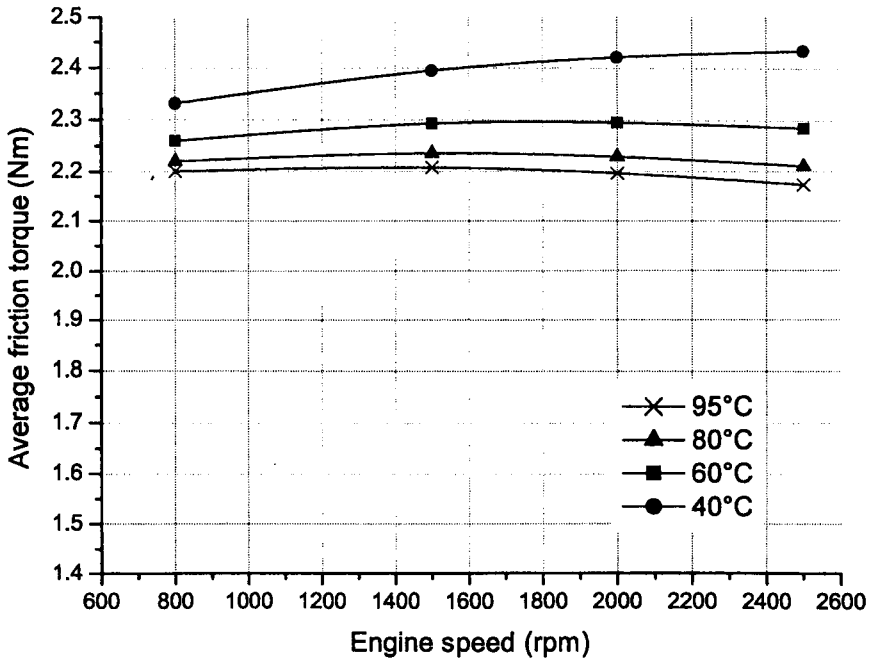

(a). SAE 0W20 without friction modifier

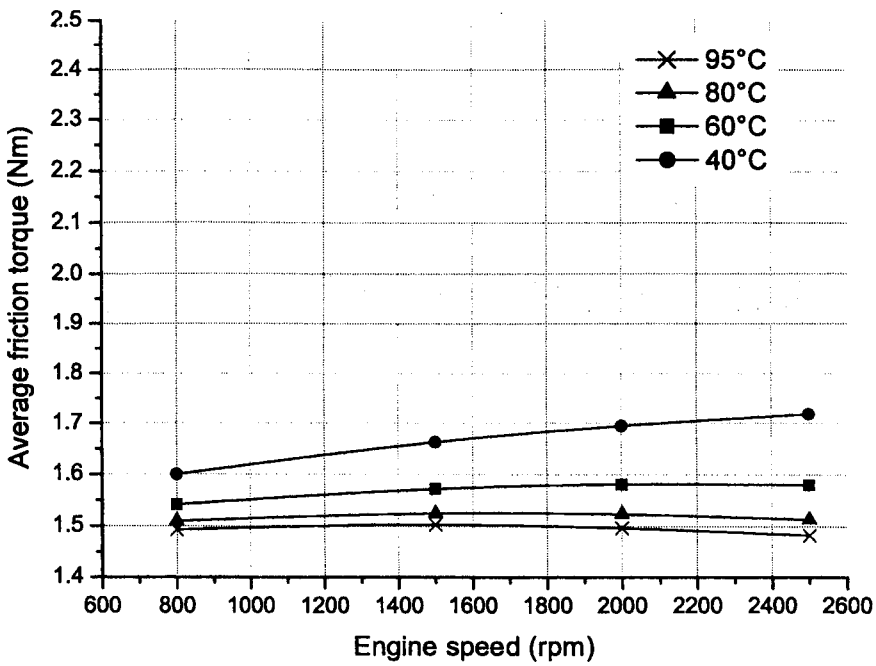

(b). SAE 0W20 with friction modifier

Figure 4.9(a)(b). Predicted inlet camshaft friction torque averaged over cam event only. SAE 0W20 without and with friction modifier

The overall order of magnitude of the predicted friction torques and the measured data are similar at engine speeds of 1500rpm and above, which is encouraging for such a complex mechanical and chemical system. For example, comparing theory with experiments for the SAE 0W20 oil without friction modifier, figure 4.9(a), at lower speeds and higher temperatures the model underestimates friction torque, whereas at high speeds and lower temperatures it is overestimated. However, there is a much reduced sensitivity to engine speed and temperature with the predicted torques when compared to the measured data. The general decrease of predicted friction torque with increasing temperature also indicates a greater sensitivity to viscous effects than is evident in the experiments.

The average predicted friction torque figure 4.9, is mainly the sum of the cam/follower interface friction and the viscous friction generated in the camshaft bearings over the cam event only. The model predicts the coefficient of friction at the cam/follower interface reaching its limiting value (μ_{lim}) very quickly in the cam event and remaining nearly constant for the subsequent period spanning the cam nose with little sensitivity to speed and oil temperature. The small rise in average predicted friction torque with increasing speed evident in figure 4.9 is due to viscous effects in the camshaft bearings. The similarly modest fall seen in some of the higher temperature curves at the higher speeds is due to a reduction in the severity of lubrication at the cam/follower interface, as observed in the experiments.

Figure 4.10 shows the predicted friction torque over the cam event only excluding the friction losses from the camshaft bearing. A decrease in friction torque with engine speed is predicted which is consistent with the trend obtained experimentally. This is because, as mentioned above, the model predicts coefficient of friction reaching its limiting value for a major part of the cam event. The difference in friction torque with changing speed figure 4.9 and 4.10, is therefore dominated by the hydrodynamic shear losses of the cam event and the camshaft bearings.

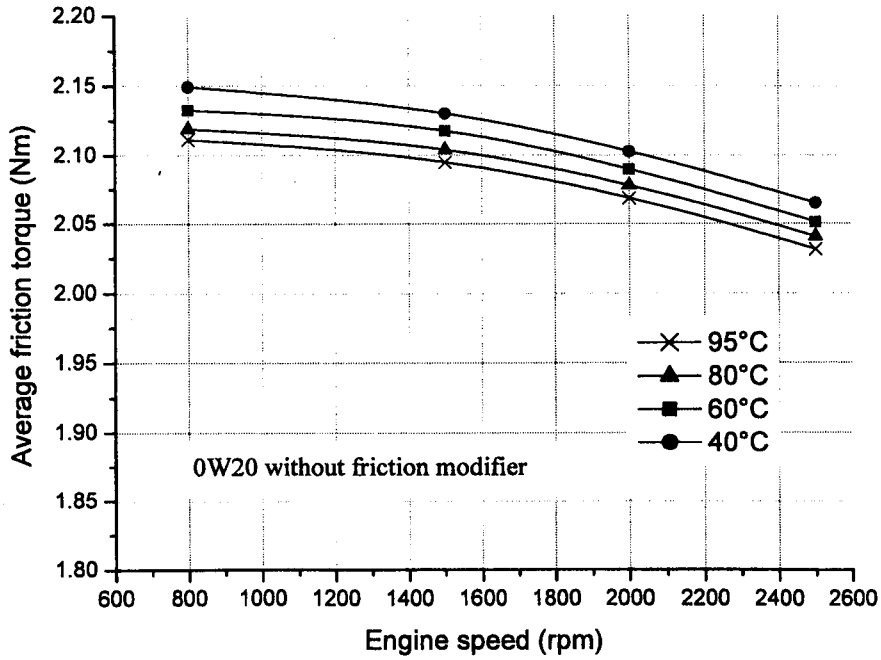

(a). SAE 0W20 without friction modifier

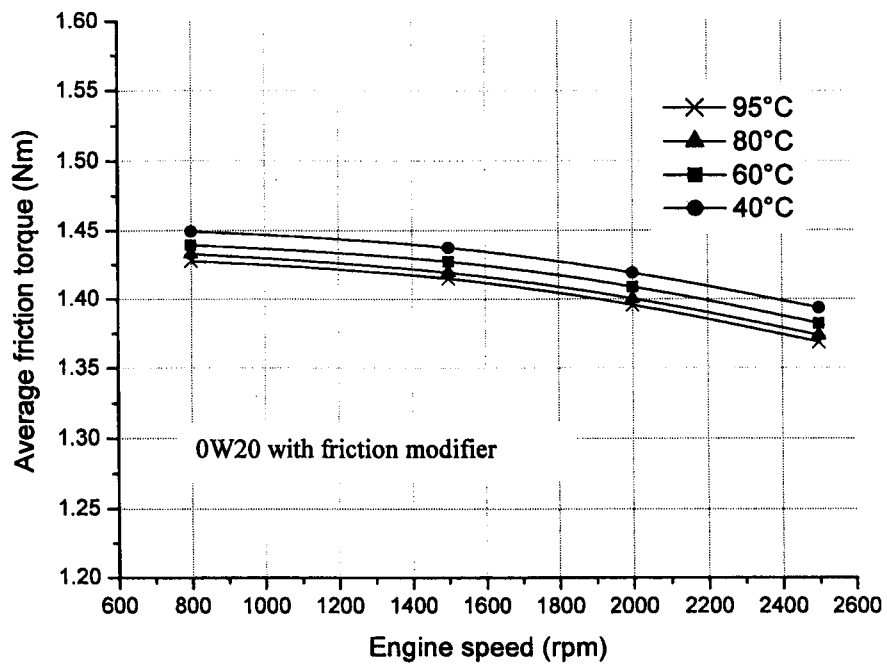

(b). SAE 0W20 with friction modifier

Figure 4.10(a)(b). Predicted inlet camshaft friction torque averaged over the cam event excluding bearing losses. SAE 0W20 without and with friction modifier

The experimental data in figures 4.6(a) and 4.7(a) clearly shows a transition to more severe boundary lubrication at the lowest speed of 800rpm with sharp increases in friction torque, exacerbated by rising temperature. The theoretical results in figure 4.9(a)(b) do not follow this trend with underestimation of friction and a decrease in friction torque with rising temperature in a manner akin to fluid film behaviour. This clearly shows that the model is found wanting under these conditions, either through the application of elastohydrodynamic lubrication theory at the cam/follower interface, in the manner of equations 2.27 and 2.28, and/or the use of a fixed limiting friction coefficient for a given oil across all operating conditions. Most notably, variations in temperature are likely to influence the limiting friction coefficient. Alternatively, or even additionally, the camshaft bearings may encounter mixed lubrication, which is not considered in the model. As one of the aims of this research was to validate and direct future model development, this outcome is regarded in a positive light.

The instantaneous predicted inlet camshaft drive torque at an engine speed of 1500rpm for the SAE 0W20 lubricant without friction modifier, figure 4.11, clearly shows the results are more influenced by shear losses as compared to mixed and boundary friction losses.

Comparing the theoretical results for both the oil types, figures 4.9, it can be seen that the trends are very similar but they differ significantly in magnitude. The model predicts much higher average torques for the oil without friction modifier at all speed and temperatures, essentially because the limiting coefficient of friction (μ_{lim}) for the SAE 0W20 oil without friction modifier oil is 0.12 compared to 0.08 for the friction modified oil. The load at any particular speed and temperature is the same for both oils and their viscometric properties are similar, as documented in Appendix II. Given the tendency for the coefficient of friction to reach its limiting value for much of the cam event for this valve train, as noted previously, the predictions are therefore dominated by boundary friction as described by equation 2.28. This can be very clearly seen in figure 4.12.

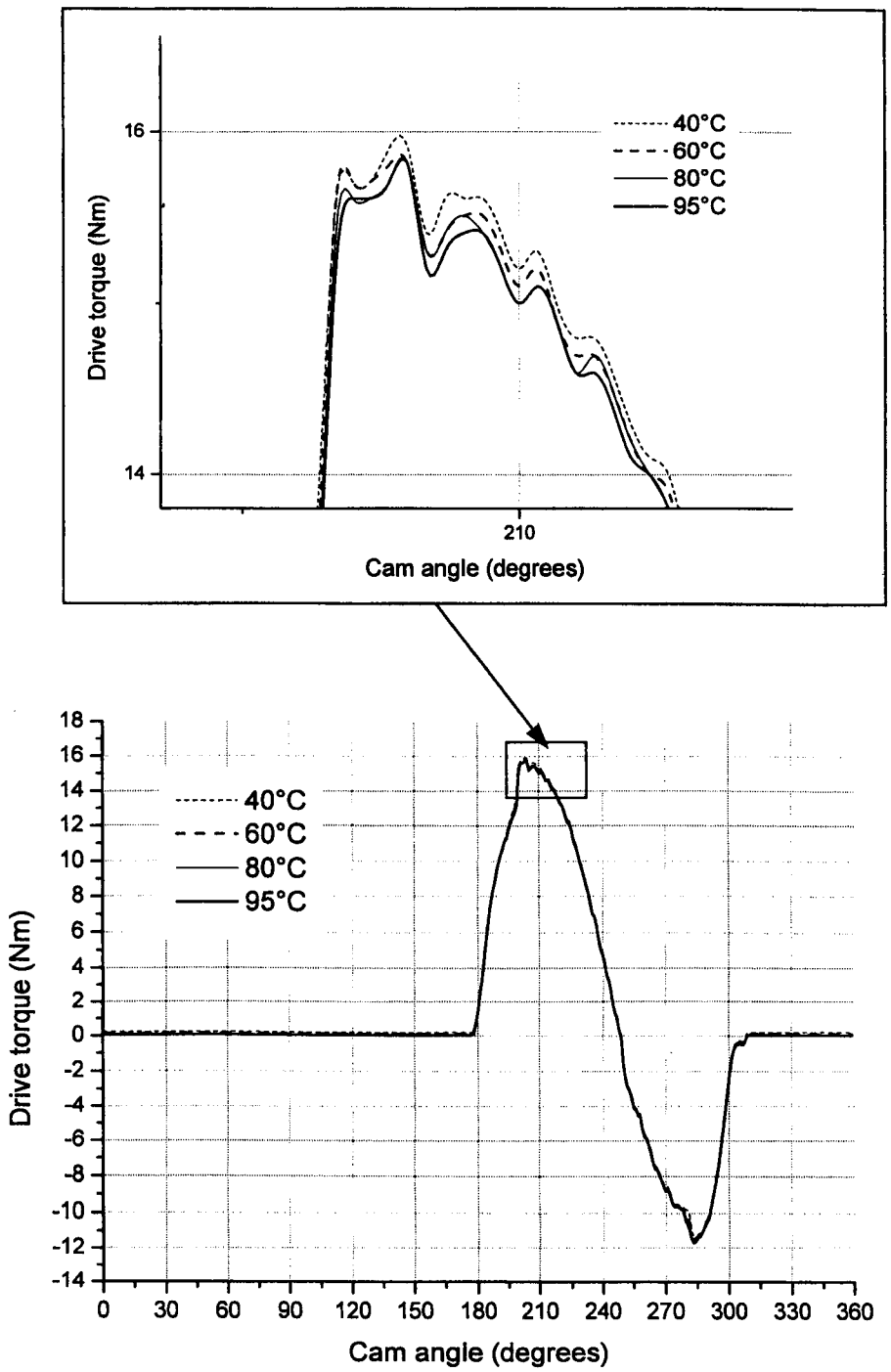

Figure 4.11. Predicted instantaneous inlet camshaft drive torque, engine speed 1500rpm, SAE 0W20 without friction modifier

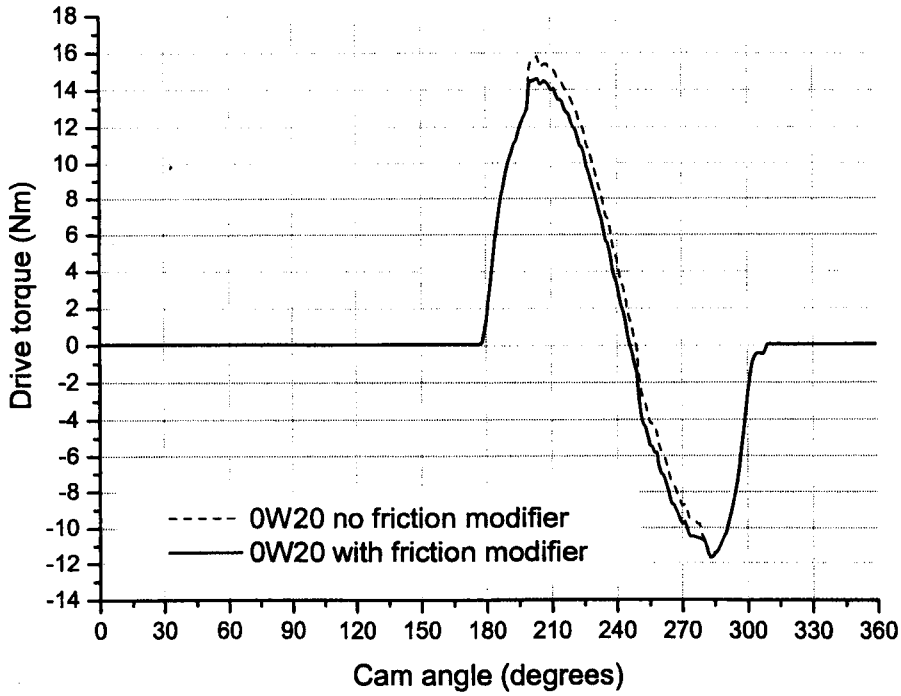

Figure 4.12. Predicted instantaneous inlet camshaft drive torque, engine speed 1500rpm, SAE 0W20 with and without friction modifier at 60°C oil temperature.

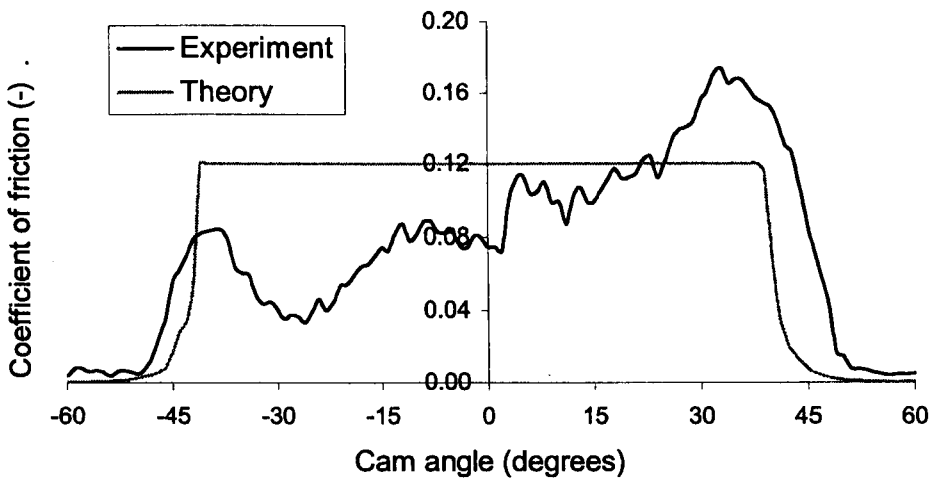

Figure 4.13. Experimental and predicted instantaneous coefficient of friction for the inlet camshaft.

Oil temperature 60°C, 1500rpm engine speed, SAE 0W20 without friction modifier.

In figure 4.13, the predicted cyclic variation of friction coefficient at the cam/follower interface is compared to the experimental equivalent for an operating condition where the correlation between theoretical and experimental average friction torque is good. The experimental value is in fact something of a hybrid, being derived from the subtraction of the computed geometric torque from the measured drive torque. The agreement between detailed instantaneous theory and experiment is also good in figure 4.13 providing strong evidence that boundary lubrication does indeed predominate for up to 70% of the cam event under these conditions. It can be seen that during valve opening, corresponding to negative cam angles in figure 4.13, the experimental friction coefficient is smaller than during valve closing, positive cam angles. This perhaps belies the hybrid origin of this data and may in part highlight the occurrence of oil leakage from the hydraulic element in the follower. As noted previously, such leakage may disrupt the geometric torque as compared to the ideal with a loss of spring compression and a decrease in geometric torque on both sides of the cam nose. In the context of figure 4.13, this would result in comparatively less experimental friction torque during valve opening and higher values during closing due to the change in direction of geometric torque, as evident in the friction coefficient data presented.

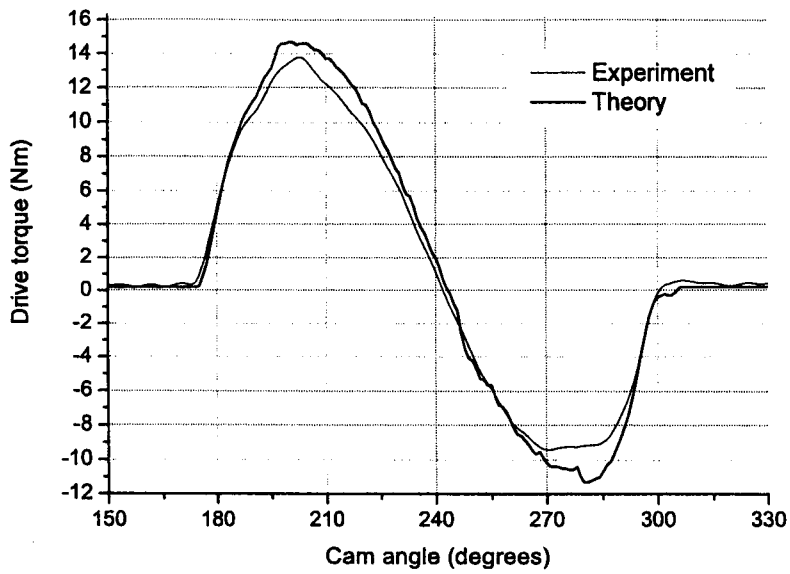

Figure 4.14. Comparison of experimental and theoretical instantaneous inlet camshaft drive torque, Oil temperature 40°C and 1500rpm, SAE 0W20 with friction modifier.

A comparison between the experimental and theoretical instantaneous drive torque at 40°C and 1500rpm for the SAE 0W20 with friction modifier is provided in figure 4.14. There is good agreement although the predicted friction torque is more than the experimental during valve opening and less during closing, remembering that friction torque is positive throughout. This is consistent with the behaviour observed for the cam/follower interface alone in figure 4.13. To either side of the cam event it can be seen that the experimental drive torque consistently exceeds the theoretical value. Camshaft bearing friction is dominant at such times and thus it would appear that the model has failed to accurately characterise the frictional losses of the bearings under these operating conditions.

The measured instantaneous drive torque for a range of speeds and temperatures for the SAE 0W20 oil without friction modifier is shown in figure 4.15. It can be seen that for any particular speed the drive torque increases as the temperature increases. Bearing in mind that the geometric torque remains constant for a particular speed, the increase in torque must therefore be due to an increase in friction torque with temperature, which is consistent with figure 4.6(a).

Consider in more detail figure 4.15(a), which contains the results for the lowest engine speed where, as noted previously, the correlation between friction torque from theory and experiments was poor. The increase in torque with rising temperature occurs during the cam event and to a lesser extent in the intervening time periods where camshaft bearing friction is dominant. The lubrication conditions at 95°C are the most severe with high friction levels during the cam event, indicative of boundary lubrication, and also during the intervening periods, suggesting mixed lubrication conditions for the camshaft bearings.

Comparing figures 4.15(a) through to figure 4.15(c), it is apparent that the severity of the lubrication conditions diminishes with increasing speed as the overall torque levels fall and the influence of temperature at any given speed reduces. Once again this behaviour is consistent with the mean data of figure 4.6(a)(b).

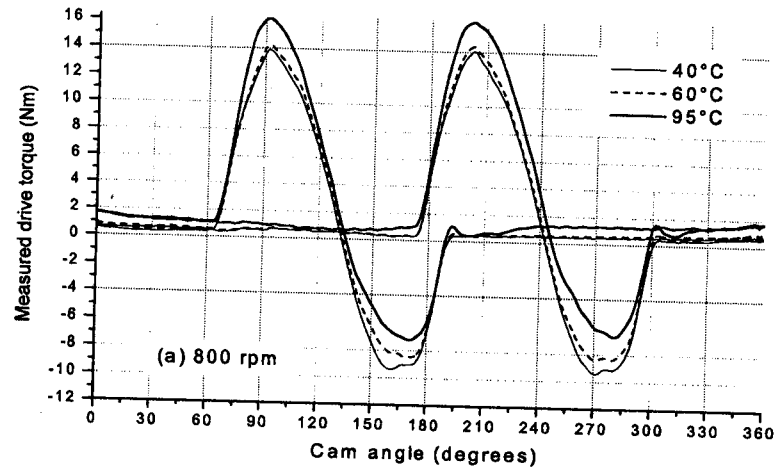

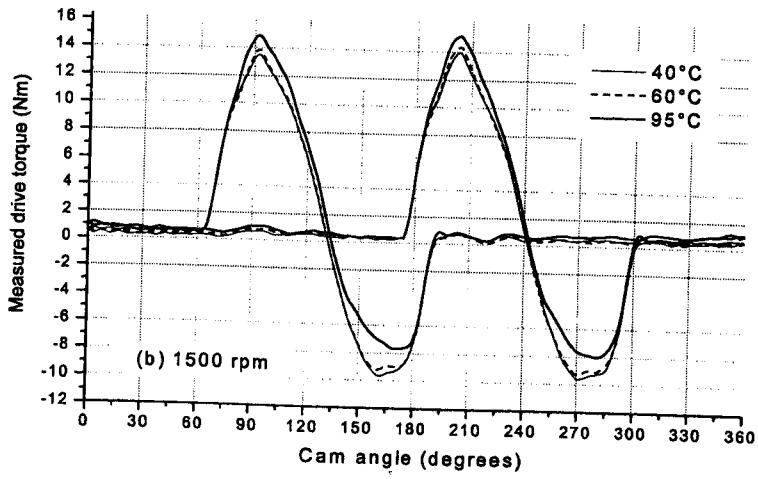

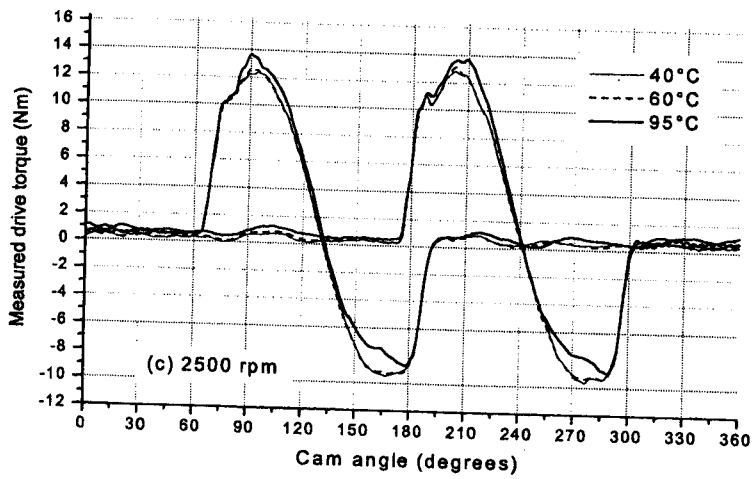

Figure 4.15(a)(b)(c). Experimental instantaneous exhaust and inlet camshaft drive torque at 800, 1500 and 2500 rpm engine speed at temperatures of 40°C, 60°C and 95°C. SAE 0W20 without friction modifier

4.5 EFFECT OF DIFFERENT LUBRICANTS ON ENGINE VALVE TRAIN FRICTION LOSS

Experiments were also carried out with two additional lubricants, SAE 10W40 and SAE 5W30 with friction modifier. Engine valve train drive torque was measured under similar conditions to the SAE 0W20, that is under motored conditions at engine speeds of 800rpm, 1500rpm, 2000rpm and 2500rpm for lubricant temperatures of 40°C, 60°C, 80°C and 95°C.

4.5.1 EFFECT OF LUBRICANT TEMPERATURE ON FRICTION TORQUE

It can be seen in figure 4.16 that for any lubricant, at any engine speed, the curves show an upward trend of the average friction torque with an increase in the bulk inlet temperature. It is well known that an increase in the bulk inlet temperature leads to a decrease in the lubricant viscosity and consequently a decrease of the oil film thickness which in turn causes an increase in the shear rate between the two surfaces. The increase in shear rate thus increases the friction between the two surfaces, but this effect is limited to a certain extent as the lubricant viscosity decreases at the same time. Also reduction of the film thickness results in more asperities coming into contact resulting in an increase in friction. As the friction torque is associated with so many complicated interacting factors it is quite possible that under certain circumstances the increase in bulk inlet temperature will have little effect on increasing the friction torque and sometimes the reverse effect may result. This effect can be clearly seen in figure 4.16 where at temperatures of 40°C and 60°C the increase in friction torque is comparatively small as compared to 80°C and 90°C temperatures. In figure 4.16(a) for engine speed 1500rpm, there is a slight decrease in friction torque for lubricants SAE 10W40 and SAE 5W30 as the temperature increases from 40°C to 60°C. This is mainly because at low temperatures the viscosity is high which under hydrodynamic lubrication conditions results in high shear losses, which then decrease as temperature increases causing a decrease in lubricant viscosity. But above 60°C mixed to boundary lubrication becomes dominant and a rise in temperature results in an increase in friction. The benefit of the friction modifier present in the SAE 0W20 and SAE 5W30 is clearly evident at high lubricant temperatures, figure 4.16. Figure 4.17 shows the effect of different lubricants on the instantaneous drive torque at engine speeds of 800rpm and 2500rpm and 95°C bulk lubricant inlet temperature, keeping in mind that the geometric

torque is constant at any one engine speed and thus all the variation is mainly because of friction losses.

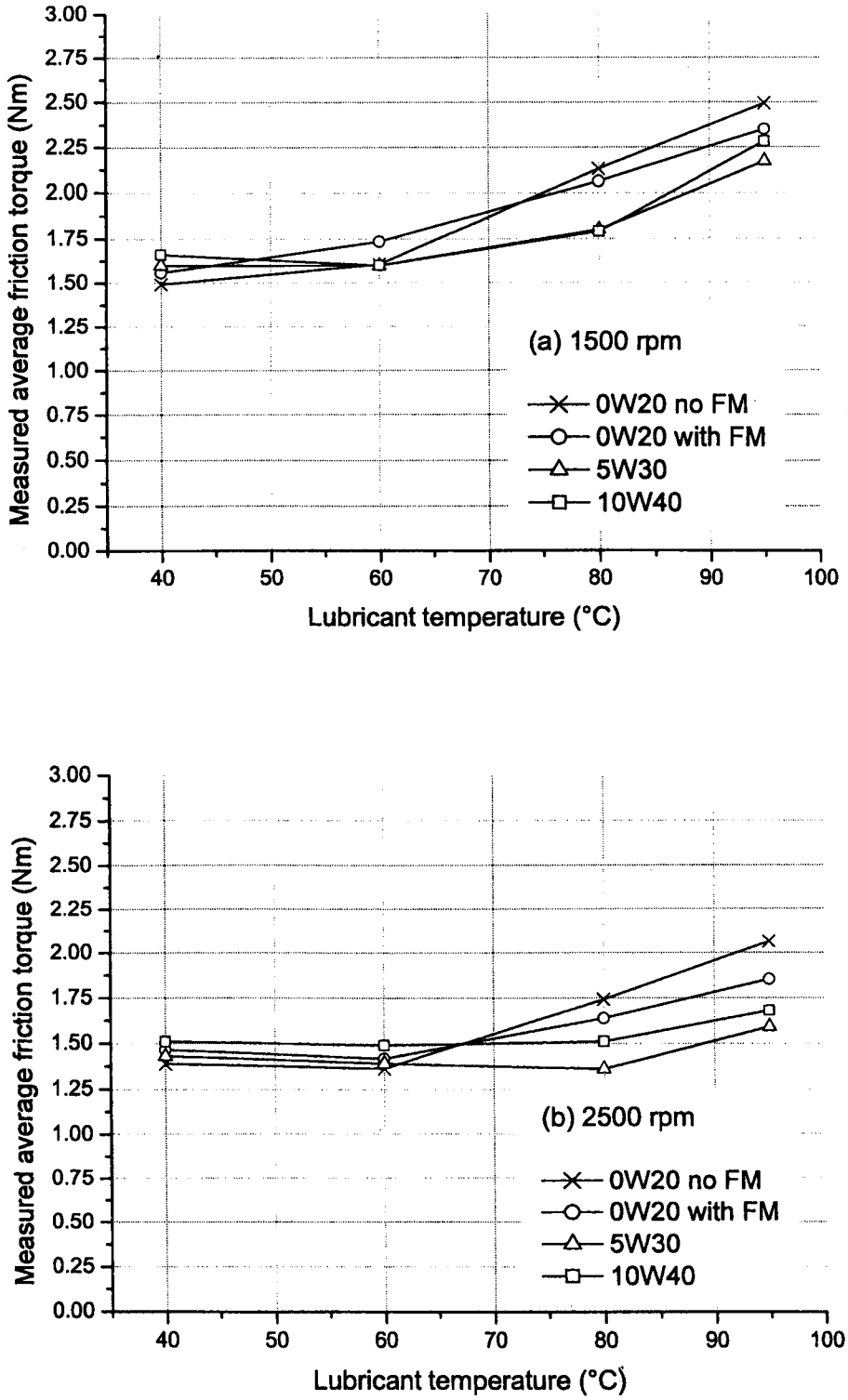

Figure 4.16(a)(b). Experimental inlet camshaft friction torque averaged over the cam event only

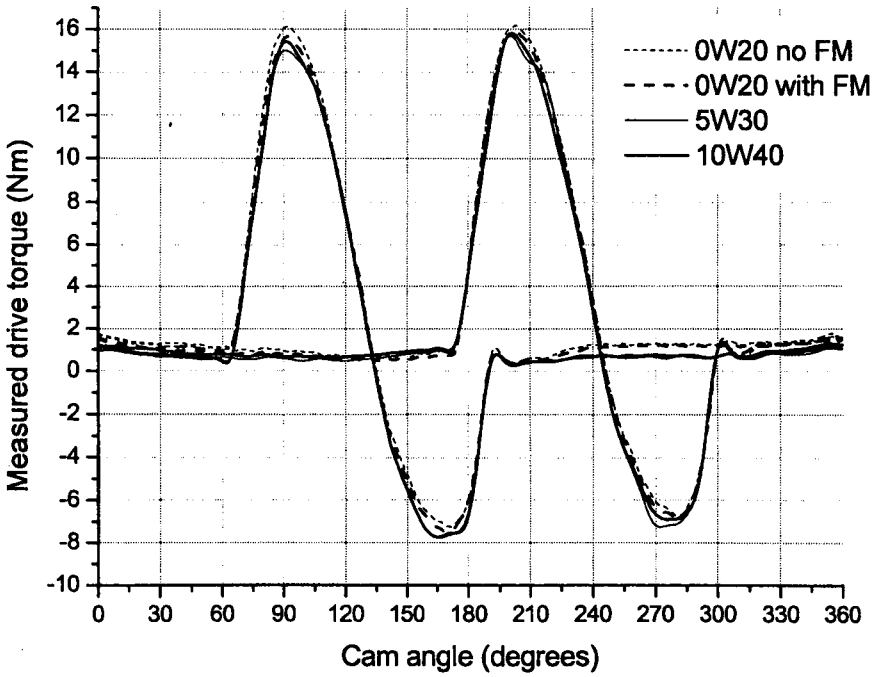

(a). Engine speed 800rpm

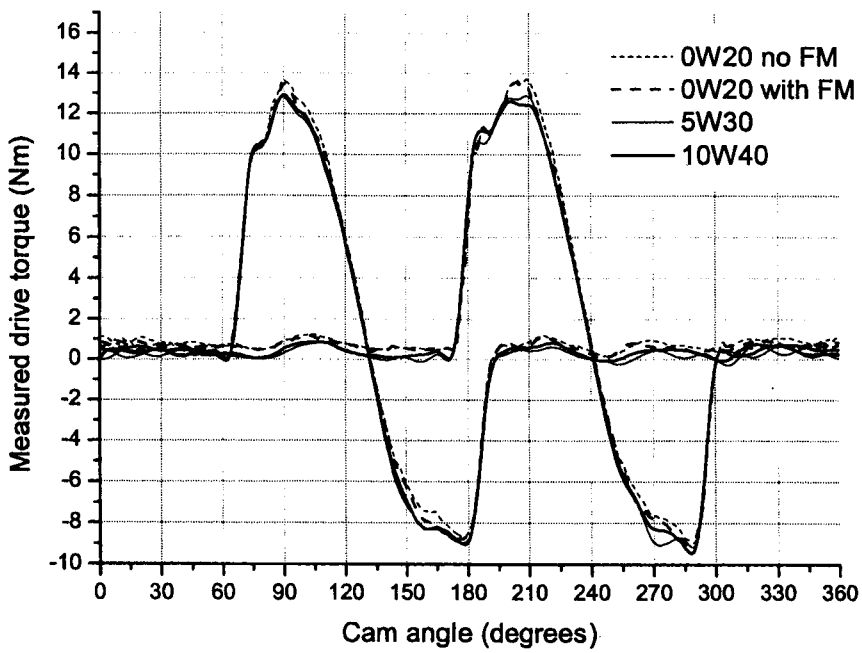

(b). Engine speed 2500rpm

Figure 4.17(a)(b). Experimental instantaneous exhaust and inlet camshaft drive torque at engine speed 800rpm and 2500rpm, 95°C lubricant temperature.

4.5.2 EFFECT OF ENGINE SPEED ON VALVE TRAIN FRICTION TORQUE

The effect of camshaft rotational speed on the average friction torque for the SAE 0W20 lubricant with and without friction modifier has been described earlier in this chapter. The response of all four lubricants to engine speed is shown in figure 4.18 at 40°C and 95°C lubricant temperatures. Generally there is a downward trend of the average friction torque as the camshaft speed increases. The increase of the camshaft speed not only results in an increase in the entraining velocity but also leads to a reduction of the inertia load in the cam nose region, as mentioned earlier. This dual action is of great benefit in promoting the formation of an elastohydrodynamic film at the cam/follower interface.

4.6 ENGINE VALVE TRAIN FRICTION LOSS UNDER FIRED CONDITIONS

As mentioned earlier, under motored conditions the camshaft torque transducer measures the sum of geometric and friction torque, which is a function of tribological performance. Under fired conditions, the camshaft torque transducer measures two additional torques. One is the inertial torque of the complete camshaft assembly due to speed variation throughout the complete engine cycle, figure 4.19, and the other is the torque required by the exhaust camshaft for opening the valve against the cylinder pressure gas force, and is referred to as gas torque in this thesis. The inertia torque is the product of the mass inertia of the camshaft assembly and the angular acceleration. The encoder connected to the crankshaft measures the angular acceleration of the camshaft. The gas torque is the product of gas force acting on the exhaust valve (valve area × cylinder pressure) and the eccentricity of the point of contact of cam/follower from the follower centre line. Thus before averaging the drive torque measured under fired conditions, the effects of the inertia torque and the gas torque was removed from the output data.

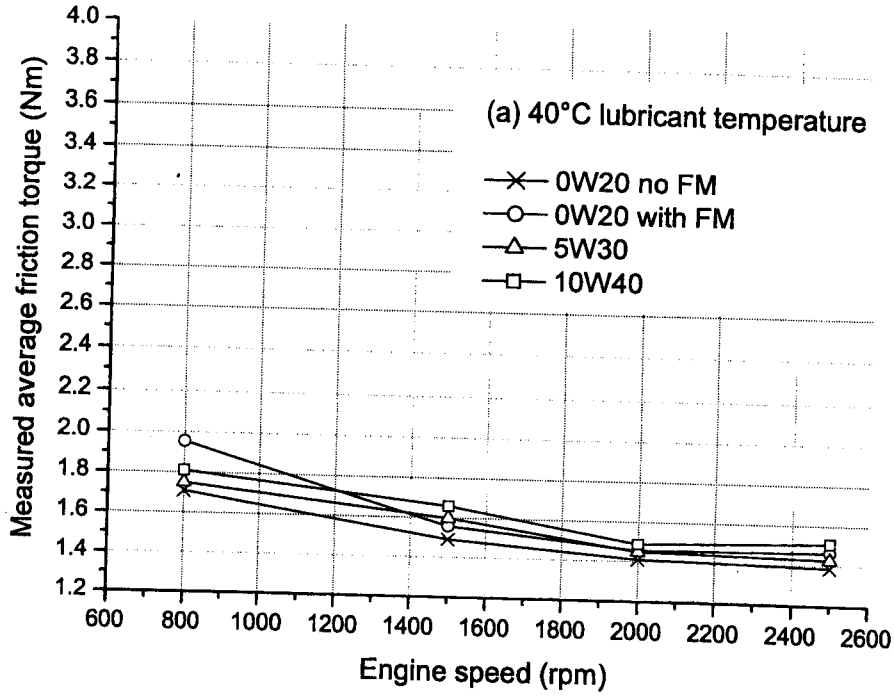

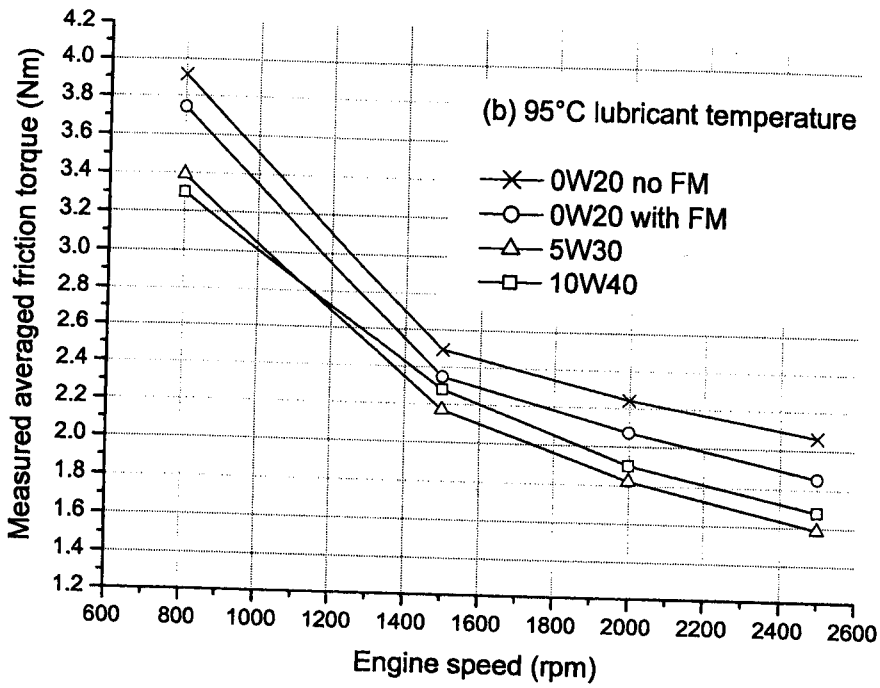

Figure 4.18(a)(b). Experimental inlet camshaft friction torque averaged over cam event only, lubricant temperature 40°C and 95°C

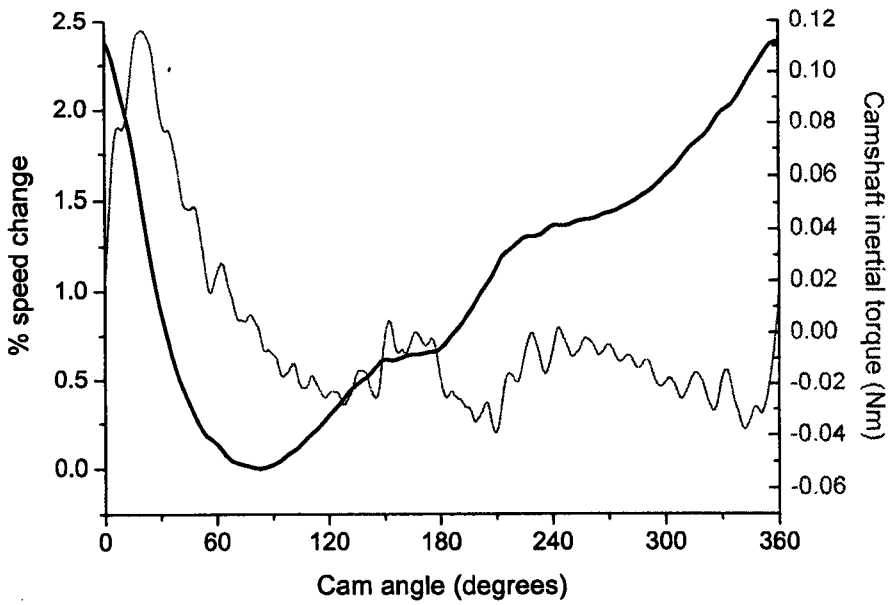

Figure 4.19. Camshaft speed variation and predicted assembly inertial effect. Engine speed 2000rpm, under fired conditions.

The experiments under fired conditions were carried out using two fully formulated lubricants, SAE 10W40 and SAE 5W30 with friction modifier. The variation of instantaneous drive torque and average friction under fired conditions with engine speed is presented in figures 4.20 and 4.21 respectively for the SAE 10W40 oil at a lubricant inlet temperature of 95°C. The inertia and gas torque have been removed from the data in both the figures, although the inertia has a relatively small contribution on the drive torque for the given conditions, as can be seen by comparing figures 4.19 and 4.20. Figure 4.22 shows the variation of instantaneous valve train friction with lubricant temperature for the SAE 10W40 at an engine speed of 2000rpm for motored and fired conditions respectively.

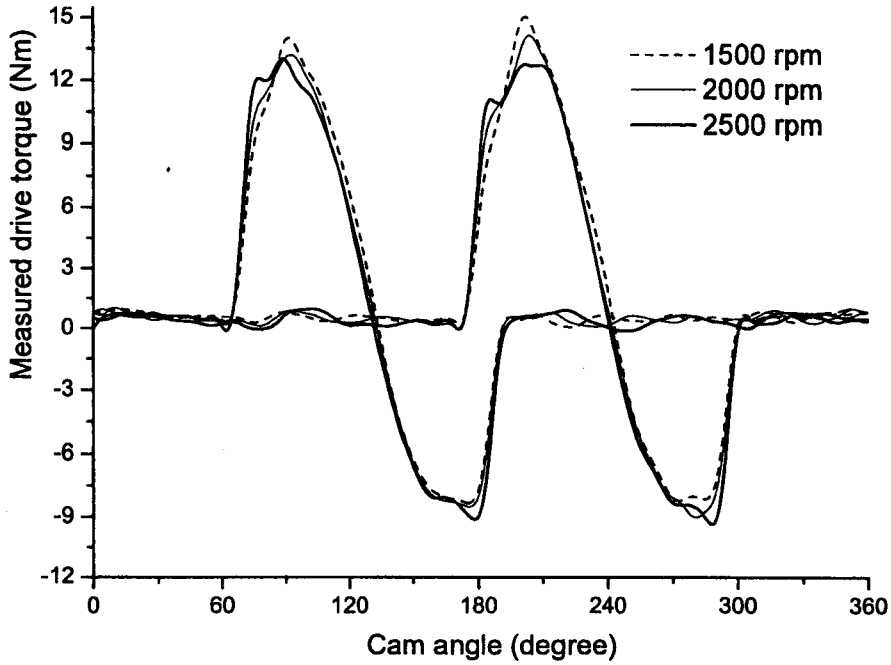

Figure 4.20. Instantaneous valve train drive torque under fired conditions, 10W40, 95°C oil inlet temperature

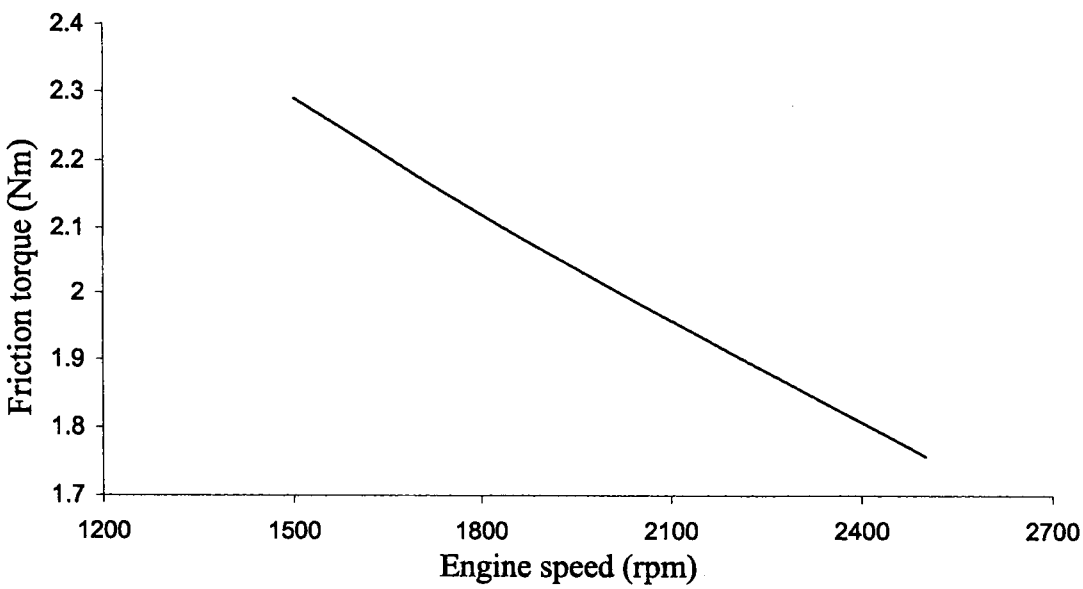

Figure 4.21. Average valve train friction torque under fired conditions, SAE 10W40, 95°C oil inlet temperature

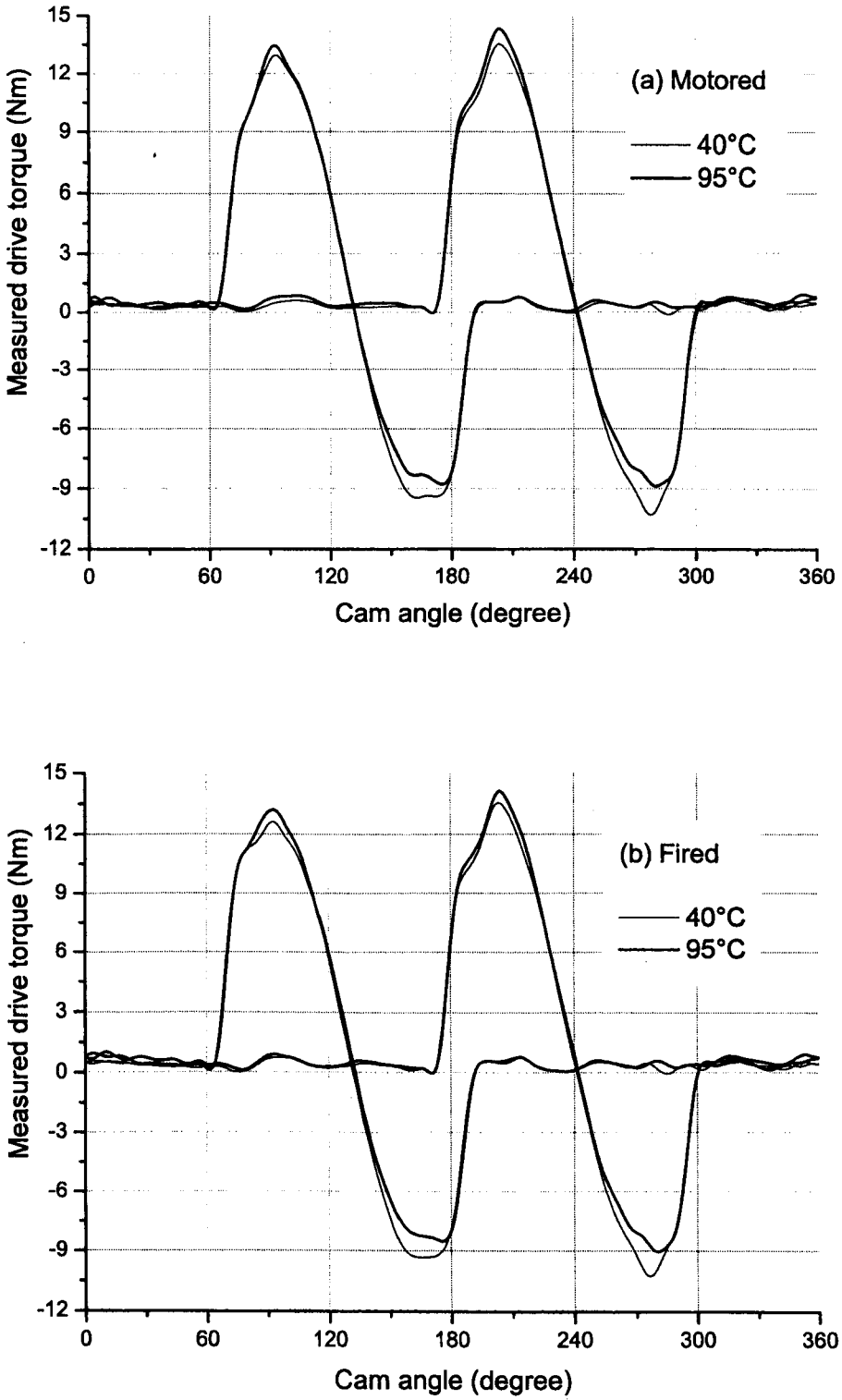

Figure 4.22(a)(b). Instantaneous camshaft drive torque under motored and fired conditions, 2000rpm, SAE 10W40.

4.6.1 DIFFERENCE IN VALVE TRAIN FRICTION BETWEEN MOTORED AND FIRED CONDITIONS

By comparing figures 4.22(a) and 4.22(b) for motored and fired conditions it can be seen that there are significant differences in the shape of the exhaust camshaft curves whereas the inlet camshaft data remain nearly the same. A clearer picture can be seen in figure 4.23, comparing the motored and fired valve train torques for an engine speed of 2000rpm and oil temperature of 95°C. There is hardly any difference in the inlet camshaft drive torque but a sharp rise in torque for the exhaust camshaft during valve opening can be seen under fired conditions.

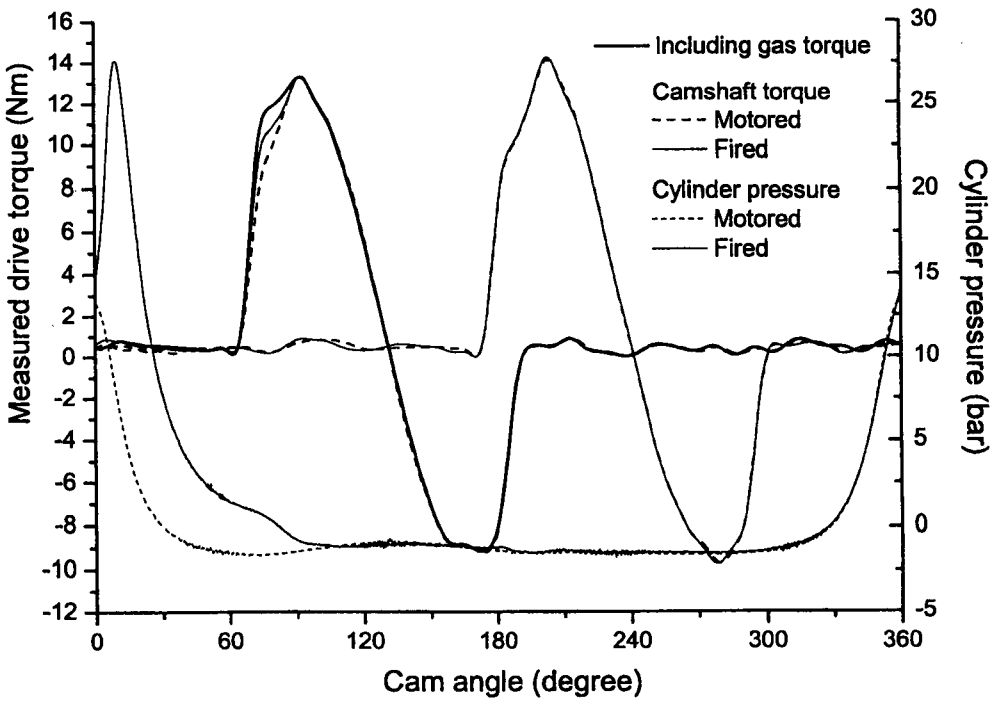

Figure 4.23. Drive torque under motored and fired conditions, 2000rpm, oil 80°C, SAE 10W40.

When comparing the results with the cylinder pressures it becomes clear that this increase in friction torque is due to the extra loading acting at the cam/follower interface as a result of additional work carried out by the cam to open the valve against the cylinder pressure acting on the valve face. Experiments were also carried out under fired condition with lubricant SAE 5W30 and figure 4.24 shows the difference between

the motored and fired exhaust camshaft average friction torque. It can be seen that the average friction torque remains nearly constant for any given engine speed and lubricant temperature.

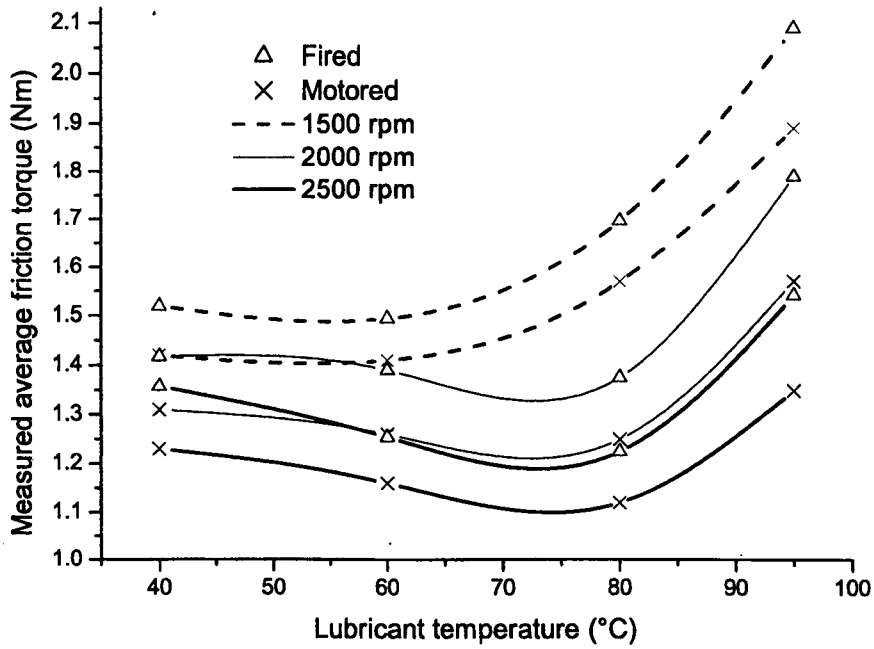

Figure 4.24. Average exhaust camshaft friction torque for cam profile period only, SAE 5W30

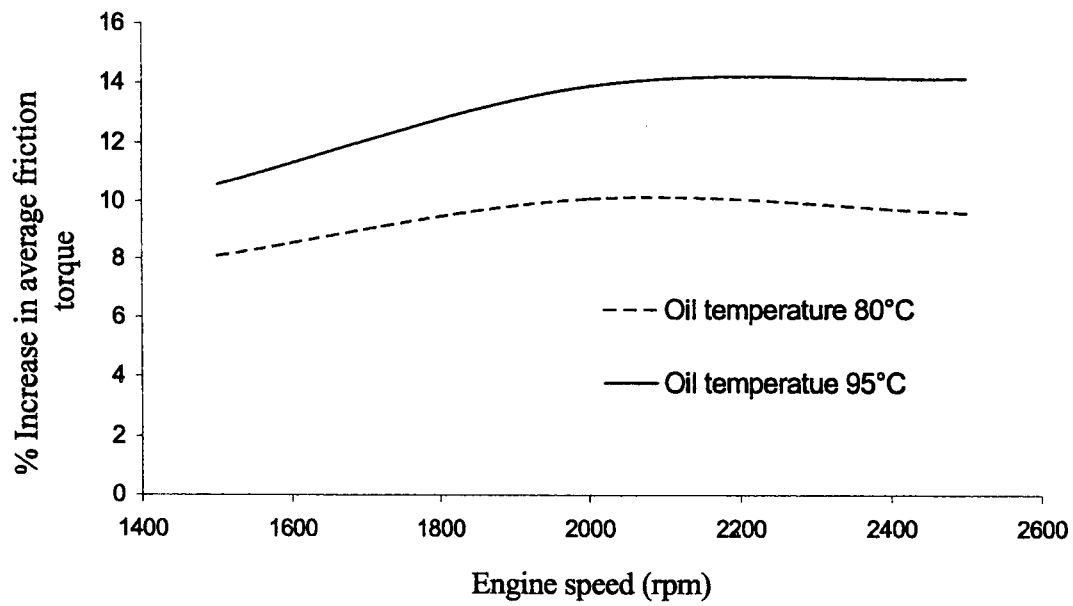

Figure 4.25. % Increase in exhaust camshaft friction torque, fired (half load) versus motored conditions, SAE 5W30.

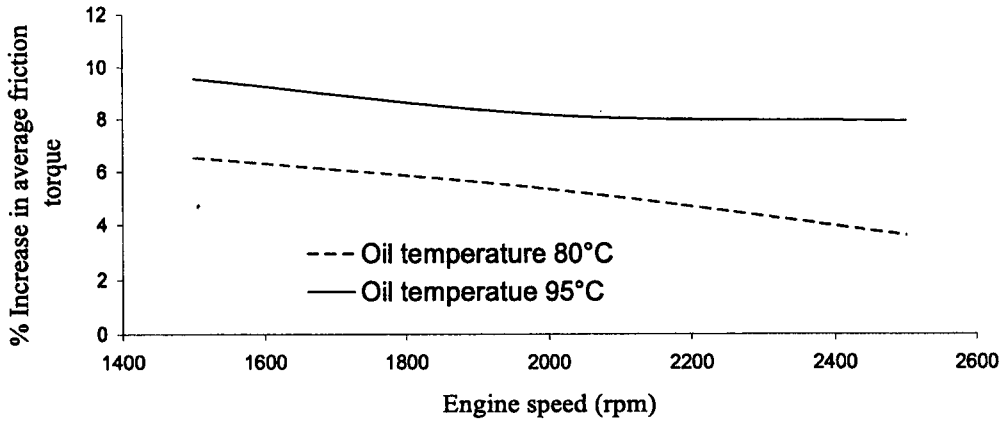

Figure 4.26. %Increase in total valve train friction torque, fired (half load) versus motored conditions, SAE 5W30.

The exhaust camshaft friction torque difference between fired and motored generally increases as the engine speed increases, figure 4.25. It increases from 8% to 10% and 10% to 14% for engine speeds of 1500rpm to 2500rpm for oil temperatures of 80°C and 95°C respectively. The percentage increase in total average engine valve train friction torque under fired condition as compared to motored, remains fairly constant as shown in figure 4.26 at around 4% to 7% and 9% to 10% for lubricant temperatures of 80°C and 95°C respectively.

4.7 CONCLUSIONS

A new technique to measure instantaneous and mean camshaft drive torque in a running engine, without modification of the drive train, has been developed and demonstrated to be a powerful experimental tool. The technique has been successfully applied to the inlet and exhaust camshafts under motored and fired conditions of a single-cylinder, four-valve, gasoline research engine with direct-acting overhead camshafts acting on flat-faced, hydraulic lash-adjusted bucket followers. Measured valve train drive torque and friction torque decreased with increasing engine speed but increased with increasing oil temperature in a manner consistent with the results of other researchers. Experiments on a range of lubricants: SAE 10W40; SAE 5W30 with friction modifier and SAE 0W20 with and without an organic friction modifier, showed

that valve train friction was reduced for the oils containing friction modifier at higher operating temperatures.

Comparative results were obtained from an existing mathematical model for the tribology of the valve train. At engine speeds of 1500rpm and above, the model predicted friction of the same order as the experimental data. However, there was a much reduced sensitivity to engine speed and temperature in the predictions. Divergence of theory and experiments with higher oil temperatures at low speed suggests that the model underestimates the severity of the lubrication under such conditions in both the cam/follower interface and the camshaft bearings. Detailed comparison of friction coefficients from theory and experiment shows encouraging correlation but also indicates that some oil may leak from the hydraulic lash adjuster during the cam event, reducing spring compression and the hence the geometric torque. The comparison of experiments and theory has validated the model and directed future developments of the analysis in relation to the severity of lubrication in both the cam/follower interface and the camshaft bearings and in incorporating the dynamic behaviour of hydraulic lash adjusters.

Total valve train friction was also measured under fired conditions and found to be greater than motored friction. The difference increases as the speed increases. A variation of 4% to 10% average friction torque was found under fired condition as compared to motored for an engine speed range from 1500 to 2500 rpm. There was hardly any difference in the inlet camshaft friction torque between motored and fired but a significant difference in the exhaust camshaft friction was observed. The percentage increase in exhaust valve train friction at a lubricant temperature of 95°C under fired conditions ranged from 10% to near 14% as engine speed increased from 1500 to 2500 rpm, compared to motored conditions.

PART II

ENGINE PISTON ASSEMBLY FRICTION

Chapter five

PISTON ASSEMBLY FRICTION MODEL

5.1 INTRODUCTION

A significant part of engine mechanical power loss is due to piston assembly/cylinder bore friction. The losses arise from the interaction of the cylinder liner, compression rings, oil control ring and piston skirt. Piston ring lubrication models have been under developed for many years. In the early investigation Furuhama [1959] carried out the lubrication analysis for a single piston ring whereas Lloyd [1969] demonstrated that an optimum ring profile existed that maximised the oil film thickness for a given engine conditions. Wakuri et al [1978] considered the effects of cavitation and squeeze film on ring analysis. The effect was also considered by Dowson et al [1979] who applied these effects on the complete compression ring pack along with the effects of lubricant starvation. Ruddy [1979] extended this work and included mixed lubrication analysis.

As compared to the piston ring lubrication analysis, piston skirt lubrication has received little attention. The piston throughout the combustion cycle exhibits significant secondary motions. Lateral movement across the cylinder and rotation about the gudgeon pin causes the piston to tilt in the bore, as described by Chittenden and Priest [1993].

Based on the above mentioned research work, Yang [1992] developed the piston assembly module of the FLAME engine friction model, assessing the individual performance of compression rings and oil control ring. The piston skirt analysis was based on a very simple model, calculating the shear losses by assuming that the piston and the cylinder are concentric. A more realistic and complex piston skirt model has been developed by Chittenden and Priest [1993], based on the work of Li et al [1982] known as the Leeds Piston Skirt Lubrication and Dynamics Analysis.

Most previous numerical studies have been on either the piston skirt or the piston rings. This chapter outlines piston assembly module of the FLAME engine friction model developed by Yang [1992] and the Leeds Piston Skirt Lubrication and Dynamics Analysis. Thus considering the performance of the piston assembly as a whole, combining the analysis of both the piston rings including oil control ring and the piston skirt lubrication.

To study the contribution of each component it is important to analyse each separately. The compression rings act as a gas seal to the combustion chamber and there is a substantial variation of gas pressure throughout the ring pack at certain times in the engine operating cycle.

The lubrication analysis of a compression ring requires detailed understanding of all the forces acting on it. One of the main forces acting on the ring is the combustion pressure force that can be determined relatively with ease with the help of a pressure transducer whereas the measurement of inter-ring gas pressure is not an easy task. The first part of this chapter describes the so-called orifice and volume theory used to predict gas pressure between compression rings. The second part describes the friction loss generated by the compression rings by analysing hydrodynamic lubrication of a single ring and then applying the technique to the rest of the ring pack. The chapter also describes in detail the parameters required to estimate frictional loss generated by the compression rings like, ring kinematics, loading, variations of lubricant film thickness and lubricant transport mechanism. The frictional loss generated by the oil control ring/cylinder liner interaction is also addressed. Finally the piston skirt/cylinder liner friction is explained using both a simple viscous traction approximation and a more complex analysis that involves piston secondary motion.

5.2 INTER-RING GAS PRESSURE

The main purpose of piston rings is to prevent leakage of gases from the combustion chamber. It is of course, acknowledged that a single ring cannot form a perfect seal and in most cases a ring pack is used to share the gas pressure gradient from combustion chamber to crankcase. In spite of this, some gas leakage may still be expected to occur through the rings. If the ring is performing properly then the pressure

of the oil film between the ring face and the liner will prevent the blow-by. Practical and experimental experience suggest that in most cases the gas pressure loading on the top flank of the ring is greater than that on the lower flank, pushing the ring against the groove lower surface during most of the working period but still there will be some gas leakage between the ring and its groove as ideal condition does not always exist. Axial movement of the ring (ring flutter) due to unbalanced forces may cause excessive gas leakage. Despite the possibility of blow-by due to ring flutter and ring lift caused by the change in direction of piston motion and the gas escaping through the face of the piston ring, it is acknowledged that the ring gaps are the primary route for gas leakage and thus are of most importance in determining the inter-ring gas pressure.

Eweis [1935] was the first to propose the so-called orifice and volume model addressing engine blow-by. Later the model was developed by Ting and Mayer [1974] and applied extensively by Ruddy et al [1981] and Kuo et al [1989], and is now the popular way of predicting inter-ring gas pressures. The model assumes that the ring gaps are the only gas leakage paths and that the gas flow is an adiabatic flow. The ring pack comprises of a series of square-edged orifices and adjacent volumes. This model is used as the basis for the present analysis.

To predict the inter-ring gas pressure using the orifice and volume method, two equations are required, equation for the flow rate through the orifice and an expression describing the rate of change of pressure within a volume.

In deriving the equation for the mass flow rate through the orifice it is assumed that the rate of heat transfer is very small for the flow to be assumed to be adiabatic. It is also assumed that the gas flow is isentropic (entropy remains constant) and obeys the ideal gas law. Then the mass flow rate according to Ruddy [1992] can be derived as

$$\dot{m} = AK_c \left[\frac{2\gamma}{(\gamma-1)RT_t}\right]^{\frac{1}{2}} p_t \left(\frac{p}{p_t}\right)^{\frac{1}{\gamma}} \left[1-\left(\frac{p}{p_t}\right)^{\frac{\gamma-1}{\gamma}}\right]^{\frac{1}{2}} \qquad 5.1$$

and the non-dimensional form is given by

$$\frac{d\bar{m}_{n-1}}{d\theta} = K_i \left(\frac{A_n}{A_1}\right)\left[\frac{\bar{P}_{n-1}}{\sqrt{\bar{T}}_{n-1}}\right]\left(\frac{\bar{P}_n}{\bar{P}_{n-1}}\right)^{\frac{1}{\gamma}}\left[1-\left(\frac{\bar{P}_n}{\bar{P}_{n-1}}\right)^{\frac{\gamma-1}{\gamma}}\right]^{\frac{1}{2}} \qquad 5.2$$

where,

$$K_i = \frac{K_c A_1}{V_1 \omega}\left[\frac{2\gamma R T_o}{\gamma - 1}\right]^{\frac{1}{2}}$$

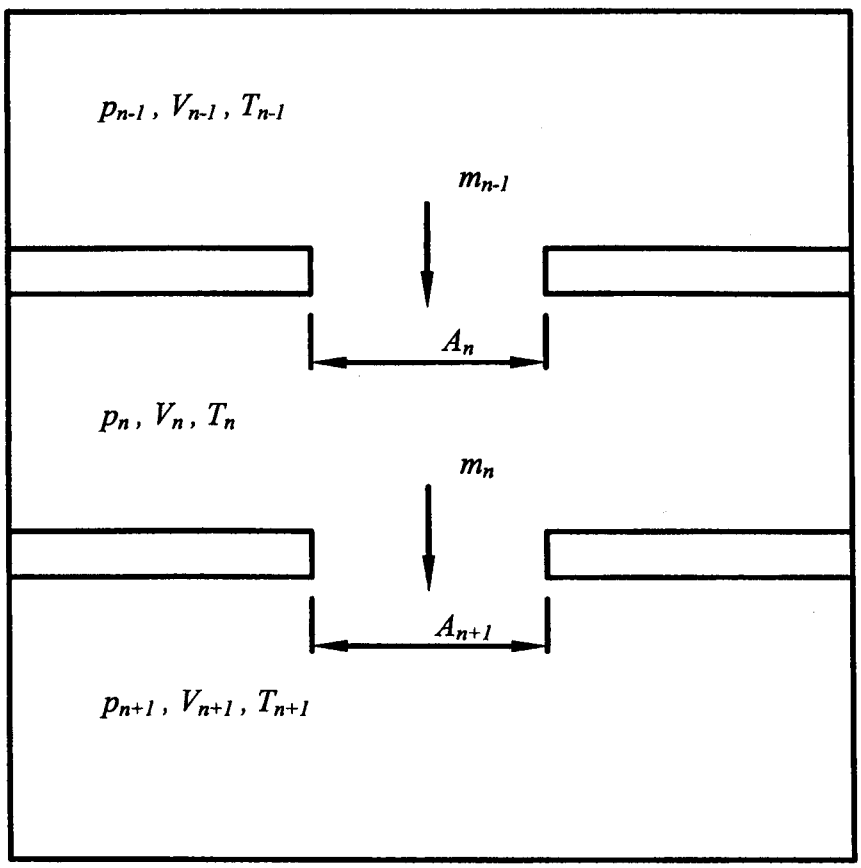

Figure 5.1. Ring pack gas flow, orifice and volume model for inter-ring gas pressure prediction.

According to figure 5.1, at any instant the pressure within a volume is given by,

$$p_n = \frac{RT_n}{V_n}\left(m_i + m_{in} - m_{out}\right) \qquad 5.3$$

where at any crank angle,

m_i, mass of gas in the inter-ring volume.

m_{in}, mass of gas entering the inter-ring volume region.

m_{out}, mass of gas leaving the inter-ring volume region.

Differentiating equation 5.3, the non-dimensionalised form is given by Yang [1992],

$$\frac{d\overline{P}_n}{d\theta} = \overline{T}_n\left(\frac{V_1}{V_n}\right)\left(\frac{d\overline{m}_{n-1}}{d\theta} - \frac{d\overline{m}_n}{d\theta}\right) \qquad 5.4$$

As $\overline{P}_n = \dfrac{p_n}{p_{at}}$ and p_{at}=atmospheric pressure

Thus from equation 5.2 and 5.4, the inter-ring gas pressure can be calculated as

$$(p_n)_{\theta+d\theta} = (p_n)_\theta + \frac{d\theta}{2}\left[\left(\frac{dp_n}{d\theta}\right)_\theta + \left(\frac{dp_n}{d\theta}\right)_{\theta+d\theta}\right] \qquad 5.5$$

Where,

$(p_n)_\theta$ = p_n at crank angle θ.

n = refers to ring number.

$d\theta$ = crank angle increment.

When the pressure ratio adjacent to the ring increases, the gas flow velocity increases until it reaches the local speed of sound. At this point the gas reaches maximum value, since the cross sectional area of the orifice is constant. The pressure ratio at this point is called the critical pressure ratio. Normally as the gas flow velocity increases the flow area decreases but when the critical pressure point is reached, any increase in gas flow above this point is then associated with increase in flow area.

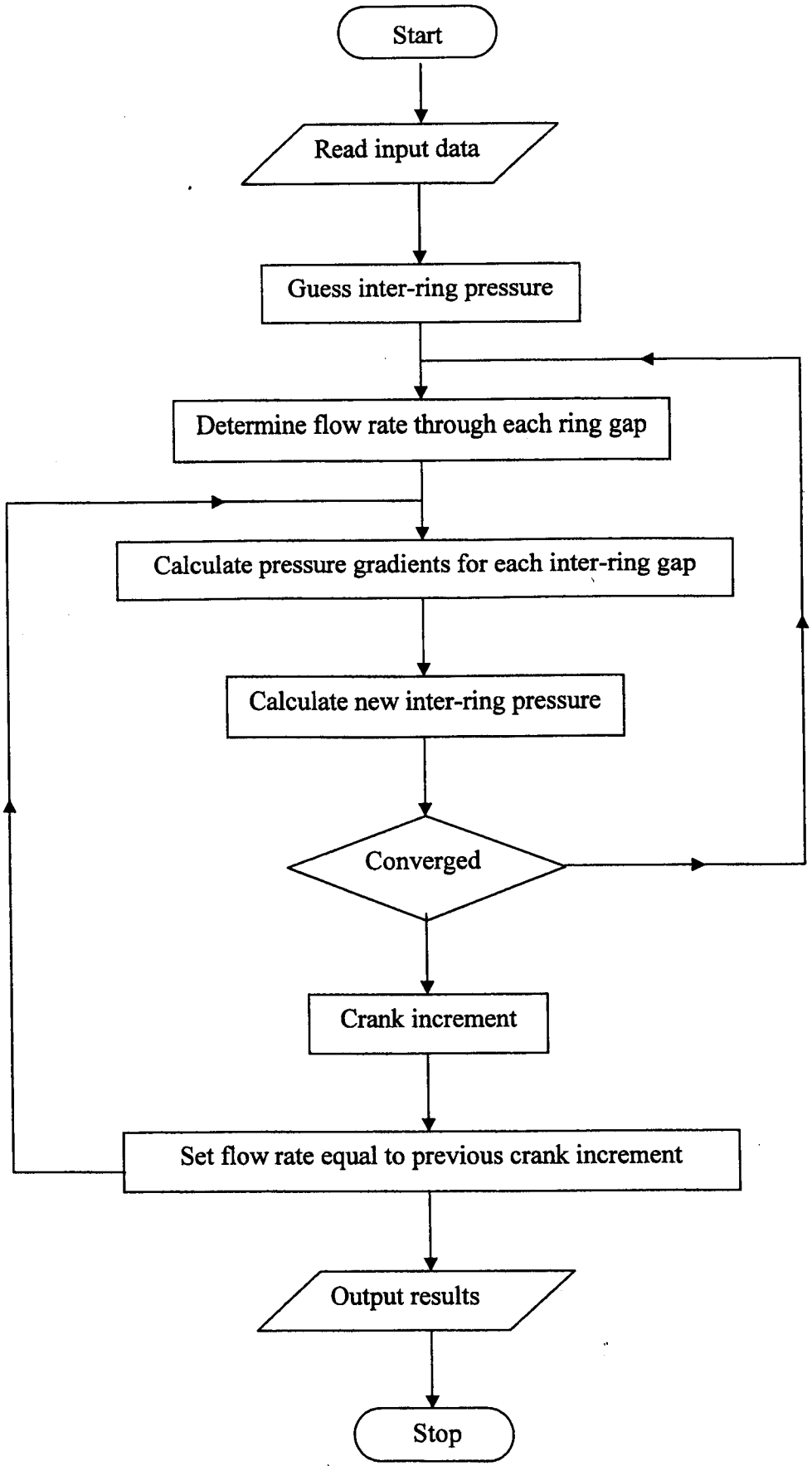

Figure 5.2. Inter-ring gas pressure prediction flow chart.

For $\gamma = 1.3$ and the discharge coefficient $K_c = 0.65$ for a square edged orifice, then the critical pressure ratio becomes 0.546 and the equation 5.2 reduces to

$$\frac{d\bar{m}_{n-1}}{d\theta} = 0.227 K_i \left(\frac{A_n}{A}\right)\left(\frac{p_{n-1}}{\sqrt{\bar{T}_{n-1}}}\right) \qquad 5.6$$

Based on equations 5.2, 5.5 and equation 5.6 a computer program has been developed by Ruddy et al [1981], later introduced by Yang [1992] in the FLAME engine friction model, to calculate the inter-ring gas pressure required to determining the engine piston assembly friction, figure 5.2.

5.3 COMPRESSION RING, POWER LOSS

The main purpose of a compression ring is to act as a gas seal for the combustion chamber. It experiences pressure-loading variation throughout the engine cycle. The rings are manufactured with a small spring force to force the ring against the liner, but this action is substantially enhanced by the gas pressure acting on the inner face of the ring. It is assumed that a thin oil film separates the compression rings from the liner and thus Reynolds equation can be used to determine the film thickness throughout the engine cycle. For the piston ring lubrication analysis and to solve the Reynolds equation it is necessary to determine the following parameters,

- Shape of the piston ring face.
- Piston ring sliding speed.
- Cyclic variation of piston ring loading.
- Lubricant viscosity.

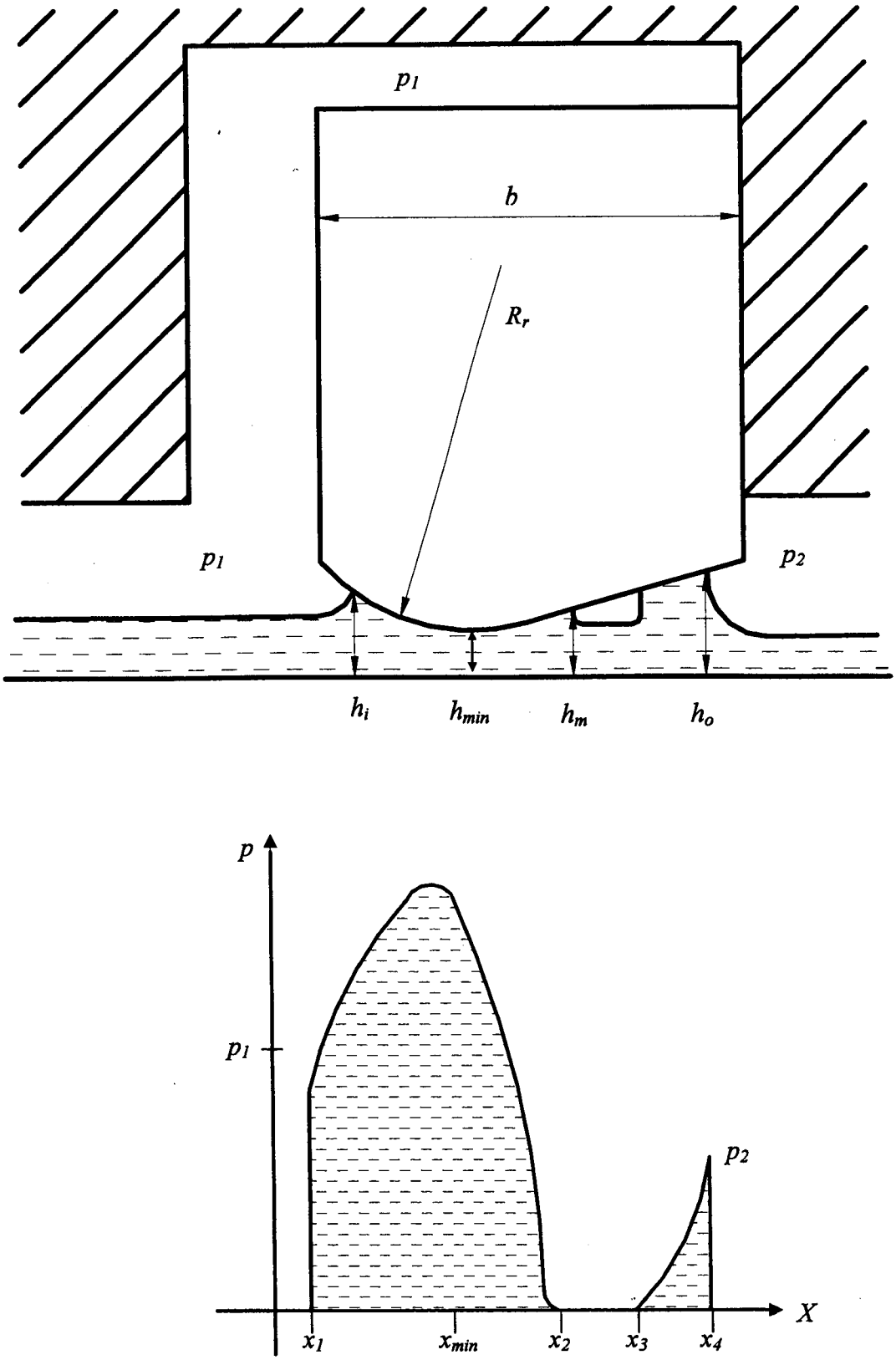

Figure 5.3. Hydrodynamic film shape and pressure distribution at the compression ring and cylinder liner interface.

5.3.1 SHAPE OF PISTON RING FACE

It is assumed in the present work that the surfaces of the liner and the rings are smooth and the circumferential curvature is neglected reducing the problem to two-dimensional case. The effective radius of curvature of the ring face is much larger than the width of the ring and thus the ring face profile can be represented as a parabola. The line of minimum film thickness may be offset from the mid-plane of the ring by a distance that is called the ring face offset. The offset is positive if the line of minimum film thickness is displaced towards the combustion chamber. Thus according to figure 5.3, the shape of the ring face can be expressed as, Yang [1992]

$$h(x) = h_{\min} + \frac{(x - x_{\min})^2}{2R_r} \qquad 5.7$$

5.3.2 KINEMATICS

To calculate the lubricant film thickness at the liner/ring interface it is important to determine the entraining and sliding velocities. During an engine cycle ring lift may occur in the piston groove due to the force balance. If this lift is neglected, the axial cyclic velocity of the ring can be assumed to be identical to that of the piston. Thus the axial velocity of the piston and hence the rings is given by,

$$U_r = R_a \omega \left[\sin\theta + \frac{\sin 2\theta}{2\left(\left(\frac{L}{R_a}\right)^2 - \sin^2\theta\right)^{\frac{1}{2}}} \right] \qquad 5.8$$

In order for the lubricant to experience converging/divergent space to solve Reynolds equation, it is considered that the liner transports the lubricant that is, the piston rings remain stationary and the cylinder liner moves past the ring at the speed of the piston. The equivalent liner velocity U_l is then equal in magnitude but opposite in direction to the sliding velocity of the piston rings. According to figure 5.3, it is assumed that pressure p_1 is greater than pressure p_2 and thus the pressure p_1 is applied at the back of

the ring. If p_2 is greater than p_1, the ring is assumed to move to the other flank of the ring groove resulting in pressure p_2 being applied at the back face of the piston ring.

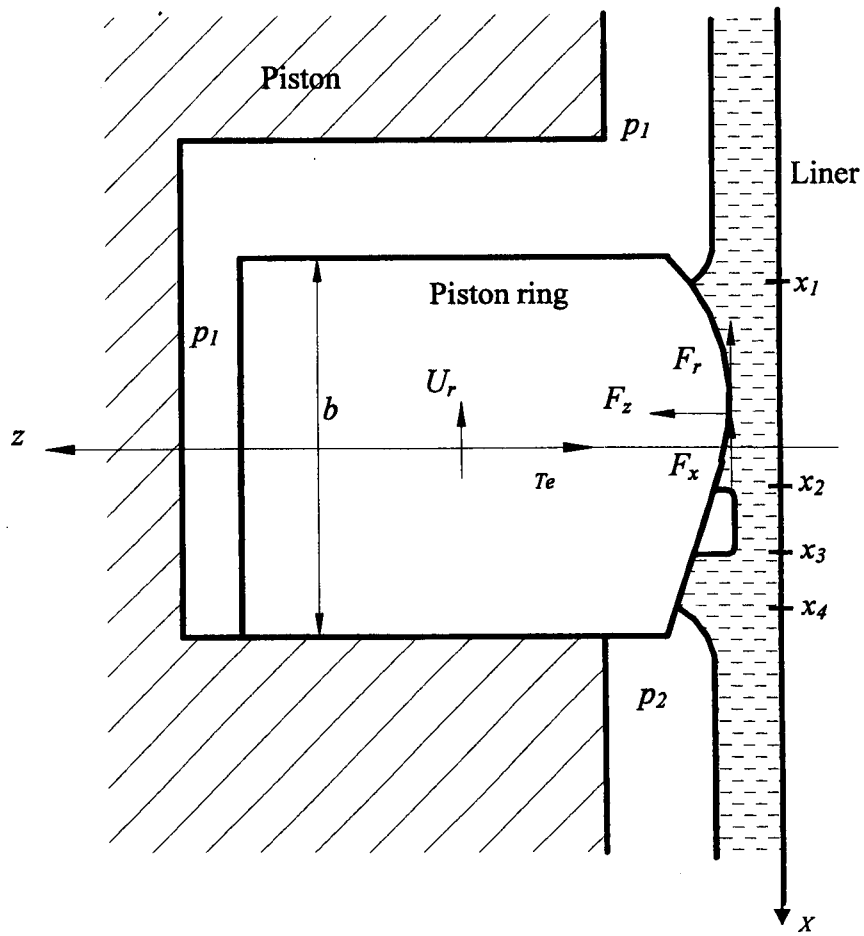

Figure 5.4. Forces acting on a single piston ring.

5.3.3 PISTON RING LOADING

The forces acting on the piston ring according to figure 5.4 are,

- Gas force above and below the ring.
- Viscous traction and lubricant pressure force within the film.
- Piston ring elastic tension.
- Reaction from the contacting flank between the ring and the piston ring groove.

The gas pressure also exerts force at the back of the compression rings. The gas pressure above the top ring is the combustion chamber whereas the gas pressure below

the last compression ring is the crankcase pressure. The inter-ring pressure is determined by the orifice-volume method described in the start of this chapter. In figure 5.4, F_z is the hydrodynamic force acting per unit circumferential length in the radial direction and F_r is the viscous traction force.

It is assumed in the present study that the net radial force is supported by the hydrodynamic action in the oil film produced by the entraining velocity and squeeze action. If the lubricant supply is insufficient to flood the ring, part of the ring face will be exposed to the gas pressure above and below the ring, p_1 and p_2 figure 5.4. If the radial force between the ring and the groove is neglected, the hydrodynamic force is then balanced as,

$$F_z = p_1(b - x_1) - p_2(b - x_4) + T_e b \qquad 5.9$$

5.3.4 LUBRICATION OF PISTON RING

The parabolic shape of the ring and the straight liner produces a convergent/divergent clearance, assuming that the liner transports the lubricant. The divergent region will theoretically produce a sub-ambient pressure profile. In reality, the lubricant cannot withstand pressures below saturation level without releasing dissolved gases or pressures below vapour pressure without boiling and will thus result in causing film rupture called cavitation. Gumbel [1921] recognised the inability of the fluid to sustain large and continuous negative pressures and believed to be effectively producing a cavitation region, assuming all negative pressures are set to zero. The experimental evidence of cavitation has been reported by Brown and Hamilton [1978].

Referring to figure 5.3 the pressure within the oil film at the entraining inlet, at location x_1 must equal the gas pressure p_1. The oil pressure due to the oil wedge effect rises from p_1 at location x_1 to a maximum and then falls to atmospheric or saturation pressure due to cavitation at the point of film rupture x_2, where the film thickness is defined by h_m. Because of the pressure p_2 at the trailing edge of the ring, the oil film must reform at some location x_3 so that a positive pressure can be reached to the boundary pressure p_2 at the trailing outlet at some location x_4 where the film thickness is defined as h_o.

Thus three pressure regions can be defined along the ring face, a positive pressure region where the pressure varies from p_1 at x_1, to atmospheric at x_2, a cavitation region from x_2 through to x_3 where the film ruptures and the pressure is constant, normally taken as atmospheric, and finally the third region from x_3 to x_4 where the oil film is redeveloped and the pressure rises from atmospheric pressure to pressure p_2. For the piston ring lubrication analysis it is vital to determine these pressures and locations using Reynolds equation.

5.3.4.1 THREE DIMENSIONAL REYNOLDS EQUATION AND FILM THICKNESS.

Reynolds equation is the governing equation for the pressure distribution in a fluid film bearing. The assumptions used to derive the three-dimensional incompressible Reynolds equation are as follows,

- The lubricant is a Newtonian fluid.
- Fluid inertia and weight forces are ignored.
- Fluid flow is laminar.
- No slip occurs between the lubricant and the boundary solids.
- Lubricant properties are constant across the thickness of the film.
- Fluid pressure across the thickness of the film remains unchanged.
- The lubricant is incompressible.
- Curvature of the surfaces is large compared with the film thickness.

According to the above assumptions, the three dimensional incompressible Reynolds equation is expressed as,

$$\frac{\partial}{\partial x}\left(h^3\frac{\partial p}{\partial x}\right)+\frac{\partial}{\partial y}\left(h^3\frac{\partial p}{\partial y}\right)=6\eta\left\{\frac{\partial}{\partial x}(U_1+U_2)h+\frac{\partial}{\partial x}(V_1+V_2)h+2(w_h-w_o)\right\} \quad 5.10$$

The above equation can be simplified as the term $\frac{\partial}{\partial x}(V_1+V_2)h=0$ as the velocity of piston ring and the change of oil film thickness along the circumferential direction is zero. Also the velocity of the piston ring U_2 =0 and liner U_1 =U_l, as explained previously. Similarly $\frac{\partial}{\partial x}(U_1h)$ can be written as $U_1\frac{\partial h}{\partial x}$. Further simplifying is carried

out by substituting $(w_h - w_o)$ with $\frac{\partial h}{\partial t}$, this is permissible if the surfaces are impermeable so no fluid seeps in or out.

Thus equation 5.10 reduces to

$$\frac{\partial}{\partial x}\left(h^3 \frac{\partial p}{\partial x}\right) + \frac{\partial}{\partial y}\left(h^3 \frac{\partial p}{\partial y}\right) = 6\eta\left\{U_l \frac{\partial h}{\partial x} + 2\omega \frac{\partial h}{\partial \theta}\right\} \qquad 5.11$$

At the left-hand side, the first term consists of the variation of pressure in the *'x'* direction that is the direction of liner motion and the second term is the variation in *'y'* direction which in the present case would be equal to zero.

$$\frac{\partial}{\partial x}\left(h^3 \frac{\partial p}{\partial x}\right) = 6\eta\left\{U_l \frac{\partial h}{\partial x} + 2\omega \frac{\partial h}{\partial \theta}\right\} \qquad 5.12$$

The first term in the right-hand side describes the normal wedge action whereas the second term expresses the squeeze film effect.

The integration of the above equation gives an expression for the axial pressure gradient for the inlet region,

$$\frac{dp_a}{dx} = \frac{1}{h^3}\{6\eta U_l + 12\eta\omega + C_1\} \qquad 5.13$$

where C_1 is an integration constant.

The hydrodynamic pressure within the lubricating film in the inlet region can be calculated by integrating equation 5.13,

$$p_a = 6\eta U_l I_1 + 12\eta\omega \frac{dh}{d\theta} I_2 + C_1 I_3 + C_2 \qquad 5.14$$

where

$I_1 = \int \frac{1}{h^2} dx$, $I_2 = \int \frac{x}{h^3} dx$, $I_3 = \int \frac{1}{h^3} dx$ and C_2 is another integration constant.

For the ring of parabolic profile, the integrals, I_1, I_2, and I_3 have analytical solutions. A solution of equation 5.14 requires that the integration constants C_1 and C_2 and the cavitation and reformation locations x_2 and x_3 should be determined.

Constants C_1 and C_2 and location x_2 can be determined by applying the following boundary conditions to equation 5.13 and 5.14.

$$p_a = p_1 \qquad (x = x_1)$$

$$p_a = \frac{dp_a}{dx} = 0 \qquad (x = x_2)$$

The reformation boundary x_3 can be determined by considering the continuity of flow and the boundary pressure conditions at the trailing edge of the ring. According to Reynolds equation, the expression for the volume rate of flow per unit circumferential length for the present case is given by

$$Q = -\frac{h^3}{12\eta}\frac{dp}{dx} + \frac{U_1 h}{2} \qquad 5.15$$

Also the flow rate per unit length at the cavitation boundary x_2 can be expressed as,

$$\frac{U_1 h_m}{2} \qquad 5.16$$

since $\frac{dp}{dx} = 0$.

This flow rate at the cavitation boundary must be equal to that past the outlet region of the ring. Thus equating equation 5.15 to 5.16,

$$\frac{dp_b}{dx} = 6\eta U_1 \left(\frac{h - h_m}{h^3} \right) \qquad 5.17$$

where 'p_b' is the hydrodynamic pressure in the region between x_3 and x_4. Integrating the above equation and applying the following boundary conditions, the integration constant and the reformation location x_3 can be calculated.

$$p_b = p_2 \qquad (x = x_4)$$

$$p_b = 0 \qquad (x = x_3)$$

Knowing the entire integration constants and the cavitation and reformation boundary locations, the oil pressure p_a in the region x_1 and x_2 in front of the cavitation region and the oil pressure p_b in the area x_3 and x_4 behind the cavitation region can be calculated. Thus the hydrodynamic radial force per unit length F_z, can be determined by direct integration as

$$F_z = \int_{x_1}^{x_2} p_a dx + \int_{x_3}^{x_4} p_b dx \qquad 5.19$$

This force is equal to the load applied radially on the ring as expressed by equation 5.9. Combining equation 5.9 and equation 5.19, the change of film thickness with respect to crank angle $\frac{dh}{d\theta}$ can be calculated. Both the quantities $\frac{dh}{d\theta}$ and h_{min} are not known initially. $\frac{dh}{d\theta}$ can be calculated if an initial estimate is made of h_{min} at some crank angle where the film thickness is expected to change only slightly. Once $\frac{dh}{d\theta}$ is known, values of h_{min} can be calculated for a complete engine cycle using the well-known Trapezoidal rule,

$$h_{\theta+d\theta} \approx h_\theta + \frac{d\theta}{2}\left[\left(\frac{dh}{d\theta}\right)_\theta + \left(\frac{dh}{d\theta}\right)_{\theta+d\theta}\right] \qquad 5.20$$

where h_θ is the minimum film thickness at crank angle θ and $d\theta$ is the crank angle increment.

If the calculated film thickness at each crank angle is found to be greater than the composite roughness of the ring and cylinder liner, it is assumed the ring is operating in the hydrodynamic regime and the friction is due to the shearing of the fluid. The friction force per unit circumferential length is determined as,

$$F_r = \int_{x_1}^{x_4} \left(\eta \frac{du}{dz}\right) dx \qquad 5.21$$

where the velocity gradient according to Cameron [1981], for static piston ring and movable liner in the presence of lubricant pressure difference in x-axis direction is given by

$$\frac{du}{dz} = \frac{h}{2\eta}\frac{dp}{dx} + \frac{U_l}{h}$$

Thus equation 5.21 can be expressed, according to the boundary locations as,

$$F_r = \int_{x_1}^{x_2}\left(-\frac{h}{2}\frac{dp_a}{dx} + \eta\frac{U_l}{h}\right)dx + \int_{x_3}^{x_4}\left(-\frac{h}{2}\frac{dp_b}{dx} + \eta\frac{U_l}{h}\right)dx \qquad 5.22$$

The average frictional power loss for a compression ring over one complete engine cycle is then given by,

$$H_r = \frac{1}{2\pi}\int_0^{2\pi} F_r \pi D U_l d\theta \qquad 5.23$$

where D is the engine cylinder bore.

It is assumed that the viscosity of the lubricant film varies according to the axial temperature variation of the cylinder liner. The cylinder liner measured surface temperature at several points is often available and the intermediate temperature values along the liner at any point in a stroke can be interpolated by fitting a quadratic curve to the available temperature data. If the appropriate viscosity-temperature characteristics of the lubricant are provided, the viscosity of the lubricant film between the ring and cylinder liner can be calculated at any crank angle. In this research project, nine thermocouples were fitted on the liner to monitor the liner surface temperature at different locations, details can be found in chapter eleven.

It is known that the predicted film thickness generally falls below the composite surface roughness for the ring and liner near both the piston dead center positions. Under such conditions boundary lubrication is assumed to occur and a constant coefficient of friction of 0.12 is applied for the SAE 0W20 without friction modifier.

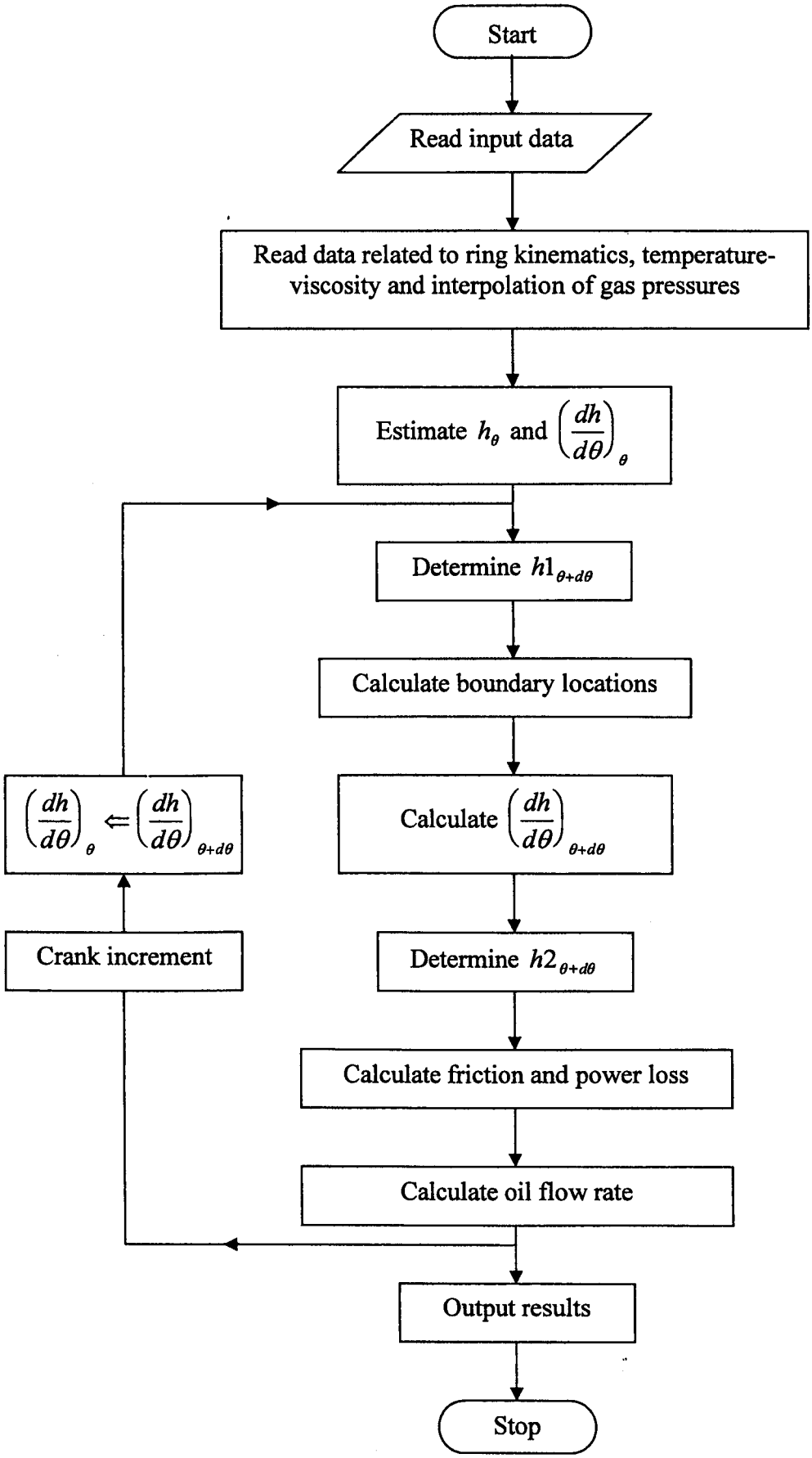

Figure 5.5. Flow chart for a single ring lubrication analysis.

5.3.4.2 LUBRICANT FLOW RATE

In the present study it is assumed that the only way for oil to pass the piston rings is between the ring face and the cylinder liner. The lubricant flow rate can be calculated at the point where only Couette flow takes place, that is $\frac{dp}{dx} = 0$. Thus the volume flow rate of lubricant 'Q', per unit width at any crank angle is given by,

$$Q = \frac{1}{2} U_l h_m \qquad 5.24$$

Integration of this quantity with respect to crank angle over the complete engine cycle gives the net volume rate of flow of lubricant. The sign of this net flow indicates whether the oil flows towards the combustion chamber or towards the crankcase.

The computer program flow chart for a single ring lubrication analysis is illustrated in figure 5.5.

5.4 LUBRICATION ANALYSIS FOR A COMPLETE RING PACK

In most of the cases the sealing of the combustion chamber is made more effective by having more than one compression ring and in such case the lubrication of the rings and the cylinder liner largely depends on the interaction of the ring pack. If plentiful lubricant is available at the inlet edge of the ring, the ring is said to have fully flooded lubrication, but if the inlet region is not flooded than the ring is said to undergo starved lubrication. The situation for two adjacent compression rings working in a pack is shown in figure 5.6. The oil film thickness for the first ring is calculated by the method described earlier.

To calculate the film thickness for the second ring it is important to determine the oil film thickness left by the first ring and its effect on the position of the inlet boundary of the second ring. The information is then used to evaluate the film thickness for the second ring. According to the principle of continuity, the volume rate of flow past the

second ring cannot exceed that past the first ring in the absence of any oil supply between the rings.

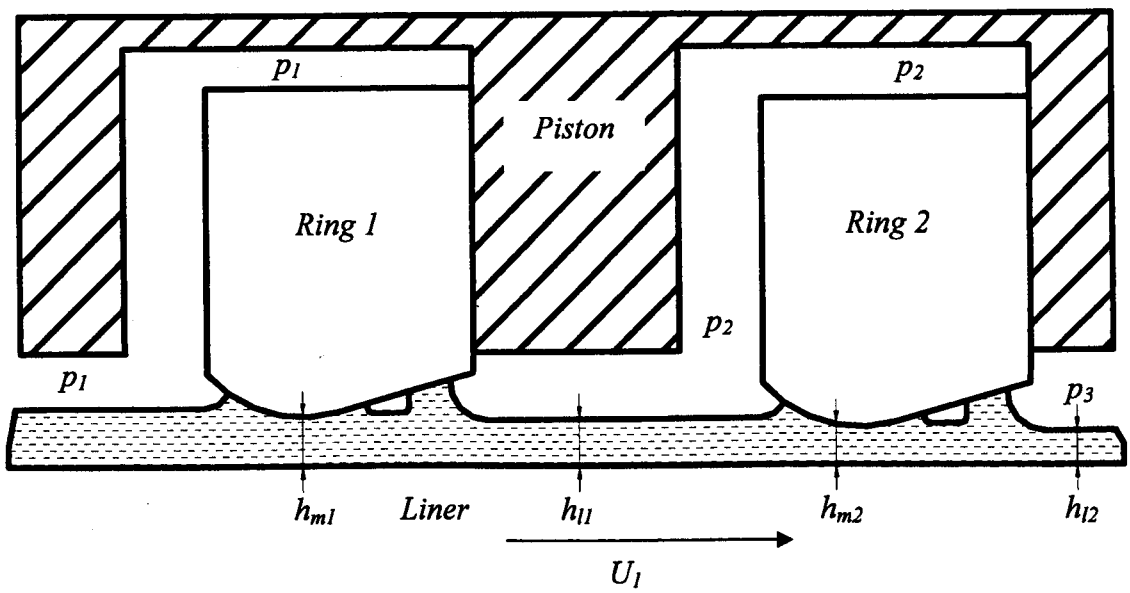

Figure 5.6. Lubricant flow in a piston ring pack.

The magnitude of volume flow rate past the first ring is given by equation 5.24. The same quantity of oil must flow through the inter-ring region with velocity U_l. If the thickness of the film in the inter-ring region of the liner is h_l and with no fresh supply of oil available, then

$$\frac{U_l h_m}{2} = U_l h_l \qquad 5.25$$

For the lubrication analysis of the ring pack it is initially assumed that *ring 1* is fully flooded and the lubrication theory for a single ring is used to determine film thickness h_m and minimum film thickness h_{min}. Using equation 5.25, the film thickness in the inter-ring region is calculated which is then available for *ring 2*. The film thickness may not be sufficient to flood *ring 2* and this may disturb the location of the inlet boundary. Thus an iterative procedure is used to determine the inlet boundary. Initially the minimum film thickness at each crank angle for all rings is calculated assuming all

rings are fully flooded. The thickness of the oil film available for *ring 2* is then assumed to be h_{min} of *ring 1*. This film information is then used to calculate the initial location of the inlet boundary of *ring 2* and using the lubrication theory for a single ring, h_{min} and flow rate pass *ring 2* is calculated. Continuity equation 5.25 is then used to check the flow rate. If the continuity equation is not satisfied the film thickness at the inlet boundary to ring 2 is progressively reduced and the procedure is repeated until the continuity equation of flow is satisfied.

As mentioned above for the ring pack analysis it is assumed that the top ring is fully flooded but this may not be the case. Modern engines are splash lubricated from the sump and thus the fully flooded assumption can be true for the bottom ring during downward stroke. The lubrication of top ring purely relies on the net upward travel of oil through the ring pack and therefore it is assumed that the lubricant available for the top on the up stroke is the lubricant left by it on the liner during down stroke giving more realistic assumption than the previous. Thus for the top ring the continuity flow equation on the up stroke can be expressed as

$Q_{upstroke} \leq Q_{downstroke}$

Where 'Q' is the volume flow rate per unit circumferential length.

Along with the compression rings one more ring is usually fitted in the groove near the upper end of the piston skirt, the oil control ring. The function of this ring is to restrict the amount of oil available to the compression rings and to distribute oil circumferentially around the liner. The working face of the oil control ring is normally narrower than the compression rings and the tangential load is greater. It is therefore assumed that the control rings work in the mixed to boundary lubrication regime. Thus for the present study boundary lubrication is assumed and the friction is equal to the product of the normal load and the coefficient of friction (0.12 for SAE 0W20 without friction modifier). The normal load for the ring is assumed to be only due to the elastic tension of the ring.

The clearance between the piston and the liner varies along the piston axis due to the barrel shape of the piston required to accommodate the severe temperature gradient from the combustion chamber to the crankcase and to prevent edge loading on tilted pistons. Due to the relatively light loading and large contact area, the piston skirt

normally operates in the hydrodynamic lubrication regime, Thring [1989]. A very simple piston skirt power-loss analysis was used by Yang [1992], assuming that the piston remains concentric with the cylinder liner axis throughout the cycle and that resistance to motion is caused by the shearing of the lubricant filling the clearance between the piston and the liner. An average piston/liner clearance value was applied through out the engine cycle. Thus the total piston skirt power-loss due to the viscous shear of lubricant at any instance can be calculated as

$$F_{skirt} = \int_0^l \frac{\eta U}{c} dx \qquad 5.26$$

Where 'c' is the radial clearance. The local liner temperature reading determines the axial variation of lubricant viscosity.

A much more realistic approach has been used for piston skirt friction calculation lifting the assumption that the piston remains concentric in the liner resulting in complex analysis of piston motion. The primary movement of a piston is up and down the cylinder but there my also be significant secondary movement as it rotates around the gudgeon pin causing the piston to tilt within the cylinder or translates across the cylinder resulting in a larger clearance on one side of the bore than the other. This secondary motion can cause surface contact between the skirt and liner causing increase in friction force, Nakayama et al [1997]. Models have been developed by Chittenden and Priest [1993] and Dursunkaya et al. [1994] to study this secondary motion and to investigate the influential factors of load, speed, piston clearance and gudgeon pin offset. Using the Leeds Piston Skirt Lubrication and Dynamics Analysis model based on the Chittenden and Priest [1993], Dr R.J. Chittenden carried out the lubrication and friction loss analysis of the Ricardo Hydra piston skirt. Taking into account all the forces acting on the piston assembly, the eccentricity ratios for the top and bottom of the Ricardo Hydra piston were calculated at 2° intervals of crank angle for engine speeds of 800rpm, 1500rpm and 2000rpm. Using the piston eccentricity information, the lubricant film thickness at the top and bottom of the skirt were calculated at each crank angle, thus generating the data for angle of piston tilt. This knowledge along with the skirt profile resulted in film thickness along the skirt length. Knowing the film

thickness, instantaneous piston velocity and the lubricant viscosity via local liner temperature measurement, the piston skirt frictional loss is calculated. The results of piston skirt loss predicted using both the above methods are presented in chapter seven.

5.5 SUMMARY

The power loss generated from the piston assembly/cylinder liner interaction has been described, using the method developed by Yang [1992]. Eweis [1935] so-called orifice and volume model was used to calculate inter-ring gas pressure, to estimate gas loading on the rings. This information was then used for the prediction of frictional loss generated from the compression rings. Along with the ring loading, the kinematics and hydrodynamic lubrication theory was described for a single compression ring. The minimum film thickness calculation, friction force estimation and lubricant transport mechanism have been described. The single ring analysis was then applied to the complete ring pack.

The frictional loss contribution by the control ring has also been considered. It has been assumed to be operating in boundary lubrication conditions. Two completely independent models have been used to predict friction loss between piston skirt and cylinder liner, a simple full film lubrication analysis assuming the piston remains concentric with the cylinder liner and a more complex and realistic approach where the secondary motion of piston is taken into account.

This piston assembly friction model has been used to predict power-loss of a single cylinder Ricardo Hydra gasoline engine. The results obtained are described in chapter seven and are compared with the experimental data obtained from the same engine.

Chapter six

EXPERIMENTAL METHOD OF MEASURING PISTON ASSEMBLY FRICTION

6.1 INTRODUCTION

The main targets of future internal combustion engines are better fuel economy, lower exhaust emissions and higher engine performance. One way of obtaining this is by reducing engine friction. It is understood that the piston assembly accounts for the largest part of mechanical losses in the engine and thus the lubrication between the piston assembly and liner interface is a key area for potential improvement by reducing frictional losses. Although many studies on piston friction losses have been made, it is an area that is difficult to analyse as it involves complex lubrication conditions. To date a variety of techniques have been developed to measure piston assembly friction losses in a firing engine. But no attempt has been made so far to measure the piston assembly friction losses at realistic speeds and loads simultaneously with friction measurements in other parts of the engine (bearing and valve train).

The two most popular method of measuring piston assembly friction under fired conditions are the "floating liner" method and the "IMEP method" (indicated mean effective pressure). In the floating liner method the liner is isolated from the surrounding structure and is axially supported on a series of load cells. The friction force moves the liner axially and thus the force is measured directly. Forbes and Taylor [1943] made the first attempt to measure the piston assembly friction in a firing engine. The experiment was carried out using an elastically mounted cylinder liner. A very small amount of liner movement was allowed in the axial direction. The axial movement of the liner was recorded photographically.

Leary and Jovellanos [1944] and Livengood and Wallour [1945] later continued this work. Furuhama and Takiguchi [1979] made a significant contribution to the direct piston assembly friction measurement using the floating liner method. The experiments where carried out on a modified single cylinder diesel engine, figure 6.1. The axial

movement of the liner was measured with the help of a piezo-electric load washer fitted at the bottom of the liner. A special sealing arrangement was used to seal the gas pressure at the top of the liner and to reduce any friction force caused by this arrangement. The piston crown was modified to accommodate the sealing arrangement. Also, to reduce the effect of lateral movement of the liner on the load cell a special bar and an annular plate were used, called a lateral stopper. Although the effect of lateral movement was reduced, the annular plate introduced an extra force. Because of this the experiments were carried out at speeds of not more than 1400rpm.

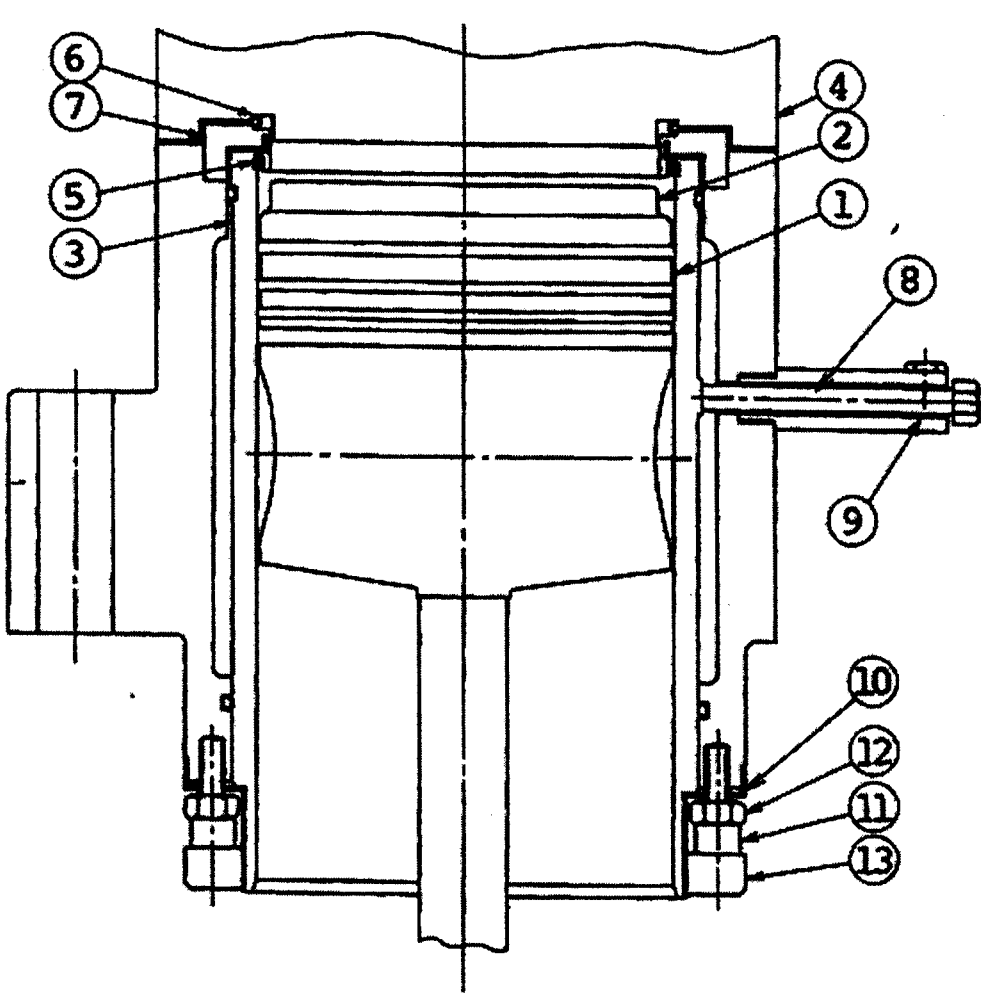

1. Piston
2. Relieved top land
3. Cylinder liner
4. Cylinder head
5. Gas seal O-ring
6. Seal ring
7. O-ring holder
8. Lateral stopper (bar)
9. Elastomer
10. Lateral stopper (ring)
11. Piezo pickup
12. Clamping bolt
13. Clamp screw

Figure 6.1. Apparatus for, floating liner technique used by Furuhama and Takiguchi [1979], for piston assembly friction measurement.

Richez et al [1982] measured the piston friction force using a modified floating liner method. A multi-cylinder engine was used for this experiment. In the experiment the third and fourth cylinder connecting rods were attached to the original pistons. The piston rings of these pistons were removed to reduce friction. On top of this piston a test piston was fitted via the piston rod connecting the original piston to the test piston so that the original piston acts as a crosshead bearing. The cylinder and water jacket for these modified cylinders were replaced with an independent single unit accommodating both the original and test pistons. The camshaft mechanism was extensively modified. A force transducer was used at the bottom of the cylinder liner. Although this method reduced some of the problems in the floating liner method, for example the diverse effect of lateral force on the force transducers, it introduced new problems, such as alignment of the cylinder head and the liner, slap forces on the liner from the unguided piston, excessive flexibility of the force transducer support structure and vibration.

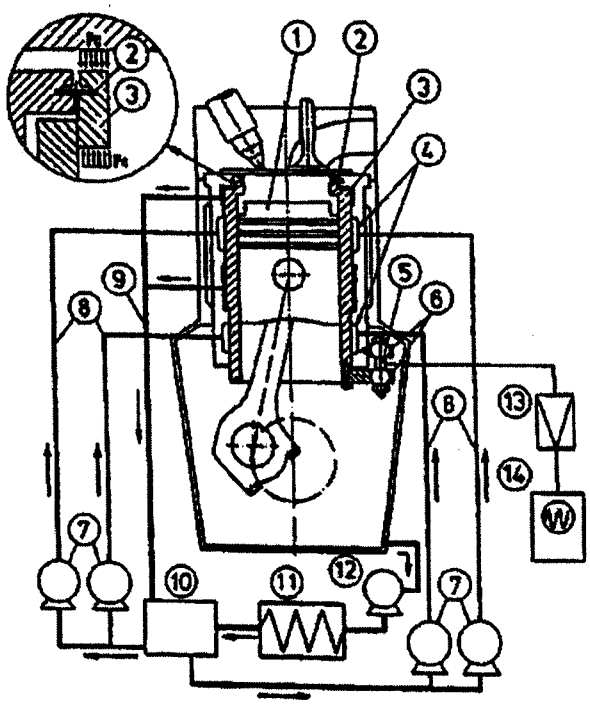

Figure 6.2. Wakuri et al [1995], improved gas seal floating liner apparatus.

Parker, Adams and Donnison [1989], Sherrington [1988], Cerrato et al [1984] and Rogowski [1961] in their individual work, used the floating liner method for piston assembly friction measurements. They faced similar problems in their experiments, such as gas sealing at the liner top end, the effect of piston guide force on the force sensor and vibration.

A notable effort was made by Wakuri et al [1995] to improve the floating liner method. The liner was isolated from the cylinder block and the cylinder head and was firmly supported by eight hydrostatic bearings in the radial direction, with free movement in the axial direction. The technique used to seal the combustion gas and balancing of gas force was very effective and the instantaneous friction force was measured with the load sensors at the bottom of the liner, figure 6.2.

Cho et al [2000] used the floating liner method to study the behaviour of piston rings. The measurement system was designed to control the effect of the secondary motion and the temperature of the cylinder wall and lubricant. The friction force between the barrel shaped piston ring and cylinder liner was measured under flooded oil conditions. The measurement system was developed by modifying an engine, shown in figure 6.3(a). Cho used a strain gauge type load cell instead of the piezo type to determine absolute friction force reading. The secondary motion of the piston was controlled by a pipe slider and a guide liner mechanism. The piston friction force was measured under motored conditions and not fired. The cylinder pressure was held at atmospheric with the aid of vents.

Recently Kikuchi [2003] used the floating liner method to investigate the effect of direct injection gasoline engines on piston assembly friction. It was concluded that cylinder fuel wetting reduces piston friction during the compression stroke because of the lower oil viscosity on the cylinder bore surface caused by fuel dilution. Figure 6.3(b) shows the main configuration of the device. The friction force was measured via eight 3-component force sensors placed on the movable cylinder liner in the thrust direction. Although the inertial vibration generated in the movable liner through the piston friction due to the lack of rigidity of the liner support was reduced, it could not be prevented entirely.

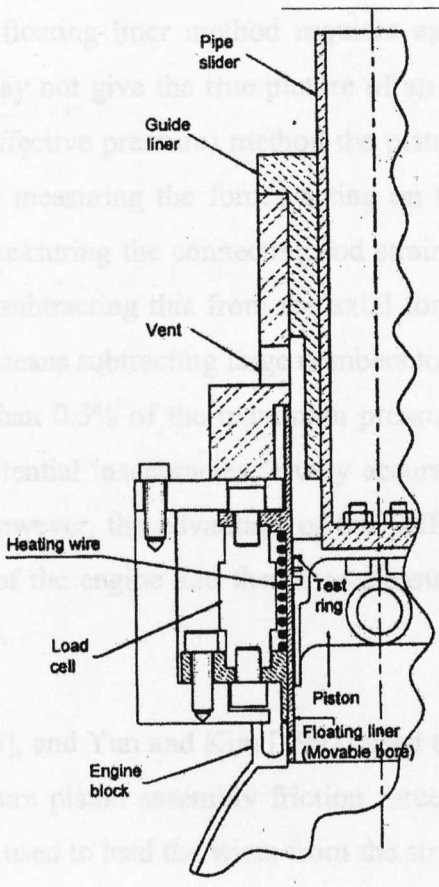

Figure 6.3(a). Piston-ring friction force measuring system with slider mechanism Cho et al [2000].

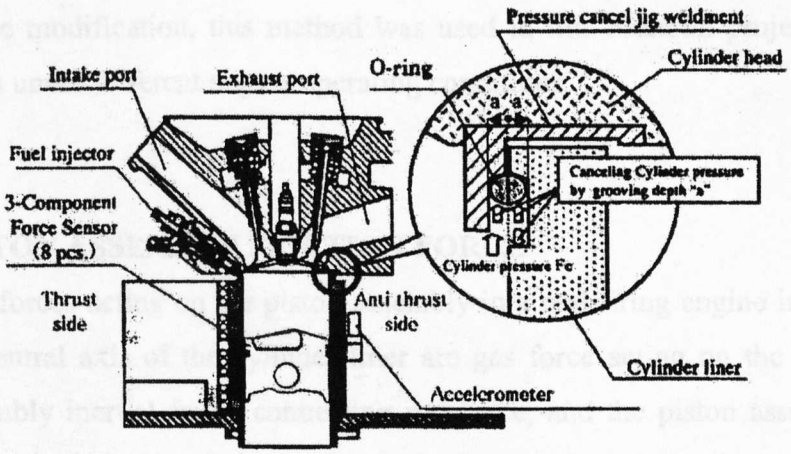

Figure 6.3(b). Cross-section of the single cylinder experimental engine used by Kikuchi et al [2003].

It can be seen that the floating liner method requires extensive modification of the engine and as a result may not give the true picture of an actual firing engine. In the IMEP (indicated mean effective pressure) method the piston assembly friction force is determined indirectly by measuring the forces acting on the piston assembly and the connecting rod that is, measuring the connecting rod strain to determine the small end axial reaction force and subtracting this from the axial forces due to cylinder pressure and piston inertia. This means subtracting large numbers to determine the friction force, which is normally less than 0.5% of the maximum pressure force. As this method is liable to considerable potential inaccuracies, a very accurate measurement system and sensors are required. However, the advantage of the IMEP method is that it requires almost no modification of the engine and therefore measures the true piston assembly friction in a firing engine.

Uras and Patterson [1985], and Yun and Kim [1992] used the IMEP method on a multi-cylinder engine to measure piston assembly friction force. A special device called a grasshopper linkage was used to lead the wires from the strain gauges on the connecting rod to the side of the crankcase. Although this method was successful in achieving results, there was a limitation on the engine operating speed and load as at high speeds the wires broke. The frequency response of the sensors was also a limiting factor.

As the IMEP method allows true measurement of piston assembly friction without any major engine modification, this method was used in this research project to measure piston losses under different engine operating conditions.

6.2 PISTON ASSEMBLY FRICTION FORCE

The forces acting on the piston assembly in a real firing engine in the direction along the central axis of the cylinder liner are gas force acting on the piston crown, piston assembly inertial force, connecting rod force, and the piston assembly friction force. Using the information from a 720 pulse per revolution encoder connected to the front end of the crankshaft and simple geometry, the direction of all the above forces can be determined. Thus if any of the three forces mentioned above are known, the fourth can be calculated. This is the basic principle of the IMEP (indicated mean effecting pressure) method used for measuring piston assembly friction losses.

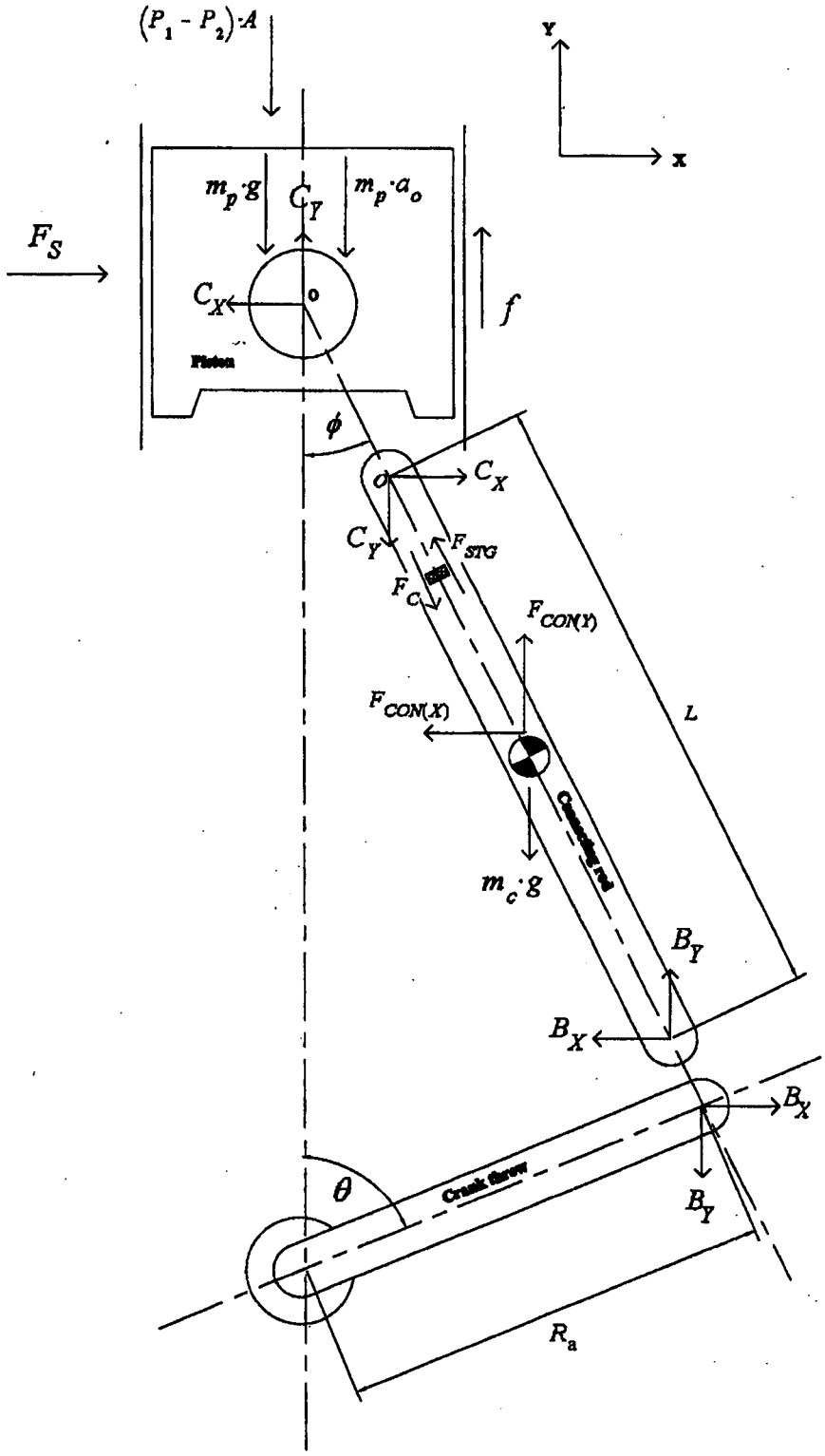

Figure 6.4. Forces acting on piston assembly and connecting rod.

To measure piston assembly friction, very accurate measurement of gas force and connecting rod force is required. Normally the gas and connecting rod force are in the order of 10,000 N to 30,000 N force whereas the friction force is somewhere near 50 N to 300 N force. Thus any small error in measuring gas or connecting rod force will result in high inaccuràcy, for example an error of 0.1% in measuring gas or connecting rod force can result in nearly 15% error in piston assembly friction force.

To measure instantaneous piston assembly friction in a real firing engine, experiments were carried out on a single cylinder Ricardo Hydra gasoline engine, the design of this being based on a real engine, a GM 2.0 litre Cavalier engine. The engine specification is given in Appendix I. A detailed description of all the forces acting on the piston assembly and connecting rod is shown in figure 6.4. The mathematical calculations required to determine piston assembly friction force are as follows,

6.2.1 FORCES ACTING ON THE PISTON ASSEMBLY

According to figure 6.4, the sum of all the forces acting on the piston assembly in axial direction is given by

$$C_Y = (P_1 - P_2).A + m_P.g - f + m_P.a_o \qquad 6.1$$

In equation 6.1 the terms,

$P_1 - P_2$ is the net gas pressure acting on the piston assembly, P_1 is the cylinder pressure whereas P_2 is the crankcase pressure acting on the bottom area of the piston assembly.

A, is the calculated average cylinder bore area (bore=85.99mm).

a_o, is the piston axial acceleration calculated every 0.5° crank angle.

$m_p.g$, is the piston assembly weight (m_p= 577.8g).

$m_p.a_o$, is the piston assembly inertial force and can be calculated as,

Piston acceleration × (mass of piston + piston rings + piston pin + connecting rod section 'A', figure 6.5)

For measuring piston assembly inertial force, the mass of connecting rod section 'A' (87g), is added to piston assembly mass as it is always in translational motion.

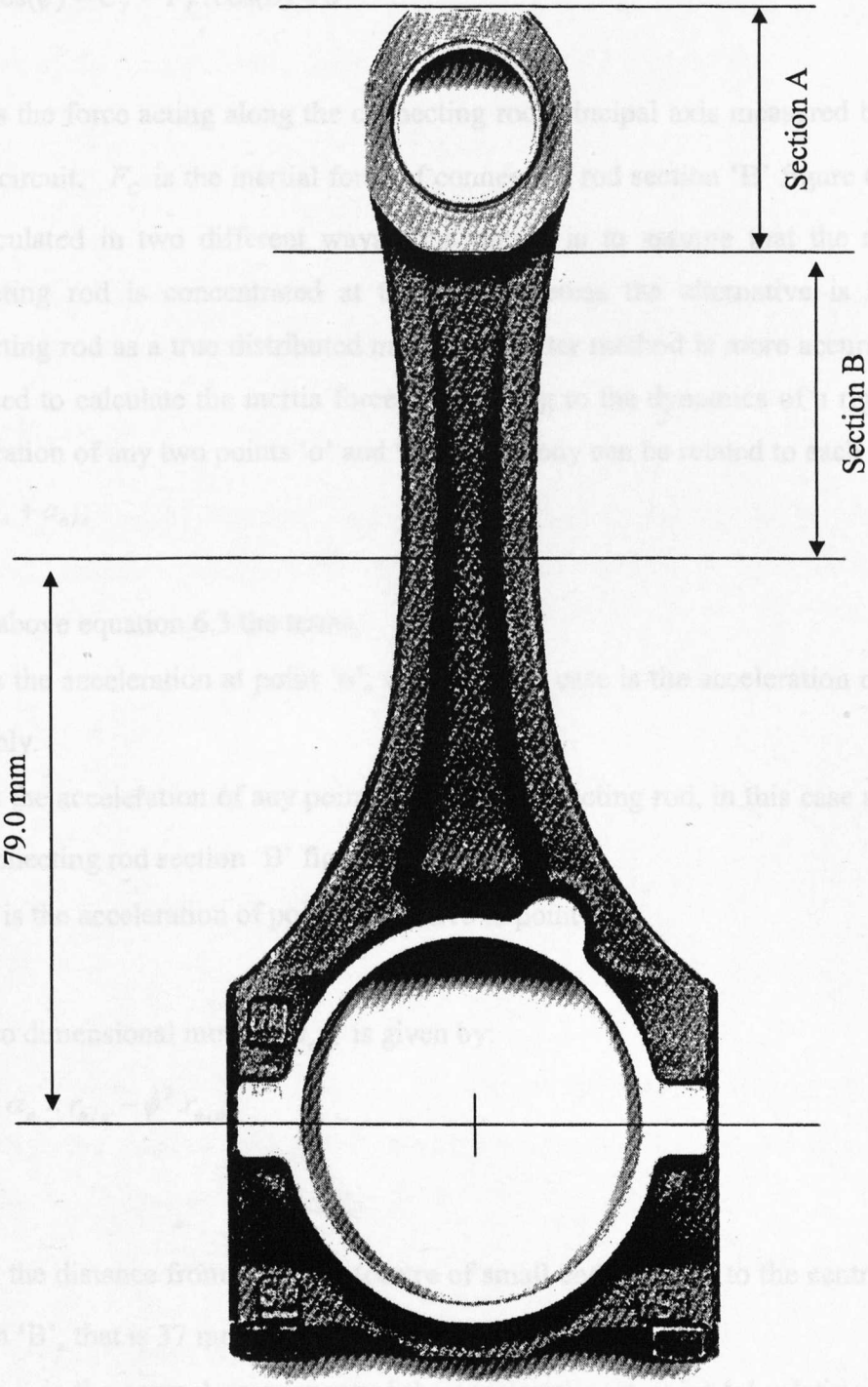

Figure 6.5. Sectioning of the connecting rod for inertia calculations.

6.2.2 FORCES ACTING ON THE CONNECTING ROD

According to figure 6.4 and the full bridge strain gauge circuit fitted at a distance of 79.0 mm from the big-end bearing centre, the components of forces in the axial direction at the point where strain gauges are fitted is given by,

$$F_{STG}.\cos(\phi) - C_Y - F_C.\cos(\phi) = 0 \qquad 6.2$$

F_{STG} is the force acting along the connecting rod principal axis measured by the strain gauge circuit. F_C is the inertial force of connecting rod section 'B' figure 6.5, and can be calculated in two different ways. One option is to assume that the mass of the connecting rod is concentrated at the ends whereas the alternative is to treat the connecting rod as a true distributed mass. The latter method is more accurate and thus was used to calculate the inertia force. According to the dynamics of a rigid body the acceleration of any two points 'o' and 'c' on the body can be related to each other as;

$$a_c = a_o + a_{o/c} \qquad 6.3$$

In the above equation 6.3 the terms,

'a_o' is the acceleration at point 'o', which in this case is the acceleration of the piston assembly.

'a_c' is the acceleration of any point 'c' on the connecting rod, in this case any point on the connecting rod section 'B' figure 6.5.

'$a_{o/c}$' is the acceleration of point 'c' relative to point 'o'.

For two dimensional motion, $a_{o/c}$ is given by:

$$a_{o/c} = \alpha_c \times r_{o/c} - \dot{\phi}^2.r_{o/c} \qquad 6.4$$

where

$r_{o/c}$ is the distance from point 'o' (centre of small end bearing) to the centre of mass of section 'B', that is 37 mm.

$\alpha_c \times r_{o/c}$ is the normal component of the acceleration at point 'c' relative to point 'o'. The inertial force due to this component results in the bending of the connecting rod.

The strain gauges in the Wheatstone bridge cannot sense this force and is thus neglected, Patterson [1983].

$\dot{\phi}^2.r_{o/c}$ is the component of acceleration in line with the principal axis of the connecting rod. Thus the acceleration of any point 'c' on the connecting rod section 'B' in the direction of the principal axis, according to equation 6.3 is given by,

$$a_c = a_o.\cos(\phi) - \dot{\phi}^2.r_{o/c} \qquad 6.5$$

Also the inertial force of the connecting rod section 'B' in the direction along the neutral axis of the connecting rod can be expressed as,

$$F_C = \int_a^b A_C.\rho.a_c.dr$$

The limits 'a' and 'b' represent the length of connecting rod section 'B'. Using a solid modeling computer package I-DEAS, the total mass and centre of mass of connecting rod section 'B' was calculated.

Therefore,

$$F_C = m_B.\left[(a_o.\cos(\phi)) - (r_{o/c}.\dot{\phi}^2)\right] \qquad 6.6$$

where,

m_B is the mass of section 'B', 72g.

The contribution of inertial force of the component $(m_B.r_{o/c}.\dot{\phi}^2)$ in equation 6.6 is relatively very small as compared to the piston assembly friction. For example, at 1000 engine rpm the inertial force is 1.0 N force.

6.2.3 PISTON ASSEMBLY FRICTION FORCE

According to the strain experienced by the connecting rod strain gauge circuit and figure 6.4, the piston assembly friction force can be calculated by combining equations 6.1 and 6.2,

$$f = (P_1 - P_2).A_P - F_{STG}.\cos(\phi) + m_p.g + F_C.\cos(\phi) + m_p.a_o \qquad 6.7$$

6.3 EXPERIMENTAL MEASUREMENT OF VARIABLES REQUIRED FOR PISTON ASSEMBLY FRICTION MEASUREMENT

For piston assembly friction measurement, equation 6.7, the following information is required at every 0.5° crank angle;

1. Piston assembly axial acceleration, 'a_o'.
2. Connecting rod angular position and velocity, '$\phi, \dot{\phi}$'.
3. Gas force, $(P_1 - P_2).A$.
4. Connecting rod force, F_{STG}.

According to figure 6.4, the above mentioned variables can be calculated as,

6.3.1 PISTON ASSEMBLY ACCELERATION

Piston displacement:

Piston displacement from TDC position can be expressed as;

$$S = R_c.\cos(\theta) - R_c + \sqrt{L^2 - R_c^2.\sin^2(\theta)} - L$$

$$S = -R_c\left[1 - \cos(\theta) + \left\{\frac{1 - \sqrt{1 - \lambda^2.\sin^2(\theta)}}{\lambda}\right\}\right] \qquad 6.8$$

Where $\lambda = \dfrac{R_c}{L}$

R_c = crank length

L = connecting rod length

The reading from the encoder incremental and index pulse was used to determine crank angle 'θ'.

Piston velocity:

Piston velocity can be calculated by differentiating equation 6.8 thus,

$$\frac{d}{dt}S = \frac{d}{d\theta}S.\frac{d}{dt}\theta$$

$$\frac{d}{dt}\theta = \omega$$

$$\frac{d}{d\theta}S = -\left(R_c.\sin(\theta) + \frac{1}{\sqrt{L^2 - R_c^2.\sin^2(\theta)}}.R_c^2.\sin(\theta).\cos(\theta) \right)$$

$$\frac{d}{dt}S = -R_c.\omega.\left(\sin(\theta) + \frac{\lambda}{2}\frac{\sin(2\theta)}{\sqrt{1-\lambda^2.\sin^2(\theta)}} \right) \qquad 6.9$$

Piston acceleration:

Assuming constant crankshaft angular velocity, piston acceleration can be calculated by differentiating equation 6.9,

$$\frac{d^2}{dt^2}S = -R_c.\omega^2.\left(\cos(\theta) + \frac{\lambda.\cos(2\theta) + \lambda^3\sin^4(\theta)}{\sqrt{\left(1-\lambda^2.\sin^2(\theta)\right)^3}} \right)$$

As the experiments are carried out on a single cylinder 4 stroke gasoline engine, the engine speed varies throughout complete engine cycle under both motored and fired conditions and thus crankshaft angular acceleration is considered. Figure 6.6 and 6.7 show the crankshaft acceleration and its effect on piston assembly acceleration. Considering crankshaft acceleration, piston assembly acceleration can be calculated as,

$$\frac{d^2}{dt^2}S = -R_c.\left[\alpha.\left\{ \sin(\theta) + \frac{\lambda}{2}\frac{\sin(2\theta)}{\sqrt{1-\lambda^2.\sin^2(\theta)}} \right\} + \omega^2.\left\{ \cos(\theta) + \frac{\lambda.\cos(2\theta) + \lambda^3\sin^4(\theta)}{\sqrt{\left(1-\lambda^2.\sin^2(\theta)\right)^3}} \right\} \right]$$

..... 6.10

The information from the encoder incremental pulse and the data acquisition board timer/counter chip was used to determine crankshaft angular velocity and acceleration, using equations 3.4 and 3.5 respectively.

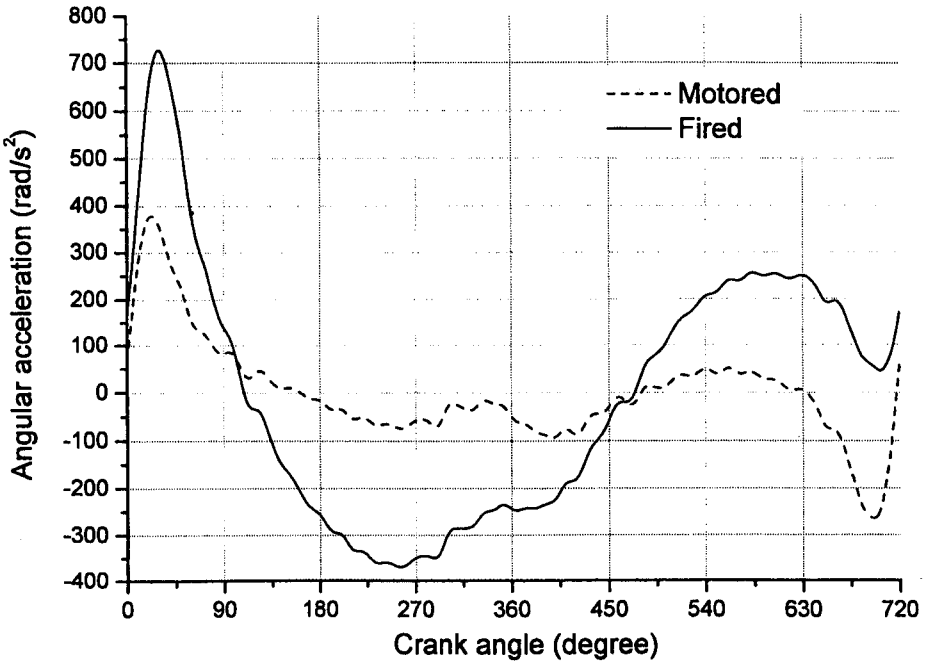

Figure 6.6. Crankshaft angular acceleration under motored and fired conditions, 1000rpm.

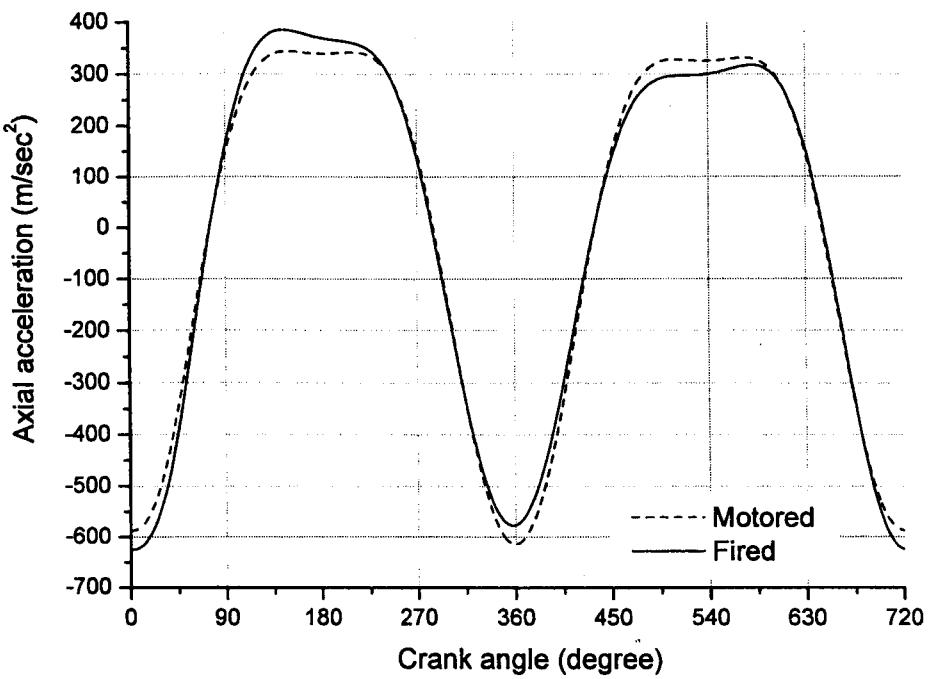

Figure 6.7. Effect of crankshaft angular acceleration on piston assembly axial acceleration under motored and fired conditions, 1000rpm.

6.3.2 CONNECTING ROD ANGULAR POSITION AND VELOCITY

Connecting rod angular position 'ϕ':

From figure 6.4, connecting rod angular position with respect to cylinder central axis is given by;

$$\phi = \sin^{-1}\left(\frac{R_c.\sin(\theta)}{L}\right) \qquad 6.11$$

Connecting rod angular velocity '$\dot{\phi}$':

Differentiating equation 6.11;

$$\dot{\phi} = \omega.\frac{1}{\sqrt{1-\frac{R_c^2}{L^2}.\sin^2(\theta)}}.R_c.\frac{\cos(\theta)}{L} \qquad 6.12$$

6.3.3 GAS FORCE

Gas force is the axial force exerted by the combustion pressure on the piston assembly. It is calculated by measuring the net cylinder pressure and multiplying by the average cylinder bore area. The bore area was determined by measuring bore diameter at different locations and taking an average, 85.99 mm. The engine crankcase was open to atmospheric pressure. The Ricardo Hydra engine was originally fitted with an un-cooled Kistler 6121 piezo-electric pressure transducer having a sensitivity of 14.1pC/bar pressure. It was fitted at the front position of the engine, on the side of the cylinder head. Piezo-electric pressure transducers are preferred for cylinder pressure measurement because of their high frequency response, small size, light weight, low power consumption and relative insensitivity to environmental conditions. But along with such advantages there are a few disadvantages and to measure piston assembly friction very accurately it is important to address issues that can affect the results. The following are factors that have an adverse effect on the measurements required for piston assembly friction analysis,

1. *Cylinder pressure transducer long term inter-cycle drift.* Piezoelectric transducers only measure dynamic pressures and consequently cannot provide absolute pressure measurements.

2. *Cylinder pressure transducer thermal shock.* The change in temperature of the transducer-measuring surface affects the output because of varying Young's modulus and resonant frequency of the quartz crystal and by causing expansion/contraction of the diaphragm.
3. *Cylinder pressure transducer low pressure resolution and accuracy.* In a firing engine the maximum cylinder pressure is typically 40-60 times greater than the intake pressure. It is very important to have a high resolution for measuring piston assembly friction and pumping losses.
4. *Effects due to cylinder pressure transducer mounting.* The performance of a pressure transducer can be greatly affected by the way it is mounted. The installation bore of an indicating sensor in the cylinder head is deformed due to the cylinder pressure. This deformation is impressed upon the sensor housing and thus on the sensor membrane of a threaded type pressure transducer. The radial deformation of the indicating bore is converted into an axial deformation of the transducer housing when the thread flanks of the bore moves into those of the sensor. Via the membrane an axial deformation of the measuring element is generated, resulting in an error signal.
5. *Incorrect crank angle phasing.* For the piston assembly friction measurement, inaccuracy of TDC position by 0.1° crank angle will give an error of not more than 1% in instantaneous piston assembly friction. From the P-V diagram, the engine IMEP can be calculated directly. IMEP calculated from dynamometer torque measurement is an estimate of true value. Brown [1967], indicated that phase accuracy of the order of 0.1° crank angle was required to keep the error in IMEP to less than 1% for diesel engines whereas the figure for gasoline engine, it is 0.2° to 0.3° crank angle.
6. *Electrical and magnetic fields.* Electrical and magnetic fields are present in a test cell. They can induce electric current into the measuring cables. The most common source of noise is the ignition current of the engine's ignition system.
7. *Incorrect pressure measurement calibration.* Poor calibration of the cylinder pressure transducer has the same negative effect as a bad sensor. This error has a relatively proportional effect on IMEP measurements.

To measure gas force very accurately the above mentioned effects were addressed as follows.

6.3.3.1 CYLINDER PRESSURE PEGGING

Piezoelectric pressure transducers measure relative pressure and to relate it to an absolute value and to remove long term drift, pressure pegging is carried out. A number of pressure referencing techniques are available and are explained by Randolph [1990]. Mainly pegging is carried out by either accurately measuring or calculating numerically the absolute pressure during part of the engine cycle. Most commonly used pegging methods are:

- Pegging to inlet manifold pressure near intake BDC position using an absolute inlet manifold transducer.
- Pegging to exhaust manifold pressure near the exhaust TDC position using absolute exhaust manifold transducer.
- Using numerical referencing techniques.
- Using a switch adaptor to expose the piezo-electric cylinder pressure transducer to a known pressure during part of the engine cycle.
- Pegging by using an absolute pressure transducer exposed to the cylinder pressure near BDC.

The most accurate pegging method is the last one that is using a second (absolute) pressure transducer mounted on the cylinder liner near the BDC position. This technique was used in this research. Absolute cylinder pressure measurement was carried out using a Kulite XCE-152 piezo-resistive pressure transducer having a rating pressure of 7 bar and maximum pressure of 14 bar. It has a sensitivity of 14.545 mV/bar and compensated temperature range from 25°C to 232°C. This miniature pressure transducer is 7 mm in length and 3 mm in diameter having a pressure sensing area of 1.9 mm, figure 6.8(a). The signal conditioning was performed using a high performance Fylde FE-379-TA transducer amplifier. The transducer gain was set to 10. The miniature pressure transducer was mounted to the side of the cylinder wall such that it is not exposed to the cylinder pressure until approximately 120° after TDC position. At this point combustion is normally complete and the pressure falls to 5% to 10% of its peak value. To pass the transducer through the water jacket a special tube 'A' was machined. One end of this tube was rigidly fasten to the cylinder block while the other end was pushed against the outer cylinder liner wall via a high temperature o-ring, allowing for any liner thermal expansion. The pressure transducer was held in its place using a special sleeve 'B', figure 6.8(b). The pressure transducer was exposed to the

cylinder pressure via a 1 mm long channel having a bore of 0.5 mm, figure 6.9. The channel hole from the piston side was chamfered by hand using a grinding stone. Resonance frequency error was not considered because of the very short channel length and very small transducer pressure sensing area, resulting in a very high natural frequency thus eliminating resonance problems.

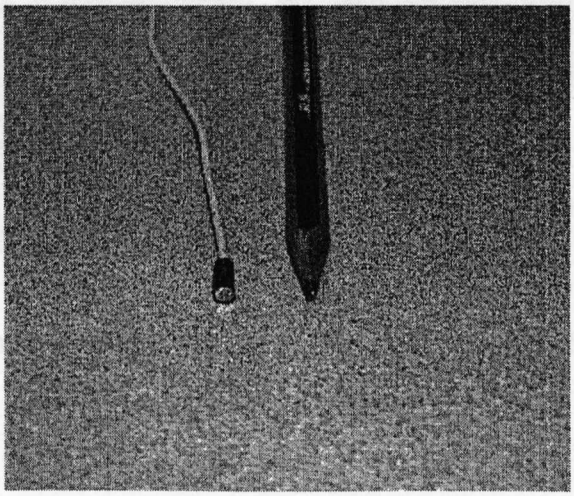

(a) Piezo-resistive pressure transducer for cylinder pressure pegging.

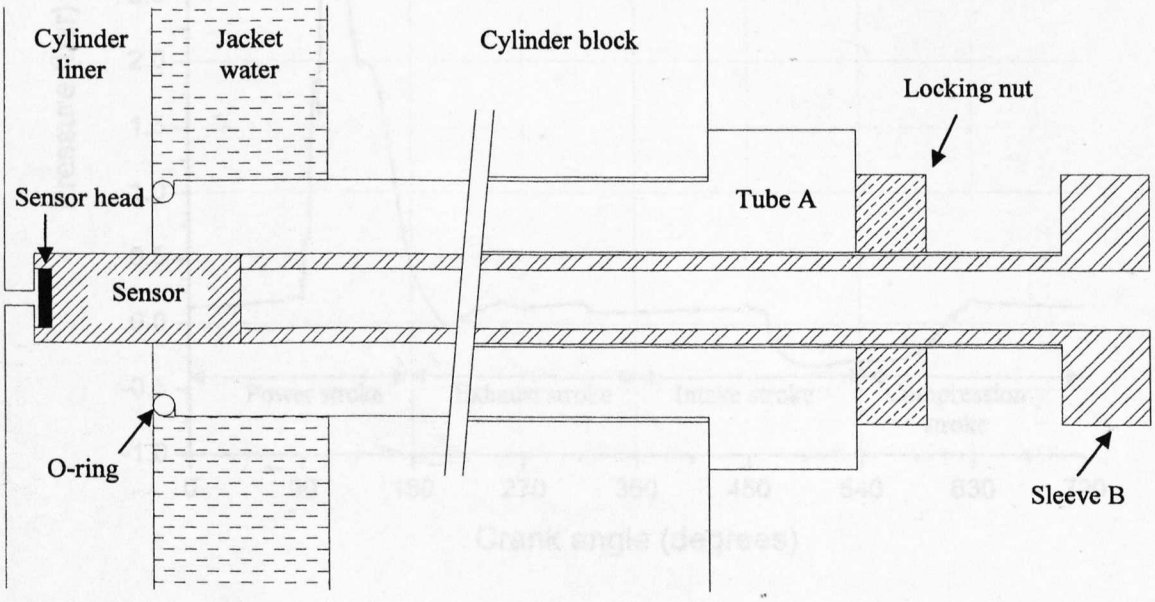

(b) Piezo-resistive pressure transducer installation (not to scale).

Figure 6.8(a) (b). Piezo-resistive pressure transducer and its installation.

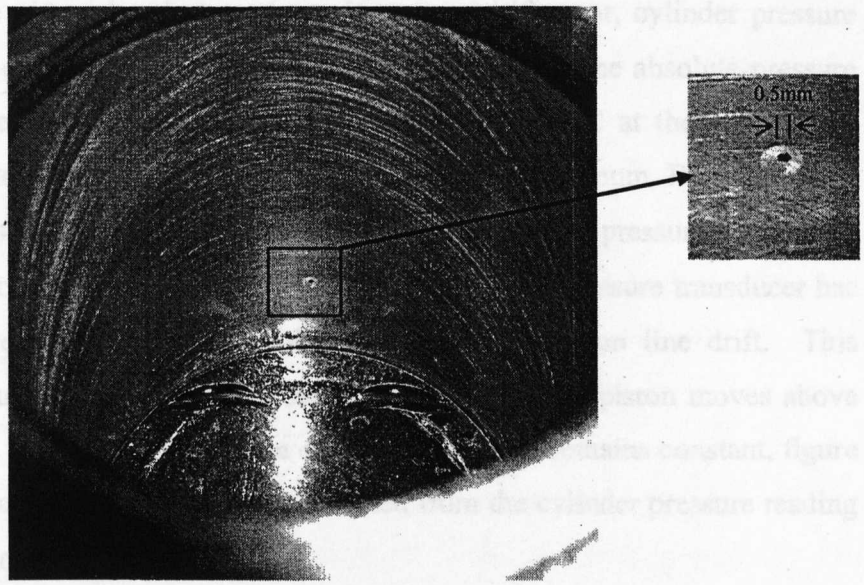

Figure 6.9. 1mm long and 0.5mm bore pegging channel at 120° after TDC.

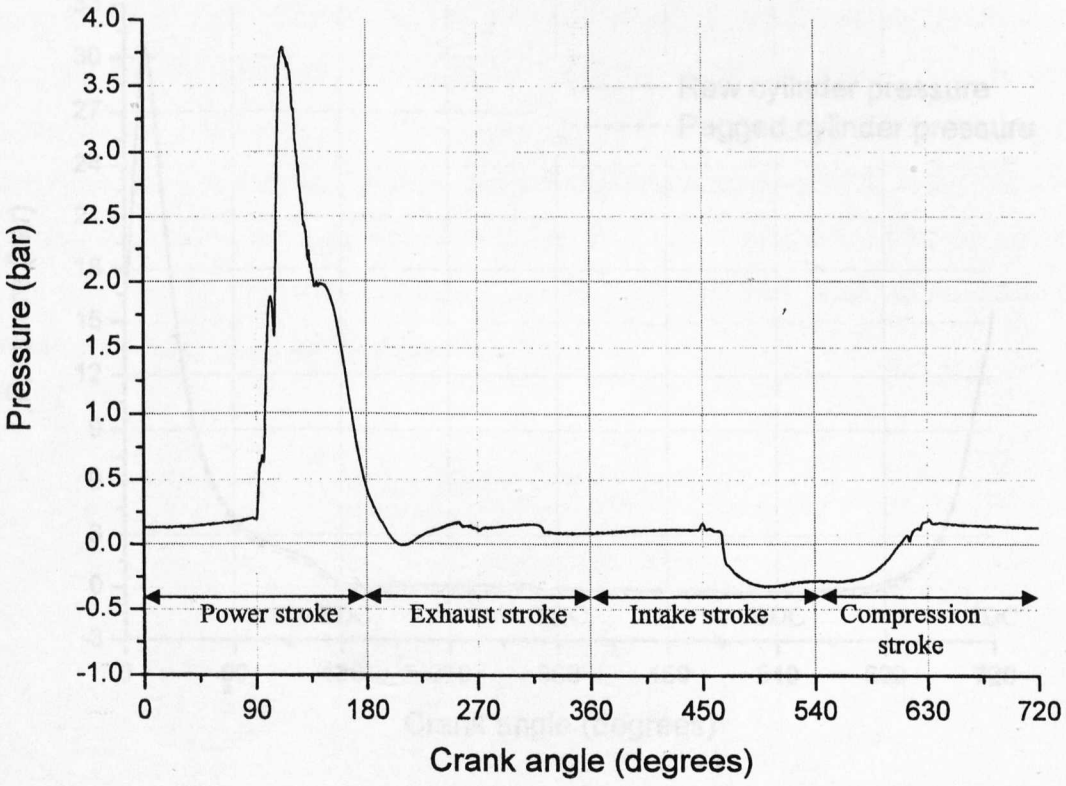

Figure 6.10. Pressure measured by liner absolute pressure transducer.

In order to eliminate piezo-electric transducer long-term drift error, cylinder pressure pegging was carried out in each engine cycle. The reading from the absolute pressure transducer was related to the cylinder pressure at 10° after BDC at the start of the compression stroke, as the pressure change in the cylinder is minimum, Brown [1967], figure 6.10. The pressure difference is then applied to the cylinder pressure reading for the complete engine cycle, figure 6.11. The miniature absolute pressure transducer has an inline temperature compensation module to prevent any datum line drift. This transducer was also used to monitor crankcase pressure when the piston moves above the pegging channel. It can be seen that the crankcase pressure remains constant, figure 6.10. The average crankcase pressure was subtracted from the cylinder pressure reading for calculating gas force.

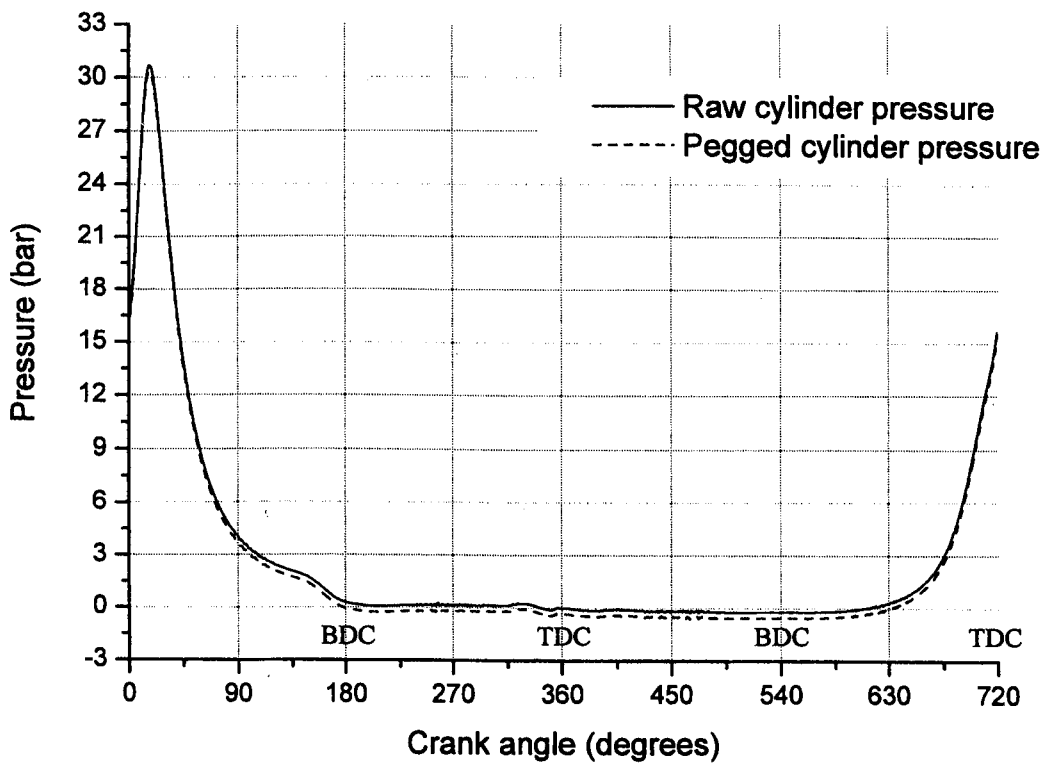

Figure 6.11. Effect of pressure pegging on cylinder pressure reading.

6.3.3.2 WATER-COOLED PIEZO-ELECTRIC PRESSURE TRANSDUCER

The intermittent flames of the combustion gasses heat up the diaphragm of a cylinder pressure transducer. This short time heating takes place in milliseconds and provides a measuring error due to thermal stresses in the sensor resulting in short term drift. The Ricardo Hydra engine was originally fitted with an un-cooled pressure transducer. In order to measure cylinder pressure accurately with high resolution, a high sensitivity water-cooled pressure transducer was installed to the cylinder head. This was a Kistler 6067B having a sensitivity of 26.1 pC/bar at a cooling water temperature of 50°C. It is a plugged sensor having no threads, figure 6.12, so that the gap between the mounting bore and the deformation sensitive part avoids problems caused by deformation of the cylinder head at high pressures. It was flush fitted to avoid any acoustic delays and pressure drop. A special bridge was welded to the cylinder head for the installation of this new pressure transducer, figure 6.13. The short-term drift is nearly eliminated because of the advanced integrated water cooling passage in the transducer. The Kistler 6067B has a double-walled diaphragm further minimising the short-term drift. A separate distilled water-cooling system was developed for the pressure transducer to keep the water temperature and pressure constant and to avoid deposits in the sensor. It is recommended by Kistler to keep the water flow rate constant at 0.8 litres per minute and temperature of 50°C. A water regulating valve and a thermocouple was fitted to the cooling circuit to control and monitor the cooling water temperature. The thermocouple was fitted very close to the transducer cooling water outlet, figure 6.13.

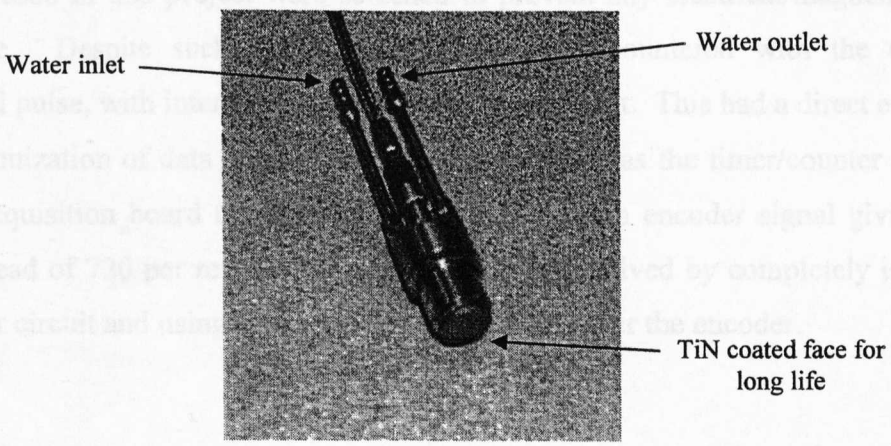

Figure 6.12. Plug type Kistler 6067B water-cooled piezo-electric pressure transducer.

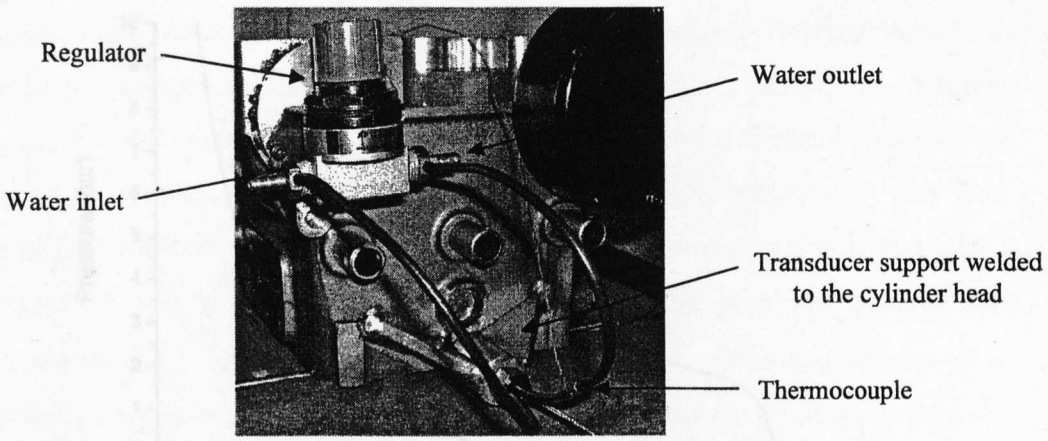

Figure 6.13. Water cooling circuit to control and monitor cylinder pressure transducer coolant.

Figure 6.14 shows the section of the PV-diagram where gas exchange process takes place, called the pumping loop. This pumping loop data was taken using the water cooled Kistler 6067B pressure transducer. Compare this to figure 6.15, showing the data taken in the same cylinder and at nearly the same conditions but with an un-cooled pressure transducer Kistler 6121. The gas exchange process in figure 6.15 shows an implausible crossover in pressures, forming what is called the bow tie effect. This is due to the transducer thermal effects and is expected from an un-cooled pressure transducer, Lancaster et al [1975].

All cables used in this project were screened to prevent any electrical/magnetic noise interference. Despite such efforts, problems were encountered with the encoder incremental pulse, with interference from the ignition circuit. This had a direct effect on the synchronization of data acquisition channel sampling, as the timer/counter chip on the data acquisition board treated the ignition event as an encoder signal giving 721 pulses instead of 720 per revolution. The problem was solved by completely isolating the encoder circuit and using a rechargeable battery to power the encoder.

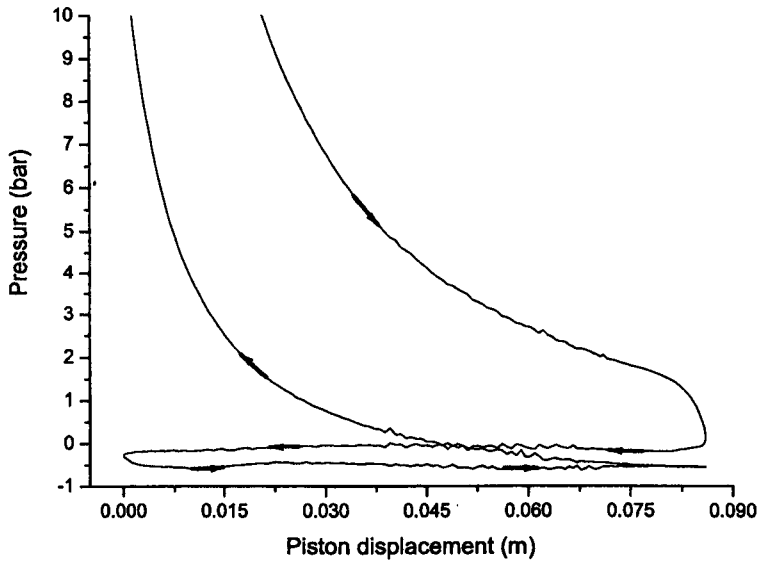

Figure 6.14. Pumping loop measured using water cooled cylinder pressure transducer, Kistler 6067B.

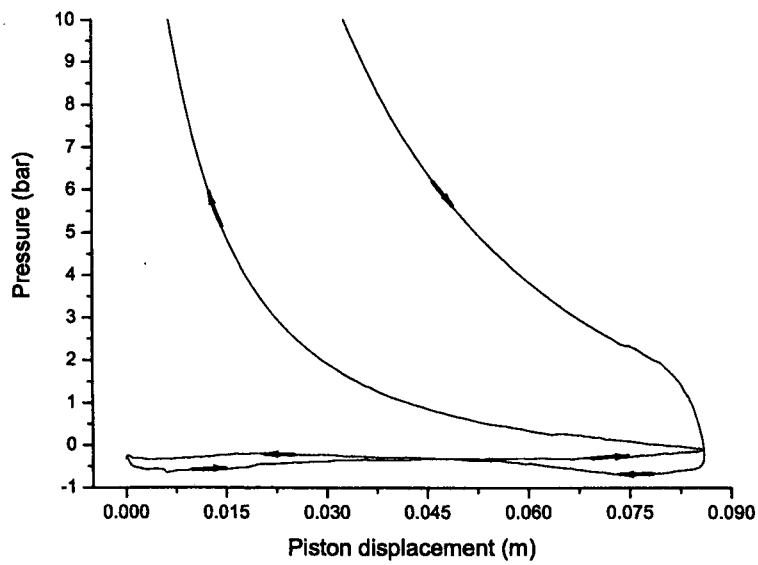

Figure 6.15. Pumping loop measured using uncooled cylinder pressure transducer, Kistler 6121.

6.3.3.3 PRESSURE TRANSDUCER CALIBRATION

In order to achieve high accuracy of cylinder pressure measurement it is necessary to recalibrate the transducer at frequent intervals. Piezoelectric pressure transducers have only dynamic response and therefore cannot be calibrated statically but it is in fact possible to calibrate quasi-statically on a deadweight tester. A Kistler 5011 charge amplifier was used for signal conditioning. The transducer was calibrated for a pressure range of 0-43 bar for half load engine condition, figure 6.16. The pressure transducer was loaded to each pressure on the deadweight tester, returning in between to ambient pressure and re-setting the amplifier. At each loaded pressure 300 samples, at a rate of 600 samples per second, were taken and averaged to increase resolution and remove noise. A plot was made of the output voltage versus the applied pressure. The calibration was carried out at the normal engine operating conditions, that is water cooling temperature of 50°C and a flow rate of 0.8 litres per minute. An average of three calibrations was used to calculate the pressure-voltage relation, 4.45 bar/volts. The calibration was carried out with the same charge amplifier, connecting wires, data acquisition board and channel as used in the experiments to take account of any offset in the system.

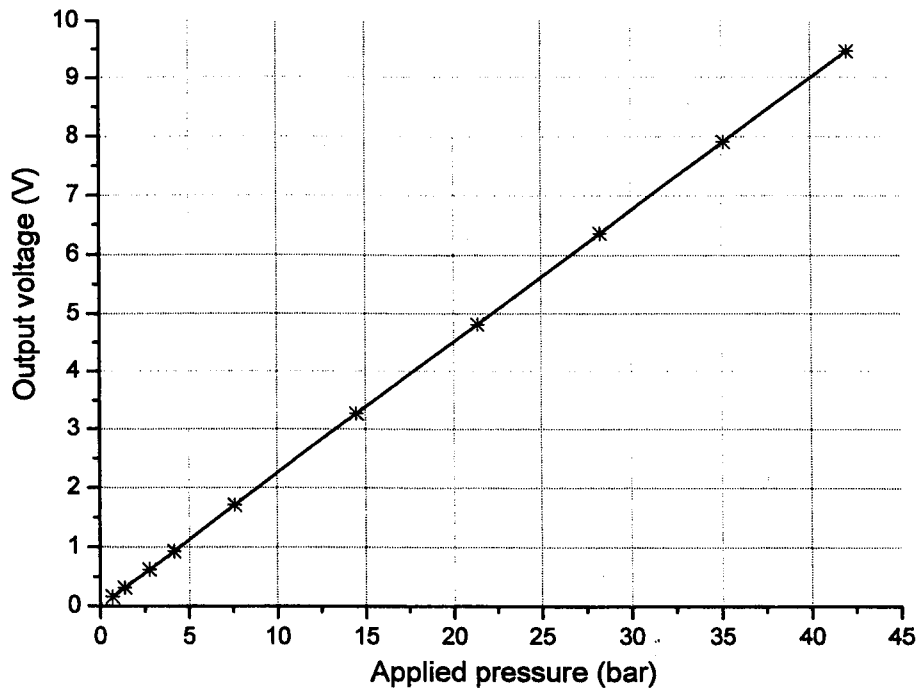

Figure 6.16, Cylinder pressure transducer calibration graph, pressure range 0-43 bar.

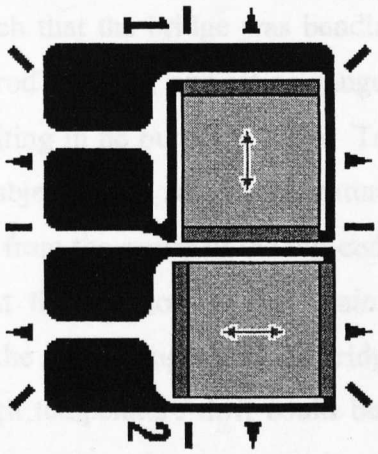

Figure 6.17, WK-06-06TT-350, 90° Tee Rosette strain gauge.

6.3.4 CONNECTING ROD FORCE

Instantaneous connecting rod force was measured using Micro Measurements WK-06-06TT-350 resistive type strain gauges, each having a resistance of 350Ω. These gauges are small 90° tee rosette strain gauges having self-temperature compensating qualities, figure 6.17. The advantages of such gauges are,

- They are little affected by temperature changes during measurement.
- Their zero-drift caused by temperature changes is so small that the measuring accuracy of micro strain is greatly improved.
- Even if the object surface has a large temperature gradient, measurement is possible without any significant temperature effect.
- Stable measurement is ensured for a long time.

The gauges were applied parallel to the neutral axis of the connecting rod figure 6.18. A full Wheatstone bridge gauge circuit was used to increase sensitivity and output voltage. The gauges were connected in a circuit in such a way that the output voltage was 2 x (1+connecting rod Poisson's ratio) times greater than for a single strain gauge output signal. The output voltage of the strain gauge circuit is directly proportional to the gauge factor, strain and excitation voltage. A high performance Fylde FE-379-TA

transducer amplifier was used for stable excitation voltage and for strain gauge output amplification. The orientation of the gauges in the Wheatstone bridge and on the connecting rod were such that the bridge was bending and temperature compensated. Thus under connecting-rod bending, one set of gauges experience tension whereas the other compression, resulting in no output voltage. Temperature compensation requires that all the gauges be subject to the same temperature. For this reason the gauges are fitted at the same height from the centre of the big-end bearing. To be on the safe side a thermistor was fitted at the location of the strain gauges to measure the surface temperature. Although the strain gauges and the bridge were temperature compensated, any error caused by high temperature drift could be removed afterwards. The wires connecting the strain gauges to each other were kept loose by giving the wires one or two loops to prevent the resistance of the wires to changing due to connecting rod dimensional change. The magnitude of the Wheatstone bridge output voltage depends on the magnitude of the excitation voltage. Increasing the excitation voltage increases the output voltage but also results in an increase in the current flow through the circuit. This high current flow dissipates heat and thus affects the system accuracy. Thus calibration of the excitation voltage was required and was carried out by balancing the bridge so that the output voltage was zero and then increasing the output voltage until the bridge became unbalanced. This gave the maximum allowable bridge excitation voltage of 6 volts.

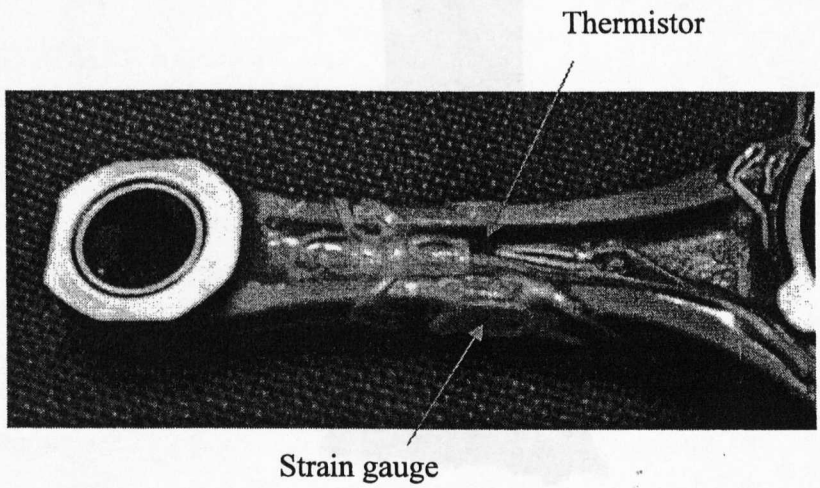

Figure 6.18. Instrumented connecting rod for connecting rod force measurement.

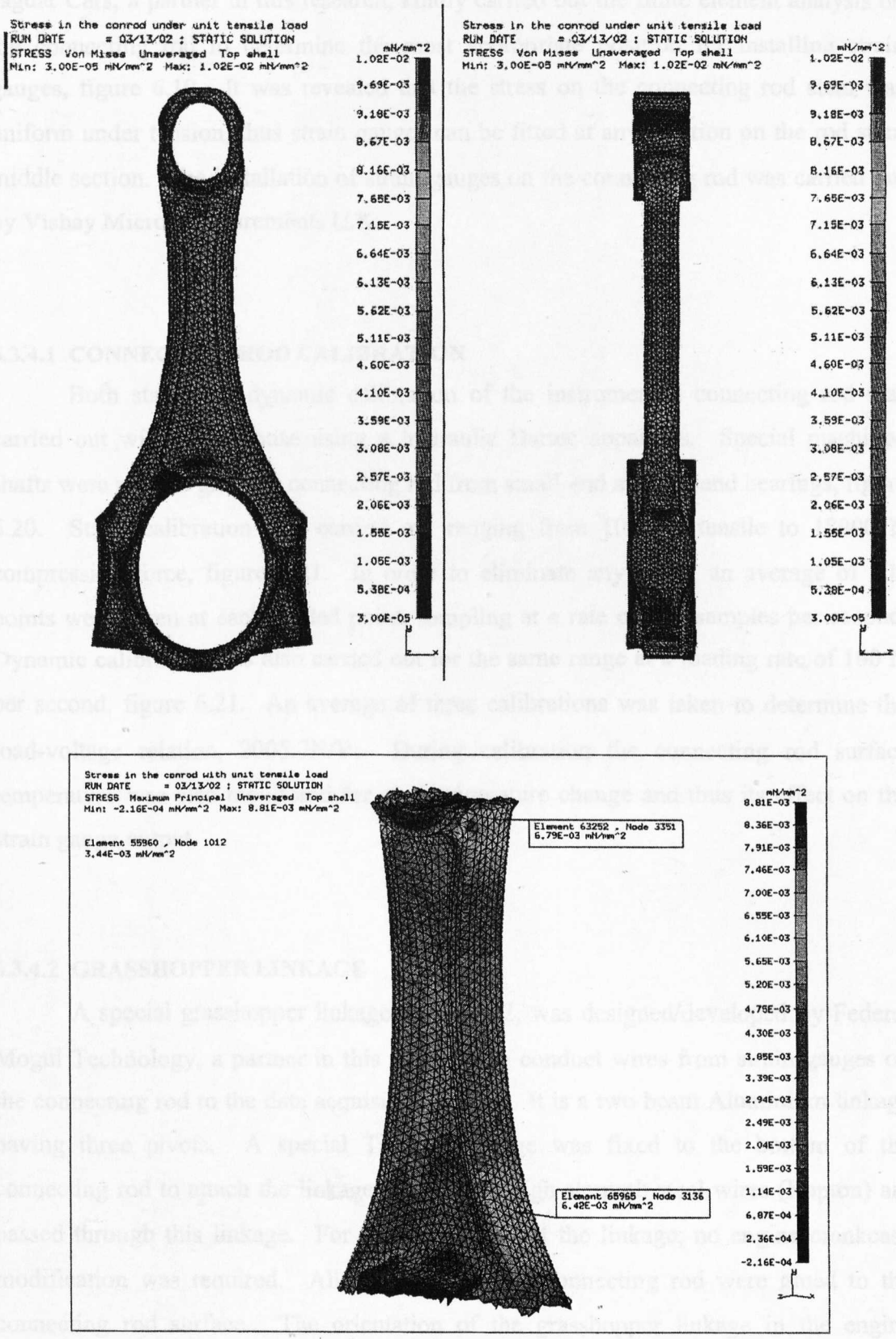

Figure 6.19. Connecting-rod stress calculated using finite element analysis, under tensile loading.

Jaguar Cars, a partner in this research, kindly carried out the finite element analysis on the connecting rod to determine the most appropriate position for installing strain gauges, figure 6.19. It was revealed that the stress on the connecting rod stem was uniform under tension, thus strain gauges can be fitted at any location on the rod stem middle section. The installation of strain gauges on the connecting rod was carried out by Vishay Micro-Measurements U.K.

6.3.4.1 CONNECTING ROD CALIBRATION

Both static and dynamic calibration of the instrumented connecting rod was carried out within the house using a hydraulic Dartec apparatus. Special machined shafts were used to grab the connecting rod from small-end and big-end bearings, figure 6.20. Static calibration was carried out ranging from 1000 N tensile to 18000 N compression force, figure 6.21. In order to eliminate any noise, an average of 300 points were taken at each loaded point, sampling at a rate of 600 samples per second. Dynamic calibration was also carried out for the same range at a loading rate of 100 N per second, figure 6.21. An average of three calibrations was taken to determine the load-voltage relation, 2005.7N/V. During calibration the connecting rod surface temperature was also monitored for any temperature change and thus its effect on the strain gauge output.

6.3.4.2 GRASSHOPPER LINKAGE

A special grasshopper linkage figure 6.22, was designed/developed by Federal Mogul Technology, a partner in this research, to conduct wires from strain gauges on the connecting rod to the data acquisition system. It is a two beam Aluminium linkage having three pivots. A special Titanium bridge was fixed to the bottom of the connecting rod to attach the linkage. 24 special high strength steel wires (Kapton) are passed through this linkage. For the installation of the linkage, no engine crankcase modification was required. All the wires on the connecting rod were glued to the connecting rod surface. The orientation of the grasshopper linkage in the engine crankcase can be seen in figure 6.23. High quality plugs were fitted at the sides of the connecting rod for connecting the lower bearing cap to the connecting rod, figure 6.24.

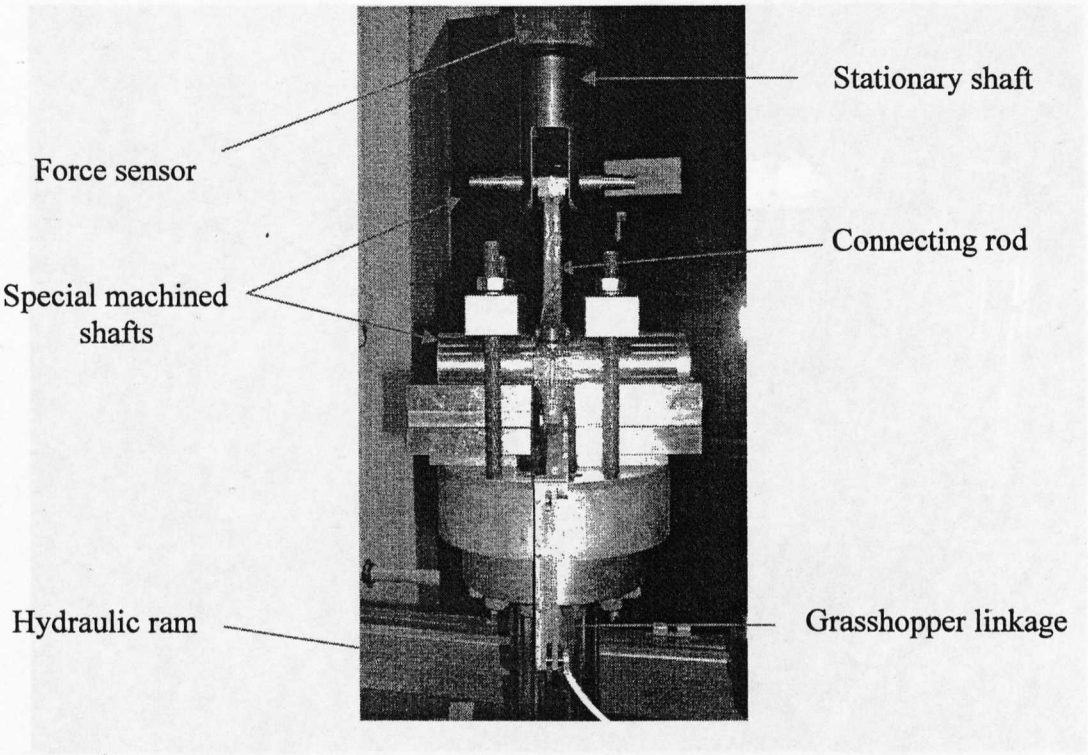

Figure 6.20. Connecting rod calibration using hydraulic Dartec apparatus.

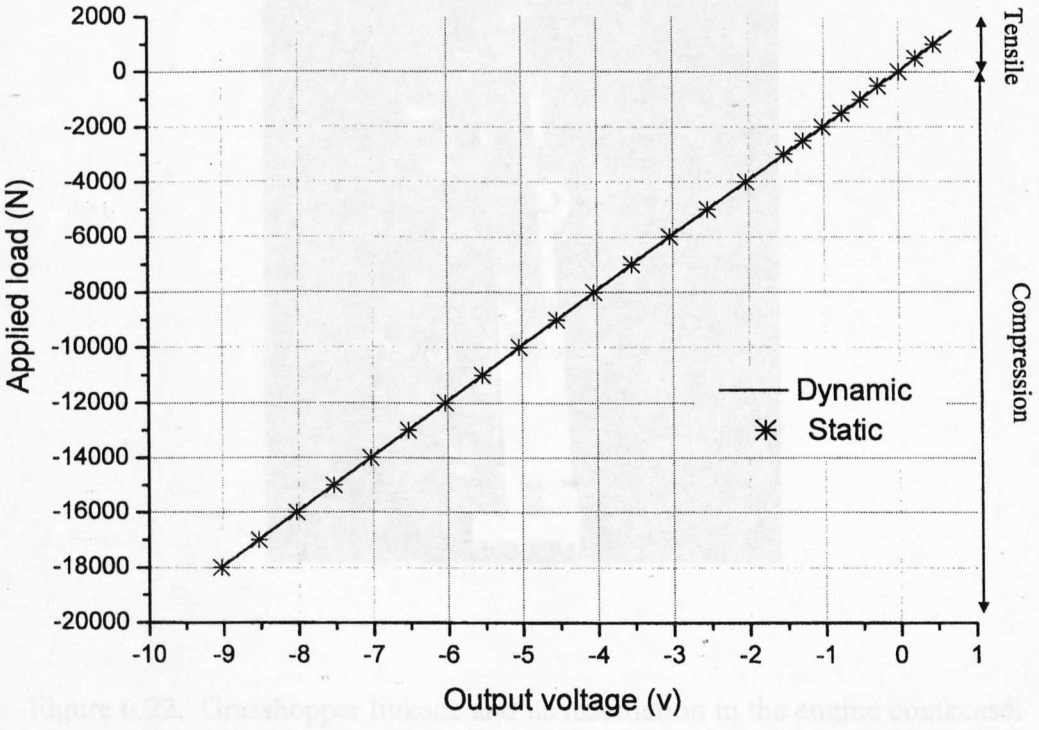

Figure 6.21. Instrumented connecting rod static and dynamic calibration graph.

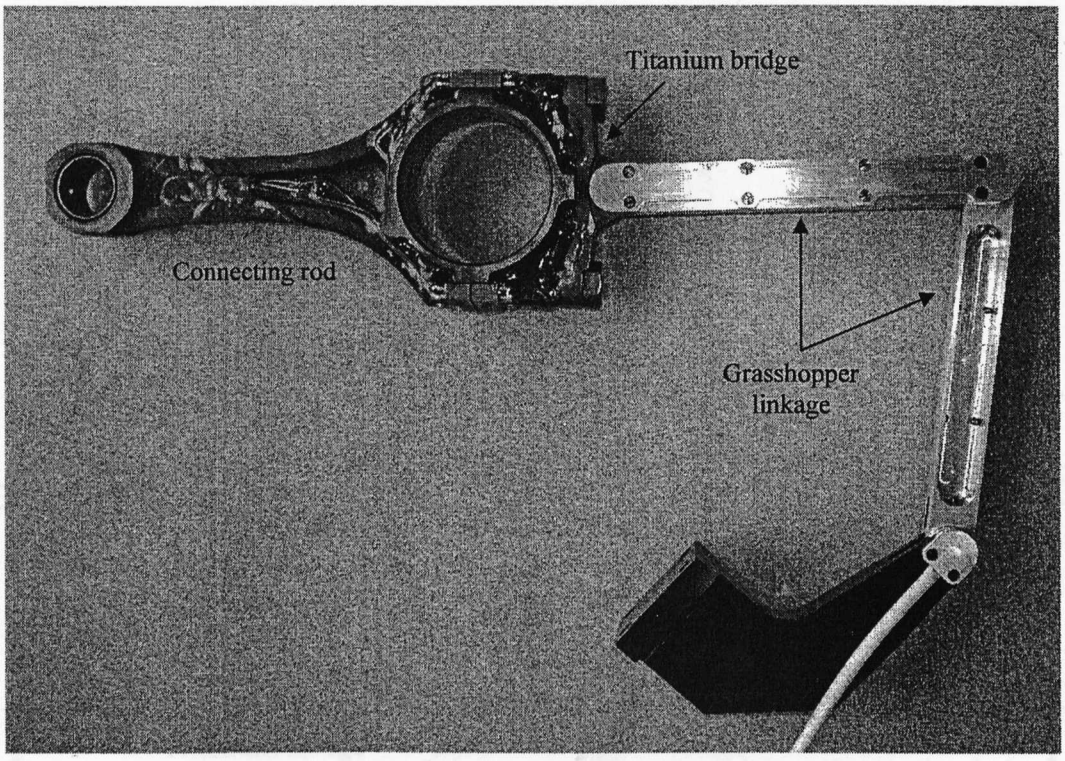

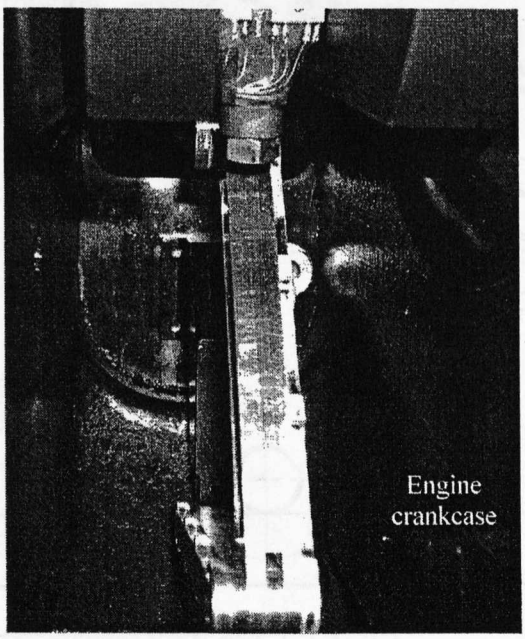

Figure 6.22. Grasshopper linkage and its installation in the engine crankcase.

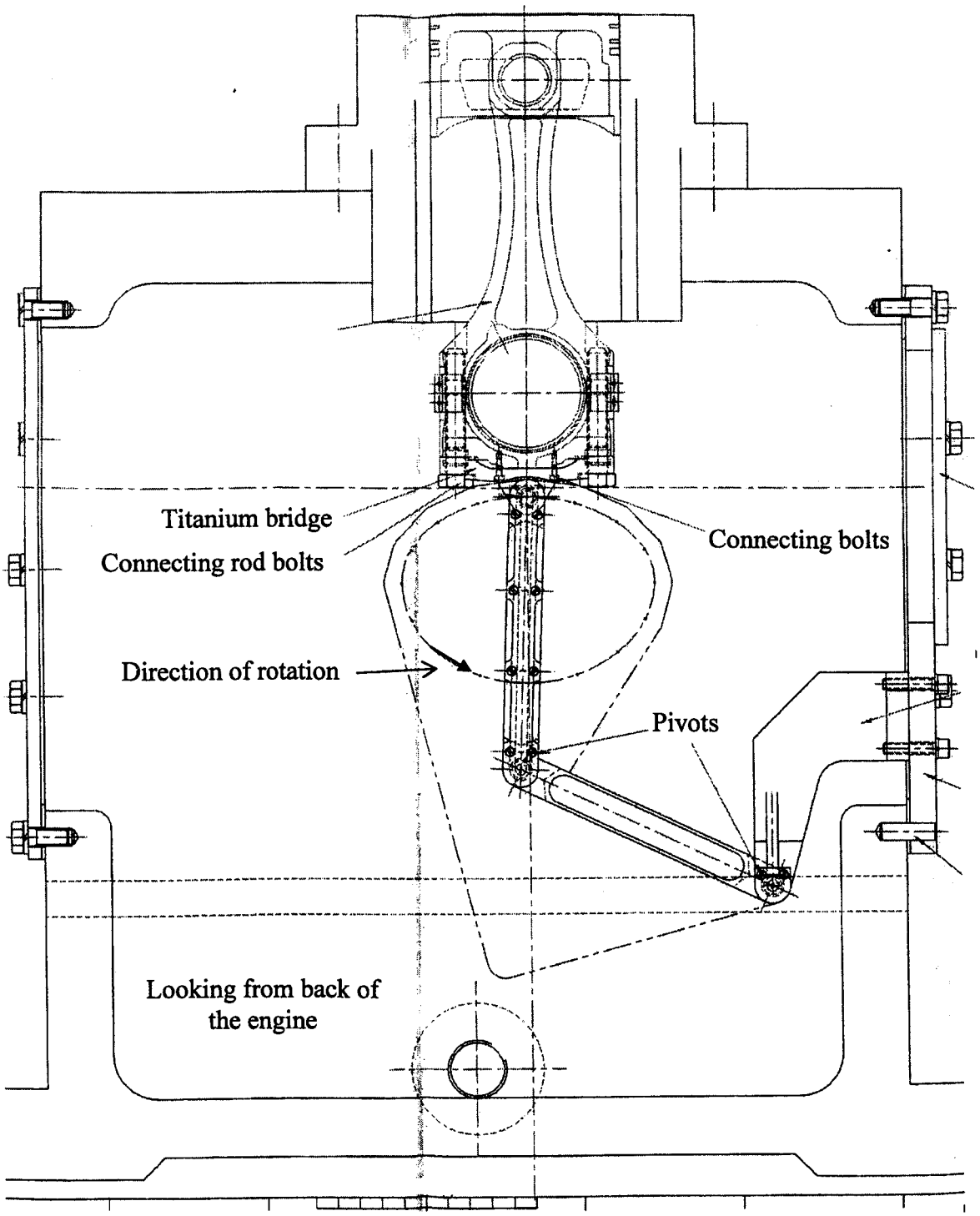

Figure 6.23. Crankcase cross-section and grasshopper linkage orientation.

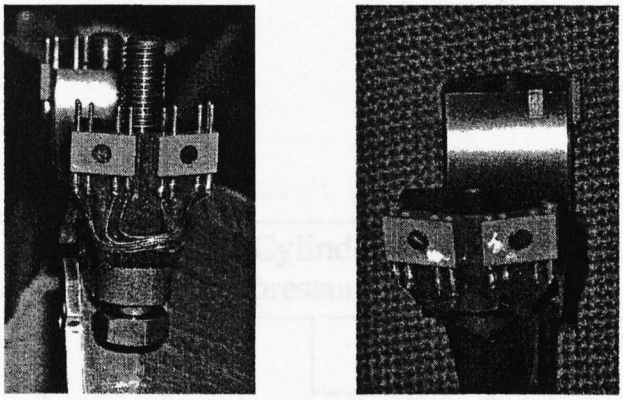

Figure 6.24. High quality plugs having 24 terminals in total.

6.4 SUMMARY

Two main methods of measuring piston assembly friction in a firing engine have been described, the floating liner and the IMEP methods. The IMEP method has been adopted to measure instantaneous and average piston assembly friction as no major engine modification was required, giving a true picture of piston assembly friction loss in a real firing engine. This method requires accurate measurement of forces acting on the piston assembly and connecting rod. Thus all the factors affecting the readings have been outlined and the ways to diminish such effects have been discussed.

The calibration of the cylinder pressure transducer and connecting rod was carried out and all the forces acting on the piston assembly and connecting rod studied carefully. As the experiments were carried out on a single cylinder engine, the effect of crankshaft acceleration and thus its response in the piston assembly inertia have also been analysed. An absolute resistive pressure transducer, fitted on the cylinder liner was used to peg cylinder pressure transducer reading to calculate absolute pressure. A 24-wire grasshopper linkage was used to conduct the wires from the connecting rod to the data acquisition system. Figure 2.5 summarises the procedure carried out to measure experimentally piston assembly friction.

This IMEP method was used to validate FLAME piston assembly friction model outline in the previous chapter. Experiments have been carried out to measure piston assembly friction under different engine operating conditions and are described in the next chapter.

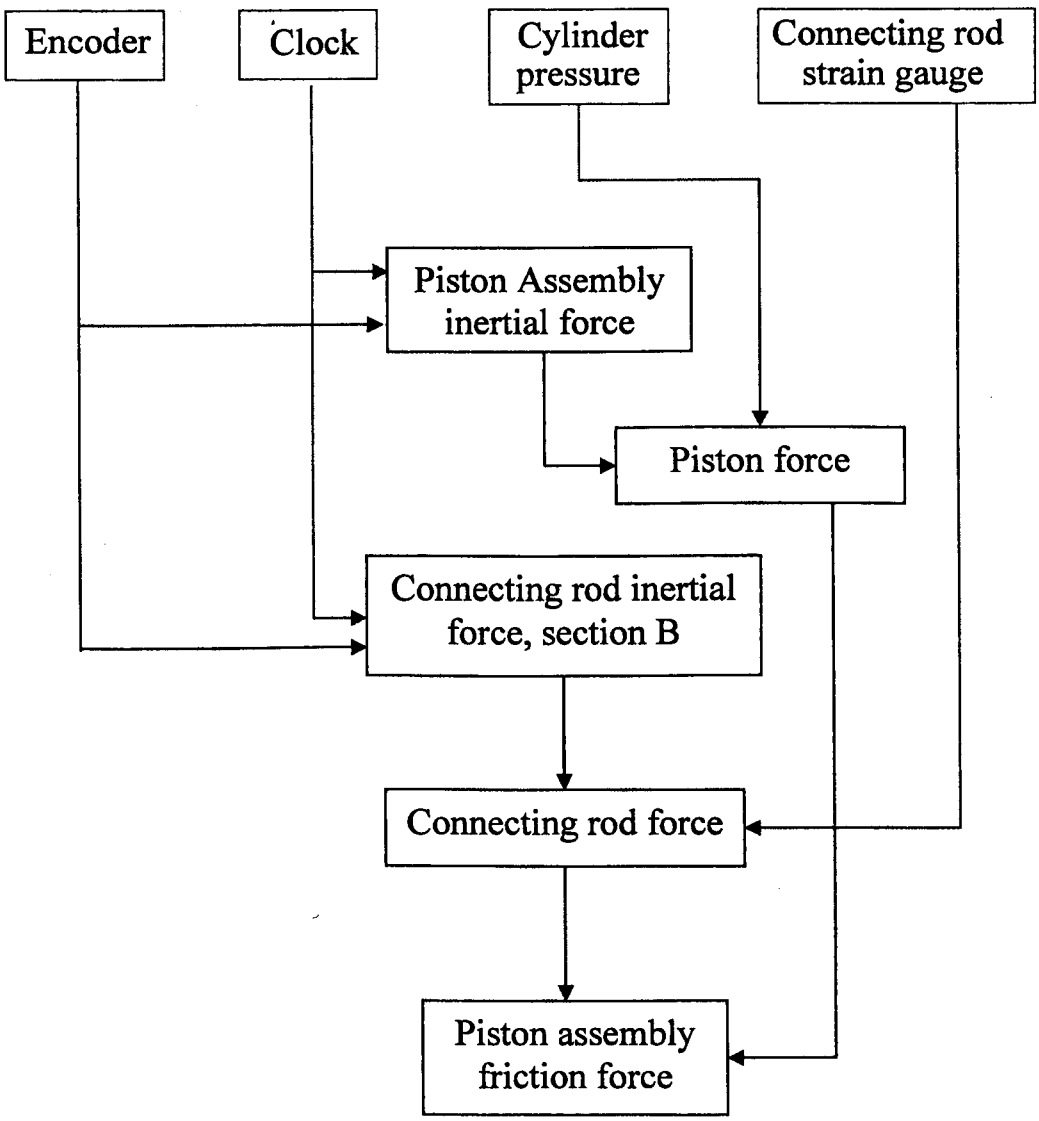

Figure 6.25. Flow chart of the experimental measurement of piston assembly friction.

Chapter seven

EXPERIMENTAL AND THEORETICAL EVALUATION OF PISTON ASSEMBLY FRICTION

7.1 INTRODUCTION

The friction between the piston assembly and the cylinder liner has a great influence on the fuel economy of reciprocating engines. To understand the effect of different lubricants and engine component design on the engine performance and fuel economy it is important to measure losses generated by different engine components in a real firing engine. This chapter describes the experimental results for the piston assembly friction loss under both fired and motored conditions measured on a single cylinder gasoline engine without any major engine modification, using the well-known IMEP method described in detail in the previous chapter.

Measured data are also compared with predicted results using the FLAME piston assembly friction model and the Leeds Piston Skirt Lubrication and Dynamics Analysis model. The detailed description of the instrumentation and engine data acquisition system required to measure average and instantaneous piston assembly friction is given in chapter eleven. The effect of different lubricants, oil temperatures and engine speeds on the piston assembly friction is discussed in this chapter.

The first part of this chapter describes the experimental procedure and the data post processing required to measure the piston assembly friction loss. The experimental results are explained in the second part, looking at the effect of oil viscosity and engine speeds on the piston assembly friction, followed by the predicted results. Finally comparisons between experimental and predicted results are presented.

7.2 EXPERIMENTAL PROCEDURE

To measure piston assembly friction, under both motored and fired conditions, and to validate the engine piston assembly friction model the following information was logged during the test run,

- Crankshaft angular position.
- Crankshaft angular velocity and acceleration.
- Crankcase lubricant inlet temperature.
- Cylinder liner near surface temperature at nine different locations.
- Cylinder pressure, using a piezoelectric pressure transducer.
- Cylinder pressure transducer cooling water temperature.
- Cylinder absolute pressure, pegged using an absolute resistive liner pressure transducer.
- Connecting rod force using axial strain gauges.
- Connecting rod surface temperature at the location of the strain gauges.
- Engine TDC position.

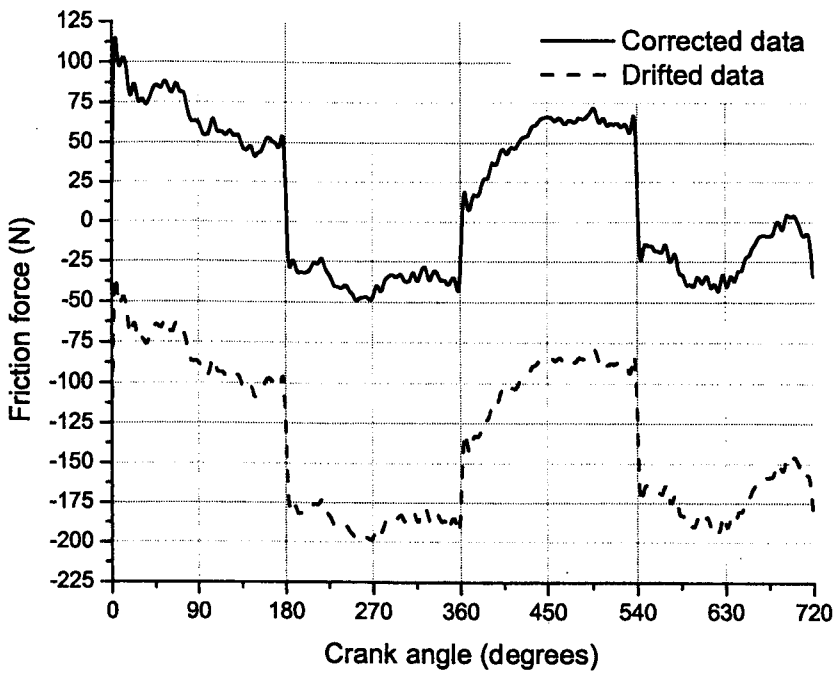

Figure 7.1. Effect of connecting rod strain gauge temperature drift (surface temperature 51°C) on the piston assembly instantaneous friction, engine speed 800rpm.

Initial tests indicated that the signal from the liner absolute pressure transducer and the connecting rod strain gauges drifted with temperature despite using an inline temperature compensation module for the pressure transducer and using temperature compensated strain gauges on the connecting rod. Figure 7.1 shows the effect of connecting rod strain gauge signal drift with temperature on the instantaneous piston assembly friction force at engine speed 800rpm and lubricant inlet temperature 40°C. Under such operating conditions the connecting rod surface temperature near the strain gauges was 51°C Hence a test procedure was developed to take such effects into account. Before each experiment, zeroing of the liner absolute pressure transducer at stabilised running conditions was carried out by moving the piston to TDC position. Thus exposing the liner pressure transducer to atmospheric pressure via the crankcase and resetting the amplifier. The liner transducer was again exposed to crankcase pressure immediately after the experiment and any temperature drift was recorded and removed from the liner pressure transducer readings.

A slightly different approach was used for the connecting rod as two different offsets were needed to be addressed, the initial offset and the strain gauge temperature drift. The initial offset is the offset in the complete system from strain gauges, amplifier to the data acquisition system and is taken when the system is completely installed and no load is applied on the connecting rod strain gauges. If the connecting rod and piston assembly along with the grasshopper linkage is assembled into the engine with no load acting on the piston crown, the initial offset reading could not be taken, as friction between the piston assembly and the liner existed. To get true initial offset reading, a somewhat tedious method was used. Before installing the grasshopper linkage, the engine cylinder head and liner was removed from the engine. Without assembling the piston assembly, only the connecting rod along with the grasshopper linkage was first installed in the engine crankcase, tightening the big-end bearing according to the required torque. All the connections from the connecting rod strain gauges to the data acquisition system were made and the signal zeroed at the amplifier, as there was no load acting on the connecting rod. The Fylde amplifier stored the offset reading. After adjusting the offset, the engine was completely assembled.

The experiments were carried out under stable engine running conditions. To address the strain gauge temperature drift during each experiment the connecting rod surface

temperature close to the location of the strain gauges was recorded using a thermistor. At the end of each experiment the engine was allowed to run at slightly higher engine load and high lubricant temperature for a few minutes causing the connecting rod surface temperature to rise a few degrees above the recorded value. The engine was then stopped and positioned at TDC position and the big-end bearing lower cup was removed and then turned to nearly BDC position thus allowing the piston assembly along with the upper part of the connecting rod to hang in the liner. The bearing lower cup, connected to the grasshopper linkage was placed on the crankcase floor. The strain gauge terminals on both the upper and lower connecting rod bearing cups were connected via a short jumper cable, completing the strain gauge and thermistor circuit. The engine was then allowed to cool down and the temperature-offset value was determined at the thermistor-recorded values as there is no load acting on the connecting rod upper part.

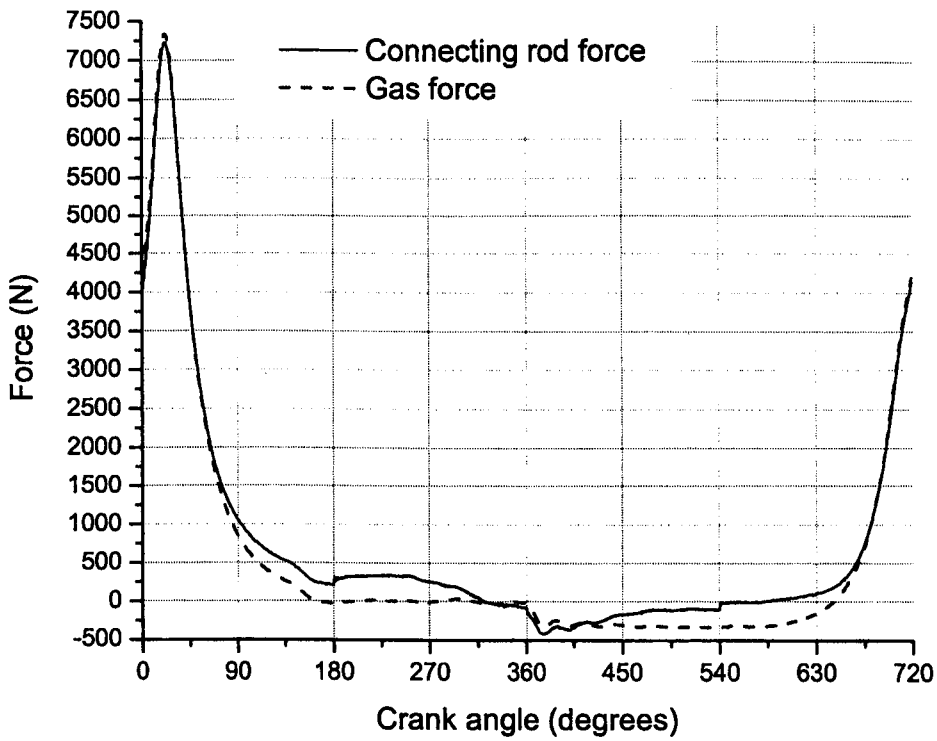

Figure 7.2. Synchronised simultaneous measurement of gas force and forces acting on the connecting rod, 1500rpm, ½ load.

The instantaneous IMEP method for determining piston assembly friction required simultaneous logging of the following data: cylinder pressure, cylinder liner absolute pressure; crankshaft angular position and the connecting rod force at every 0.5 degrees of crank angle. These were synchronised and triggered via the encoder TTL signal, as any slight phase shift can result in large errors as can be seen in figure 7.2, especially the area where there is a sharp rise and fall of forces acting on the piston assembly. Thus a special and complex simultaneous sampling data acquisition system and triggering method was used and is explained in detail in chapter eleven.

7.3 POST PROCESSING

The signals from the cylinder pressure transducer and the connecting rod strain gauges were digitally filtered to remove any induced noise. A Butterworth filter having a cut-off frequency of 200 Hz was used for filtering the data giving special attention to the potential phase shifts. Figure 7.3 shows the effect of digital filtering of the data obtained from both the cylinder pressure transducer and the connecting rod strain gauges on the instantaneous piston assembly friction at an engine speed of 800rpm. The signal to noise ratio was further improved by averaging up to sixty engine cycles.

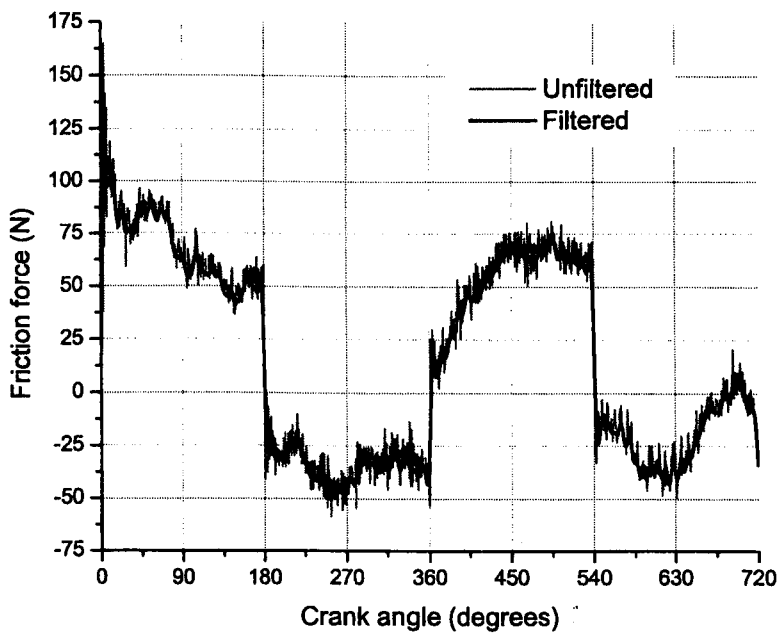

Figure 7.3. Effect of digital filtering on instantaneous piston assembly friction, engine speed 800rpm, ½ load.

7.4 PISTON ASSEMBLY FRICTION, EXPERIMENTAL RESULTS

Piston assembly friction measurement was carried out on a single cylinder Ricardo Hydra gasoline engine under both fired and motored conditions with lubricant inlet temperatures of 24°C, 40°C, 60°C and 80°C. The piston assembly friction was measured at engine speeds of 800rpm (¼ load), 1500rpm (½ load) and 2000rpm (½ load), the upper limit being defined by the capabilities of the grasshopper linkage and the vibration of the engine. For validation of the FLAME piston assembly friction model SAE 0W20 lubricant without friction modifier was used.

The experiments were carried out in four sets, obtaining measurements at three different speeds for each lubricant temperature. Initial experiments revealed that the accuracy of the results could be easily reduced if offsets from the instruments required to measure piston assembly friction were not taken into account. However, despite addressing the offsets issue from connecting rod strain gauges and the liner absolute pressure transducer mentioned earlier, another problem faced during the experiments was a slight signal offset due to the amplifier temperature change, causing a drift of connecting rod signal. This drift effect was reduced by replacing the upper cover of the amplifier with a wire mesh and using an external fan to blow air into the amplifier circuit, thus significantly reducing the drift effect. A One-hour warming time was specified for the complete instrumentation system before experiments were carried out.

One of the parameters required to measure piston assembly friction is the reciprocating inertial force of the piston assembly and the connecting rod. Figure 7.4 shows the calculated piston assembly inertial force at different engine speeds, having a total mass of 577.8g. It can be seen that as the engine speed increases the inertia force increases substantially from 150N at 800rpm to nearly 800N at 2000rpm engine speed. These forces were calculated from the crankshaft angular velocity/acceleration and the piston displacement. A similar, but somewhat lesser effect can be seen in figure 7.5, which shows the reciprocating inertial force of section 'B' (figure 6.5) of the connecting rod, with a mass of 72g. A very accurate procedure discussed in the last chapter, was used to measure and calculate these forces as any error may result in complete loss of piston assembly friction force measurement.

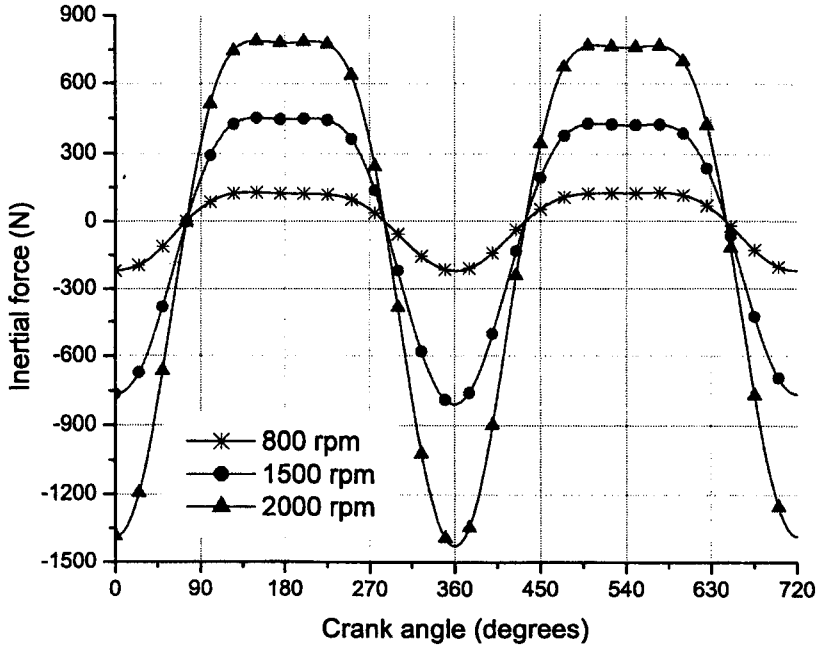

Figure 7.4. Piston assembly reciprocating inertial force, (mass: 577.8g).

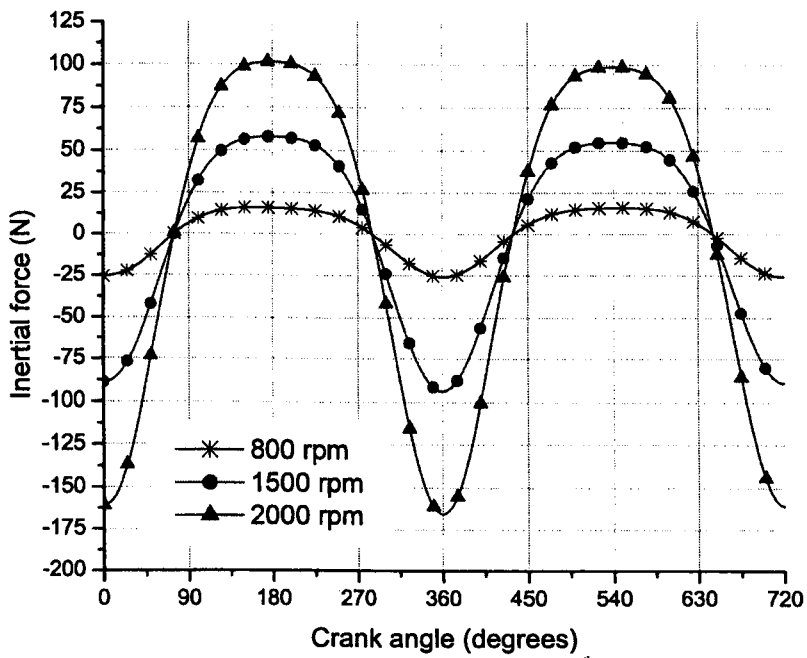

Figure 7.5. Connecting rod section 'B' (figure 6.5, mass: 72g), reciprocating inertial force.

7.4.1 PISTON ASSEMBLY FRICTION UNDER FIRED CONDITIONS

In all the graphs for instantaneous piston assembly friction in this chapter, 0 degrees is the engine TDC fired position, start of the power stroke. A typical cyclic variation of friction force for a piston assembly at an engine speed of 800rpm is shown in figure 7.6. The sudden change in sign of the friction force at the end of each stroke is due to the change in direction of piston travel. Despite addressing the combustion pressure transducer drift, explained in detail in chapter six, it was seen that at low lubricant temperature under fired conditions, the pressure transducer calibration slightly drifted at the end of the compression stroke (figure 7.6, between 675° and 720°), causing the friction force to cross the zero datum line slightly. The effect was reduced considerably at higher lubricant temperature.

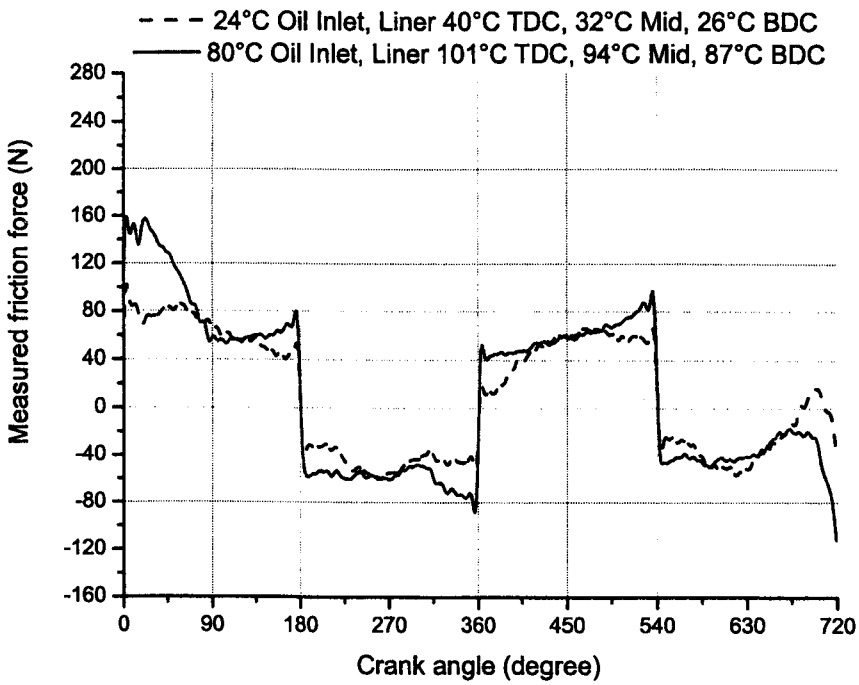

Figure 7.6. Piston assembly friction force, engine speed 800rpm, ¼ load, lubricant SAE 0W20 without FM.

At any engine operating conditions, the maximum friction takes place at the start of the power stroke as the lubrication condition at this point is in the boundary regime due to the peak combustion pressure resulting in high compression ring radial loading. At the

end and start of each stroke the piston/liner friction is more towards boundary lubrication whereas at mid stroke it is generally hydrodynamic because of relatively high entraining velocity.

In the hydrodynamic lubrication regime, a thin layer of lubricant film separates the two sliding surfaces and shearing of this film generates friction loss. Under such a lubrication regime, viscosity plays a vital role. In the mixed lubrication regime, that is in the presence of both a lubricant film and metal-to-metal contact, lubricant chemistry becomes more important. The coefficient of friction decreases with increasing viscosity whereas in the hydrodynamic regime the friction coefficient increases with an increase in viscosity. Under elastohydrodynamic lubrication conditions, normally takes place at very high contact loading, the lubricant viscosity increases as the pressure on the oil film increases. Hence there is an optimum viscosity at a given operating conditions which provides minimum friction and maximum engine output.

While examining the friction results it is important to bear in mind that the measured piston assembly friction force is the summation of four main components: two compressions rings, an oil control ring and the piston skirt. Therefore a change of a variable may produce different and even conflicting effects for each component. For example at moderate lubricant temperatures the piston skirt operates in the hydrodynamic regime whereas the piston rings operate in the boundary to hydrodynamic lubrication regimes. Any increase in lubricant temperature would bring the piston ring lubrication conditions more towards boundary, increasing the friction loss whereas the decrease in viscosity would reduce the friction contribution from the piston skirt due to a reduction of shear loss. During piston assembly friction measurement the cylinder liner surface temperature was also measured at TDC, BDC and mid stroke. Although the inlet lubricant temperature was kept constant the temperature at the liner surface was different. The liner surface temperatures at the above mentioned locations are given in the measured instantaneous piston assembly friction figures.

Figure 7.6 shows the piston assembly friction at an engine speed of 800rpm for lubricant inlet temperatures of 24°C and 80°C. It can be seen that at a lubricant temperature of 24°C, at the start of the power stroke the piston assembly friction is high

due to severe lubrication conditions resulting in boundary lubrication, but as the piston picks up velocity, just before and after mid stroke, the friction decreases due to a high entraining velocity dragging more lubricant into the piston/liner interface. Thus the piston/liner interface enters into the hydrodynamic lubrication regime. At mid stroke, the entraining velocity is high and under hydrodynamic lubrication conditions, this results in an increase in friction due to high shear rate (figure 7.6). A similar picture can be seen for other piston strokes. Whereas at 80°C lubricant temperature the friction at the start and end of each stroke is high as the film thickness in this region is relatively small due to low entraining velocity and low lubricant viscosity but at mid strokes there is a slight decrease in friction. A very similar picture can be seen in figures 7.7 and 7.8 for engine speeds of 1500rpm and 2000rpm respectively. One of the main factors responsible for the difference in friction loss during upward and downward piston strokes is the flow/availability of lubricant on the liner surface, as the piston uncovers and covers the liner. The flow/availability of lubricant is also dependent on the engine speed. Some noise was experience at high engine speed and lubricant inlet temperature at nearly 300° engine cycle, figure 7.8. This could be because of the piston ring flutter effect or the engine vibration.

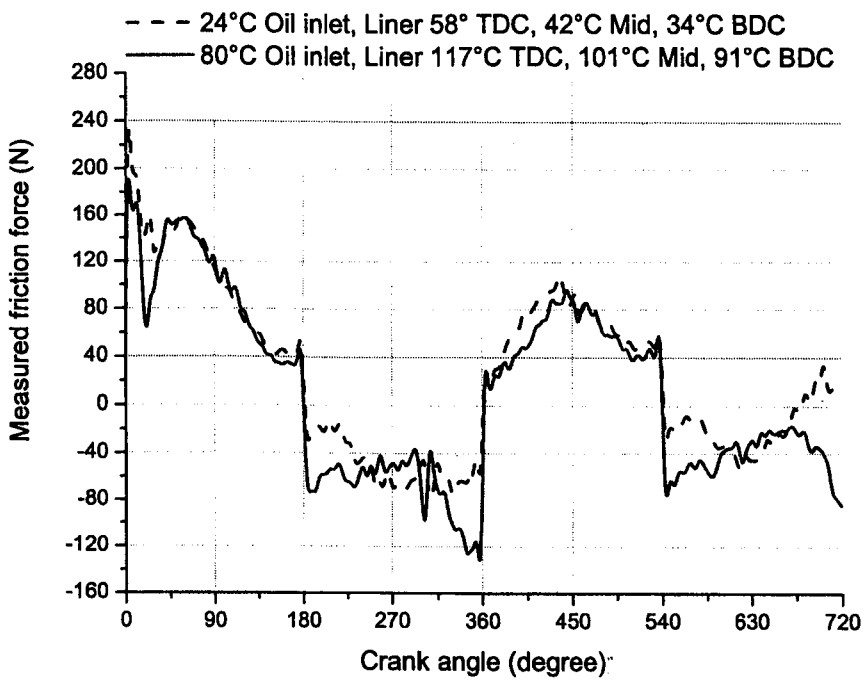

Figure 7.7. Piston assembly friction force, engine speed 1500rpm, ½ load, SAE 0W20 without FM.

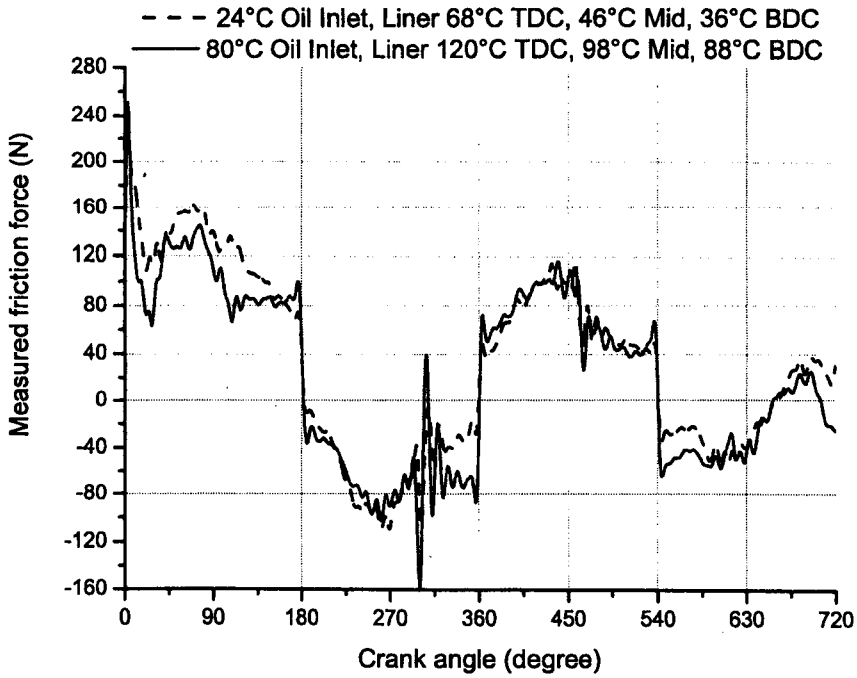

Figure 7.8. Piston assembly friction force, engine speed 2000rpm, ½ load, SAE 0W20 without FM.

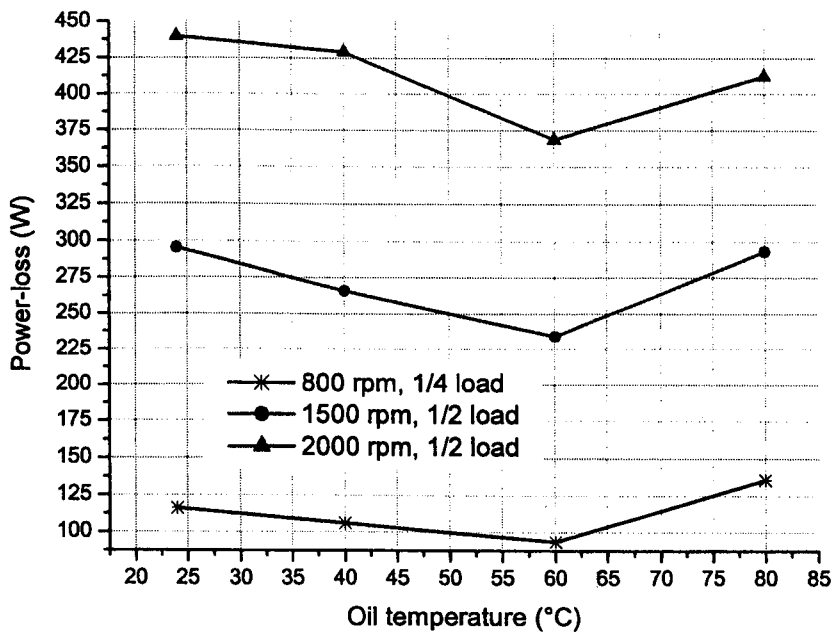

Figure 7.9. Piston assembly average power loss, SAE 0W20 without FM.

Figure 7.9 clearly shows the average piston assembly power loss correlating with the Stribeck curve at any engine speed. The friction coefficient is related to viscosity, surface speed and load, and according to the theory of hydrodynamic lubrication the viscosity increases sharply as the lubricant temperature decreases. At any engine speed it can be seen that the friction decreases as lubricant inlet temperature increases, whereas at 80°C and above, the friction increases due to low lubricant viscosity, causing boundary to mixed lubrication to be more dominant. At an engine speed of 1500rpm, figure 7.9, the friction loss at a lubricant inlet temperatures of 24°C and 80°C is nearly the same, a clear indication of change of friction characteristic from shear loss to surface interaction whereas at 2000rpm the increase in average friction at 80°C is relatively small as compared to low engine speeds due to high entraining velocity.

7.4.2 COMPARISON BETWEEN MOTORED AND FIRED PISTON ASSEMBLY RESULTS

Experiments were also carried out under motored conditions at engine speeds of 800rpm, 1500rpm and 2000rpm using the SAE 0W20 lubricant without friction modifier. The motored piston assembly friction measurement was undertaken at the same time as experiments were carried out under fired conditions. The experiment was first carried out under fired conditions and then under motored. The time difference between performing experiments under fired and motored conditions for similar lubricant temperatures was a few seconds. Thus most of the difference in friction between motored and fired is due to the effect of combustion gas on piston assembly lubrication. While studying the difference it is important to bear in mind that although the motored experiments were carried out just after fired conditions, there was a slight temperature drop in the liner near surface temperatures of 3°C to 5°C.

Figure 7.10 shows the measured instantaneous piston assembly friction at an engine speed of 800rpm and lubricant inlet temperature of 24°C for both motored and fired conditions. During the power stroke the higher piston assembly friction under fired conditions is due to the severe lubrication conditions caused by the high combustion gas pressure and temperature. Whereas during other parts of the piston strokes there is a slight increase in piston assembly friction under motored condition as compared to fired. This can be justified as at such a low lubricant inlet temperature the

lubrication regime at the piston/liner interface is mostly under mixed to hydrodynamic lubrication and under such conditions, a slight fall in lubricant temperature will increase the shear power-loss due to increase in lubricant viscosity. A similar but somewhat greater difference in piston assembly friction during the power stroke can be seen in figure 7.11, identifying severe lubrication conditions at the piston/liner interface, due to low viscosity lubricant resulting in severe boundary lubrication. Whereas during exhaust and intake strokes there is a slight decrease in friction under motored conditions as compared to fired caused by the decrease in lubricant temperature at relatively low viscosity improving the piston assembly lubrication conditions. A similar picture can be seen in figures 7.12 and 7.13 for an engine speed of 2000rpm and lubricant temperatures of 24°C and 80°C.

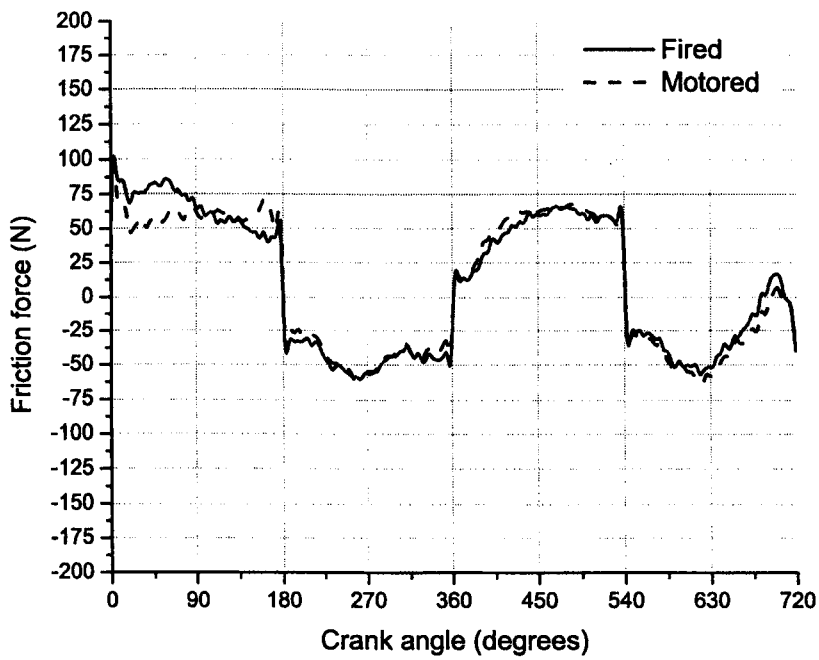

Figure 7.10. Engine speed 800rpm, ¼ load, lubricant temperature 24°C, SAE 0W20 without FM.

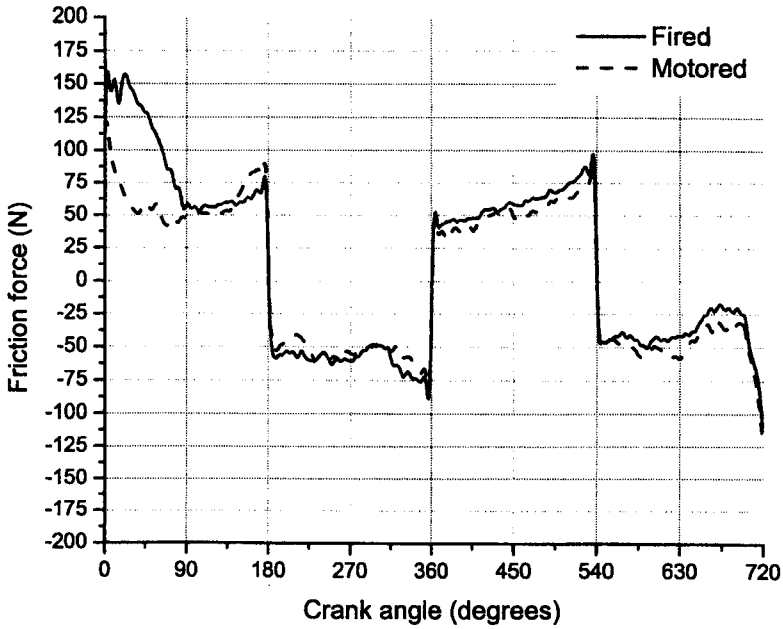

Figure 7.11. Engine speed 800rpm, ¼ load, lubricant temperature 80°C, SAE 0W20 without FM.

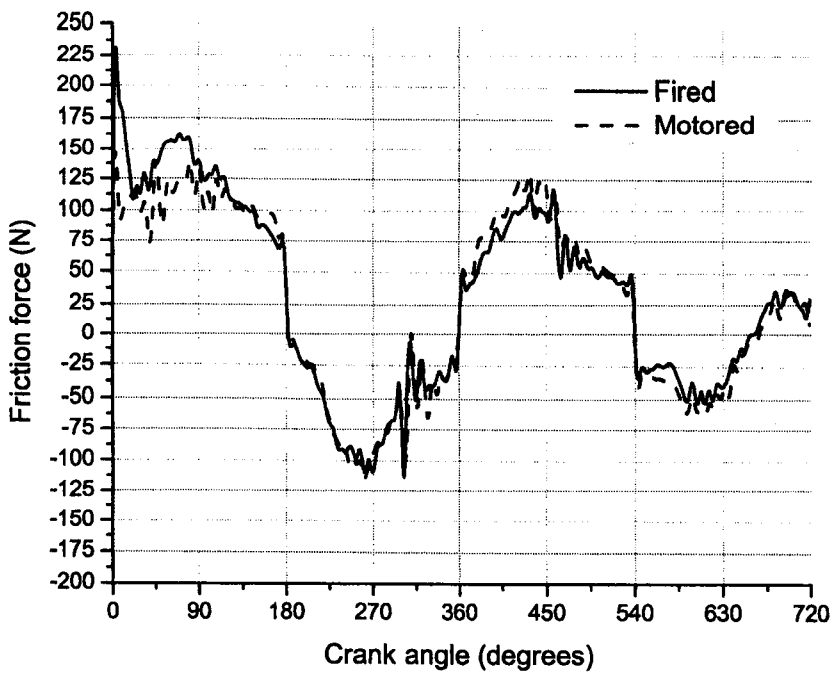

Figure 7.12. Engine speed 2000rpm, ½ load, lubricant temperature 24°C, SAE 0W20 without FM.

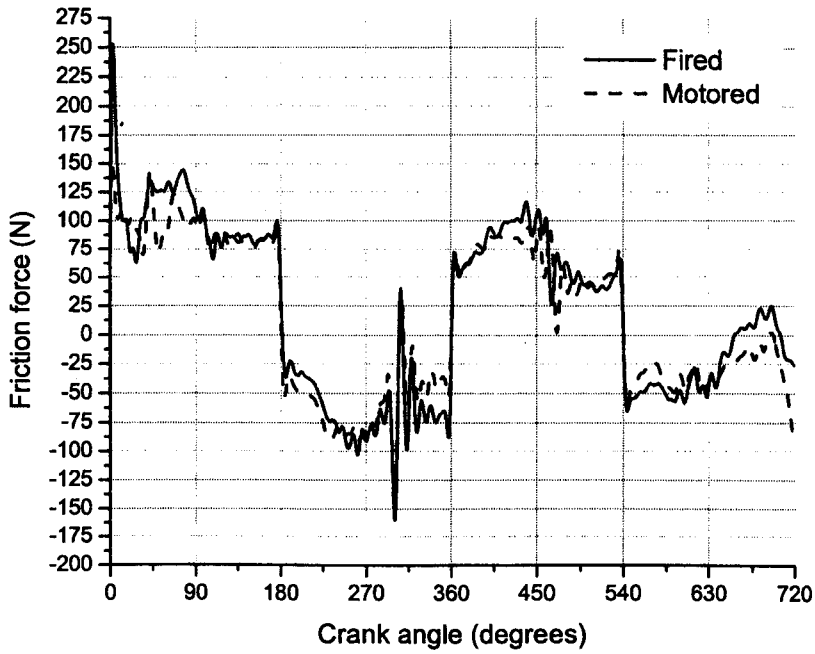

Figure 7.13. Engine speed 2000rpm, ½ load, lubricant temperature 80°C, SAE 0W20 without FM.

An overall picture of average piston assembly friction difference between motored and fired conditions can be seen in figure 7.14. The piston assembly friction trend under motored conditions is similar to fired conditions, with friction under fired conditions slightly higher than motored, mainly due to the effect of high combustion gas pressure and temperature on the lubrication at the piston/liner interface during the power stroke.

Due to the similarity in results, a piston/liner lubrication study can be carried out under motored conditions provided the liner is heated in such a way that the lubricant experiences similar liner surface temperatures down the stroke as was under fired conditions. Under motored conditions the piston/liner friction loss follows the Stribeck curve, a decrease in friction with temperature increase due to reduction in shear loss and then an increase in friction caused by high lubricant temperature resulting in mixed to boundary lubrication.

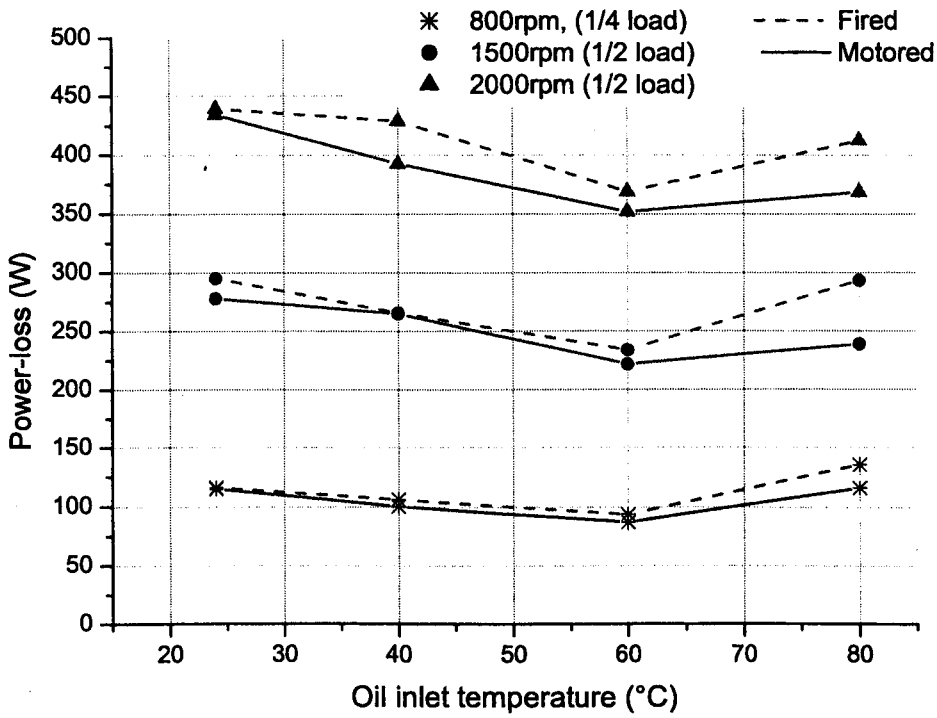

Figure 7.14. Piston assembly friction under both motored and fired conditions.

7.5 PREDICTED RESULTS AND COMPARISION WITH MEASURED PISTON ASSEMBLY FRICTION

Measured data are also compared with the predicted results using the FLAME piston assembly friction model for the compression and oil control rings and the Leeds Piston Skirt Lubrication and Dynamics Analysis model for the piston skirt/liner interaction, described in chapter five. The Ricardo Hydra inlet data file for the FLAME piston assembly friction model is given in Appendix I. Figure 7.15 shows the predicted and measured instantaneous piston assembly friction at an engine speed of 800rpm and lubricant inlet temperatures of 24°C and 80°C. It is clear from these figures that the predicted piston assembly friction result correlates very well with the measured data, especially at high lubricant temperature.

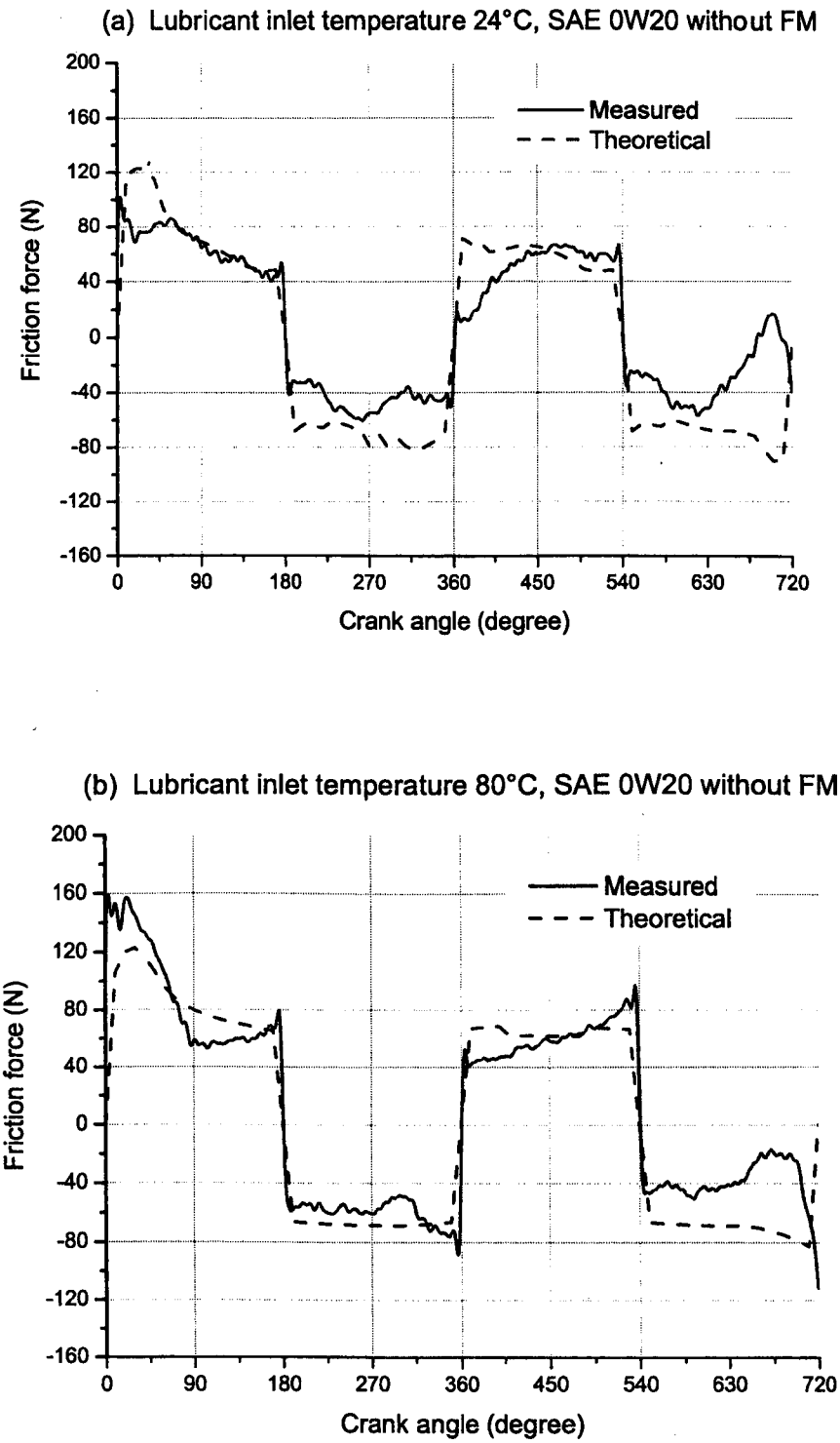

Figure 7.15. Predicted and experimental measurement of instantaneous piston assembly friction, engine speed 800rpm, ¼ load.

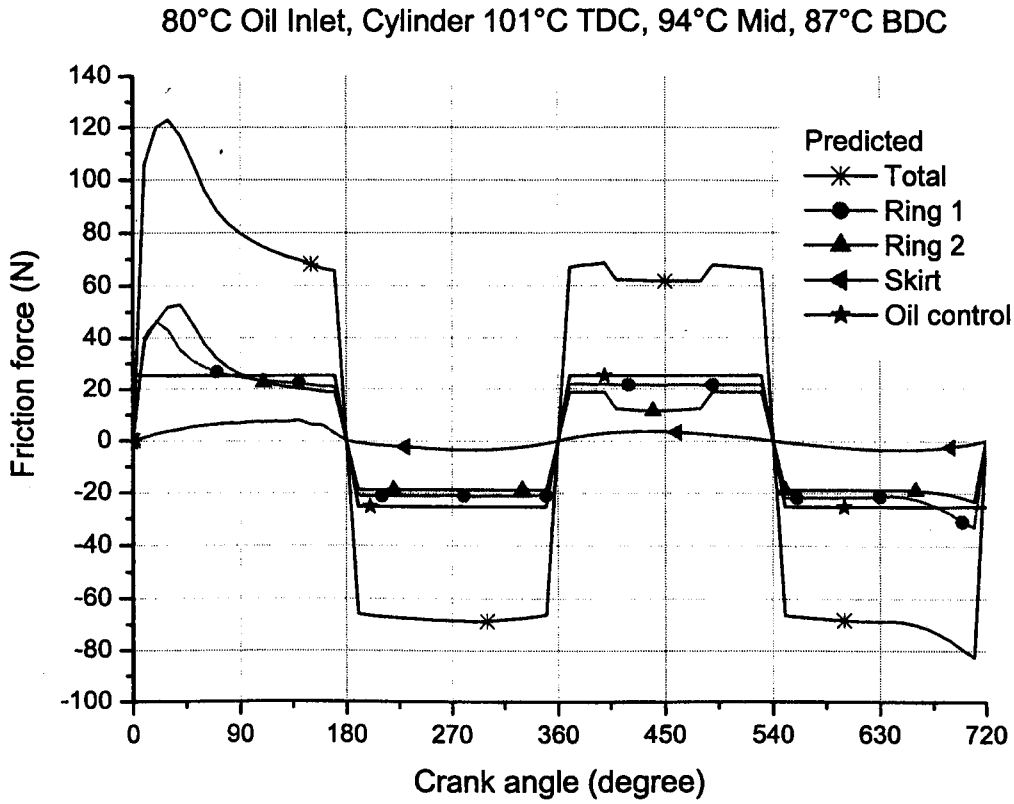

Figure 7.16 Predicted piston assembly component friction at engine speed 800rpm.

The computed friction force data for the individual components are shown in figure 7.16, to provide an indication of the relative importance of the friction losses associated with each element and its contribution towards total piston assembly friction. It is assumed that the oil control ring works in the boundary regime and hence the friction force is proportional to the load acting upon it. Thus the oil control ring generates more friction loss than any of the compression ring except during the start of the power stroke were the losses due to compression ring/liner interface exceed that of the oil control ring. The lubrication regime at the piston skirt and liner interface is hydrodynamic and can be seen as a nearly sinusoidal signal in figure 7.16.

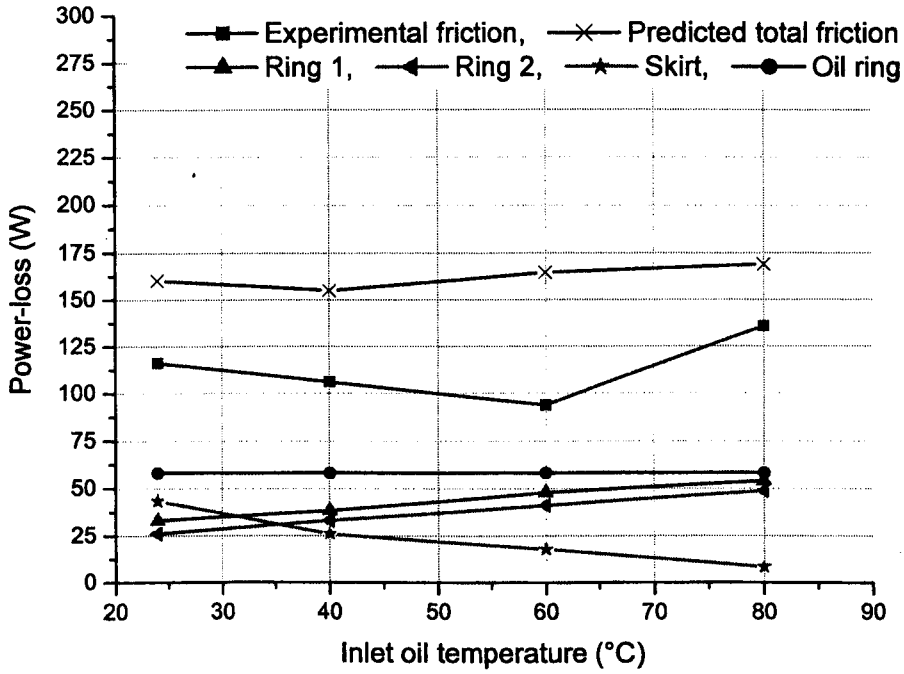

Figure 7.17. Predicted piston assembly component power-loss and experimental result at engine speed 800rpm, ¼ load.

Comparing the average measured and predicted piston assembly friction power loss as shown in figures 7.17 to 7.19, it is clear that the calculated friction is qualitatively similar to the measured. The oil control ring produces the largest single contribution to the total friction loss of the piston assembly and this remains unaltered at any lubricant temperature because the assumption that boundary lubrication occurs throughout the stroke removes any lubricant influences. The role of the oil control ring is to distribute the lubricant around the circumference of the cylinder liner and to limit the lubricant flow to the compression rings. The gas pressure above and below the oil control ring is assumed to be equal to crankcase pressure and thus the only loading exerted by the control ring on the liner is due to the radial loading arising from the inherent elastic tension of the oil control ring alone as mentioned in chapter five. Due to the very narrow height of the oil control ring and high ring elastic tension loading, asperity contact takes place and the oil control ring/liner interface is normally in the boundary lubrication regime. The friction contribution from skirt/liner interaction is mainly due

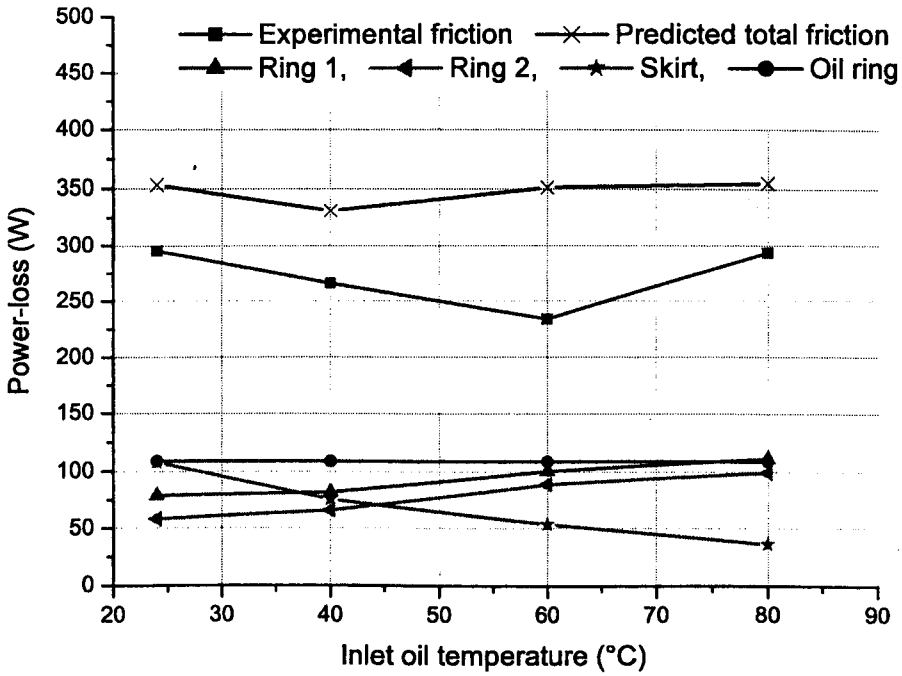

Figure 7.18. Predicted piston assembly component power-loss and experimental result at engine speed 1500rpm, ½ load.

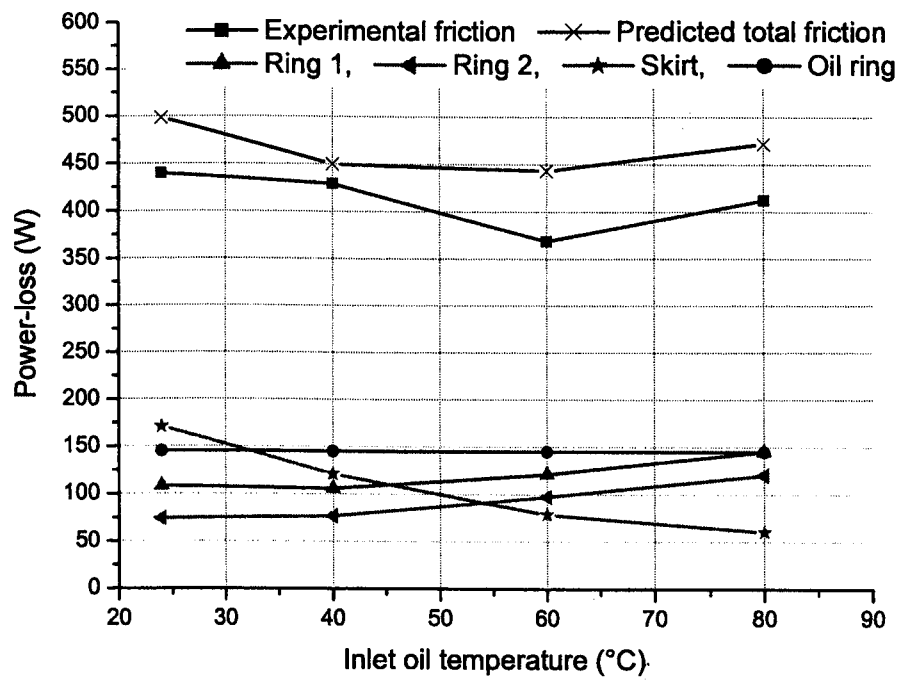

Figure 7.19. Predicted piston assembly component power-loss and experimental result at engine speed 2000 rpm

to shear loss, as evidenced by a continuous decrease in power-loss as lubricant temperature increases at any engine speed, figures 7.17 to 7.19. This correlates very well with the findings of Seki et al [2000] who used an optical measurement technique to measure film thickness between piston and liner and found continuous oil film thickness between the skirt and the liner throughout the engine stroke.

It is clear from the above figures that the predicted compression ring friction contribution increases as lubricant temperature increases at any engine speed as the compression rings work in the boundary to hydrodynamic lubrication regimes. The lubricant supply to the compression rings plays a key role in determining the ring/liner interface lubrication condition. Oil transport is an important and complicated issue in the analysis of lubrication of ring pack and oil consumption in an engine. There are a number of factors that will affect the lubrication of the compression rings: the ring geometry; distortion of the piston and liner; the accumulation of lubricant within the ring pack; the gas flow through the pack and the dynamic behaviour of the ring, such as ring tilting. The second compression ring contributes in controlling the volume of oil available for the top ring so that sufficient oil is present to generate an adequate film to survive in extreme conditions of high gas temperature and pressure. The second ring delivers a controlled amount of lubricant to the top ring as excess lubricant will lead to high oil consumption yet too little oil will result in top ring scuffing. Thus the top ring experiences a relatively starved lubrication condition compared to the second ring.

The predicted piston assembly loss in figure 7.20 is calculated using two different skirt analyses, the piston/liner concentric analysis and the more complex and realistic analysis that introduces piston secondary motion, explained in detail in chapter five. The power loss generated by the compression rings and the oil control ring is the same for both the predicted cases. The highest power loss shown in figure 7.20 is produced by the simple piston skirt/liner lubrication analysis assuming that the piston remains concentric with the liner throughout the engine stroke and the clearance between the piston and the liner is filled with lubricant, thus over-predicting the power loss due to high shear friction. However the result obtained by considering the secondary motion of the piston skirt correlates very well with the measured piston assembly power loss. The snap shot of the piston orientation at a number of crank angle positions at various engine speeds can be seen in figures 7.21 to 7.23 obtained via the Leeds Piston Skirt

Lubrication and Dynamics Analysis model. It can be seen that although the pattern of piston secondary motion at any engine speed is nearly similar but as the speed increases, the higher cylinder pressures and the increase in inertial effects result in higher component loading and an increase in the degree of skirt movement within the liner.

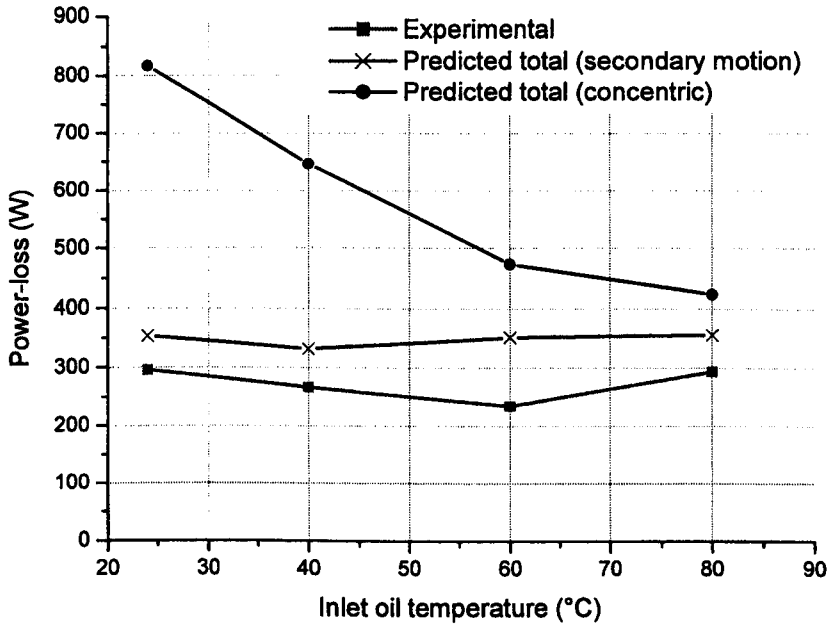

Figure 7.20. Comparison of the predicted piston assembly friction for two different piston skirt analysis, 1500rpm.

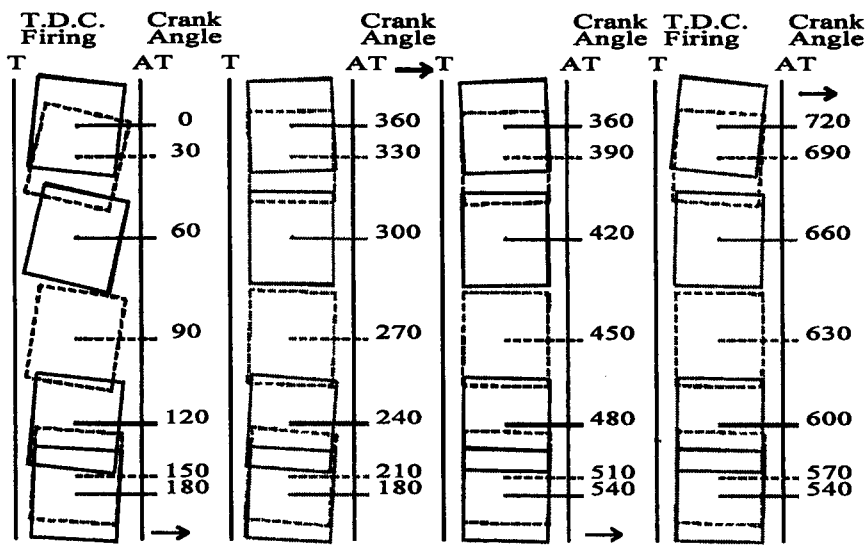

Figure 7.21. Predicted piston secondary motion at engine speed 800rpm.

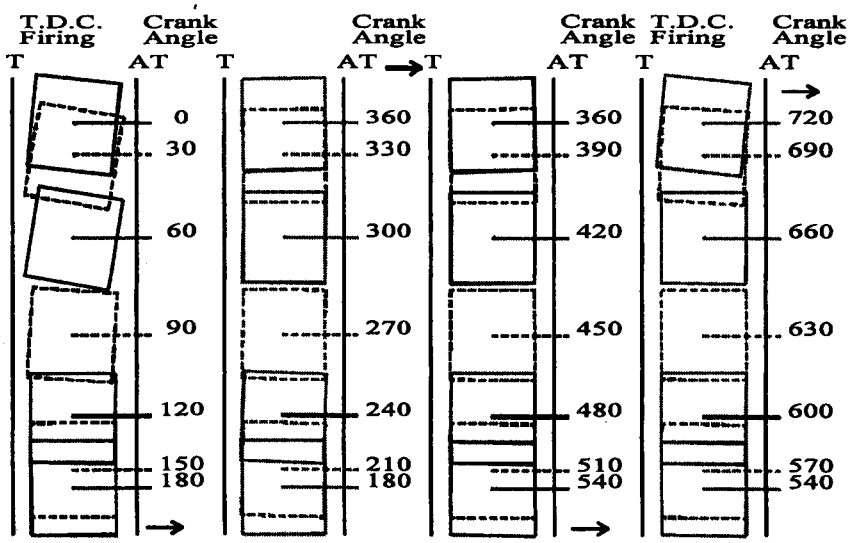

Figure 7.22. Predicted piston secondary motion at engine speed 1500rpm.

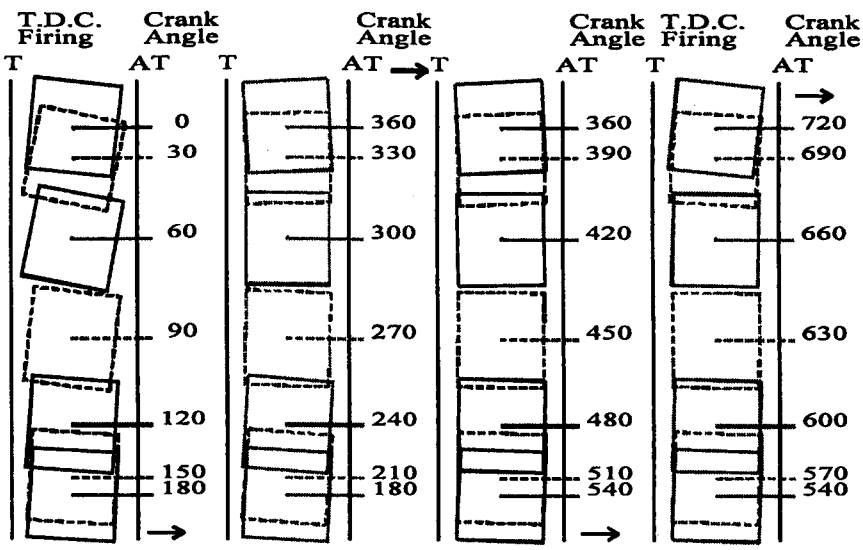

Figure 7.23. Predicted piston secondary motion at engine speed 2000rpm.

7.6 DIFFERENT LUBRICANTS AND PISTON ASSEMBLY FRICTION

Lubricant viscosity has a significant impact on the performance and economy of an engine. To investigate the effect of different lubricants on piston assembly friction, experiments were also carried out with SAE 5W30 a slightly more viscous lubricant than SAE 0W20, see Appendix II for lubricant properties. Due to the relatively high lubricant viscosity of SAE 5W30, the change in lubrication regime during the piston strokes at an engine speed of 800rpm can be clearly seen in figure 7.24 as compared to figure 7.6 for SAE 0W20 lubricant. With SAE 5W30 the reduction in shear loss at mid strokes and increase in friction near the end of piston strokes with increasing lubricant temperature, especially during down strokes is more prominent in figure 7.24.

The behaviour of both the lubricants at different engine speeds and lubricant temperatures is given in figure 7.25 for piston assembly friction power loss. At any engine speed it can be seen that as temperature increases the piston assembly friction for both the lubricants decreases but at 80°C for the SAE 0W20 the friction loss increases whereas for the SAE 5W30 relatively less friction loss is experienced. At low lubricant temperatures the frictional loss for SAE 0W20 was less than the more viscous lubricant SAE 5W30 as hydrodynamic lubrication was dominant. Whereas at 80°C lubricant inlet temperature the friction loss for lubricant SAE 0W20 sharply increased, indicating a change in lubrication regime and exceeding that of SAE 5W30. Thus the benefit of high viscosity lubricant, SAE 5W30 can be seen at higher lubricant temperatures, figure 7.25.

As the piston assembly exhibits boundary, mixed and hydrodynamic lubrication, perhaps there is an optimum viscosity at given operating conditions or lubricant temperature, which delivers minimum friction loss and maximum engine output, as higher and lower viscosities would increase overall frictional losses and decrease engine output.

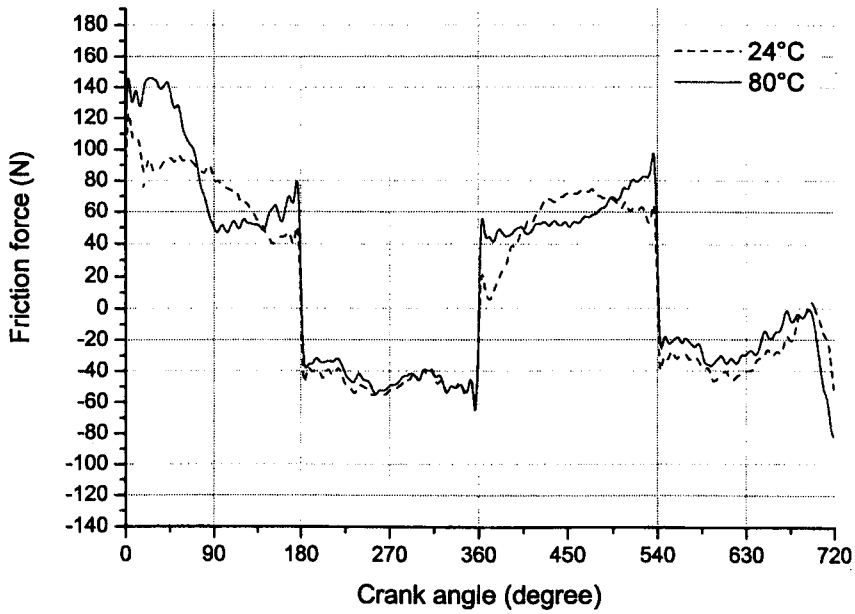

Figure 7.24. Piston assembly friction at engine speed 800rpm, lubricant SAE 5W30.

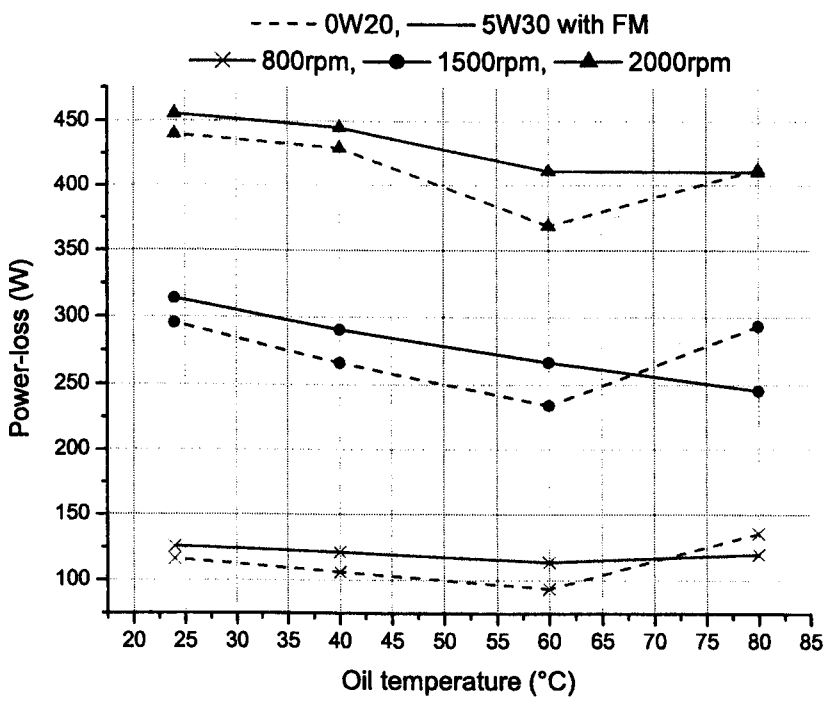

Figure 7.25. Comparison of piston assembly friction using SAE 0W20 with friction modifier and SAE 5W30 lubricants.

7.7 CONCLUSIONS

Instantaneous piston assembly friction measurement was carried out on a Ricardo Hydra single cylinder gasoline engine at different engine operating conditions using the IMEP method, which was found to be a powerful tool to monitor engine performance and lubricant evaluation. The IMEP method required almost no engine modification and thus gave a true picture of piston assembly friction, as the linkage does not affect engine operation or build. For accurate measurement of piston assembly friction, a number of transducer output offsets were needed to be addressed as any slight error from the transducer could have easily ruined the results. During the experiments it was revealed the lubricant viscosity had a significant effect on the piston assembly friction.

A slight error reading for the friction was seen at low lubricant temperature where the piston assembly friction results showed the opposite sign at the end of the compression stroke. This is due to the drift in pressure transducer calibration, which is sensitive to environmental temperature. Using a higher resolution pressure transducer can further reduce this pressure drift. The piston assembly friction measurement at high lubricant temperature showed the drift effect diminished to a great extent.

The average piston assembly friction under fired conditions was higher than under motored conditions mainly due to the effect of cylinder pressure and temperature. It was clear from the experimental results that the piston assembly friction was primarily in the mixed to boundary lubrication regime at high lubricant temperatures and more hydrodynamic at low temperatures. The measured piston assembly friction results followed the Stribeck curve at any engine speed.

The experimental results were also compared with predicted data obtained using the FLAME piston assembly friction model. It was concluded that the predicted results correlated very well with the measured data at all engine speeds and lubricant temperatures. The piston skirt friction was predicted using both a concentric piston/liner and the more realistic and complex method involving piston secondary motion. It was seen that the former over-predicted friction due to high shear loss whereas the results obtained by the latter method were better correlated to the measured results. The piston ring lubrication is boundary to mixed near dead centres and

hydrodynamic during mid strokes whereas piston skirt friction is mostly hydrodynamic throughout the stroke.

This experimental technique was also used to study the influence of two different lubricants SAE 5W30 and SAE 0W20 without a friction modifier, on piston assembly friction. The measured data showed the benefit of a high viscous lubricant on piston assembly friction at high temperatures whereas an opposite effect was seen at low lubricant temperatures. This experimental technique can therefore be used to screen different lubricants.

A very advanced data acquisition system was developed to perform piston assembly friction measurement using a high-speed simultaneous sampling data acquisition board. The details of the complete data acquisition system can be found it chapter eleven.

PART III

ENGINE BEARING FRICTION

Chapter eight

ENGINE BEARING FRICTION MODEL

8.1 INTRODUCTION

One of the major contributors to engine friction losses are the engine bearings. Any reduction in bearing friction losses will certainly increase fuel economy and engine efficiency. The third part of the engine friction model FLAME developed by Yang [1992] and later modified by Dickenson [2000], addresses the frictional losses generated from engine bearings and is described in this chapter.

The engine bearing friction model presents the lubrication and frictional analysis of both the big-end and main bearings. For calculating engine bearing friction it is important to determine the bearing loading at each crank angle. The first part of this chapter describes a simplified approach for calculating big-end and main bearing loading. The second part explains the lubrication analysis using Reynolds equation for a dynamically loaded journal bearing by the most widely used Short Bearing Mobility Method and the Finite Width Method. The third and final part of this chapter explains the analytical method of calculating power losses for dynamically and steady loaded journal bearings.

8.2 BIG-END AND MAIN BEARING LOADING

Both the big-end and main bearings of an automotive reciprocating engine are dynamically loaded journal bearings. To determine the bearing frictional losses it is vital to calculate the magnitude and direction of the bearing loading with respect to crank angle.

8.2.1 BIG-END BEARING LOADING

The loading experienced by the big-end bearing consists largely of three components,

(a) Gas force acting on the piston assembly.

(b) Reciprocating inertial force of the piston assembly and connecting rod upper part.
(c) Rotating inertial force associated with the rotating parts (connecting rod lower part).

The gas force acts on the piston crown in the direction of the cylinder axis and can be calculated as the product of combustion chamber gas pressure and the averaged cylinder bore area, as explained in chapter six. The reciprocating inertial force can be determined by considering the connecting rod as a two point mass system. Thus the reciprocating mass consists of the mass of piston assembly and one-third mass of the connecting rod and is located at the small-end bearing. The remaining two-third part of the connecting rod mass is assumed to be on the crank and is fixed at the big-end bearing, resulting in rotational inertial force.

The gas force acting on the piston surface due to combustion chamber pressure can be calculated as,

$$F_G = \frac{\pi}{4} pD^2 \qquad 8.1$$

Where, p = pressure and D = bore averaged diameter.

The acceleration of the reciprocating part 'a_a' is given by differentiating equation 6.9,

$$a_a = \frac{d^2}{dt^2} S = -R_a.\omega^2.\left(\cos(\theta) + \frac{\lambda.\cos(2\theta) + \lambda^3 \sin^4(\theta)}{\sqrt{\left(1-\lambda^2.\sin^2(\theta)\right)^3}} \right)$$

where λ = crank length/connecting rod length and R_a = crank radius.

The reciprocating inertial force can thus be expressed as,

$$F_{rec} = \left(m_p + \frac{1}{3} m_c \right) a_a \qquad 8.2$$

Also the rotating inertial force is given by,

$$F_{rot} = \frac{2}{3} m_c R_a \omega^2 \qquad 8.3$$

As m_c = connecting rod mass and m_p = piston assembly mass.

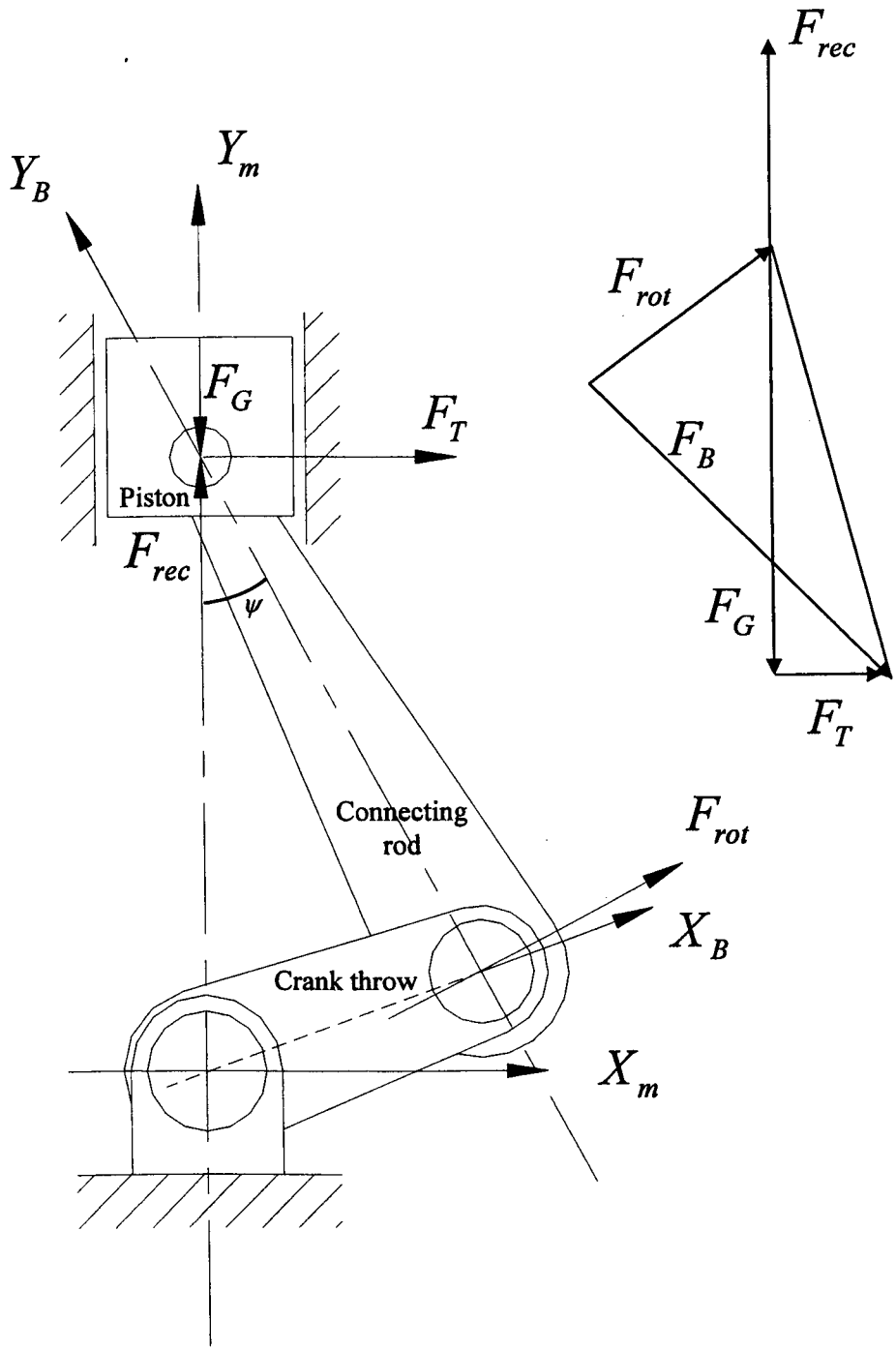

Figure 8.1. Forces acting on big-end bearing.

Using the connecting rod two-point mass system, the side thrust force due to the obliquity of the connecting rod acting through the piston normal to the cylinder liner can be calculated according to figure 8.1 as,

$$F_T = (F_G + F_{rec})\tan(\dot{\psi}) \qquad 8.4$$

where ψ = angle between connecting rod axis and cylinder liner axis.

The resultant of the vector sum of F_{rec}, F_G, F_T, and F_{rot}, forces figure 8.1, provides the instantaneous load on the big-end bearing 'F_B' at any particular crank angle. In this analysis all the forces are drawn relative to the axes fixed to the connecting rod centre line.

8.2.2 MAIN BEARING LOADING

The big-end bearing loads are relatively simple to calculate whereas the main bearing loading is slightly complicated as it consists of the force partly from the reaction of the big-end bearing loading F_B and partly from the out-of-balance forces of the crankshaft (crank webs + crank pin). This is an indeterminate problem because both the crankshaft and crankcase have finite stiffness and the interactions of big-end bearings loading and crankshaft out-of-balance forces make the calculations very complex. Thus for a multi-cylinder engine a simplified determinate system is used in which the crankshaft and crankcase is considered rigid and the crankshaft is treated as if it were pin jointed at the axial mid-position of each main bearing. Under such determined system it is assumed that the reaction forces from the big-end bearing and the crank webs + crank pin are carried by the adjacent main bearings. Fortunately, for the validation of the engine bearing friction model the experiments are carried out on a single cylinder gasoline engine having only two main bearings.

For the calculation of the main bearing loading the big-end bearing and the crankshaft out-of-balance forces are resolved into two components that is acting along and perpendicular to the cylinder axis. Figure 8.2 shows the load evaluation process for the forces along the x-axis for a multi-cylinder and single cylinder engine, and a similar method can be used for loads along the y-axis.

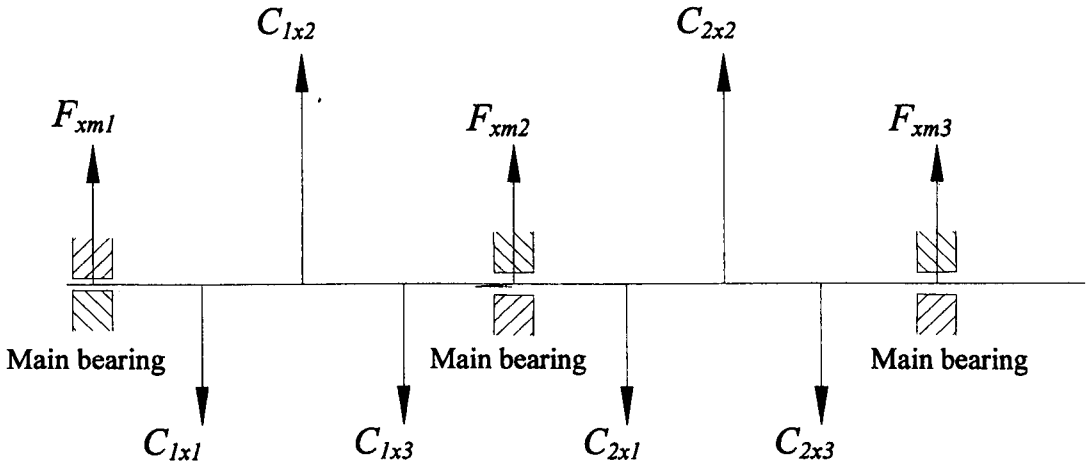

=

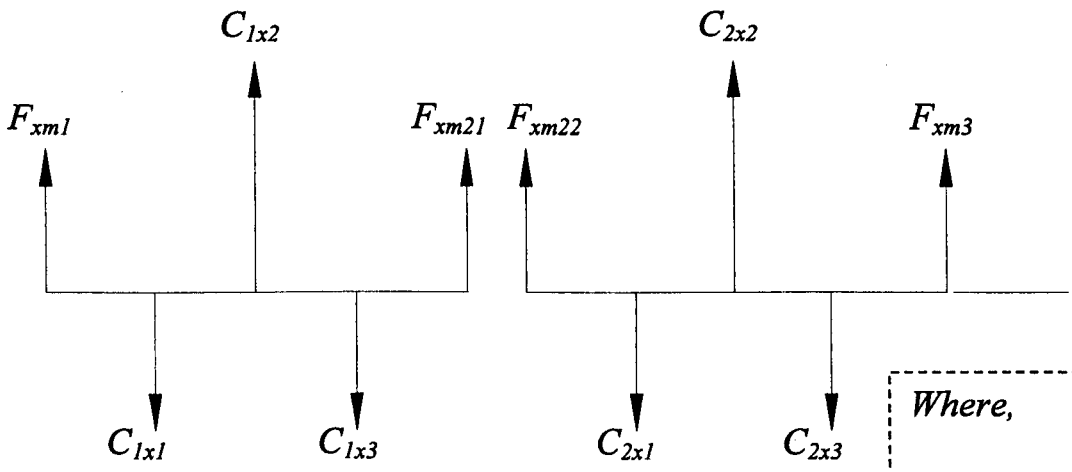

Where,

$F_{xm1} = F_{xm1}$

$F_{xm2} = F_{xm21} + F_{xm22}$

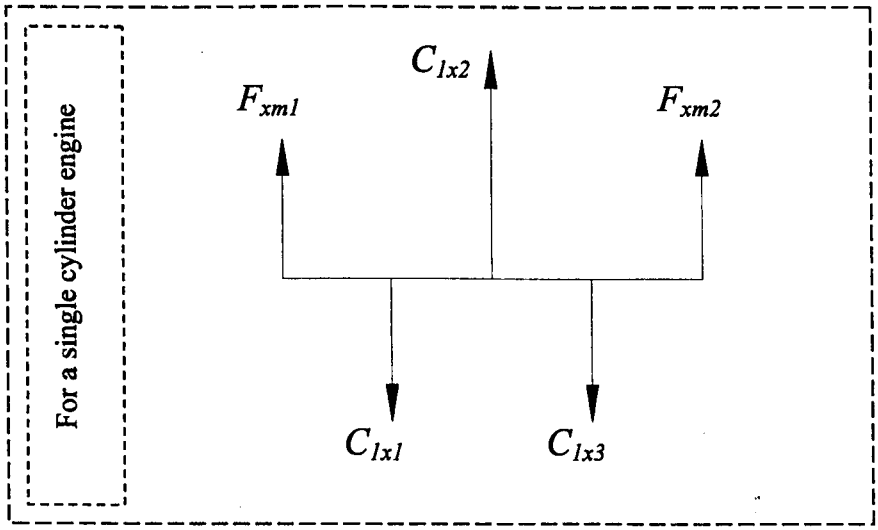

Figure 8.2. Main bearing loading evaluation process

8.3 REYNOLDS EQUATION FOR BEARING ANALYSIS

The fluid film bearing equation for pressure distribution was derived by Osborne Reynolds and is well known as Reynolds equation. The complete three-dimensional Reynolds equation with its assumptions is explained in chapter 5, equation 5.30 and is given by,

$$\frac{\partial}{\partial x}\left(h^3\frac{\partial p}{\partial x}\right)+\frac{\partial}{\partial y}\left(h^3\frac{\partial p}{\partial y}\right)=6\eta\left\{\frac{\partial}{\partial x}(U_1+U_2)h+\frac{\partial}{\partial x}(V_1+V_2)h+2(w_h-w_o)\right\}$$

For a bearing lubrication application, U_1 and U_2 are the surface velocities. V_1 and V_2 are the transverse velocities along the bearing centre, and are assumed to be zero for this application, as the bearing and shaft do not move in the horizontal direction along the bearing centre line. Furthermore (w_h-w_o) can be expressed as *dh/dt* as this is allowable if the bearing surfaces are impermeable so no fluid seeps in or out.

Thus Reynolds equation for crankshaft bearing reduces to,

$$\frac{\partial}{\partial x}\left(h^3\frac{\partial p}{\partial x}x\right)+\frac{\partial}{\partial y}\left(h^3\frac{\partial p}{\partial y}\right)=6\left(U\frac{dh}{dx}+2\frac{dh}{dt}\right) \qquad 8.5$$

Where, $U=U_1+U_2$,

From figure 8.3, the film thickness at any angle from the point of maximum film thickness can be calculated as (Taylor [1993]),

$$h=c+e.\cos(\alpha) \qquad 8.6$$

where,

$\varepsilon=\frac{e}{c}$, known as the eccentricity ratio. 8.7

Also

$$x=r\alpha \qquad 8.8$$

Thus introducing equation 8.6, 8.7 and 8.8 in equation 8.5, the simplified form is given by,

$$\frac{\partial}{\partial\alpha}\left[(1+\varepsilon\cos(\alpha))^3\frac{\partial p}{\partial\alpha}\right]+r^2\frac{\partial}{\partial y}\left[(1+\varepsilon\cos(\alpha))^3\frac{\partial p}{\partial y}\right]$$
$$=12\eta\left(\frac{r}{c}\right)^2\left[\dot{\varepsilon}\cos(\alpha)+\varepsilon\sin(\alpha)\left(\dot{\phi}-\frac{w_b+w_j}{2}\right)\right] \qquad 8.9$$

As,

$$\frac{\partial h}{\partial x}=\frac{-c\varepsilon}{r}\sin(\alpha)$$

and

$$\frac{\partial h}{\partial t}=\dot{e}\cos(\alpha)-e\frac{\partial\alpha}{\partial t}\sin(\alpha)=\dot{e}\cos(\alpha)-e\dot{\phi}\sin(\alpha)$$

The complete solution to the above equation is very complex and requires considerable numerical effort. Satisfactory analytical solutions exist like Ocvirk (short bearing solution) Sommerfeld (long bearing solution) and Goenka (finite width method) explained in much detail by Booker [1965].

The Sommerfeld solution assumes that the second term in equation 8.9 is negligible as it assumes that if the bearing is long in the axial direction then the variation of pressure in circumferential direction is much more significant than that in the axial direction, therefore the second term is dominant and the first term is discarded. The Short Bearing Solution assumes that the first term in equation 8.9 is negligible as it assumes that if the bearing is short in the axial direction then the variation of pressure in this direction is much more significant than that in the circumferential direction. This method is fairly accurate for bearings of width to diameter ratios of less than 0.7, operating at moderate eccentricity rations less than 0.6. Short bearing solutions become inaccurate at high eccentricity ratios. Besides this, it is a good method because of the simplicity of the approximated Reynolds equation and its solution, equation 8.10. This method was therefore used in this analysis.

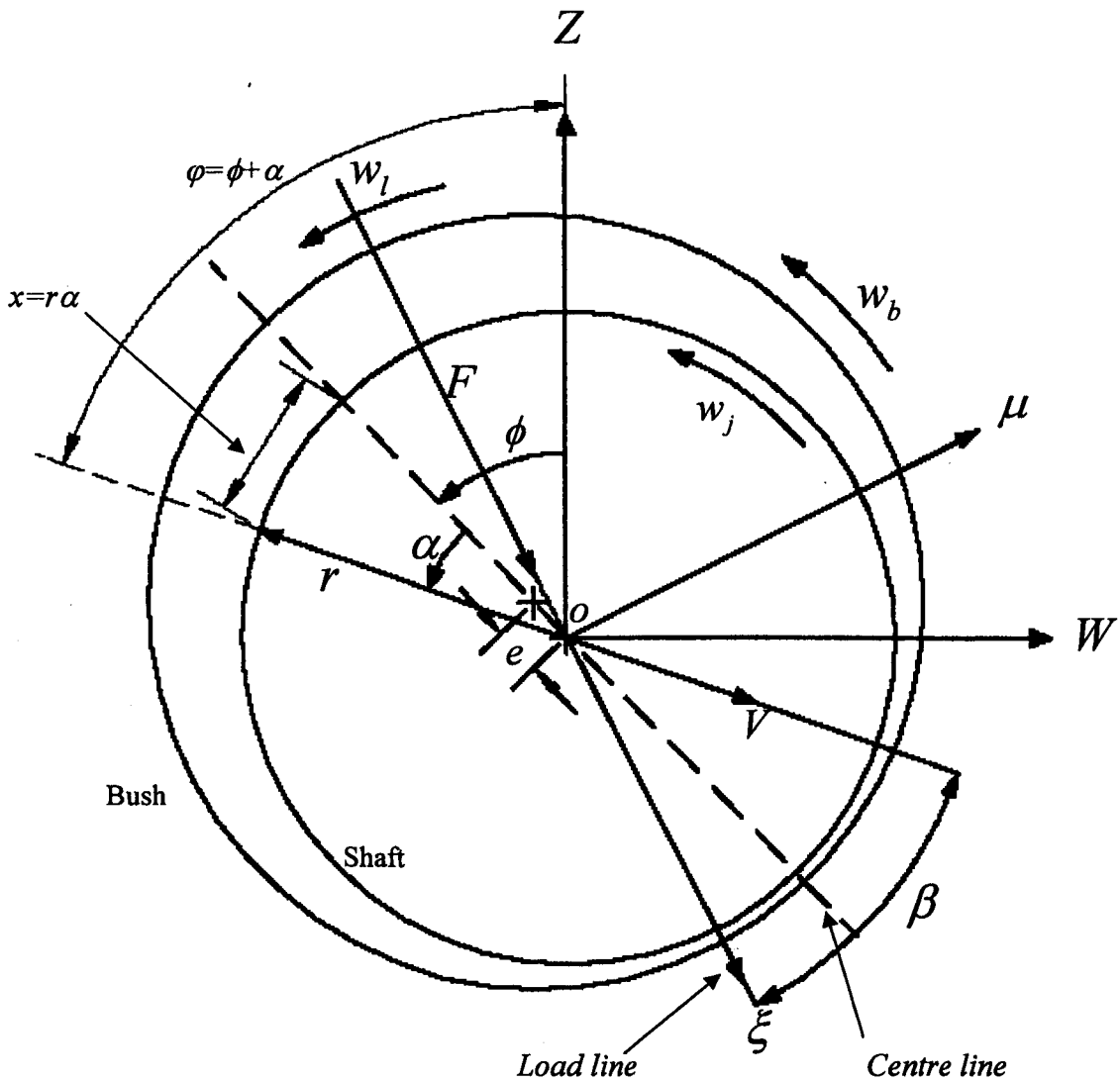

Figure 8.3. Journal bearing geometry and co-ordinate system

$$r^2 \frac{\partial}{\partial y}\left[\left(1+\varepsilon\cos(\alpha)\right)^3 \frac{\partial p}{\partial y}\right] = 12\eta\left(\frac{r}{c}\right)^2\left[\dot{\varepsilon}\cos(\alpha)+\varepsilon\sin(\alpha)\left(\dot{\phi}-\frac{w_b+w_j}{2}\right)\right] \qquad 8.10$$

Thus ignoring the first term on the left-hand side, the equation 8.10 can be solved by integrating twice and using the boundary condition that the pressure at the outer edges of the bearing is ambient on both sides,

$$p=0 \quad at \quad y=\pm\frac{b}{2}$$

Where 'b' is the width of the bearing.

Thus pressure distribution can be expressed as,

$$p=-\frac{6\eta}{c^2}\left[\frac{b^2}{4}-y^2\right]\frac{\dot{\varepsilon}\cos(\alpha)+\varepsilon\left(\dot{\phi}-\bar{w}\right)\sin(\alpha)}{\left(1+\varepsilon\cos(\alpha)\right)^3} \qquad 8.11$$

where,

$\bar{w}=\frac{w_b+w_j}{2}$, is the mean angular velocity of the journal and the bush.

If $\dot{\varepsilon}$ and $\dot{\phi}$ are all zero, that is under steady loading, then the above equation becomes,

$$p=-\frac{6\eta}{c^2}\left[\frac{b^2}{4}-y^2\right]\frac{\varepsilon\bar{w}\sin(\alpha)}{\left(1+\varepsilon\cos(\alpha)\right)^3} \qquad 8.12$$

The force applied to the lubricant film by the journal can be resolved into two components, that is parallel and perpendicular to the line passing through the centre of the journal and the bush.

Thus,

$$F^{\varepsilon} = F\cos(\phi) = \int_A p\cos(\alpha)dA$$
$$F^{\phi} = F\sin(\phi) = \int_A p\sin(\alpha)dA \qquad 8.13$$

where F = bearing load

This integration can be carried out over the entire bearing for a totally flooded bearing or over the positive portion of the pressure distribution for a cavitated bearing.

The force components for a 2π fully flooded bearing, where the limits of integration are 0 and 2π, can be calculated as,

$$F^{\varepsilon} = -\int_{\alpha_1}^{\alpha_2}\int_{-\frac{b}{2}}^{\frac{b}{2}} p.r.\cos(\alpha).dy.d\alpha$$
$$F^{\phi} = -\int_{\alpha_1}^{\alpha_2}\int_{-\frac{b}{2}}^{\frac{b}{2}} p.r.\sin(\alpha).dy.d\alpha \qquad 8.14$$

Therefore,

$$F^{\varepsilon} = \frac{\eta r b^3}{c^3}\int_0^{2\pi}\left[\frac{\dot{e}\cos^2(\alpha)}{(1+\varepsilon\cos(\alpha))^3} + \frac{e\sin(\alpha)\cos(\alpha)}{(1+\varepsilon\cos(\alpha))^3}\left(\dot{\phi}-\overline{w}\right)\right]d\alpha$$
$$F^{\phi} = \frac{\eta r b^3}{c^3}\int_0^{2\pi}\left[\frac{\dot{e}\sin(\alpha)\cos(\alpha)}{(1+\varepsilon\cos(\alpha))^3} + \frac{e\sin^2(\alpha)}{(1+\varepsilon\cos(\alpha))^3}\left(\dot{\phi}-\overline{w}\right)\right]d\alpha \qquad 8.15$$

Using the Booker's table of the journal bearing integration Booker [1965], the above equations can be expressed as,

$$F^{\varepsilon} = \frac{\eta r b^3}{c^3}\left[\frac{\pi\left(1+2\varepsilon^2\right)}{\left(1-\varepsilon^2\right)^{\frac{5}{2}}}\right]\dot{e}$$
$$F^{\phi} = \frac{\eta r b^3}{c^3}\left[\frac{\pi\varepsilon}{\left(1-\varepsilon^2\right)^{\frac{3}{2}}}\right]\left(\overline{w}-\dot{\phi}\right) \qquad 8.16$$

8.4 EQUATION OF MOTION

As $F=F^{\varepsilon}+F^{\phi}$, substituting the values of F^{ε} and F^{ϕ} equation 8.16, in equation 8.13 and rearranging, results in the components of journal centre velocity along and normal to the line of centres,

$$\dot{\varepsilon} = \frac{\dot{e}}{c} = \frac{F\left(\frac{c}{r}\right)^2}{\eta b d} M^{\varepsilon}$$

$$\varepsilon\left(\dot{\phi} - \overline{w}\right) = \frac{F\left(\frac{c}{r}\right)^2}{\eta b d} M^{\phi} \qquad 8.17$$

Where M^{ε} and M^{ϕ} are mobilities, defined as,

$$M^{\varepsilon} = \frac{\left(1-\varepsilon^2\right)^{\frac{5}{2}} \cos(\phi)}{2\pi\left(1+2\varepsilon^2\right)\left(\frac{b}{d}\right)^2}$$

$$M^{\phi} = \frac{-\left(1-\varepsilon^2\right)^{\frac{3}{2}}}{2\pi\left(\frac{b}{d}\right)^2} \sin(\phi) \qquad 8.18$$

The mobilities are dimensionless ratios of velocity to force and vary as to whether a cavitating or non-cavitating film is used. The above mobilities are for the non-cavitation film solution.

Direct integration of the equation of motion 8.17, is impossible and numerical solutions are rather complicated and time consuming. Booker [1965] developed a Mobility Method for dynamically loaded journal bearings to determine the vector sum of $\dot{\varepsilon}$ and $\varepsilon\left(\dot{\phi} - \overline{w}\right)$ representing the magnitude and direction of motion of the shaft centre. It is quick to produce a good representation of bearing behaviour and may be applied to bearings of different width to diameter rations with the use of different curve fits. The detail can be found in Booker [1965].

A similar solution is used to obtain solutions for the cavitation condition, except that the limits of film for the integration in equation 8.15, will be for the positive pressure region over a distance of π radians, between α_1 and α_2 (Yang [1992]) such that,

$$\dot{e}.\cos(\alpha_1)+e.(\dot{\phi}-\overline{w}).\sin(\alpha_1)=0$$
$$\dot{e}.\sin(\alpha_1)-e.(\dot{\phi}-\overline{w}).\cos(\alpha_1)\geq 0$$
$$\alpha_2=\alpha_1+\pi$$

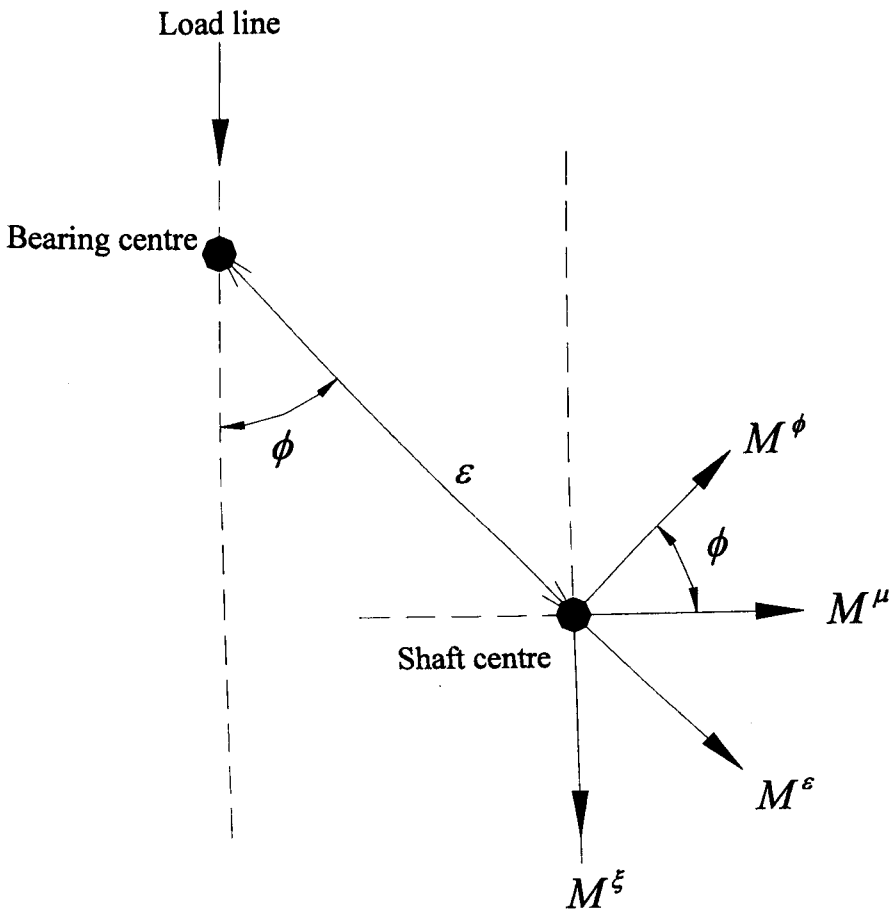

Figure 8.4, Mobility according to the frame of reference along line of centres and load line

Using curve fits, Booker [1965] also derived approximate expressions for mobility components in load frame of axes ξ and μ figure 8.4, as,

$$M^{\xi} = \frac{(1-\xi)^{\frac{5}{2}}}{\pi\left(\frac{b}{d}\right)^2}$$

$$M^{\mu} = \frac{-4\mu(1-\xi)^{\frac{3}{2}}}{\pi^2\left(\frac{b}{d}\right)^2} \quad . \qquad 8.19$$

It should be noted that the Short Bearing Mobility Method is subjected to all the assumptions applied to its own derivations (neither elastic nor thermal distortion is considered for either the shaft or the bush and the shaft is well aligned with the bearing).

The curve fits applied by Booker[1965] are based on the Short Journal Bearing approximation. In a similar manner, Goenka [1984], presented some curve fits generated by applying the Finite Width Bearing approximation which takes into consideration the lubricant pressure flow in both axial and circumferential directions. These curve fits have been developed for the case of an ideal bearing having no lubricant feed holes or geometric irregularities. Dickenson [2000], introduced Goenka's mobility components in the FLAME model allowing bearing friction analysis based on the finite width approximation to be carried out, giving choice to the user and allowing direct comparison with the results obtained by the Short Journal Bearing approximation. The finite width bearing curve fit equations for the mobility components are as follows,

$$M_x = \frac{f(\alpha,\gamma)}{\pi}\left[\sqrt{3\pi} - 0.24\gamma^2 . e^{-(\alpha+y^2)} + \frac{y^2}{1-\alpha}\left(1-0.4\sqrt{1-\alpha}\right) + \alpha^2\gamma\left[\frac{4}{3}-\gamma\right]\right]$$

$$M_y = \frac{y}{(1-\alpha)} f(\alpha,\gamma)\left[\begin{array}{l} \frac{5}{4}+\frac{1}{7}\alpha y+\frac{1}{8}\alpha^2(1+\alpha)-0.3\gamma^2\left[1+\frac{1}{2\sqrt{3}}\alpha^3\right]+\frac{2}{15}\frac{y^2}{1-\alpha} \\ -0.016\left[1-\frac{0.034}{\gamma^2}\right]\left[\frac{1}{1.03-\alpha}\right] \end{array}\right]$$

For the above expressions,

α = eccentricity in the x-direction

y = eccentricity in the y-direction

γ = bearing ration (L/D)

$$f(\alpha,\gamma)=\frac{(1-\alpha)^{5/2}}{\pi\gamma^2}\left[1+\frac{1}{2}\frac{\gamma^2}{(1-\alpha)}\right]$$

The details of the above equation can be found in Dickenson [2000].

8.5 BEARING POWER LOSS EQUATION

Martin [1985], presented the bearing friction power loss equations based on figure 8.3. These power loss equations predict instantaneous losses at a single crank angle condition. Considering only the shear effects, the power loss can be determined as,

$$H=\frac{\eta r^3 b}{c}J_1^{00}\left(w_j-w_b\right)^2 \qquad 8.20$$

Where 'J_1^{00}' is a journal bearing integral and can be found in Booker's table of journal bearing integrals, Booker [1965].

For a complete '2π' film extents,

$$J_1^{00}=\frac{2\pi}{\sqrt{1-\varepsilon^2}} \qquad 8.21$$

Whereas for 'π' film extent, 'J_1^{00}' value will depend on the film extent relative to minimum film thickness position.

For a 'π' film extending from h_{min} to h_{max} position (figure 8.5),

$$J_1^{00}=\frac{\pi}{\sqrt{1-\varepsilon^2}}$$

Also for the shaft staying concentric with the bush $\varepsilon=0$, the combined equation, 8.20 and 8.21 becomes,

$$H=2\pi\frac{\eta r^3 b}{c}\left(w_j-w_b\right)^2 \qquad 8.22$$

The above equation is known as the Petroff equation.

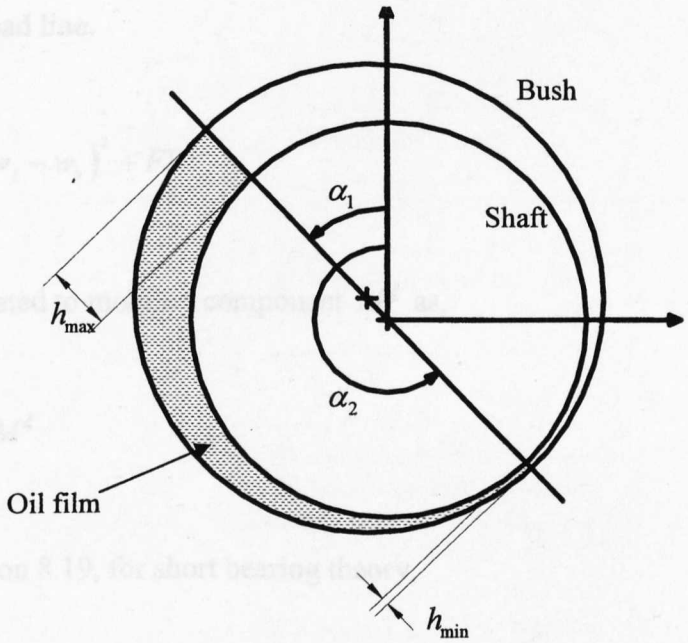

Figure 8.5, Cavitated bearing, π film.

Apart from the Shear loses the other two bearing power loss constituents are the pressure and translatory constituent, Martin [1985]. Thus the complete bearing power loss equation becomes,

$$H = \frac{\eta r^3 b}{c} J_1^{00} \left(w_j - w_b\right)^2 + \left(\frac{w_j + w_b}{2}\right) Fe \sin(\phi) + FV \cos(\beta) \qquad 8.23$$

In the above equation the first two terms are related to power loss due to the rotation of the journal and the bush and are know as shear and pressure terms respectively. The last term represents the contribution from the relative movement of the journal and bush centres and is know as the translatory term.

By adopting an appropriate frame of reference, equation 8.23 can be further simplified. Booker [1965] used a reference where the observer is rotating at an average film velocity of $\left(\frac{w_j + w_b}{2}\right)$. In this case, the second term of equation 8.23 disappears and

the last term becomes the product of bearing load and the apparent journal velocity parallel to the load line.

$$H = \frac{\eta r^3 b}{c} J_1^{00} \left(w_j - w_b \right)^2 + F V^{\xi} \qquad 8.24$$

where V^{ξ} is related to mobility component M^{ξ} as,

$$V^{\xi} = \frac{F\left(\frac{c}{r}\right)^2 c}{\eta b d} M^{\xi} \qquad 8.25$$

and from equation 8.19, for short bearing theory,

$$M^{\xi} = \frac{(1-\xi)^{\frac{5}{2}}}{\pi \left(\frac{b}{d}\right)^2} \qquad 8.26$$

Thus from equation 8.24, bearing friction power loss can be calculated at any crank angle and also its average through a complete cycle.

8.6 DESCRIPTION OF THE BEARING FRICTION PROGRAM

Engine bearing friction analysis requires knowledge of combustion pressure to calculate bearing loading. The program reads the combustion pressure data at every 10° crank angle for an in-line engine. The bearing load is then calculated at every 10° interval of crankshaft rotation for the complete engine cycle. The bearing load calculation for the main bearing starts from the front end, at the valve-train drive part and progresses to the rear last bearing, the one closest to the engine flywheel side. The output of the big-end bearing loading are according to the frame of axes attached to the connecting rod centre whereas for the main bearing loading, it is related to the cylinder centre axes. Thus for bearing behaviour analysis, two frames of reference have been used in the computation.

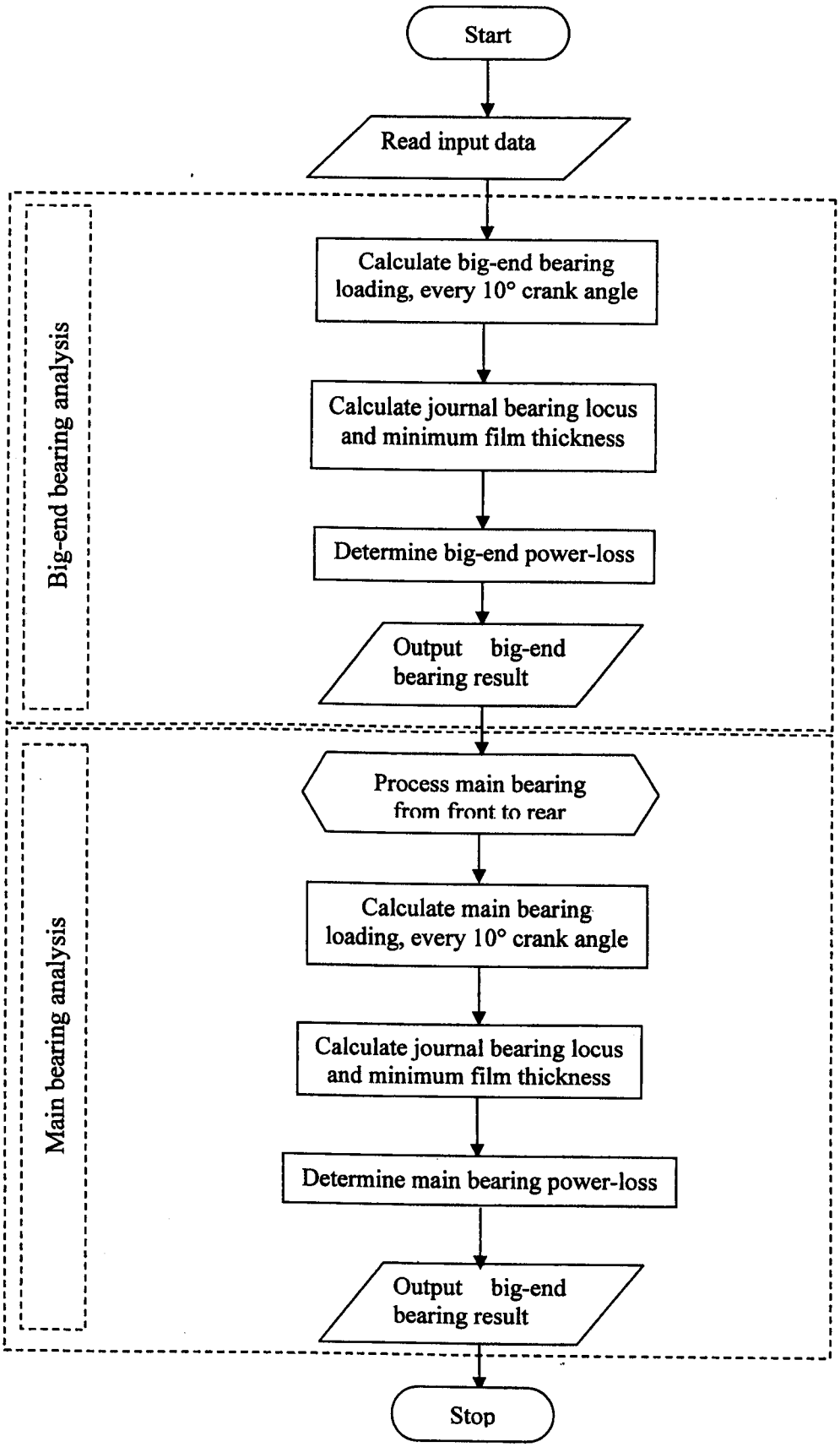

Figure 8.6, Computer program for engine bearing power-loss

The initial journal position chosen is at zero degrees of crankshaft rotation, which is the TDC position of cylinder number one. Mobility components in the load frame are then calculated and changed to give components in the computation frame. The computation frame has been fixed either to the connecting rod centre line for the big-end bearings or to the cylinder centre line for the main bearings. In the calculation of the journal centre velocities, the average angular velocity of journal and bush differs between the big-end bearing analysis and the main bearing analysis in their respective computational frame, Booker [1971].

For the big-end bearing,

$$\overline{w} = \frac{\omega}{2}\left(1 + \frac{R_a}{L}\cos(\theta)\right) \qquad 8.28$$

and for the main bearing,

$$\overline{w} = \frac{\omega}{2} \qquad 8.29$$

The initial value of the eccentricity ratio used is zero. The product of the journal centre velocity and the time interval will give the corresponding new eccentricity ratio for each step. If the journal orbit goes out of the clearance circle, the program will pull it back by halving the time interval.

The program outputs bearing friction power loss at every 10° of crankshaft rotation. The program calculates bearing losses for both π and 2π film extents. Figure 8.6 shows the bearing friction model flow chart.

8.7 SUMMARY

The complete engine bearing friction model has been described. A load evaluation for engine big-end bearing using connecting rod two point mass and for main bearing loading using a simple approach, that the crankcase is a statically determinate rigid beam, has been explained.

Reynolds equation is used for the lubrication of a dynamically loaded journal bearing and The Short Bearing Mobility Method and The Finite Width method is used for solving the equations. Methods for the calculation of both big-end and main bearing friction have also been described.

For the validation of the engine bearing friction model, experiments have been carried out on a single cylinder Ricardo Hydra gasoline engine. The predicted results have been generated for full film and ruptured film lubrication analysis using The Short Journal bearing approximation, finite width approximation and Petroff equation. The results are described in the following chapter.

Chapter nine

METHOD OF MEASURING ENGINE BEARING FRICTION WITH EXPERIMENTAL AND PREDICTED RESULTS

9.1 INTRODUCTION

No single method has been previously developed to measure engine-bearing friction under fired condition on a real firing engine. In this chapter a new method is described that allows evaluation of engine bearing friction under fired conditions on a single cylinder gasoline engine without any major engine modification.

Attempts have been made so far to calculate engine-bearing friction by measuring lubricant temperature and oil film thickness. Cerrato et al [1984] made an attempt to measure main bearing friction directly by instrumenting a single cylinder engine. Extensive engine modification was carried out. One of the two journal bearings was installed in the block by means of a composite ball and needle bearing. The bearing friction loss was measured through a load cell actuated by a reaction lever as shown in figure 9.1. The engine was also modified to measure piston assembly friction using the well-known floating liner method.

A number of experiments have also been performed to measure oil film thickness in a big-end bearing using total capacitance technique, Craig et al [1982], Choi [1992], [1993], Bates and Benwell [1988] and Filowitz et al [1982]. Bates et al [1986] and Spearot et al [1988] also measured oil film thickness by the total resistance method to investigate bearing performance. Suzuki et al [1995] and Choi et al [1993] measured minimum film thickness using the total capacitance method and compared the data with the predicted results. Choi et al [1995] carried out evaluation of friction in engine bearing from crankshaft temperature measurement. Thermocouples were fitted on the surface of the crankshaft to measure lubricant temperature at main bearing and big-end bearing of a four-cylinder gasoline engine and the friction coefficients were calculated from the measured temperatures by a heat equilibrium equation. The wires were drawn

to the front side of the crankshaft and connected to the signal-conditioning unit via slip rings.

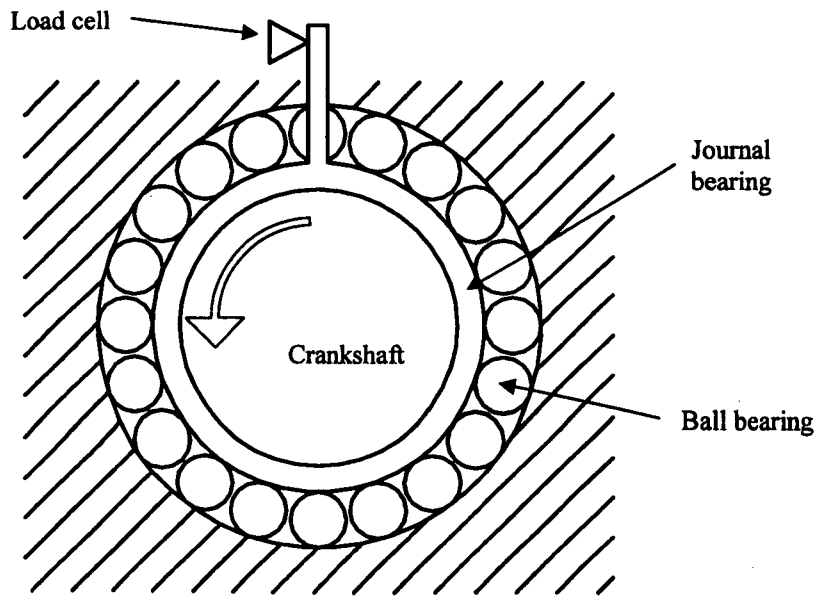

Figure 9.1. Instrumented main bearing for friction measurement, Cerrato et al [1984].

Cho et al [1999] measured the big-end bearing film thickness by using the total capacitance method and a scissor type linkage called a grasshopper linkage to bring the wiring out of the engine crankcase. Irani [1997] used capacitive measurement technique to measure hydrodynamic lubricating oil film thickness in the middle main bearing of a heavy-duty six-cylinder diesel engine. Measurement of oil film thickness as a function of the crank angle was carried out with a variation of the engine speed, load and oil temperature. Masuda [1992] measured the bearing film pressure distribution on a test rig using semiconductor type pressure transducers. The transducers were embedded into the crankshaft and the output signals were transmitted by means of slip rings. Schilowitz and Waters [1986] successfully measured the oil film thickness in the main bearing of an engine in an operating vehicle. Experiments were carried out during 0-65 mph vehicle acceleration on a test track. The oil film thickness was measured using the capacitance technique and film thickness of the order of 0.01-0.1 microns was recorded. Mihara [1995] successfully used a thin film pressure

sensor made of manganin to measure oil film pressure during engine operation. The sensor was formed directly on the sliding surface of a plain bearing.

Bates and Evans [1985] instrumented the big-end bearing of a gasoline engine in order to measure oil film thickness using capacitance probes, inserted in the bearing shell. Theoretical calculations of oil film thickness as a function of crankshaft angle was carried out to ensure that the probes were placed in the region of the absolute minimum film thickness.

Similarly Gulwadi et al [2003] carried out detail engine bearing analysis by instrumenting the main bearing of a single cylinder engine to measure inlet oil temperature and pressure, outlet temperature of the oil near the drain hole, oil flow rate and temperature at 32 different locations on the bearing surface, using eight circumferentially spaced thermocouples, at each of four axial positions.

Oil film measurements have been carried out by a number of engineers but not a single attempt has been made to measure total engine bearing friction in a real firing engine without any bearing housing modification. Thus in this chapter a very novel experimental technique has been described allowing engine bearing friction/power loss measurement to be carried out without major engine modification.

The first part of this chapter describes the method that allows total engine bearing friction losses evaluation and the instrumentation needed to perform such task. The experimental results are described in the second section whereas in the last part of this chapter, the experimental results are compared with the predicted results calculated by using the FLAME bearing friction model from Chapter eight.

9.2 EXPERIMENTAL METHOD OF ENGINE BEARING FRICTION MEASUREMENT

Experimental measurement of engine bearing friction was carried out on a single cylinder Ricardo Hydra gasoline engine, which has two main bearings and a big-end bearing. An external, electrically driven pump supplies lubricant to the crankshaft. In fact, all the auxiliaries of this engine are independently electrical driven. The advantage

of using a single cylinder engine is that the load sharing issue between main bearings is easily resolved with each bearing carrying half the load of the cylinder pressure and inertia.

The engine piston pin is not fixed to the connecting rod or the piston but remains in a floating state. As the friction losses generated by the small end bearing is negligible as compared to big-end and main bearings, the engine bearing friction is therefore mainly the sum of main bearings and big-end bearing friction. The engine bearing friction under fired conditions can be calculated as,

Bearing friction = total engine friction – piston assembly friction – valve train friction.

In order to measure engine-bearing friction under fired conditions and to validate the FLAME engine bearing friction model the following information was logged during the experiments,

- Camshaft friction torque, chapter 4.
- Piston assembly friction, chapter 6.
- Crankcase lubricant temperature.
- Big-end bearing housing temperature.
- Engine brake torque.
- Crankshaft angular position.
- Cylinder pressure via piezo-electric pressure transducer.
- Cylinder pressure pegging using liner absolute pressure transducer.

Apart from the first four parameters, the remainder is required to measure total engine friction loss.

9.3 TOTAL ENGINE FRICTION

The total engine friction loss in a fired engine can be measured by using the information of cylinder pressure and piston displacement thus generating a PV (pressure-volume) diagram, figure 9.2. In the PV diagram the large area 'A' figure 9.3,

represents the net positive work available from the compression and expansion strokes whereas the area 'B' figure 9.4, represents the net negative work expanded during the exhaust and intake strokes, also known as the pumping phase. The total engine friction losses can be derived from the indicated diagram and the engine brake torque measurement as,

Work to over come engine friction loss = Positive work – negative work – brake work

or

= indicated work – pumping work – brake work .

or

= Area 'A' – Area 'B' – Brake work.

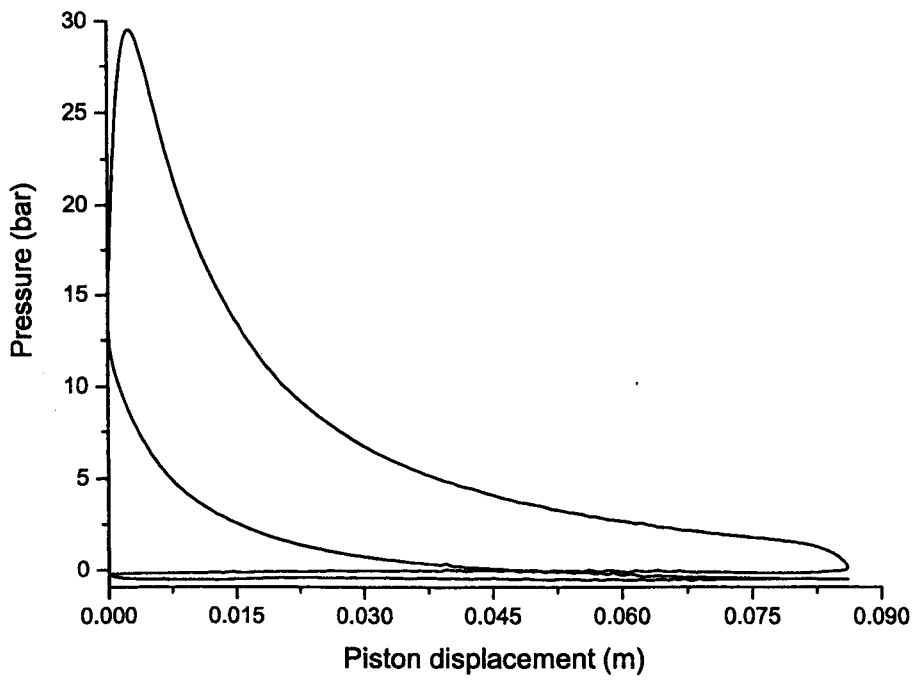

Figure 9.2. Engine PV diagram representing the indicated and pumping work.

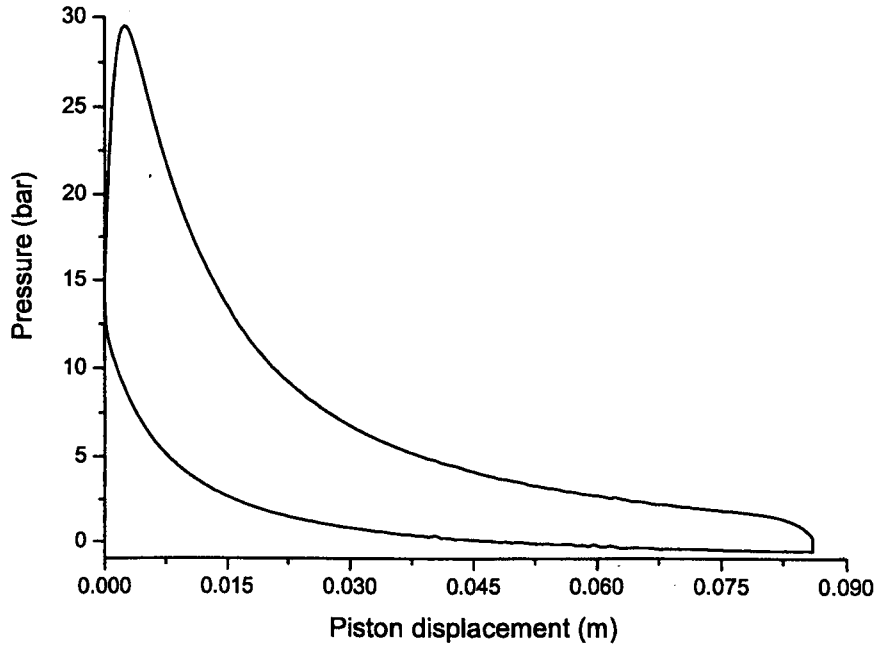

Figure 9.3. Area 'A' of PV diagram, representing the positive work.

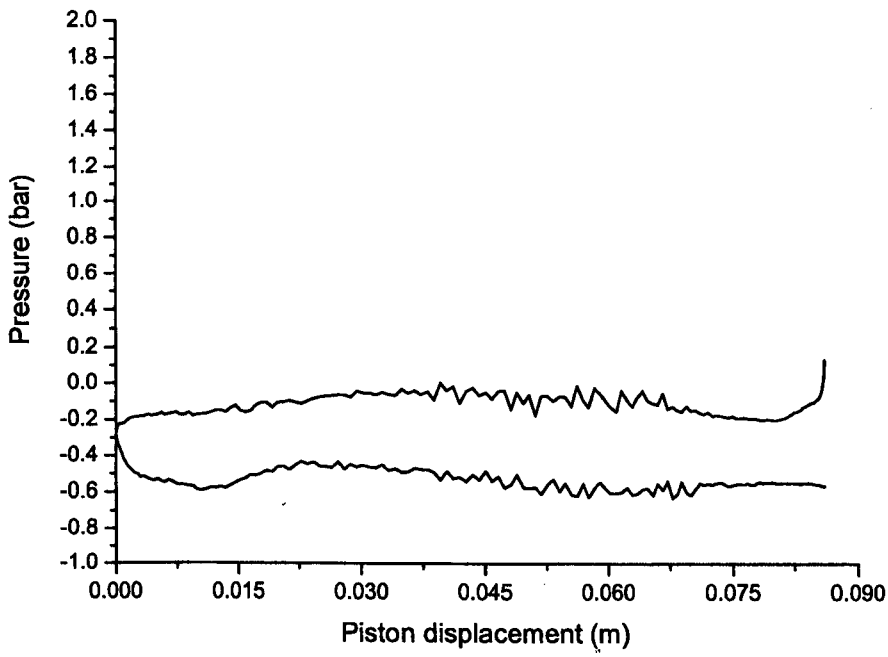

Figure 9.4. Area 'B' of PV diagram, representing the negative work.

The difference between the positive work and the negative work represents the net cylinder work. This is used to overcome friction and to do useful work. Thus the difference between the net cylinder work and the useful work in this case brake work is the friction loss.

The PV diagram is calculated by measuring cylinder pressure via a piezo-electric cylinder pressure transducer and liner absolute resistive pressure transducer. The piston displacement is determined via a 720 pulse per revolution optical encoder fitted to the crankshaft.

9.3.1 ENGINE BRAKE TORQUE

One of the main requirements to determine the total engine friction loss is to measure useful work, i.e. engine brake torque. The engine instantaneous and averaged brake torque is generated via an electrical dynamometer. The engine dynamometer has two torque arms fitted at each side. A load cell is fitted to the right torque arm that generated continuous electrical signal proportional to the applied engine brake torque.

9.3.1.1 DYNAMOMETER CALIBRATION

When measuring engine brake torque it is very important to calibrate the engine dynamometer before the experiments are carried out. The Ricardo Hydra engine dynamometer can both load and motor the engine and for calibration purposes a weight hanging arrangement is provided on each side of the dynamometer to calibrate torque in both clockwise and anti-clockwise directions. The dynamometer effective torque arm radius is fixed at 407.8 mm. To maximise accuracy and test repeatability the engine brake torque was calibrated at regular intervals. To calibrate the dynamometer the load cell electrical supply was switched on and one hour warming period was used. The main power supply to the dynamometer rotor/stator was kept switched off during calibration as at stop position or emergency stop operation, a regenerative braking is applied via the rotor/stator electrical magnetic field, which is used to arrest the engine and the dynamometer rotor rapidly. To prevent such braking during calibration it was thus important to switch off the main electrical supply. The calibration was carried out.

for both motored and fired conditions in 32 steps see figure 9.5, and for each step 300 data points were taken and averaged for greater accuracy. The weight was placed on the relevant hanger and load cell voltage was logged. At each reading, the dynamometer trunnion-bearing casing was tapped softly to alleviate effects causing undue hysteresis. The average of three measurements was calculated and thus the engine dynamometer load cell voltage output was related to the applied torque as ±0.2 volts/Nm.

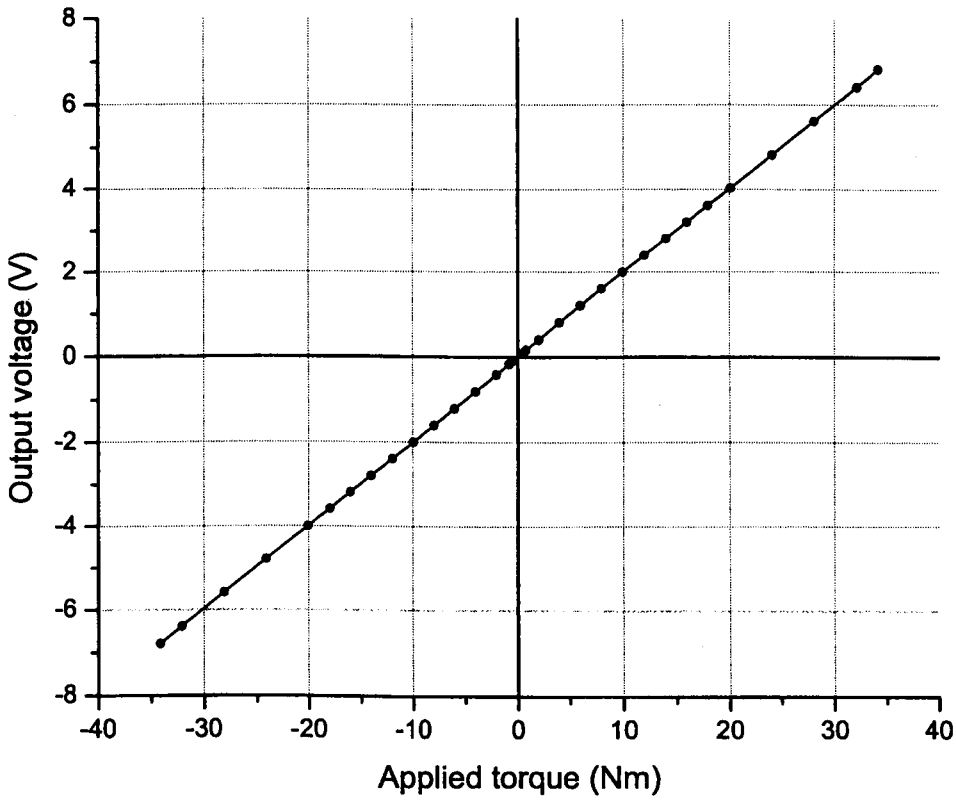

Figure 9.5. Engine brake torque calibration chart

9.3.2 CRANKCASE LUBRICANT TEMPERATURE

The inlet crankcase lubricant temperature was measured via a K-type thermocouple fitted at a location where the lubricant enters the engine block, and was assumed to be same as the main bearing lubricant temperature. Whereas for the big-end

bearing, the surface temperature of the big-end bearing upper bearing cup was measured via two thermistors and was assumed to be similar as the big-end bearing lubricant temperature.

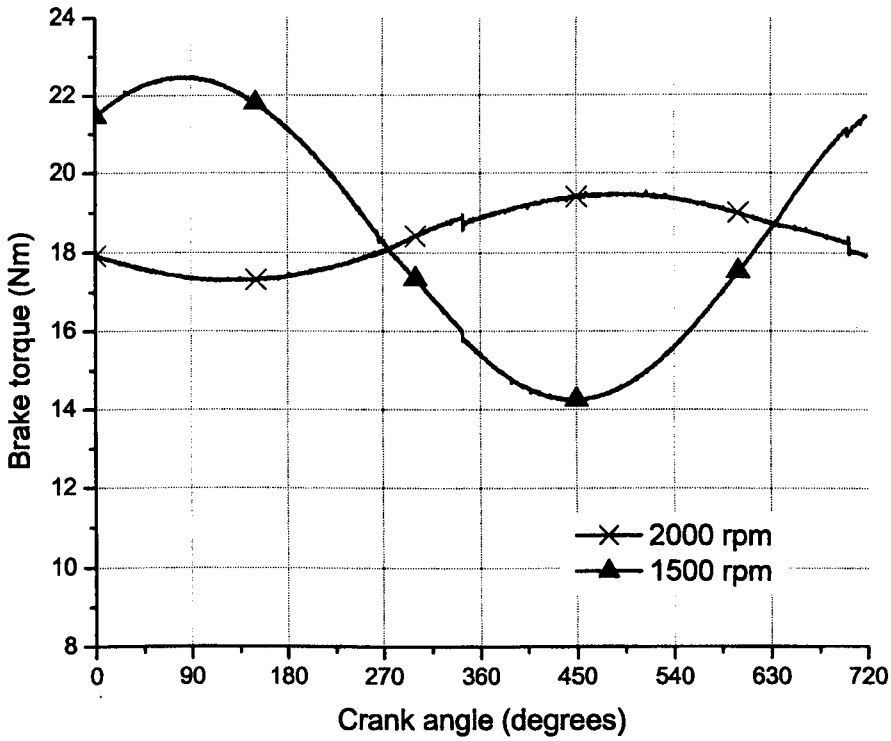

Figure 9.6. Instantaneous engine brake torque at engine speeds of 1500rpm and 2000rpm, ½ load.

9.3.3 POST PROCESSING

Instantaneous engine brake torque was measured at every half a degree crank angle (figure 9.6), and was averaged over the complete engine cycle. An average of 60-engine cycles was used.

Thus using the information of piston assembly friction (chapter seven), camshaft assembly friction (chapter four), engine brake torque and PV diagram the engine bearing friction power loss was calculated.

9.4 EXPERIMENTAL EVALUATION OF ENGINE BEARING FRICTION

The fired experiments on the Ricardo Hydra engine were carried out with crankcase inlet lubricant temperatures of 24°C, 40°C, 60°C and 80°C. The engine bearing friction was measured at engine speeds of 800rpm, 1500rpm and 2000rpm for each lubricant temperature. Two different lubricants were used: SAE 0W20 without friction modifier and SAE 5W30. Data characterising the lubricants is listed in Appendix II.

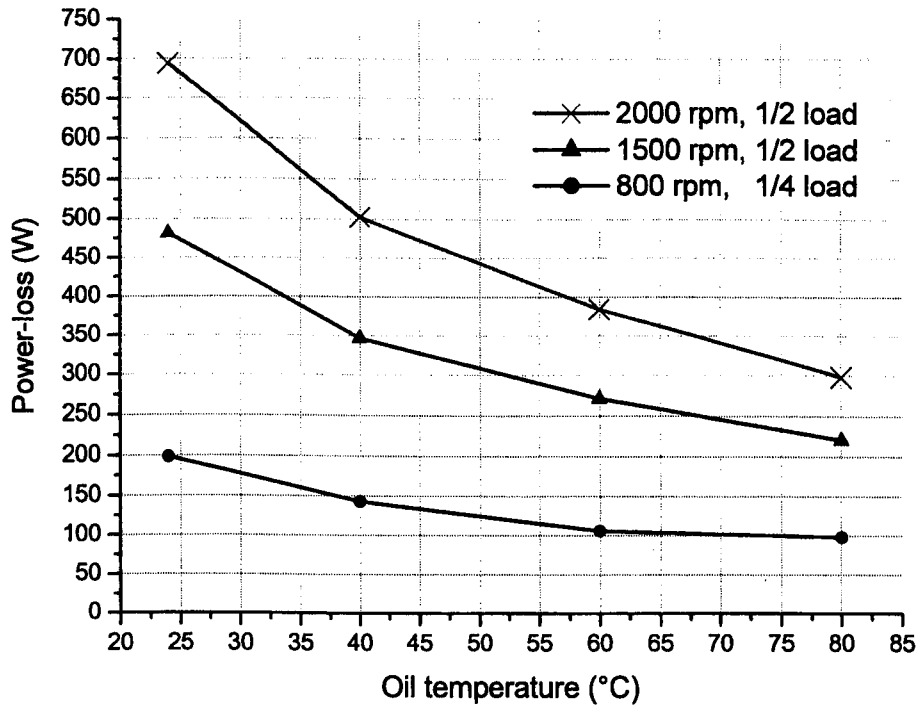

Figure 9.7. Bearing friction power loss, SAE 0W20 without friction modifier

During the experiments, the required crankcase inlet lubricant temperature was maintained and all the above information required to calculate bearing friction was logged for the complete engine speed range and oil temperature.

Figure 9.7 shows the experimental measurement of engine bearing friction loss for the lubricant SAE 0W20 without friction modifier, under fired conditions at different engine speeds. It can be seen that there is a decrease in engine bearing friction as the lubricant temperature increases at any given speed. This can be explained as the main and big-end bearings operate in the region of hydrodynamic lubrication and under hydrodynamic regime the bearing friction loss is directly proportional to lubricant viscosity and angular velocity and inversely proportional to film thickness. With increase in temperature, viscosity decreases and low viscosity lubricants generate lower hydrodynamic pressures compared to high viscous lubricants, resulting in decreased minimum film thickness. Also increase in the relative surface velocities of the bearing and shaft will increase the power loss caused by the increase in shear stress.

At a low engine speed of 800rpm, there is a gradual decrease in power loss with increase in temperature whereas a sharp decrease can be seen at higher engine speeds, 1500rpm and 2000rpm. One of the main reasons is that at 800rpm the engine load was ¼ load as compared to ½ load at higher speeds also at high entraining velocity the effect of decrease in oil temperature, significantly decreases shear loss.

9.5 PREDICTED ENGINE BEARING FRICTION LOSSES

Using the FLAME model, the predicted engine bearing friction power loss was calculated using two different approaches, the short bearing analysis and the finite width method. The FLAME engine bearing friction model input data file is given in Appendix I. Comparing the predicted results for both the methods, it can be seen that the results are very close at any engine speed and load figures 9.8 to 9.10 for both the conditions cavitation (π film) and fully flooded (2π film). The short bearing analysis neglects the circumferential flow due to pressure gradient and thus leads to a better load carrying capacity than the finite width method. Thus the minimum film thickness for the short bearing case is generally greater than the thickness predicted via the finite width analysis resulting in the friction losses calculated by the finite width bearing theory to be slightly larger than the short bearing analysis.

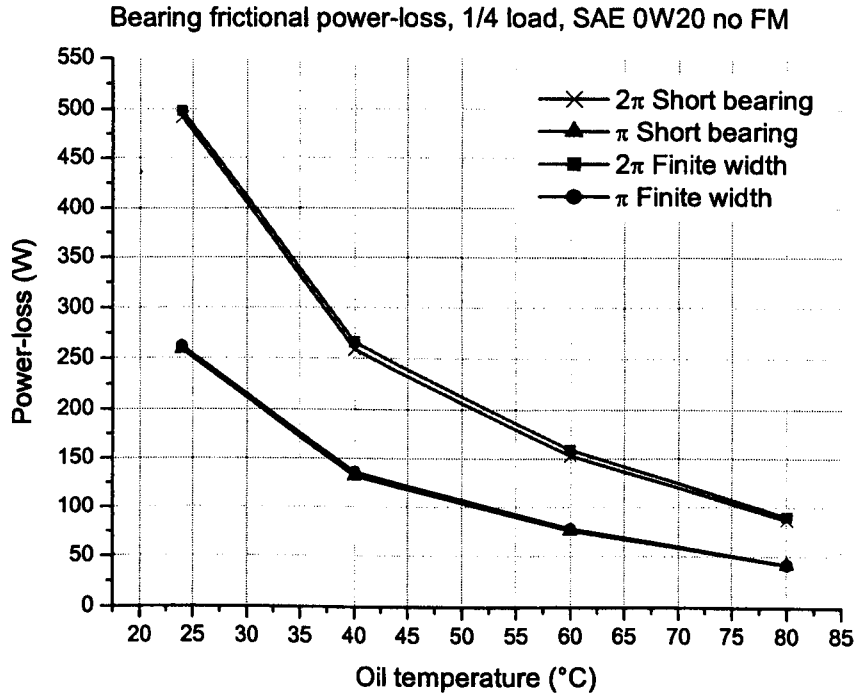

Figure 9.8. Short bearing analysis vs Finite width method, engine speed 800rpm.

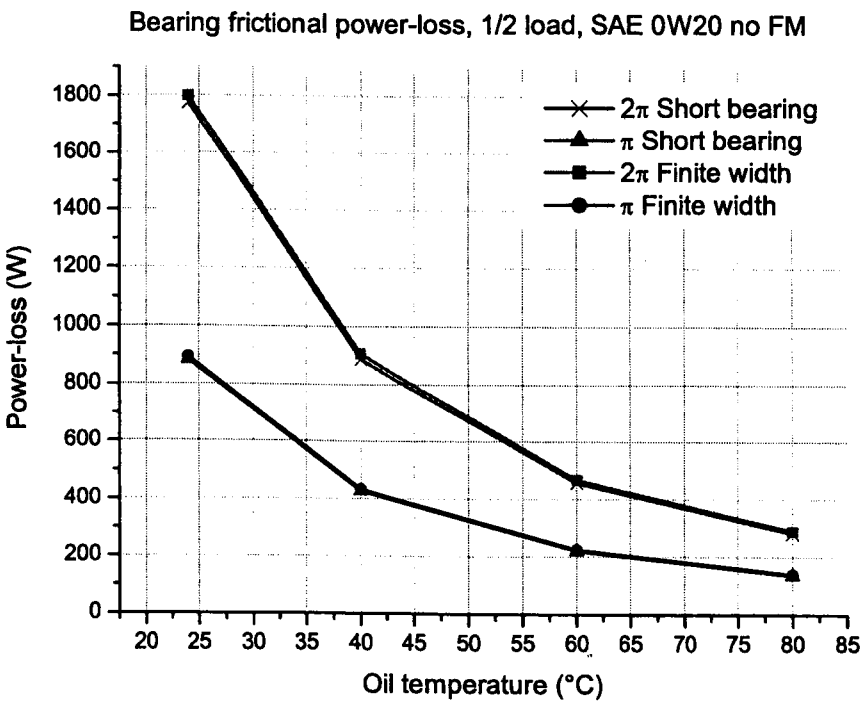

Figure 9.9. Short bearing analysis vs Finite width method, engine speed 1500rpm.

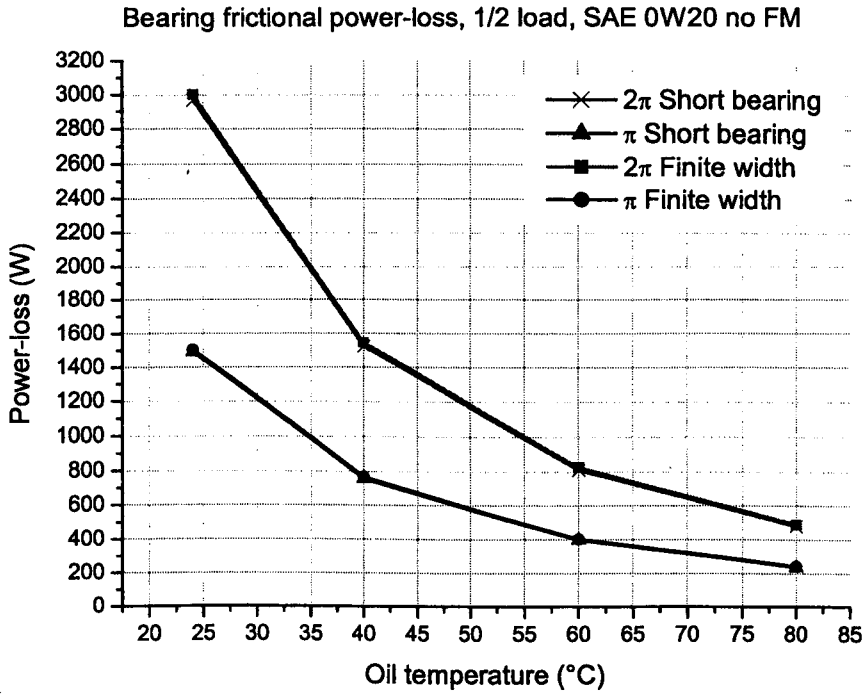

Figure 9.10. Short bearing analysis vs Finite width method, engine speed 2000rpm.

It is clear from the above figures that for the prediction obtained by one method or the other, the results are very similar but one would use the short bearing mobility method as the computational time is four times faster than that of the finite width method, Frene et al [1997]. Thus for the validation of the FLAME engine bearing friction model, the results obtained from the short bearing method have been studied in detail and compared with the measured figures.

9.6 COMPARISON BETWEEN PREDICTED AND MEASURED ENGINE BEARING FRICTION LOSS

The engine bearing friction power loss experimental results using an SAE 0W20 lubricant without friction modifier, were compared with the predicted results obtained for both the cases of lubricant film rupture condition (π film) and complete full film lubrication (2π film) condition, using the short bearing analysis. The predictions from

both the conditions will give us the lower and upper limit to power loss. In reality the actual bearing friction lies between these two conditions but more towards the cavitation conditions (π film). Bearing friction was also calculated using the classic Petroff equation, assuming zero bearing eccentricity and a full 2π lubricant film presence.

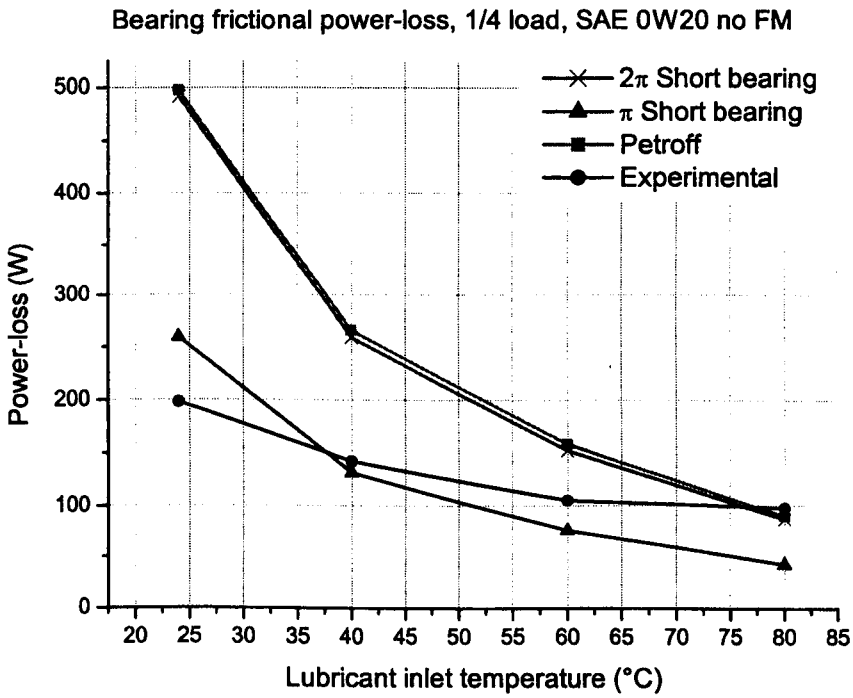

Figure 9.11. Comparison of measured and predicted bearing friction loss at 800rpm.

The engine bearing result for engine speed 800rpm, light load (¼ load) (figure 9.11), indicates that the measured bearing friction power loss lies mostly between the predicted power loss calculated for 'π' and '2π' film presence. As mentioned earlier, engine bearings operate more closely to cavitation conditions than fully flooded. This can be clearly seen in figure 9.11. At low lubricant inlet temperature 24°C, the predicted cavitation analysis result indicates higher power loss than the measured value. As the exact lubricant temperature in the engine bearing is not know and due to low viscosity and thus increased shear friction generating heat, the lubricant temperature will be higher than the inlet value, reducing the bearing power loss. Whereas at high

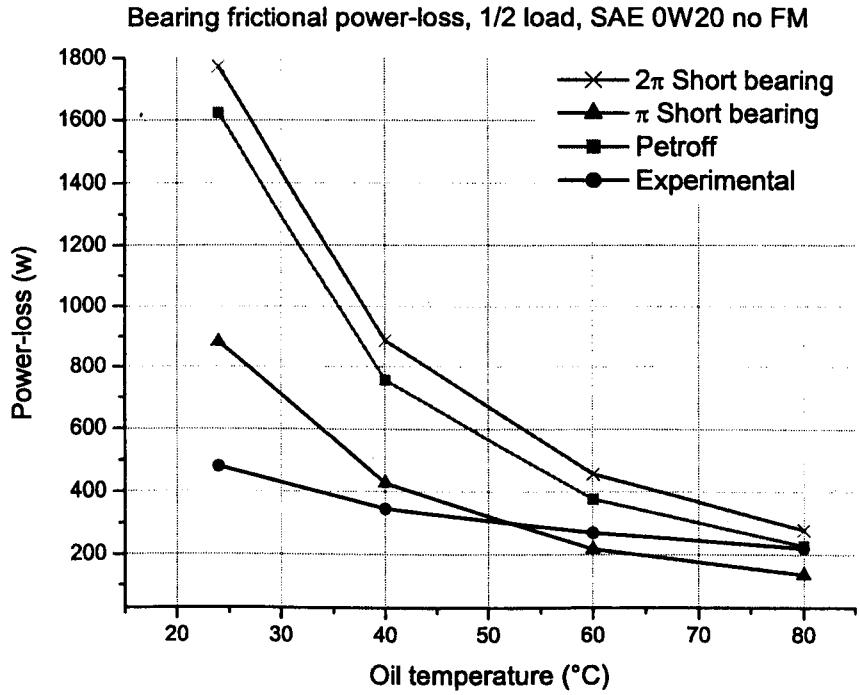

Figure 9.12. Comparison of measured and predicted bearing friction loss at 1500rpm

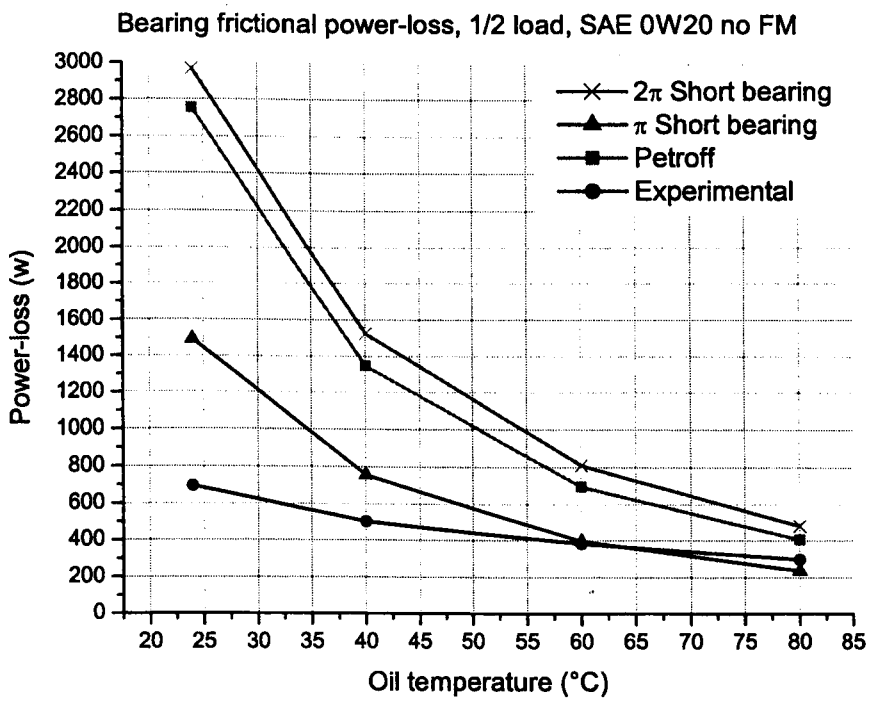

Figure 9.13. Comparison of measured and predicted bearing friction losses at 2000rpm

lubricant temperature there will be heat loss from the lubricant as it flows from the sump to the cold engine crankcase, thus reducing the lubricant viscosity and increasing shear losses at high lubricant inlet temperature. The other factor that may effect the results is the crankcase bearing seals used to prevent the leakage of lubricant form the crankcase, which are not taken into account in the predicted results.

Figures 9.12 and 9.13 show the comparison of predicted and measured bearing friction power loss at engine speeds 1500rpm and 2000rpm respectively. Overall it can be seen that the predicted results obtained by using the short bearing method for cavitation condition correlate very well with the measured results at high engine speed and lubricant temperatures.

Some factors have not been addressed in the predicted analysis, which could have some effect on the results, e.g. the use of the grasshopper linkage, resulting in an increase in bearing loading especially at the big-end bearing. Another reason is that while calculating engine bearing results it was assumed that the total engine mechanical friction loss comprises of piston assembly friction, valve train friction and bearing friction. The predicted results do not take into account camshaft belt loss, dynamometer trunnion bearing losses and small end bearing loses, which are assumed to be negligible as compared to engine bearing frictional losses.

The effects of surface elasticity deformation due to oil film pressure have not been considered although the effect is driven further by the trend of engines having to deliver higher output with lighter and smaller components. Another very important factor that is lacking in predicting bearing friction is the exact engine bearing radial clearance. Due to thermal and load distortion the bearing radial clearance changes, affecting the bearing power loss reading.

In figures 9.11 to 9.13 the measured bearing-power loss at lubricant temperature 80°C, is slightly higher than predicted using the ruptured film analysis, π film. One of the factors responsible for such variation is that the predicted analysis does not address boundary lubrication. Although journal bearings are expected to operate mostly in a hydrodynamic lubrication regime, engine loads and cylinder firing sequence can cause

journal misalignment that can cause contact with the bearing shell. Also the lubricant viscosity calculated for the predicted analysis was determined from a single value based on the measured lubricant inlet temperature which would be different from the true value as it does not account for an increase in temperature due to frictional heating. Another element that may have effect on the difference between the predicted and measured values is that for a fixed value of inlet temperature and supply pressure, oil flow rate increases with speed since the journal drags more oil into the clearance region, Gulwadi et al [2003].

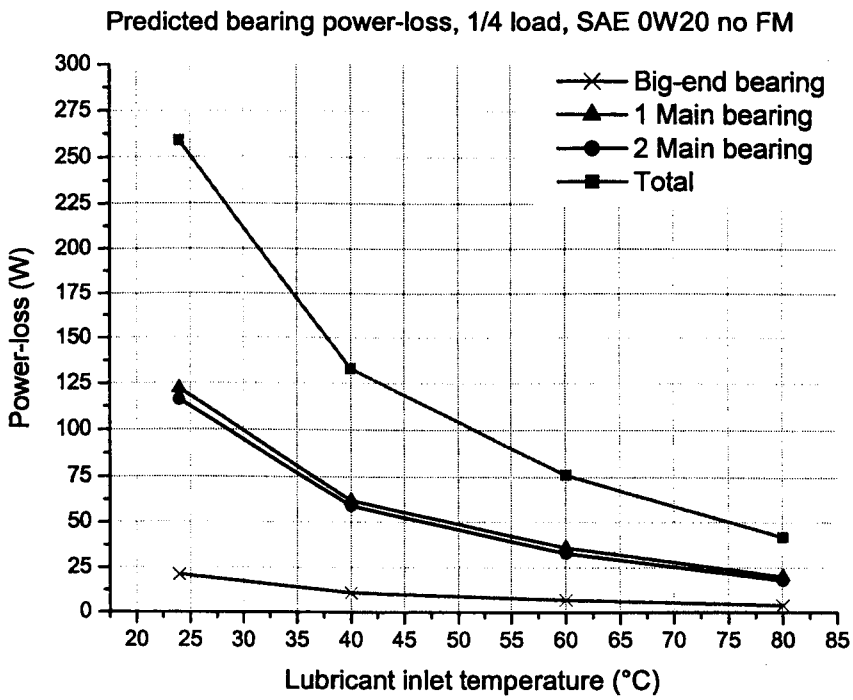

Figure 9.14. Integrated engine bearing friction, 'π' film short bearing analysis, 800rpm.

Journal bearings may also operate in the mixed lubrication regime due to excessively high operating temperatures of the oil leading to low effective oil viscosities. At low temperatures the operating clearances are large but progressively decreases as the lubricant temperature increases, Bates et al [1990]. Thus at a critical minimum clearance, the asperities on the journal and bearing surfaces may start to interact with each other.

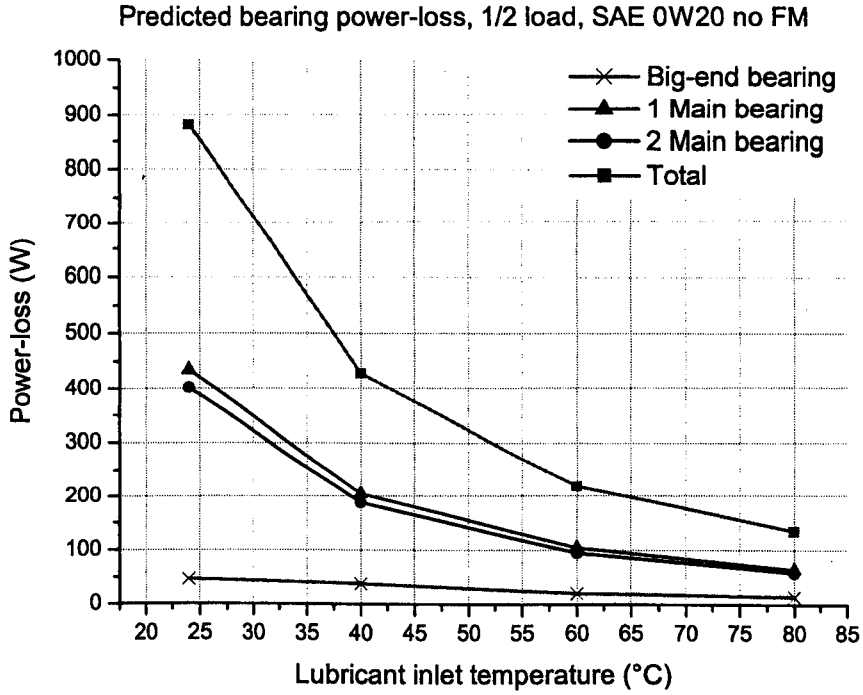

Figure 9.15. Integrated engine bearing friction, 'π' film short bearing analysis, 1500rpm.

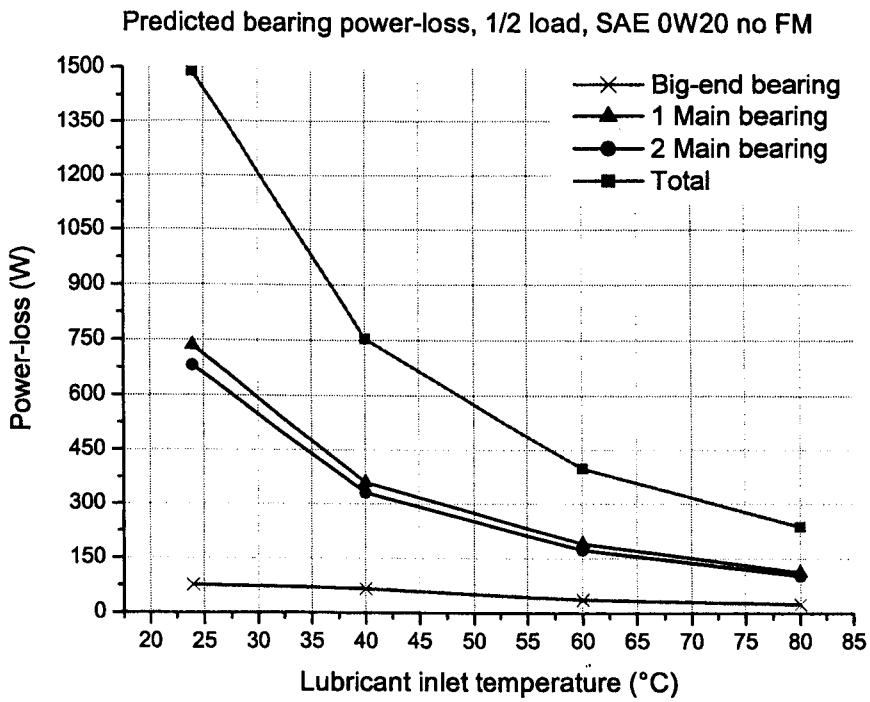

Figure 9.16. Integrated engine bearing friction, 'π' film short bearing analysis, 2000rpm.

Figures 9.14 to 9.16 show the engine bearing friction prediction at component level for different engine speeds. It can be seen that the big-end bearing wastes less energy than the main bearings. One of the reasons is the engine bearing diameter, big-end: 0.049m and main bearings 0.057m. Increase in bearing diameter increases both entraining velocity and the length of oil wedge formation resulting in an increase in the load-carrying capacity due to increase in minimum film thickness. Therefore large diameter journal bearings will result in more friction power loss than smaller ones due to the increase in shear area and shear rate of the lubricant. Whilst the engine main bearings include full circumferential groove to assume a good supply of lubricant and to control the bearing temperature, the presence of the bearing groove leads to the decrease of the load carrying capacity and also to a smaller minimum film thickness.

Another factor responsible for main bearing power loss higher than big-end bearing is the bearing length. The big end bearing length is 0.02m whereas the length of the main bearing 1 is 0.035m and main bearing 2 is 0.032m. Large bearing length results in a large load supporting area, leading to an increase of load-bearing capacity. This causes the shaft to move towards the bush centre resulting in a higher minimum film thickness. The effect of bearing length on power loss causes main bearing 1 power loss to be higher than that of main bearing 2.

As explained earlier, one of the main factors for the difference between the predicted 'π' film method and the experimental results is the uncertainly of the exact bearing radial clearance at engine operating conditions. According to Yang [1992], decrease in the engine bearing clearance results in a decrease in film thickness around the whole bearing causing an increase in shear rate thus increasing friction losses.

9.7 COMPARISON OF SAE 5W30 WITH FM AND SAE 0W20 WITHOUT FM

Experiments were also carried out using SAE 5W30 lubricant, figures 9.17 and 9.18. It was impossible to perform the experiments for both the lubricants under similar conditions as it was very difficult to maintain the temperature constant and similar for

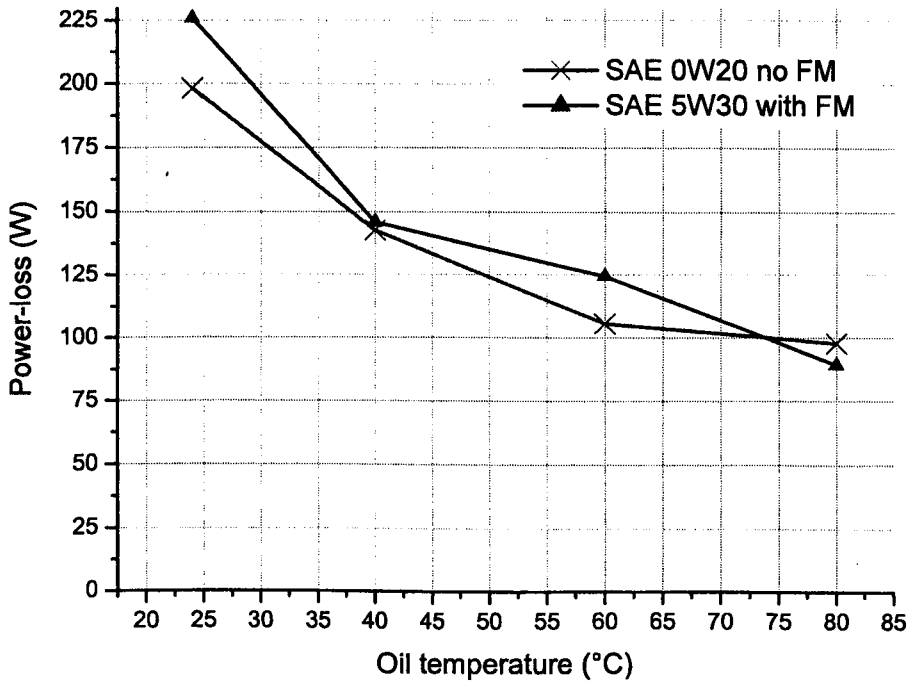

Figure 9.17. Bearing friction power loss, 800rpm, ¼ load.

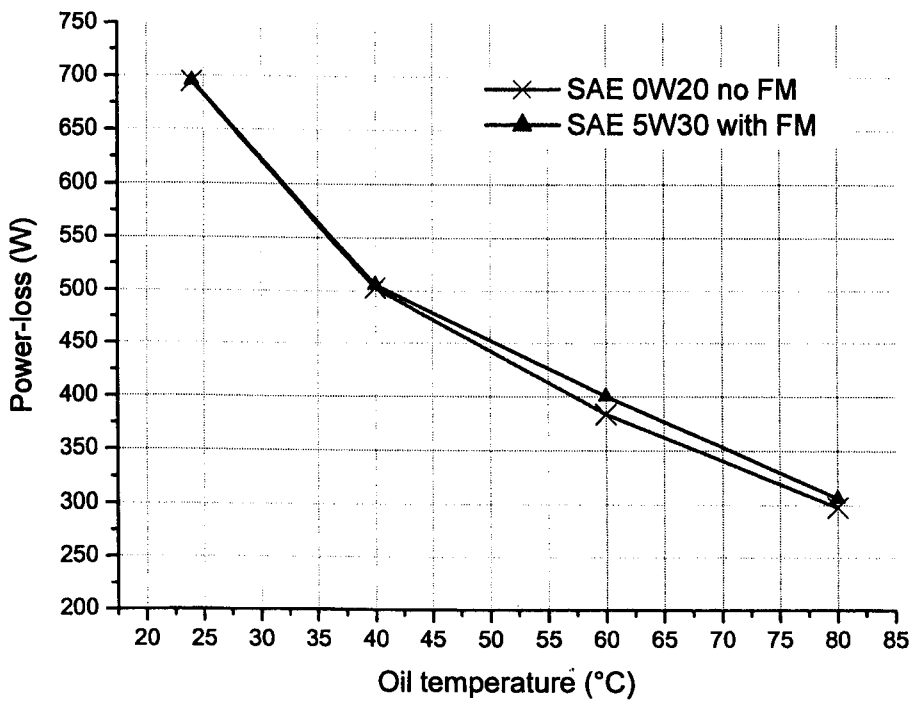

Figure 9.18. Bearing friction power loss, 2000rpm, ½ load.

the engine crankcase lubricant inlet, big-end bearing housing, valve train and piston assembly under fired conditions. But an attempt has been made to compare the results at 800rpm and 2000rpm engine speeds. For the total engine friction measurement, a single sump was used to lubricate both the camshaft assembly and engine crankcase.

It can be seen that the lubricant with higher viscosity SAE 5W30, results in a higher bearing friction power loss than SAE 0W20 without friction modifier. In figure 9.17 at crankcase inlet lubricant temperature 80°C, the SAE 5W30 generates lower losses than SAE 0W20. This can be explained as at high temperature, 80°C, the viscosity difference between the two lubricants is much smaller, (2 mPa.s). Comparing the big-end bearing lubricant temperature for both the lubricants for the above mentioned condition, for SAE 0W20 the temperature was 88°C whereas for SAE 5W30 it was 91°C. Similarly at engine speed 2000rpm, figure 9.18 with a crankcase inlet temperature of 40°C the bearing friction loss is nearly the same, but on investigating in detail it was revealed that for SAE 0W20 the big-end bearing lubricant temperature was 41°C on the other hand for SAE 5W30 it was 48°C.

9.8 CONCLUSIONS

A novel experimental technique has been described that allows measurement of engine bearing friction in a real firing engine without any major engine modification. The technique was used to measure total engine bearing power loss under different engine speeds, loads and lubricant temperatures.

Predicted engine bearing results were also calculated using the well-known short bearing theory and finite width method. The bearing power loss was calculated for both ruptured and fully flooded conditions. Frictional losses were also determined for the zero eccentricity case, using the Petroff equation.

The predicted results were compared with experimental data and it was concluded that the theoretical results obtained via the short bearing for ruptured case were very close to the measured values. For more accurate bearing friction analysis it is vital to have a true lubricant viscosity reading through measuring bearing lubricant temperature by having thermocouples places on the bearing surface.

The predicted results could be further improved by addressing some of the parameters which can have a direct effect on the engine bearing performance like the effect of the location of oil holes on the journal, surface roughness parameters for boundary lubrication and detailed lubricant properties to account for cavitation, piezo-viscous effects and the rise in lubricant temperature.

The experimental technique was also used to study the effect of two different lubricants SAE 5W30 and SAE 0W20 without a friction modifier. The measured data clearly showed the benefit of low viscous lubricant. This experimental method can act as a powerful tool for analysing engine bearing performance and lubricant evaluation.

PART IV

TOTAL ENGINE AND COMPONENT FRICTION AND THE REQUIRED DATA ACQUISITION SYSTEM

Chapter ten

TOTAL ENGINE AND COMPONENT FRICTION

10.1 INTRODUCTION

By reducing engine friction, significant gains in engine efficiency and fuel economy can be achieved. Engineers and Tribologists are constantly challenged to develop new products to meet this challenge and at the same time reduce emissions. Bench testing can provide rapid and cost effective information and is often used for developing new lubricants and testing new materials. But as the engine environment cannot be simulated completely in bench tests, engine tests are then used to verify and validate the findings. Much research work has been carried out to study the friction sources in an engine but no attempt has been made to experimentally measure friction in all the three main tribological components of an engine simultaneously, without major engine modification, in a real engine under fired conditions.

Extensive study of the main engine components i.e. valve train, piston assembly and engine bearings has made it possible for a versatile engine friction measurement system to be developed. This system allows study of the effect of different lubricants on each of the main components of an engine. The system can also be used to examine various materials and engine component design. An advanced data acquisition system has been developed to perform such a challenging task and a description can be found in the next chapter. In this chapter the effect of two different lubricants on measured engine component friction is studied. The effect of lubricant temperature and engine speed on not only component friction but also total engine friction has been analysed in detail, looking at the benefit of low and high viscosity lubricants.

10.2 TOTAL ENGINE AND COMPONENT FRICTION

Total engine and component friction measurement was carried out on a single cylinder Ricardo Hydra gasoline engine under fired conditions at crankcase lubricant inlet temperatures of 24°C, 40°C, 60°C and 80°C. The friction was measured at engine

speeds of 800rpm (¼ load), 1500rpm (½ load) and 2000rpm (½ load) using an SAE 0W20 lubricant without friction modifier and an SAE 5W30 lubricant with friction modifier. The experiments were carried out in four sets, taking measurements at three different speeds at each temperature.

The total engine friction loss was calculated using the PV-diagram as mentioned in the previous chapter. Along with the total friction, piston assembly friction was measured by the IMEP method mentioned in chapter six and the camshaft friction loss using the specially designed pulley torque-meter, as explained in chapter three. From the above-mentioned parameters the engine bearing friction was calculated as detailed in chapter nine. All these friction losses were measured simultaneously. Thus for the very first time friction in all the three main tribological components of an engine, i.e. piston assembly, valve train and engine bearings, were determined in a real engine under fired conditions.

The experimental results for piston assembly friction in chapter seven and bearing friction in chapter nine were measured simultaneously along with the valve train friction loss. Thus in this chapter the results of experimental measurement of piston assembly friction and bearing friction are the same as given in chapter seven and nine, whereas the results for the camshaft friction are different from those given in chapter four. This is because for the validation of the FLAME engine valve train friction model, chapter two, the camshaft lubricant inlet temperature was carefully controlled to maintain stable and constant lubricant temperature under motored and fired conditions using a completely independent lubricant cooling/heating system for camshaft and crankcase lubrication. The engine coolant system was controlled to keep the cylinder head temperature stable to help maintain constant lubricant temperature for the valve train by monitoring the camshaft outlet lubricant temperature. For such reason the engine crankcase lubricant temperature was mostly ten to fifteen degrees different from the camshaft lubricant temperature. Thus during valve train friction measurement, chapter four, more emphasis was given to control accurately the camshaft lubricant inlet temperature than to the engine crankcase inlet temperature. But for the measurement of piston assembly and engine bearing friction the experiments were carried out again along with the measurement of value train friction using a single lubrication system but

this time carefully controlling the crankcase lubricant inlet temperature, thus measuring the engine component friction instantaneously and simultaneously.

Two completely independent lubrication systems as mentioned above, could not be used while measuring engine component friction simultaneously as under such system three temperatures need to be controlled, the camshaft lubricant inlet temperature, the crankcase lubricant inlet temperature and the engine coolant temperature. To control these temperatures and also to keep it stable using completely independent system is nearly impossible without having an advanced PID (proportional integral and differential) master controller that controls the individual controllers of each parameter. Thus a single lubrication system was used for simultaneous engine component friction measurement.

While examining the engine component friction results for a single cylinder engine it is important to remember that the relative friction contribution from the engine bearings, especially main bearings, will be high compared to a multi-cylinder engine, as the ratio of cylinders to bearings for a single cylinder engine is higher than for a multi-cylinder engine. For a single cylinder engine the cylinder/main bearing ratio is 1:2 whereas for a four cylinder engine the ratio is 1:1.25. Similarly the cam and camshaft-bearing ratio for a single cylinder is greater than for a multi-cylinder engine.

10.2.1 ENGINE FRICTION, LUBRICANT SAE 0W20 WITHOUT FM.

Figure 10.1 shows the power loss generated from the three main engine components at an engine speed of 800rpm (¼ load), at different lubricant temperatures. The engine bearing friction loss is much greater than the piston assembly and valve train at low lubricant temperatures. As engine bearings operate in the hydrodynamic lubrication regime an increase in lubricant viscosity results in an increase in shear loss, whereas at high lubricant temperature, decrease in viscosity results in a reduction in bearing friction. According to figure 10.1, at high lubricant inlet temperatures the bearing friction is less than the piston assembly and valve train friction, which do have boundary to mixed lubrication components.

In the component friction graphs given in this chapter, the numbers following the piston assembly friction power loss data are liner BDC near-surface temperature assumed to be same as lubricant temperature, the numbers following the bearing data are the measured big-end upper cap near-surface temperature and the number following the valve train data are the camshaft lubricant inlet temperature.

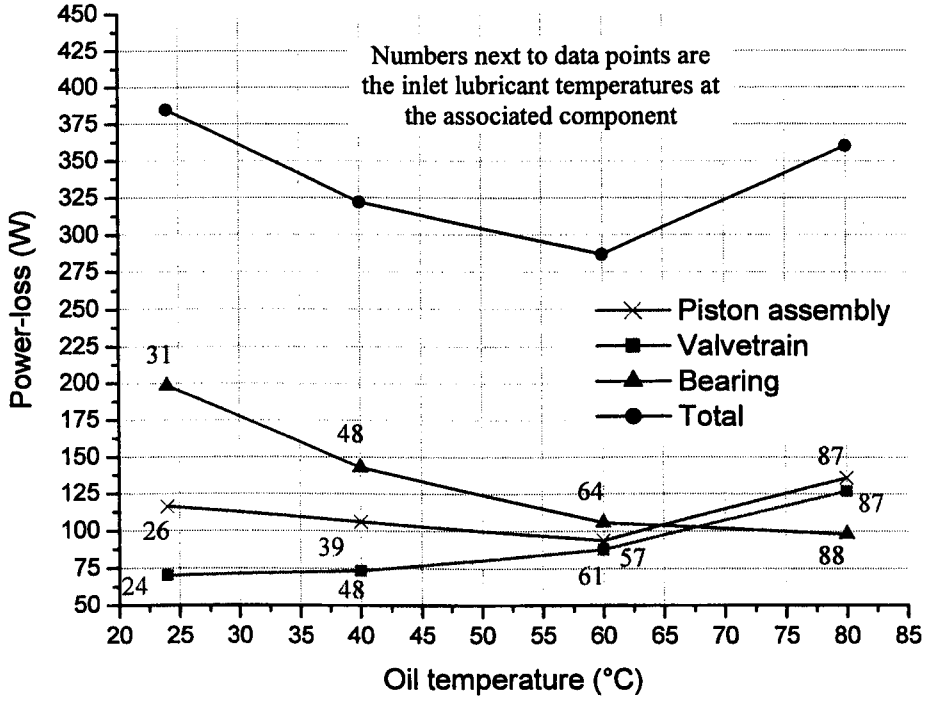

Figure 10.1. Total engine and component friction at an engine speed of 800rpm, ¼ load, lubricant SAE 0W20 without FM.

Looking in depth at the experimental conditions it is realised that although the crankcase inlet lubricant temperature was 24°C, the big-end bearing upper cap near-surface temperature at the bearing shell was 31°C, and as mentioned earlier it is assumed to be the same as the lubricant temperature. This rise in temperature is mainly due to the heat transfer from the piston assembly down to the connecting rod lower half and also due to the heat generated by the lubricant shear friction. Similarly at 40°C, 60°C, and 80°C crankcase lubricant inlet temperature, the big-end upper half near-

surface temperature, very close to the bearing shell was elevated to 48°C, 63°C, and 88°C respectively. For the main bearings, lubricant temperature is assumed to be near the crankcase inlet temperature, although there will be some difference due to heat gain/loss from the crankcase and the heat generated due to lubricant shear and thus in reality will lie between the crankcase inlet and big end bearing measured temperature.

The contribution of friction loss from the piston assembly lies between the bearing friction and the valve train friction at low lubricant temperatures but as the temperature increases its contribution becomes greater than the bearings, figure 10.1. For the piston assembly friction, there is first a decrease in friction as at low lubricant temperature hydrodynamic lubrication is dominant and then as the inlet temperature increases the piston assembly friction increases, especially from 60°C to 80°C, due to low oil viscosity increasing the metal to metal contact causing mixed to boundary lubrication condition to be more dominant. At crankcase lubricant inlet temperatures of 24°C, 40°C, 60°C and 80°C the lubricant temperatures at the liner BDC location was 26°C, 39°C, 57°C and 87°C respectively.

At low lubricant temperature, the engine valve train friction is the lowest but it exceeds bearing friction at high lubricant temperatures. As seen in figure 10.1, the valve train friction continues to increase as the lubricant temperature increases: as the lubrication condition for the engine valve train is mostly EHL (elastohydrodynamic lubrication) to boundary, lowering the lubricant viscosity increases the metal to metal contact. As mentioned earlier, there was no direct control of the camshaft inlet lubricant temperature thus the value of the crankcase and camshaft inlet temperatures varied. At crankcase inlet temperature of 40°C and 80°C the camshaft inlet temperatures were 48°C and 87°C respectively. To keep the crankcase inlet lubricant temperature stable, the engine coolant temperature was carefully controlled accordingly. This had a direct effect on the cylinder head and the lubricant temperature of the cam/tappet oil bath. Therefore the lubricant temperature at the cam/tappet interface may differ from the camshaft lubricant inlet temperature.

Figure 10.2 shows the percentage of friction contribution from each of the tribological components at lubricant inlet temperature of 24°C, derived from figure 10.1. It is clear that the bearing friction contribution is the greatest at 52% due to high shear loss

whereas valve train friction accounts for just 18% of the total engine friction and the piston assembly 30%. At the higher lubricant inlet temperature of 80°C, the contribution from the bearing friction decreases to 27% and the valve train friction increases by 16% achieving 35% of the total engine friction loss, figure 10.3. As mentioned earlier, a rise in lubricant temperature reduced the shear loss under hydrodynamic lubrication condition, therefore a sharp decrease in frictional loss is seen in bearing friction contribution, whereas under mixed to boundary lubrication a decrease in lubricant viscosity increases friction loss due to a decrease in film thickness, as can be seen in the case of the engine valve train. Similarly increase in friction loss contribution with increasing temperature is seen from 30% to 38% in the piston assembly friction, figure 10.2 and 10.3. In figure 10.1, although the total engine friction at 24°C and 80°C lubricant inlet temperature is nearly similar, a difference of just 25 watts, but it can be seen an low lubricant temperature shear loss is dominant whereas at higher temperature mixed to boundary friction becomes more influential.

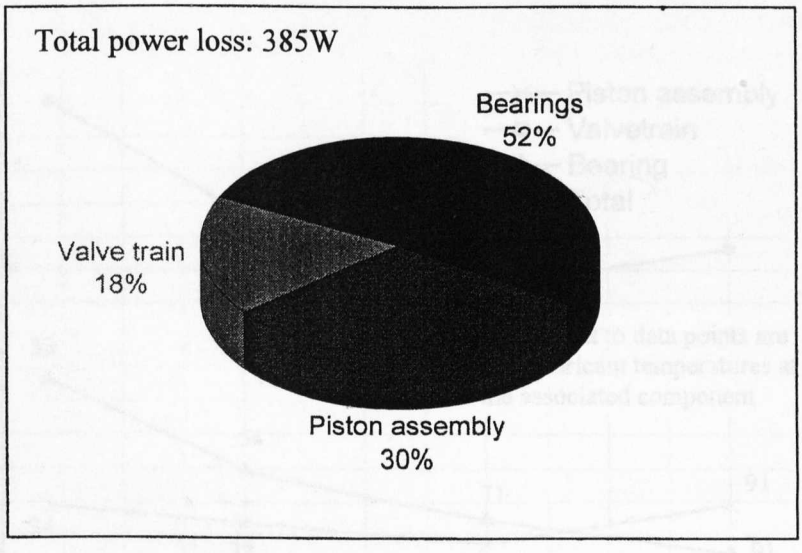

Figure 10.2. Contribution of engine component friction at an engine speed of 800rpm, ¼ load, lubricant inlet temperature 24°C, SAE 0W20 no FM

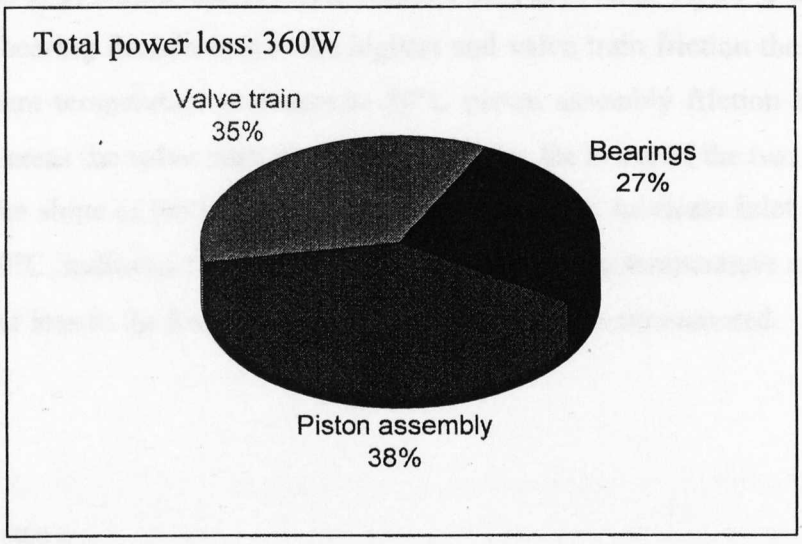

Figure 10.3. Contribution of engine component friction at an engine speed of 800rpm, ¼ load, lubricant inlet temperature 80°C, SAE 0W20 no FM

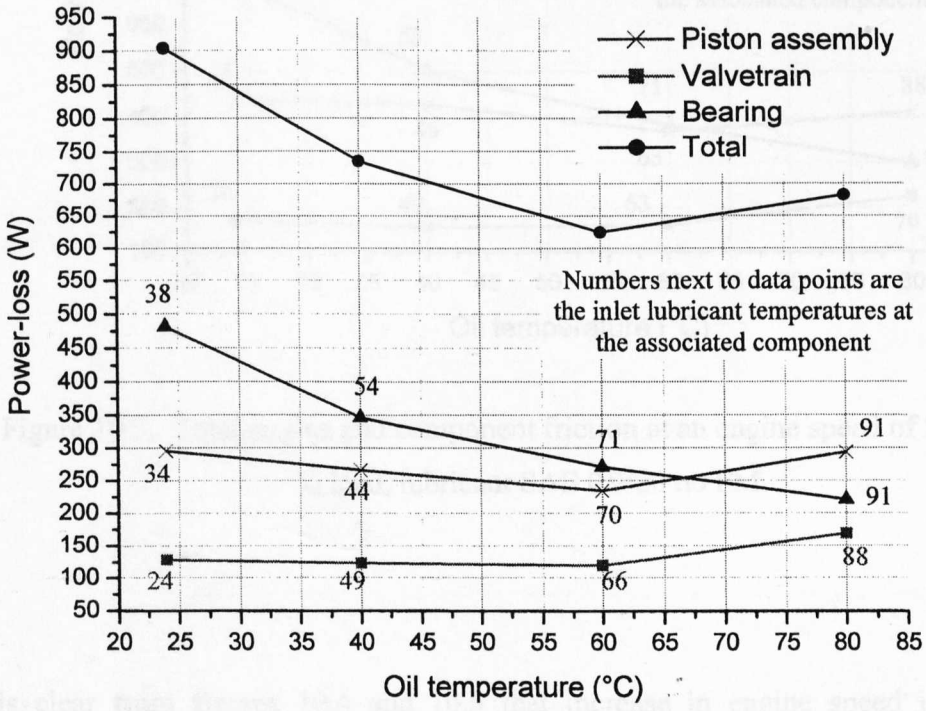

Figure 10.4. Total engine and component friction at an engine speed of 1500rpm, ½ load, lubricant SAE 0W20 no FM

A similar picture of engine component friction can be seen in figures 10.4 and 10.5 for engine speeds of 1500rpm and 2000rpm respectively, at ½ load. At 24°C inlet lubricant temperature bearing friction loss is the highest and valve train friction the lowest. But as the lubricant temperature increases to 80°C piston assembly friction loss becomes dominant whereas the valve train friction loss remains the lower of the two components. Looking at the slope of the bearing friction loss in detail at lubricant inlet temperatures of 60°C to 80°C, indicates that a further increase in lubricant temperature may cause the bearing power loss to the lowest, unless mixed lubrication is encountered.

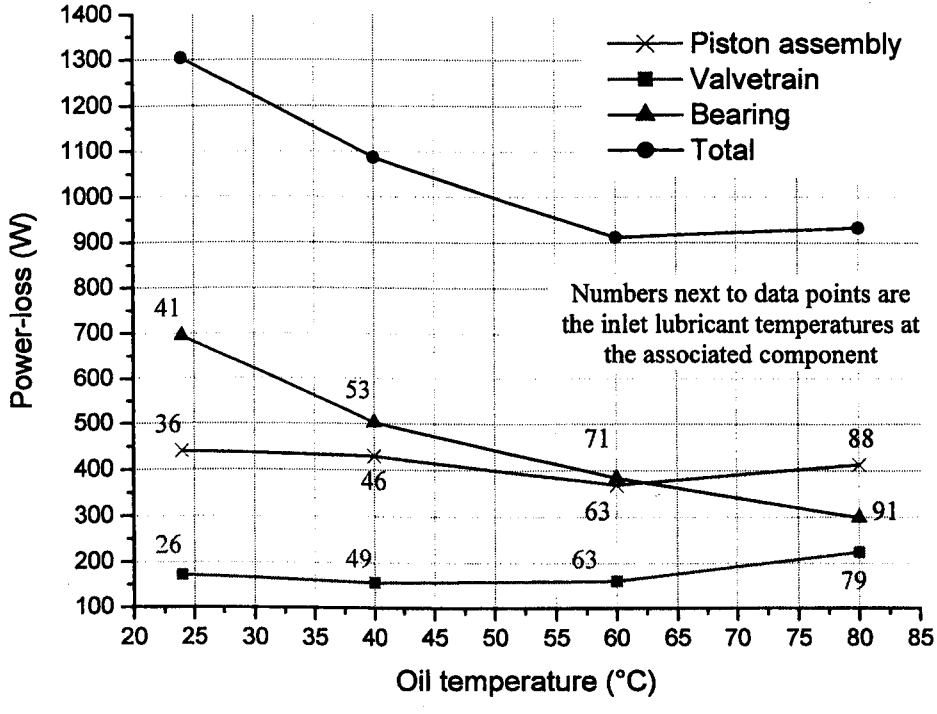

Figure 10.5. Total engine and component friction at an engine speed of 2000rpm, ½ load, lubricant SAE 0W20 no FM

It is clear from figures 10.4 and 10.5 that increase in engine speed improves the lubrication conditions for the engine valve train and piston assembly at high lubricant inlet temperatures. The friction at the cam/follower interface, which operates almost all the time in EHL or boundary lubrication conditions, dominates the power loss from the

engine valve train. The increase of engine speed will decrease cam load around the cam nose area and increase the lubricant film thickness resulting in valve train power loss being sensitive to changes in engine speed. The increase in engine speed also improved the piston assembly friction. An increase in engine speed tends to improve the lubrication conditions for the piston rings near the dead centres due to increased of entraining velocity, although the power loss due to the piston skirt increases. For both the engine speeds of 1500rpm and 2000rpm, a sharp decrease in bearing friction loss with increase in lubricant temperature can be seen due to being operated under hydrodynamic lubrication conditions.

Comparing the power loss contribution from each component at 24°C lubricant inlet temperature at engine speeds of 1500rpm and 2000rpm under half load conditions, figures 10.6 and 10.7, there is hardly any change in the percentage contribution of friction loss although the power loss increases from 904W at 1500rpm to 1304W at 2000rpm. A very similar picture is seen in figures 10.8 and 10.9 for engine speeds of 1500rpm and 2000rpm respectively, at a lubricant inlet temperature of 80°C.

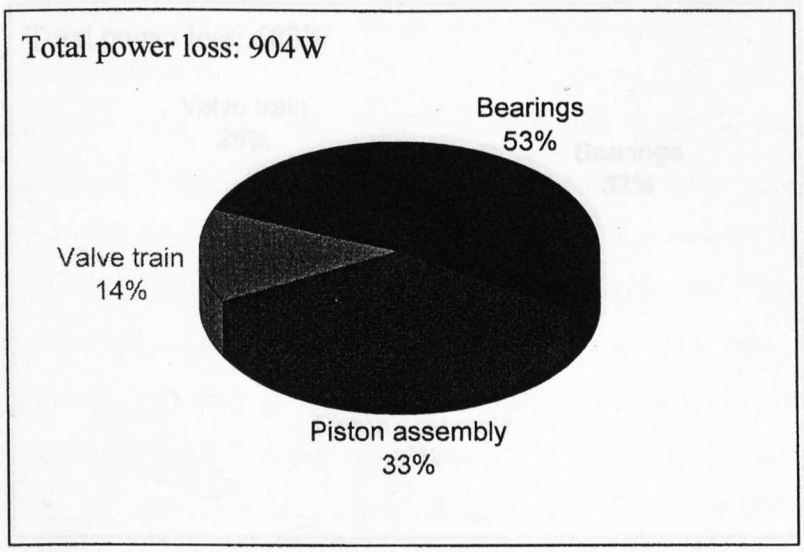

Figure 10.6. Contribution of engine component friction at an engine speed of 1500rpm, ½ Load, lubricant inlet temperature 24°C, SAE 0W20 no FM

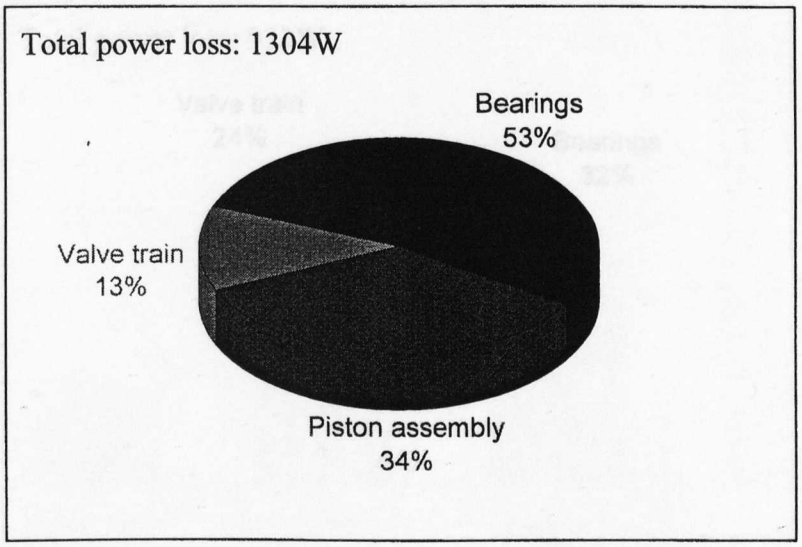

Figure 10.7. Contribution of engine component friction at an engine speed of 2000rpm, ½ Load, lubricant inlet temperature 24°C, SAE 0W20 no FM

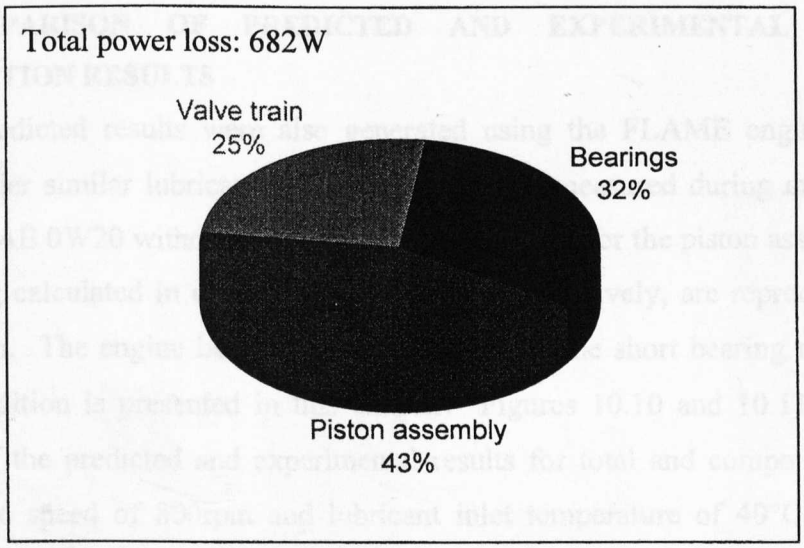

Figure 10.8. Contribution of engine component friction at an engine speed of 1500rpm, ½ Load, lubricant inlet temperature 80°C, SAE 0W20 no FM

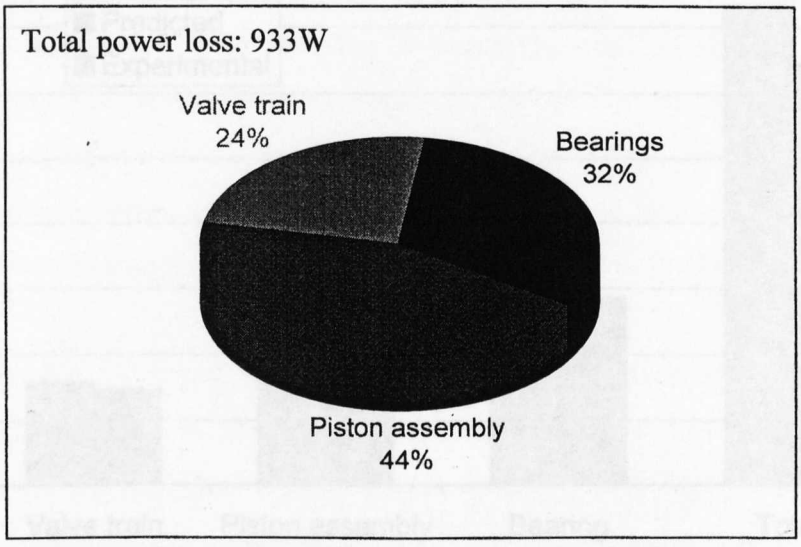

Figure 10.9. Contribution of engine component friction at an engine speed of 2000rpm, ½ Load, lubricant inlet temperature 80°C, SAE 0W20 no FM

10.2.1.1 COMPARISON OF PREDICTED AND EXPERIMENTAL ENGINE FRICTION RESULTS

The predicted results were also generated using the FLAME engine friction model and under similar lubricant inlet temperatures as measured during experiments for lubricant SAE 0W20 without FM. The predicted results for the piston assembly and engine bearing calculated in chapter seven and nine respectively, are reproduced here for comparison. The engine bearing results obtained by the short bearing method for cavitation condition is presented in this chapter. Figures 10.10 and 10.11 show the comparison of the predicted and experimental results for total and component power loss for engine speed of 800rpm and lubricant inlet temperature of 40°C and 80°C respectively. 40°C inlet lubricant temperature was chosen instead of 24°C as the lower temperature limit for comparison reason as the predicted results were closer to the experimental at 40°C rather than 24°C for valve train and engine bearing power loss (see chapter four and nine).

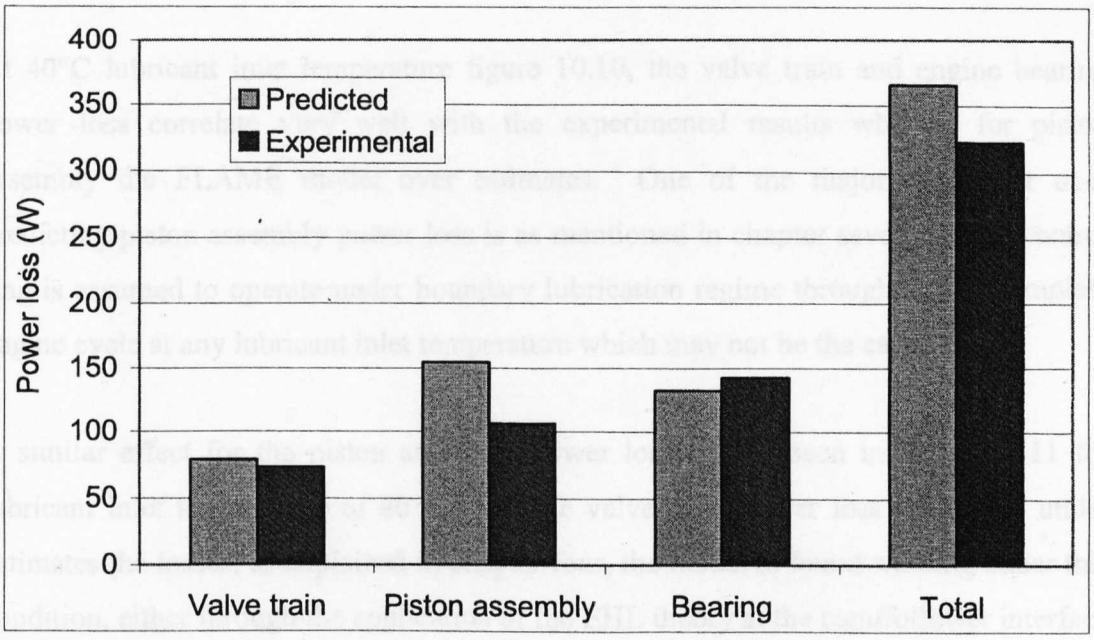

Figure 10.10. Predicted and experimental power loss at engine speed of 800rpm, ¼ load, lubricant inlet temperature of 40°C, lubricant SAE 0W20 no FM

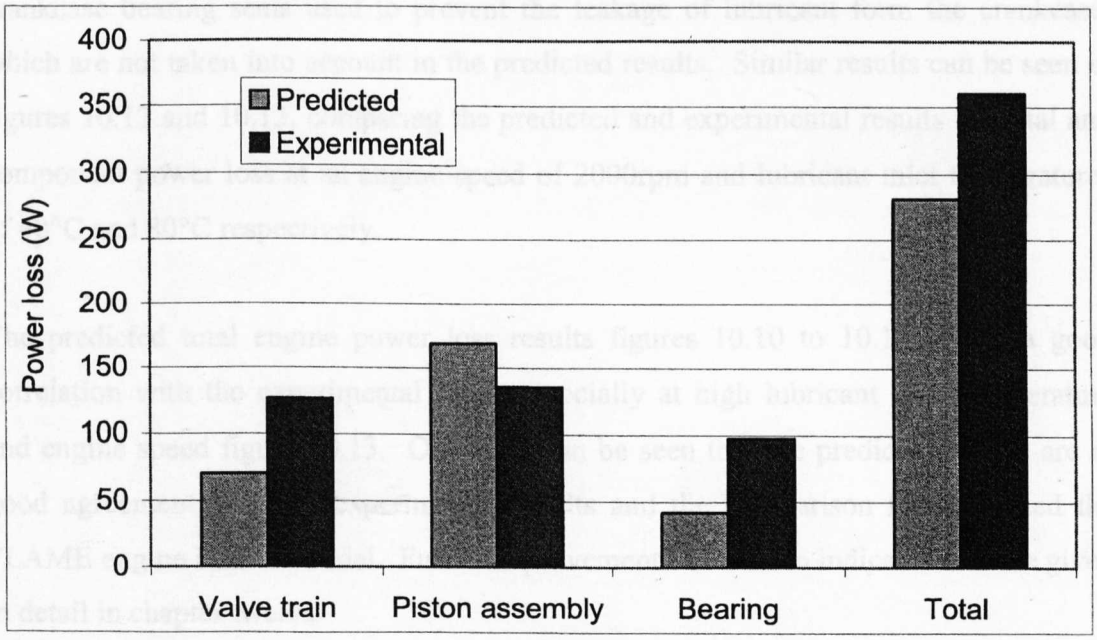

Figure 10.11. Predicted and experimental power loss at engine speed of 800rpm, ¼ load, lubricant inlet temperature of 80°C, lubricant SAE 0W20 no FM

At 40°C lubricant inlet temperature figure 10.10, the valve train and engine bearing power loss correlate very well with the experimental results whereas for piston assembly the FLAME model over estimates. One of the major factor for over predicting piston assembly power loss is as mentioned in chapter seven, the oil control ring is assumed to operate under boundary lubrication regime throughout the complete engine cycle at any lubricant inlet temperature which may not be the case.

A similar effect for the piston assembly power loss can be seen in figure 10.11 for lubricant inlet temperature of 80°C. For the valve train power loss the model under estimates the losses, as explained in chapter four, the model is found wanting under this condition, either through the application of the EHL theory at the cam/follower interface or the use of a fixed limiting friction coefficient for a given oil. The bearing power loss is under estimated at lubricant inlet temperature of 80°C, this may be due to the fact that during experiments the true value of the lubricant temperature at the shaft/bearing interface is not known which could be lower than the inlet temperature due to heat loss from the lubricant as it flows from the sump to the cold engine crankcase, thus reducing the lubricant viscosity and increasing power loss. The other factor could be the effect of crankcase bearing seals used to prevent the leakage of lubricant form the crankcase, which are not taken into account in the predicted results. Similar results can be seen in figures 10.12 and 10.13, comparing the predicted and experimental results for total and component power loss at an engine speed of 2000rpm and lubricant inlet temperatures of 40°C and 80°C respectively.

The predicted total engine power loss results figures 10.10 to 10.13 shows a good correlation with the experimental results specially at high lubricant inlet temperature and engine speed figure 10.13. Overall it can be seen that the predicted results are in good agreement with the experimental results and the comparison has validated the FLAME engine friction model. Future improvements have been indicated and are given in detail in chapter twelve.

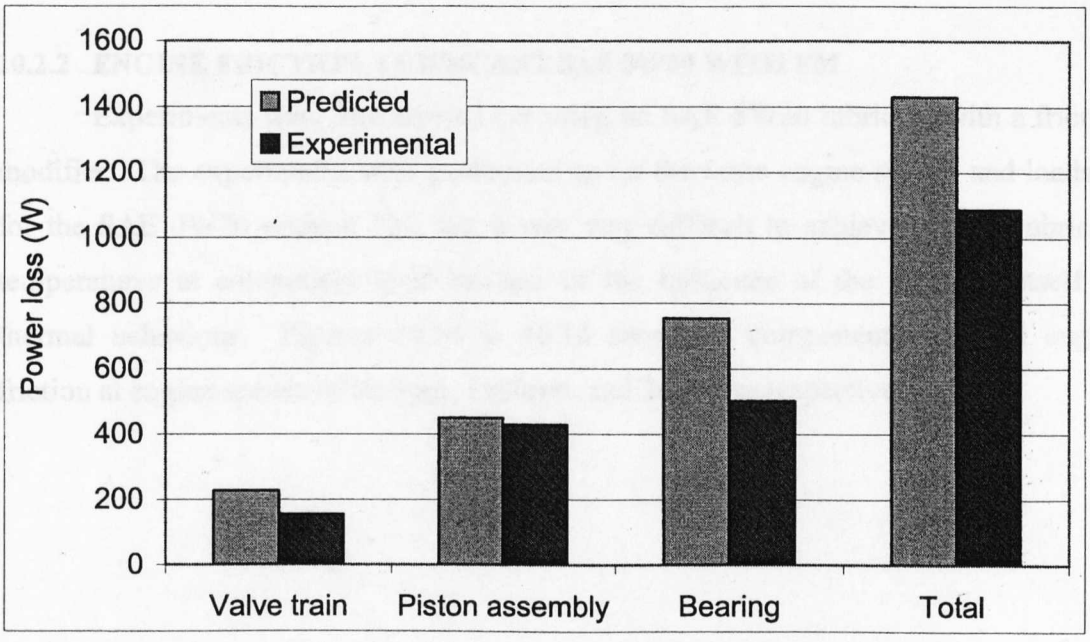

Figure 10.12. Predicted and experimental power loss at engine speed of 2000rpm, ½ load, lubricant inlet temperature of 40°C, lubricant SAE 0W20 no FM

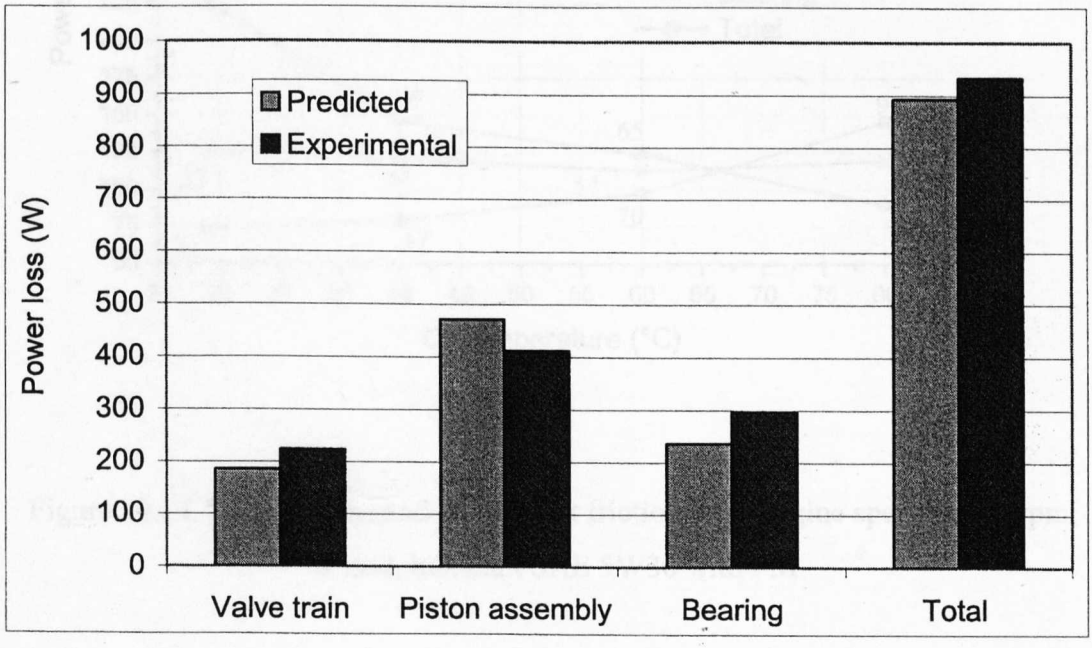

Figure 10.13. Predicted and experimental power loss at engine speed of 2000rpm, ½ load, lubricant inlet temperature of 80°C, lubricant SAE 0W20 no FM

10.2.2 ENGINE FRICTION, LUBRICANT SAE 5W30 WITH FM

Experiments were also carried out using an SAE 5W30 lubricant with a friction modifier. The experiments were performed under the same engine speeds and loads as for the SAE 0W20 without FM, but it was very difficult to achieve similar lubricant temperatures at component level because of the influence of the lubricant itself on thermal behaviour. Figures 10.14 to 10.16 show the component and total engine friction at engine speeds of 800rpm, 1500rpm and 2000rpm respectively.

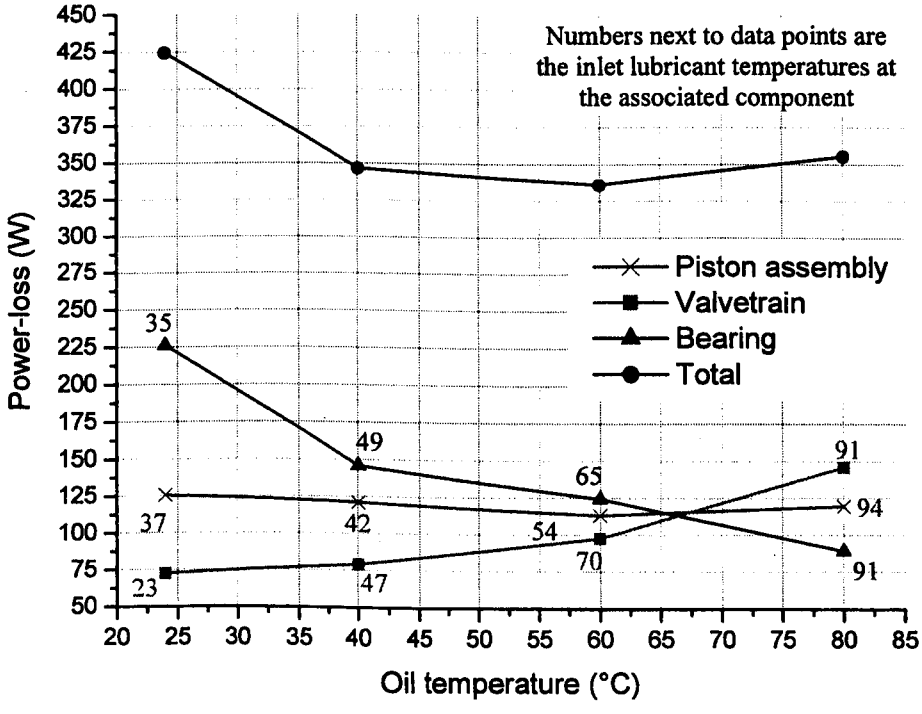

Figure 10.14. Total engine and component friction at an engine speed of 800rpm, ¼ load, lubricant SAE 5W30 with FM

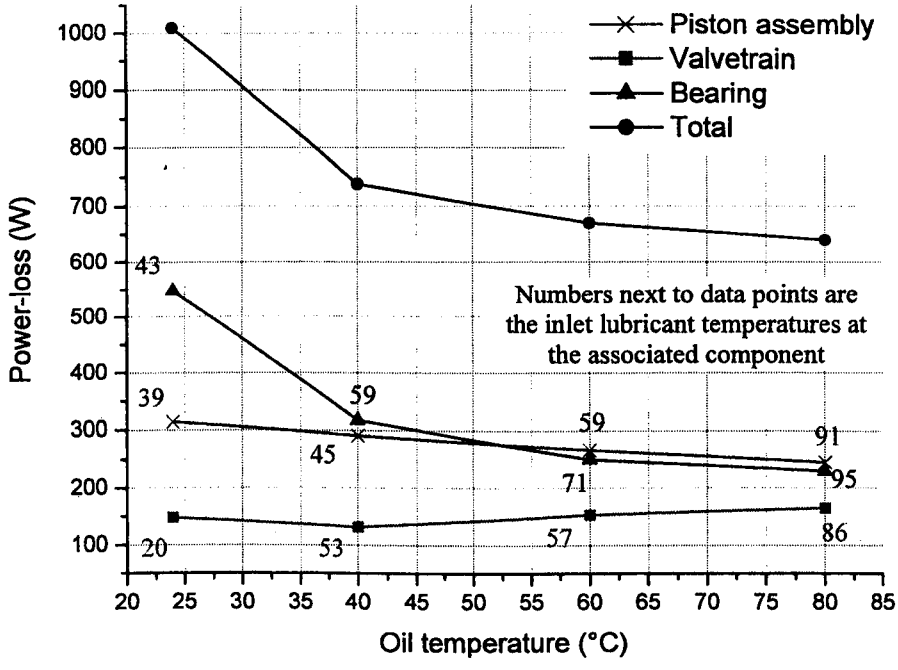

Figure 10.15. Total engine and component friction at an engine speed of 1500rpm, ½ load, lubricant SAE 5W30 with FM.

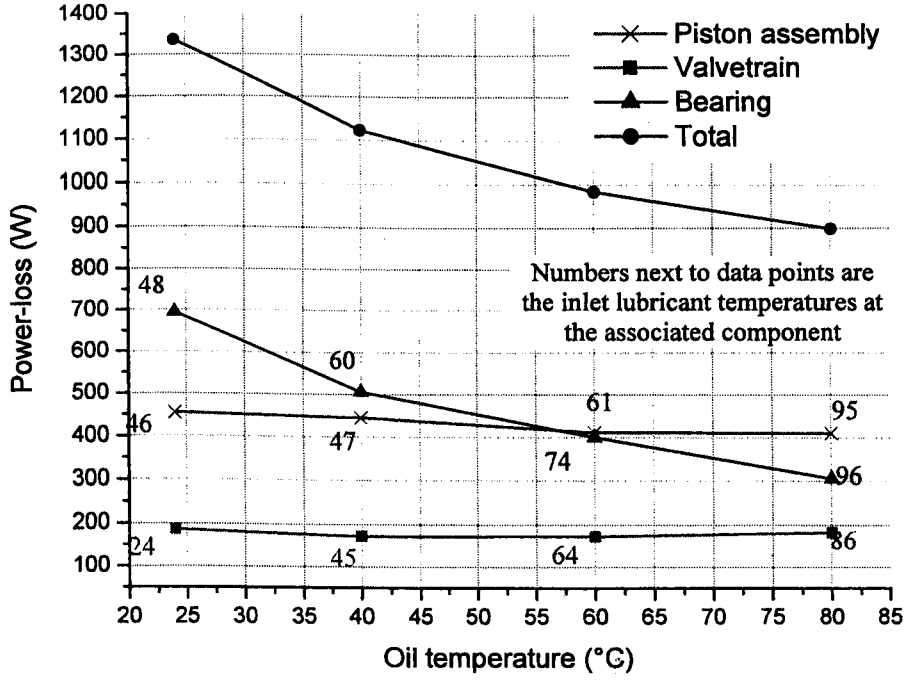

Figure 10.16. Total engine and component friction at an engine speed of 2000rpm, ½ load, lubricant SAE 5W30 with FM.

10.3 BENEFIT OF FRICTION MODIFIER AND HIGH/LOW VISCOSITY LUBRICANT

Comparing the results at an engine speed of 800rpm for both the lubricants, figures 10.1 and 10.14, the total engine friction loss is higher for the more viscous lubricant SAE 5W30 with FM at low lubricant temperatures as compared to the SAE 0W20 without FM, but at a lubricant inlet temperature of 80°C the total frictional loss is nearly the same. Looking at the slope of the engine total friction curves for both the lubricants indicates that further increase in oil temperature will result in friction loss for SAE 0W20 without FM exceeding SAE 5W30 with FM. This is mainly because of mixed to boundary friction loss becoming dominant at high lubricant temperature and under such conditions higher viscous lubricant reduces friction and also the friction modifier activates at higher temperatures (temperature sensitive), plays a major role in reducing friction.

Again for engine speeds of 1500rpm (figures 10.4 and 10.15) and 2000rpm (figures 10.5 and 10.16) at lower lubricant inlet temperatures, the total engine friction for SAE 0W20 without FM is lower than SAE 5W30 with FM. At higher temperatures the friction loss with SAE 0W20 without FM exceeds SAE 5W30 with FM and the slope of the total engine friction curves for SAE 5W30 with FM indicates that there will be a further decrease in friction loss with increase in lubricant inlet temperature as compared to SAE 0W20 without FM.

Although it was very difficult to perform the experiments under the same thermal conditions, the experiments at 1500rpm engine speed for both the lubricants are well correlated and thus the contribution of friction loss at component level is compared. At 24°C lubricant inlet temperature the percentage contribution of component friction is nearly identical for the two lubricants, figures 10.6 and 10.17. However the total engine friction loss for the SAE 5W30 with FM lubricant is about 12% higher than for the SAE 0W20 without FM lubricant as the former is more viscous, resulting in high shear loss. Whereas at a lubricant inlet temperature of 80°C, figures 10.8 and 10.18, the total engine friction loss for SAE 0W20 without FM is about 7% higher than for the SAE 5W30 with FM. Looking at the percentage frictional loss at component level at a lubricant inlet temperature of 80°C, (figures 10.8 and 10.18) shows that there is a rise in bearing friction loss and fall in piston assembly friction contribution for the SAE 5W30

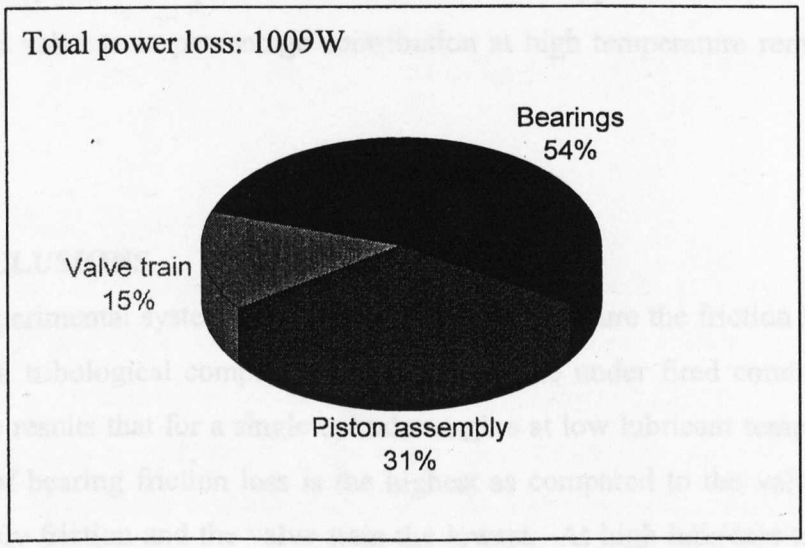

Figure 10.17. Contribution of engine component friction at an engine speed of 1500rpm, ½ load, lubricant inlet temperature 24°C, SAE 5W30 with FM.

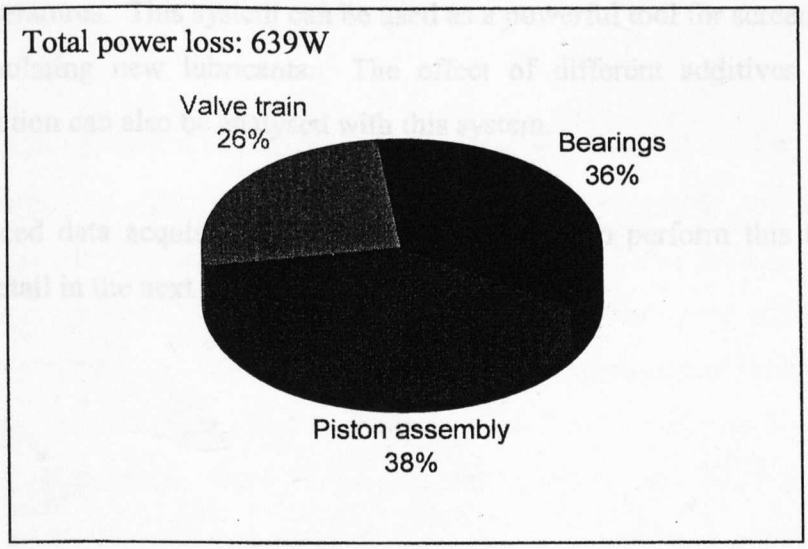

Figure 10.18. Contribution of engine component friction at an engine speed of 1500rpm, ½ load, lubricant inlet temperature 80°C, SAE 5W30 with FM.

with FM, indicating a higher viscosity lubricant with friction modifier improves the lubrication conditions at the piston/liner interface but an opposite effect is seen for the bearings. The valve train percentage contribution at high temperature remains nearly constant.

10.4 CONCLUSIONS

An experimental system has been developed to measure the friction losses in all the three main tribological components of a real engine under fired conditions. It is clear from the results that for a single cylinder engine at low lubricant temperature, the contribution of bearing friction loss is the highest as compared to the valve train and piston assembly friction and the valve train the lowest. At high lubricant temperature, piston assembly friction becomes more dominant. The total and component engine friction loss curves at different engine conditions indicate a good correlation with the Stribeck curve.

The performance of two different lubricants SAE 0W20 without friction modifier and SAE 5W30 with friction modifier on the total engine and component friction was also studied and showed the benefit of friction modifier and high viscosity lubricant at high lubricant temperatures. This system can be used as a powerful tool for screening engine oils and formulating new lubricants. The effect of different additives on engine component friction can also be analysed with this system.

A very advanced data acquisition system was developed to perform this task and is described in detail in the next chapter.

Chapter eleven

ENGINE DATA ACQUISITION SYSTEM

11.1 INTRODUCTION

Measurement of engine friction loss at component level in a real fired engine was not possible without an advanced data acquisition system. In this research project friction loss was determined in all the three main tribological components of an engine under fired conditions and the findings were used to validate the FLAME engine friction model. To achieve this aim, the engine was fitted with more than fifty different sensors and to sample/log data from such a large number of transducers; an advanced high-speed synchronised data acquisition system was designed/developed. This data acquisition system was the heart of this project.

This chapter describes in detail all the analogue and digital channels used to log data from a number of transducers and their signal conditioning units. The function of the DAQ (data acquisition) hardware is explained along with the programming code used to control the DAQ operation.

11.2 RICARDO HYDRA ENGINE DATA ACQUISITION SYSTEM

The original Ricardo Hydra Engine data acquisition system was upgraded to meet the requirements of this research project. The original DAQ system comprised a single PC-226 Amplicon DAQ board having a total sampling speed of 750 kHz, 16 analogue input channels and 12-bit A/D (analogue to digital) converter running on a 486 PC (personal computer). One channel of the PC-226 DAQ board was connected to a 16-channel extension board, Amplicon EX-201, thus giving in total a 31-channel DAQ system. The original DAQ system utilised 27 of the 31 analogue channels, mostly thermocouples. Some of the functions vital for performing this project were lacking from this DAQ system such as the simultaneous synchronised sampling of channels, high-speed sampling rate, high speed data streaming to disk rate, etc.

To meet the requirements of this project by recording and processing data at very high speeds, a new DAQ system based on a 933 MHz Pentium III PC and advanced high-speed National Instruments data acquisition hardware was developed. The programming language Labview was used to control the DAQ operations.

Due to the large number of channels needed to be logged, a special motherboard was required for the computer having 3 ISA (industry standard) and 5 spare PCI (peripheral component inter-connect) interface slots to install up to 5 PCI DAQ boards. 512 MB RAM (random access memory) was specified to allow smooth operation of the DAQ code, as recommended by National Instruments.

The new engine data acquisition system was divided into two completely independent groups. Group 1 was designed to monitor basic engine-operating conditions and transducers with relatively steady or slowly changing signals. These are relatively low speed sampling channels from which the information is required to be generally logged once a second. Group 2 deals with high-speed channels required to measure friction instantaneously in different parts of the engine. Thus two different DAQ boards were used, the National Instruments PCI-6071E for group 1 channels and the PCI-6110E for group 2 channels.

11.3 DATA ACQUISITION CHANNELS AND THE REQUIRED SIGNAL CONDITIONING UNITS

As noted above, two separate data acquisition systems were developed to record data from two groups of channels, as a function of their sampling rate.

11.3.1 GROUP 1 CHANNELS

In group 1 there are 40 analogue/digital channels sampled by using a PCI-6071E DAQ board. Most of these channels are used for monitoring engine performance and to collect data for the validation of the FLAME engine friction model. The group 1 channels comprise of the following,

a) *22 Analogue input channels* used for temperature measurements via K-type thermocouples. These channels are sampled at a rate of 300 samples per second

and averages of 30 data points were taken to reduce quantization and noise error. These thermocouples are used to measure the following temperatures,

- Air inlet temperature, required to calculate air mass flow rate.
- Coolant in/out (2 channels).
- Crankcase oil in/out (2 channels).
- Cylinder head oil in/out (2 channels).
- Cylinder head lubricant temperature at tip of the feed nozzle to the cam/follower interface (see section 3.6).
- Cylinder pressure transducer cooling water temperature. This information is required to monitor and control the pressure transducer water-cooling temperature at 50°C for accurate cylinder pressure measurements, as recommended by the manufacturer (Kistler).
- Fuel inlet temperature.
- Crankcase surface temperature, (viewed from front) left-hand, right-hand and top side (3 channels). These channels are used to monitor engine crankcase temperature, which is heated using electric heating filaments fitted around it.
- 9 thermocouples fitted around the liner at a position of 0.5mm away from the liner inner surface. These thermocouples were fitted very close to the working surface of the liner using 2mm holes drilled from the water jacket side. The liner circumferential and axial temperature variation was logged and was used to calculate lubricant viscosity required for the validation of the FLAME piston assembly friction model. These thermocouples were fitted at the following locations on the cylinder liner,

  - Piston ring 1TDC position, piston thrust side, anti-thrust side and, gudgeon pin plane.
  - Piston ring 1Mid-stroke, piston thrust side, anti-thrust side and gudgeon pin plane.
  - Piston ring 2 BDC position, piston thrust side, anti-thrust side and gudgeon pin plane.

National Instruments SCXI 1102 module fitted in the four slot SCXI 1000 chassis was used as a signal-conditioning unit for the thermocouples, figure 11.1.

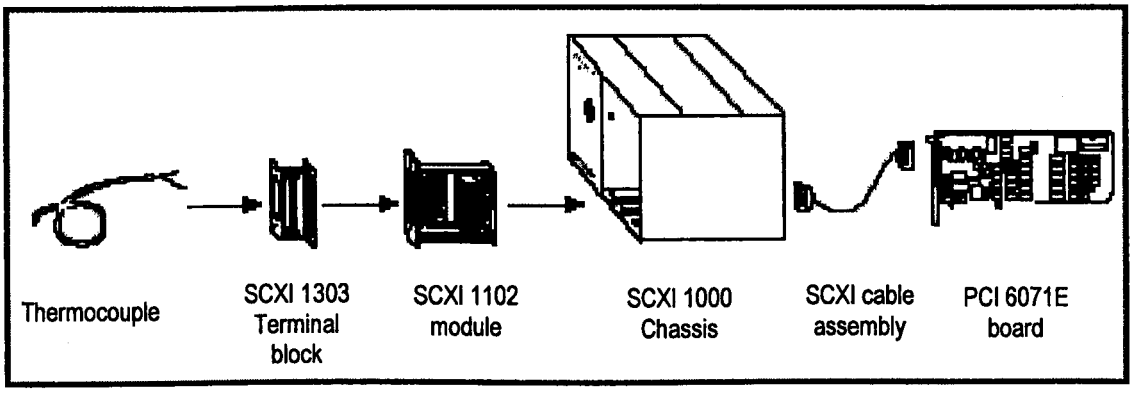

Figure 11.1. SCXI system diagram with DAQ board, NI [2003].

Low magnitude thermocouple signals are very susceptible to noise corruption and thus it is very important to keep the signal conditioning unit, cables and the DAQ board well shielded. K-type thermocouples have a temperature range of -270°C to 1372°C corresponding to a voltage range of –6.534mV to +54.874mV. The SCXI 1000 chassis and the SCXI 1102 module are fully shielded and to further reduce noise interference twisted pair cable was used for connecting the SCXI 1000 chassis with the DAQ board. This signal conditioning SCXI system improves the noise performance as the thermocouple low voltage is amplified before the signal is passed into the noisy computer chassis which if picked up, will have much less of an effect.

The thermocouple output voltage level is normally very low, thus high gain amplification was required. The SCXI 1102 module has an instrument amplifier with a maximum gain of 100 for each channel, figure 11.2. For best noise performance, it is wise to use the largest gain possible near the signal source, therefore the gain of the SCXI module was kept at 100 and additional gain setting was carried out at the DAQ board. With Labview, simply indicating high and low input limits, the driver software calculates the necessary gain at the DAQ board. The advantage of using twisted cables

is that the noise induced by the nearby power line is the same in both the cables and the SCXI 1102 has a high CMRR (common mode rejection ratio) instrument amplifier. The instrumented amplifier is a differential type and any voltage that is common between the two wires of the thermocouple is rejected. Thus the differential amplifier has two inputs and amplifies the difference between them. The voltage at both the inputs is measured with respect to common signal, giving a relatively noise free output signal. To reduce noise further, the SCXI 1102 module has a low-pass 200Hz filter for each channel. This module can also detect a break or open circuit by saturating to either full-scale positive or full-scale negative output if the input leads are open circuited. The saturation condition was monitored continuously during experiments. The SCXI 1102 module can take a maximum of 32 thermocouples. All the channels are sampled in a multiplex mode, that is all the channels pass through a single amplifier and are sampled to a single DAQ board channel. The maximum sampling speed limit of this SCXI module is 333 kilo-samples per second. The specifications of the SCXI 1000 chassis and the SCXI 1102 module are given in Appendix IV.

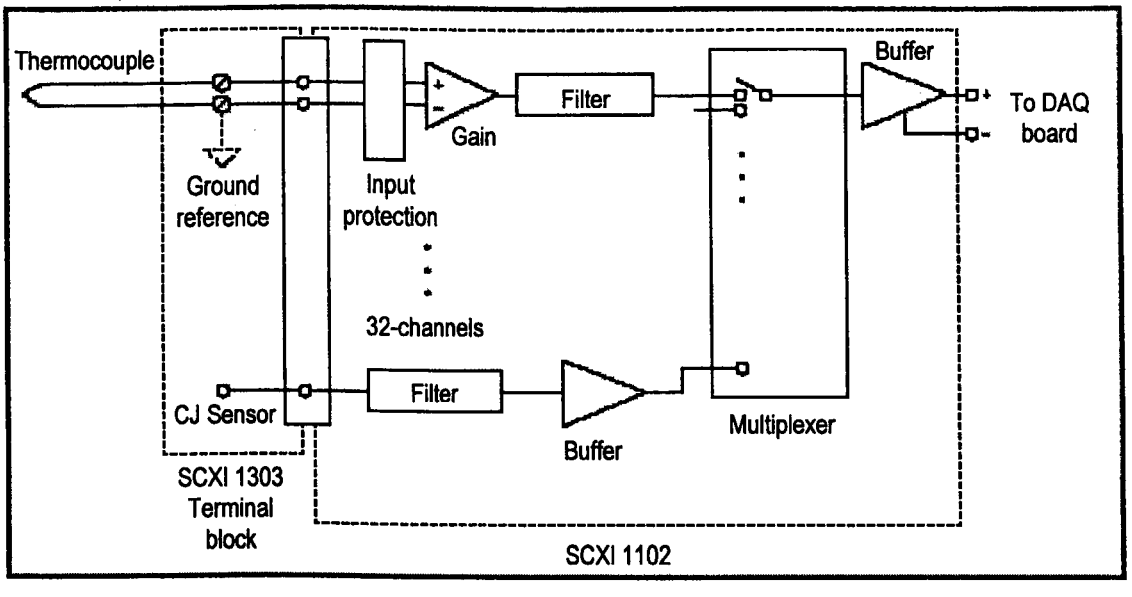

Figure 11.2. Block diagram of the SCXI 1102, NI [2003].

Thermocouple measurements require sensing of the cold junction, or reference temperature at the point where the thermocouple wires are connected to the measurement system. A shielded terminal block National Instruments SCXI 1303 was used to connect the thermocouples to the SCXI 1102 signal-conditioning module. This terminal block uses high precision thermistor to measure the CJ (cold junction) temperature, figure 11.2. The isothermal design of this block minimises temperature gradients across the screw terminal (see Appendix IV for terminal block specifications).

Thermocouple output voltages are highly non-linear with temperature and so polynomials are used to approximate the voltage-temperature curve. These polynomials are calculated knowing the type of thermocouple and the reference temperature. Labview functions are used to implement these polynomials. The polynomials are in the form,

$$T=a_0+a_1v+a_2v^2+.....+a_nv^n \qquad 11.1$$

Where v is the thermocouple voltage in volts, T is the temperature in degrees Celsius and a_0 through a_n are the coefficients for the K-type thermocouples. To reduce the computation time, the polynomials were computed in nested form.

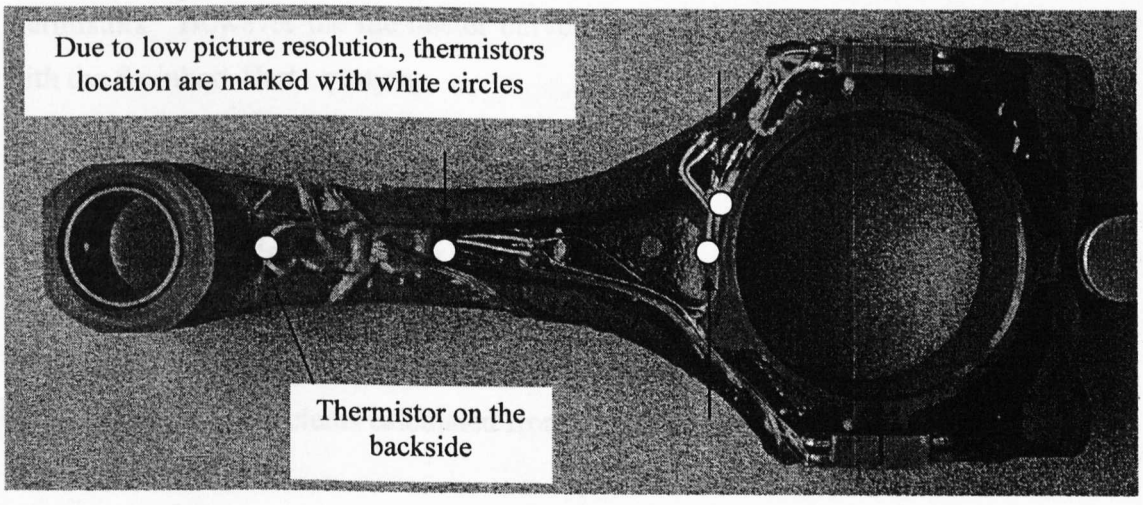

Figure 11.3. Instrumented connecting rod

b) *4 Analogue input channels* for measuring temperature via thermistors. These channels are also sampled and averaged in the same manner as the thermocouples. The thermistors measure temperature on the connecting rod surface at the following locations, figure 11.3;

- Near the strain gauges to determine apparent strain.
- Near small end bearing.
- Big end bearing housing temperature (2 analogue channels). One thermistor was fitted to the upper bearing housing at the centre position the other at a position 30° from connecting rod centre line, see figure 11.3.

Negative temperature coefficient thermistors were used for measuring temperature at the connecting rod surface. The resistance of negative temperature coefficient thermistors increases with a decrease in temperature. The main advantages of thermistors for temperature measurement are their extremely high sensitivity and relatively high resistance. The high resistance of the thermistor diminishes the effect of inherent resistance in the lead wires, which can otherwise cause significant errors.

Thermistors are highly non-linear devices and the resistance-temperature behaviour is dependent upon the manufacturing process. The manufacturers have not standardised thermistor curves and thus supply the resistance-temperature curves along with their thermistors. However the thermistor curve can be approximated relatively accurately with the Steinhart-Hart equation,

$$T(K) = \frac{1}{a_0 + a_1 \ln(R_T) + a_2 \left[\ln(R_T)\right]^3 + a_3 \left[\ln(R_T)\right]^5} \qquad 11.2$$

Where T(K) is the temperature in degrees Kelvin, R_T is the thermistor resistance and a_0, a_1, a_2, a_3 are the coefficients calculated from the resistance-temperature curve.

The thermistors were provided and installed by Federal Mogul Technology who also provided the thermistor curves given in Appendix III.

As thermistors are resistive devices a constant current source is required to measure the voltage developed across the thermistor. The level of the excitation current supplied to the thermistor is limited because of the phenomenon of self-heating. A 10μA supply current was used for the installed thermistors, as recommended by the manufacturer.

Federal Mogul Technology provided a custom-made signal-conditioning module for the thermistors. The module can measure 15 thermistor channels, each having its own amplifier, excitation supply and a low pass filter, and thus the channels are isolated from one another. The manufacturer set the level of amplifier gain and the excitation current. The measurement circuit is likely to pick up higher frequency noise from the environment, most commonly 50 or 60 Hz noise from the power lines. A low pass filter in the signal-conditioning unit removes such noise. The output signals from the signal-conditioning unit are connected directly to analogue channels of the PCI-6071E board via the National Instruments SCB-68 shielded connector block using shielded cable, figure 11.4.

c) *7 analogue input channels* for measuring piston surface temperature at different locations using thermistors. This channel was configured and programmed but was not used (see section 12.2, Further Recommendations).

d) *1 analogue input channel* to measure engine speed. Mean engine speed was measured through the magnetic pick-up sensor fitted very close to the engine flywheel. The signal is conditioned via the engine console unit. The output voltage from the console is then connected to analogue channel No. 16 of the PCI-6071E DAQ board via the SCB-68 connector block (see Appendix IV for connector block specifications), sampled at a rate of 6000 samples per second with an average of 3000 data points taken to minimise any quantization or noise error. 0-10 volts output from the engine console represent 0-6000 engine rpm.

e) *1 analogue input* channel for engine throttle position. This channel is sampled and averaged in the same way as the engine speed channel. This channel is directly connected to the PCI-6071E via input channel No. 18 using the SCB-68 connector block. Although there is no need for such a high sampling rate, this

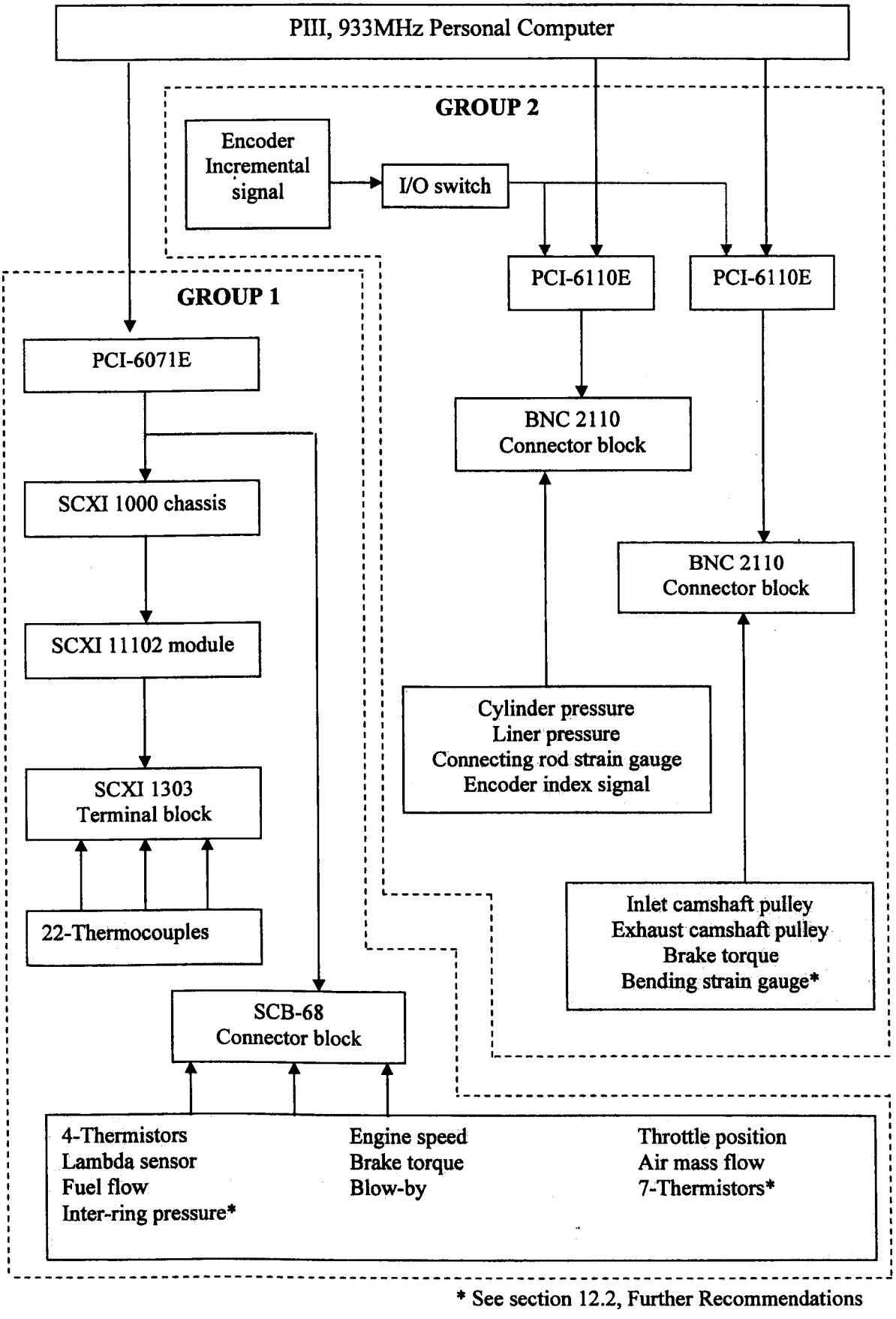

Figure 11.4. Ricardo Hydra DAQ system flow chart

channel is sampled along with the engine speed and torque channel under multiplex mode as the DAQ board does not allow two sampling rates at the very same time. The signal conditioning is carried out in the engine control console provided by Cussons. 0-10 volts indicate 0-100% throttle position.

f) *1 analogue channel* for the Lambda sensor. Lambda sensor is used to monitor the air/fuel ratio, indicating either the mixture is lean, stoichiometric or rich. This channel is also sampled along with the engine speed and throttle position channel under multiplex mode giving an average of 3000 data points. The signal is connected to the PCI-6071E through input channel No. 19 via the SCB-68 block. 0-0.4 volts indicate lean mixture, 0.5-0.9 volts indicate stichomythic and 1.0-2.0 volts indicate rich mixture.

g) *1 analogue channel* for engine brake torque measurement. Engine average brake torque is measured via a load cell connected to the swinging-arm DC dynamometer. The signal conditioning is carried out in the engine console unit giving an output voltage of ±10 volts. The sign indicates whether the engine is motored (negative sign) or fired (positive sign). The dynamometer 0-10 volts output indicates 0-50 Nm brake torque. This signal is connected to the PCI-6071E board via channel No. 17 and is sampled along with the speed and throttle channel at a rate of 6000 samples per second.

h) *1 analogue* channel for inlet air mass flow rate. Air induction mass flow rate is measured via the Cussons LFM (laminar flow meter) by measuring the pressure drop through the meter, which is proportional to the flow rate. The pressure drop is measured using a Furness differential pressure transducer (model FCO44). Due to the pulsing nature of airflow, sampling for several cycles is carried out and then mean pressure drop across LFM is determined. The sampling rate for this channel depends on the engine speed and is calculated as,

$$\text{sampling rate} = \frac{\text{engine rpm}}{60} \times 2000$$

thus giving a total of 2000 sample per revolution. An average of 20 engine revolutions (40 kilo-samples) is taken for the mass flow rate reading. 0-10 volts output signal is equal to 0-250 mm of water (pressure). This information along with the inlet air temperature is used to calculate the mass flow rate in g/sec. The signal is connected to channel No. 20 of the PCI-6071 E board.

i) *1 digital channel* for fuel flow. One of the two timer counter chips on the PCI-6071E was used to determine the amount of fuel injected per engine cycle by monitoring the injector valve opening time. During the injection event the fuel injector voltage drops from +5 volts to 0 volt and the time of injection is measured using 20 MHz 24-bit timer. An electrically driven pump keeps the fuel pressurised in a closed loop and the opening and closing of the solenoid valve controls the fuel flow. The fuel flow rate (g/sec) is calculated as,

$$\text{fuel flow rate} = \text{injection time} \times \text{specific gravity} \times \text{injector coefficient} \times \frac{(\text{speed rpm})}{120} \qquad 11.3$$

where injector coefficient represents amount of fuel in cc (cubic centimetre) injected per millisecond.

j) *1 digital input channel* to measure the blow-by flow rate. A 100 kHz counter/timer chip of the PCI-6071E board is used to calculate the blow-by flow rate by measuring the time period of the blow-by meter TTL signal generated once per revolution (1 revolution = 1 litre). The blow-by meter is basically an old dial gauge type gas meter with a very low capacity range, ideal for measuring blow-by flow rate for a single cylinder engine. Two magnetic pickup were fitted each on the dial and the pointer of this gas meter to generate a single TTL signal for one revolution.

The data from group 1 channels are updated within a second. The user selects the data record time. The 22 thermocouples are sampled with the help of National Instruments SCXI-1102 32-channel module connected to one of the channels of the PCI-6071E board. All the remaining analogue input channels of group 1 are sampled directly by.

the PCI-6071E DAQ board via the National Instruments SCB-68 connector block, including the two digital channels connected to the board counter/timer chips, figure 11.4. The PCI-6071E board has a maximum sampling rate of 1 MHz, 12-bit ADC and can handle 64 differential input channels. The board has one ADC and instrument amplifier and thus the analogue channels are sampled in multiplex mode, figure 11.5. The board also has 2 analogue output channels and 8 digital lines that in future could be used to control engine parameters such as speed, throttle position and engine load directly from the computer rather than from the engine console. One of the digital lines is used for an emergency shut down relay. The detailed specifications of PCI-6071E DAQ board can be seen in Appendix IV.

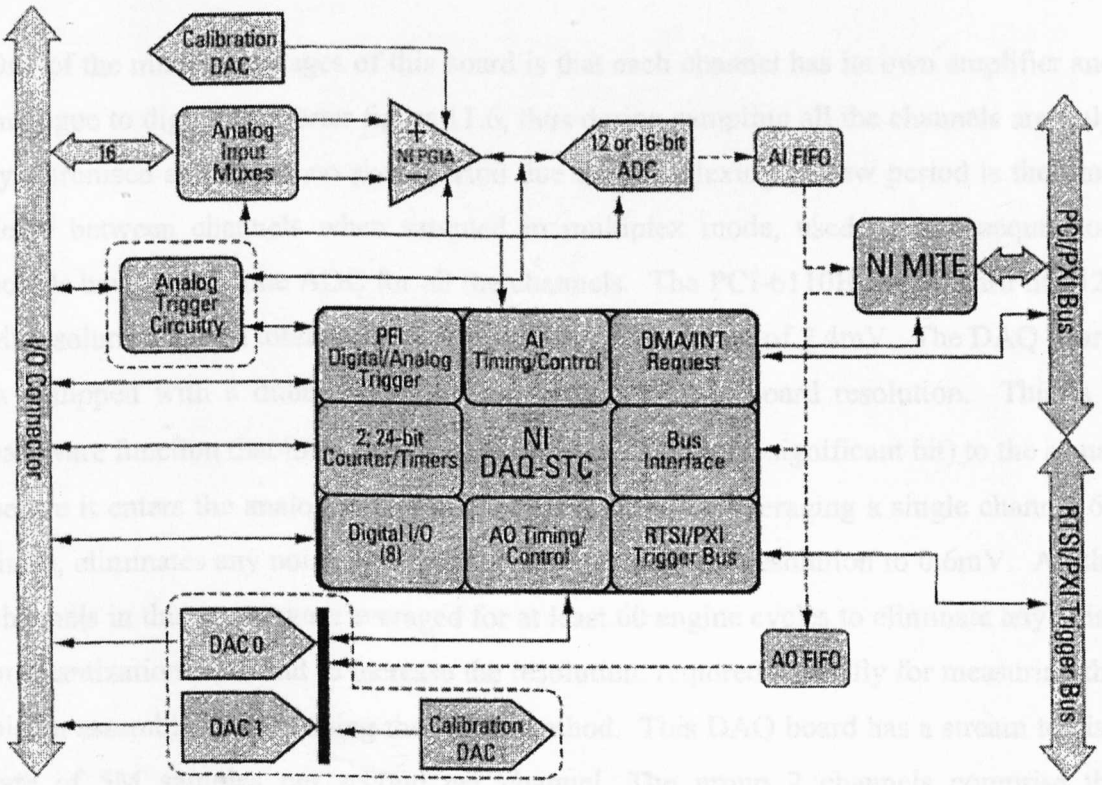

Figure 11.5. PCI-6071E block diagram, NI [2003].

11.3.2 GROUP 2 CHANNELS

Group 2 channels comprises eleven analogue/digital channels used to collect data for engine friction measurements. These channels require simultaneous sampling, as this is very important for synchronised engine component friction measurements. An optical encoder having a resolution of 720 pulses per revolution fitted to the engine crankshaft is used as an external sampling clock for these channels, thus relating every channel reading to the engine crank angle. Channels are sampled at every half a degree of crank angle, giving very accurate engine angular velocity and acceleration data. The sampling speed is dependent upon the engine speed, thus at 3000rpm each of the channels is sampled at a rate of 36000 samples per second. Group 2 channels are sampled via two National Instruments PCI-6110E DAQ boards having a sampling bandwidth of 5 MHz per channel, figure 11.4. The specifications of the PCI-6110E board can be found in Appendix IV.

One of the main advantages of this board is that each channel has its own amplifier and analogue to digital converter figure 11.6, thus during sampling all the channels are truly synchronised as there is no skew period due to multiplexing. Skew period is the time delay between channels when sampled in multiplex mode, used in data acquisition boards having only one ADC for all the channels. The PCI-6110E DAQ board has 12-bit resolution, thus a total range of 5 volts gives a resolution of 2.4mV. The DAQ board is equipped with a dither function used to increase the board resolution. This is a hardware function that introduces a noise of ±0.5 LSB (least significant bit) to the signal before it enters the analogue to digital converter and by averaging a single channel 60 times, eliminates any noise in the signal and increases the resolution to 0.6mV. All the channels in this group were averaged for at least 60 engine cycles to eliminate any noise or quantization error and to increase the resolution, required specially for measuring the piston assembly friction using the IMEP method. This DAQ board has a stream to disk rate of 5M samples per second per channel. The group 2 channels comprise the following,

a) *1 Analogue input channel* for cylinder pressure measurement. A piezo-electric pressure transducer Kistler 6067B, was used to measure cylinder pressure and the Kistler 5011B charge amplifier gain was adjusted so that 10 volts equalled 20 bars. By averaging the channel for 60 engine cycles the resolution is increased to 0.002

bars. Very high resolution and accuracy was needed for measuring instantaneous piston assembly friction. The details of the Kistler 6067B pressure transducer and Kistler 5011B charge amplifier are given in Appendix IV.

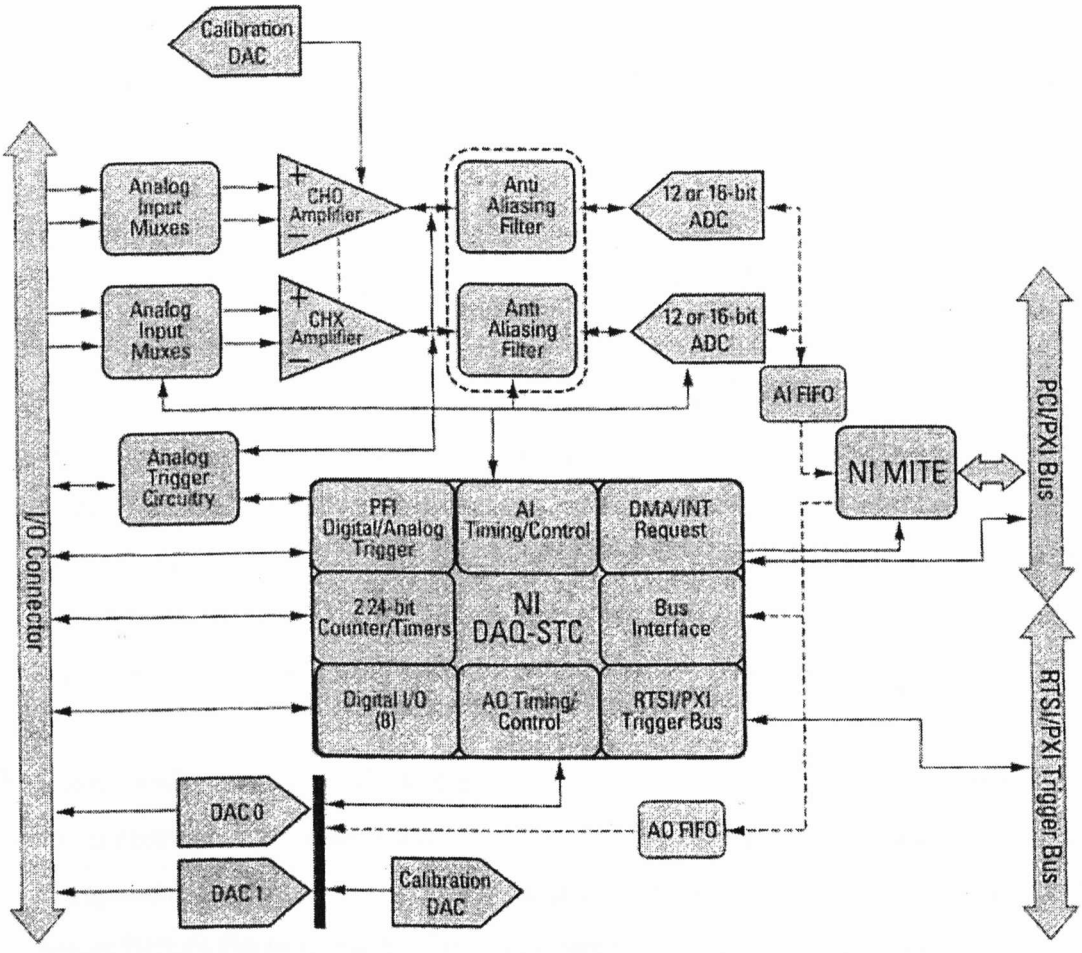

Figure 11.6. PCI-6110E simultaneous sampling board, block diagram, NI [2003].

b) *1 Analogue input channel* for the cylinder liner absolute pressure transducer. The pressure measured by the liner absolute pressure transducer Kulite XCE-152, is used to peg the cylinder pressure data. A Fylde 379TA high performance transducer amplifier was used as a signal-conditioning unit. With such an advanced data acquisition system the pressure is measured with a resolution greater than 0.001 bars. The details of the Kulite XCE-152 pressure transducer and Fylde 379TA amplifier can be found in Appendix IV.

c) *2 Analogue input channels* to measure inlet and exhaust camshaft drive torques, using the specially designed pulley torque transducers, T311-111, explained in detail in chapter three. The data from the transducers is used to measure valve train friction.

d) *1 Analogue input channel* for the strain gauge circuit measuring connecting rod axial force. With such an advanced DAQ system, having 12-bit ADC and a dither function, the resolution of the connecting rod force rises to nearly 2 N of force. The accuracy and resolution of the strain gauge reading is vital for piston assembly friction measurement. A Fylde 379TA transducer amplifier was used as a signal-conditioning unit for this channel.

e) *1 Analogue input channel* for engine brake torque measurement. Although the average engine brake torque is measured in group 1, the instantaneous brake torque is measured directly from the dynamometer load cell through the engine console unit, in this group for high accuracy. The brake torque data is used to calculate total engine friction. The DAQ board resolution, dither function and average of 60 engine cycles, increases the brake torque resolution to greater than 0.1Nm.

f) *1 Analogue input channel* for the optical encoder index signal. This signal is used to determine the crankshaft angular position, required to calculate engine component friction at every half a degree of crank angle. The details of the 755 series British Encoder can be found in chapter three and Appendix IV.

g) *1 Analogue input channel* for the strain gauge circuit measuring connecting rod bending force. This channel is used to measure the bending of the connecting rod required to measure instantaneous big end bearing friction. This channel was configured but is left for future work; see section 12.2 Further Recommendations (Chapter 12).

h) *1 Digital input channel* for the optical encoder incremental signal. A 20 MHz counter/timer chip on one of the PCI-6110E DAQ board is used to calculate the time period between each incremental pulse, required to calculate instantaneous crankshaft angular velocity and acceleration.

i) *2 Digital input channels* for the sampling clock signal. This is the same encoder incremental signal as mentioned above but is separately connected to the digital channel of each of the two PCI-6110E DAQ boards to act as an external clock for sampling the group 2 channels.

Two PCI-6110E simultaneous sampling boards are used to sample the group 2 channels, as each board can accommodate a maximum of 4 analogue input channels. All group 2 channels are connected to the board via a National Instruments BNC-2110 connector block (see Appendix IV for connector block specifications). The digital channel (encoder incremental pulse) is connected to the counter/timer of both the DAQ boards to act as a sampling clock, figure 11.4.

The PCI-6110E board simultaneously samples all the analogue channels but has no synchronisation link with the digital channels (e.g. optical encoder incremental signal). True synchronisation of analogue and digital channels is an important factor in measuring piston assembly friction by the IMEP method. Also as two PCI-6110E DAQ boards are used to sample the group 2 channels, it is important to synchronise the operation of both the boards so that all the channels are synchronised.

To synchronise the operation of both the PCI-6110E boards one digital channel from each DAQ board was configured to take the optical encoder incremental signal as an external sampling clock via an inline switch. The inline switch was used to trigger and synchronise the operation of both the boards. Before starting the sampling of all the group 2 channels, the Labview code was allowed to run thus executing the data acquisition boards, but with the inline switch off so that no signal from the encoder was allowed to pass to the data acquisition system. After both the data acquisition board were ready and waiting for the signal from the sampling clock (encoder incremental signal), the encoder inline switch was turned on allowing all the channels on both the boards, analogue and digital, to sample instantaneously and simultaneously.

The initial tests indicated that engine spark noise was induced in the encoder signal jeopardising the synchronisation operation. Isolating the complete encoder circuit from

the mains and using a rechargeable battery to power the encoder solved this noise problem.

Thus for group 1 and group 2 a total of three DAQ boards were used. The Labview programming language was used to code the operation of the DAQ boards and for post processing the data.

11.4 INTRODUCTION TO LABVIEW

A graphical based programming language called Labview (version 5.1) was used to code the DAQ program. Like the DAQ boards, National Instruments created Labview. It was chosen because it is well integrated with the National Instruments hardware.

11.4.1 BASIC CONCEPTS IN LABVIEW

Labview is a program development application unlike C or BASIC languages, which are text-based to create lines of codes; Labview uses a graphical programming language, G, to create programs in block diagram form.

Labview provides the flexibility of a powerful programming language without the associated difficulty and complexity, because its graphical programming methodology is inherently intuitive. It has extensive library functions and subroutines for most programming tasks, such as data acquisition, hardware interfacing and data storage.

Labview has special features to debug the code, such as Execution Highlights and the Probes. Execution Highlights are used to run the code slowly, step by step to debug the code and the Probes are used to check intermediate values as the code executes and can be used to check parts of the code or function giving right or wrong results. Labview is multithreaded software so unlike other programming languages it can perform more than one task at a time. This feature makes Labview codes more difficult to understand by other than the programmer.

11.5 SOFTWARE SPECIFICATIONS

Two completely independent programmes were written for sampling and logging data for group 1 and group 2 channels called "DAQ Ricardo Hydra Engine, new.vi" and "COMBINE all 9 channels.vi" respectively. The working files can be seen in Appendix V.

11.5.1 LABVIEW CODE FOR GROUP 1 CHANNELS

One main disadvantage of the DAQ boards available in the market is that they cannot sample analogue channels at two different rates at the same time. In group 1, four different scan rates are required to sample the channels. The only way to achieve this with one DAQ card is to use a sequential method. In this method the channels are sampled in four main steps. For each step, the related channels are sampled at a single required scan rate. The way this method works is described below.

- As soon as the Labview code for group 1 is executed, the timer/counter chip on the PCI-6071E is initialised and starts scanning the blow-by meter until the data acquisition is stopped.

- The data log file starts to record information in ASCII format, which can then be imported into a spreadsheet program for further analysis.

- In order to update all the channels within one second and at the same time record data and to perform post processing it was not possible to sample all the channels at a single high-speed (6000 samples per second) sampling rate. Thus only a few channels were sampled at high rates apart from the temperature channels. To sample channels at different rates a sequential method was used. In this method the board starts sampling the required channels at a single scan rate. When the required number of scans is completed, the board resets and starts scanning the other channels at a different scan rate. A total of four sequences were used to scan the channels, described below (see figure 11.7).

  - Sequence 1: Sampling four channels speed, torque, throttle and lambda position at a scan rate of 6000 samples per second per channel.

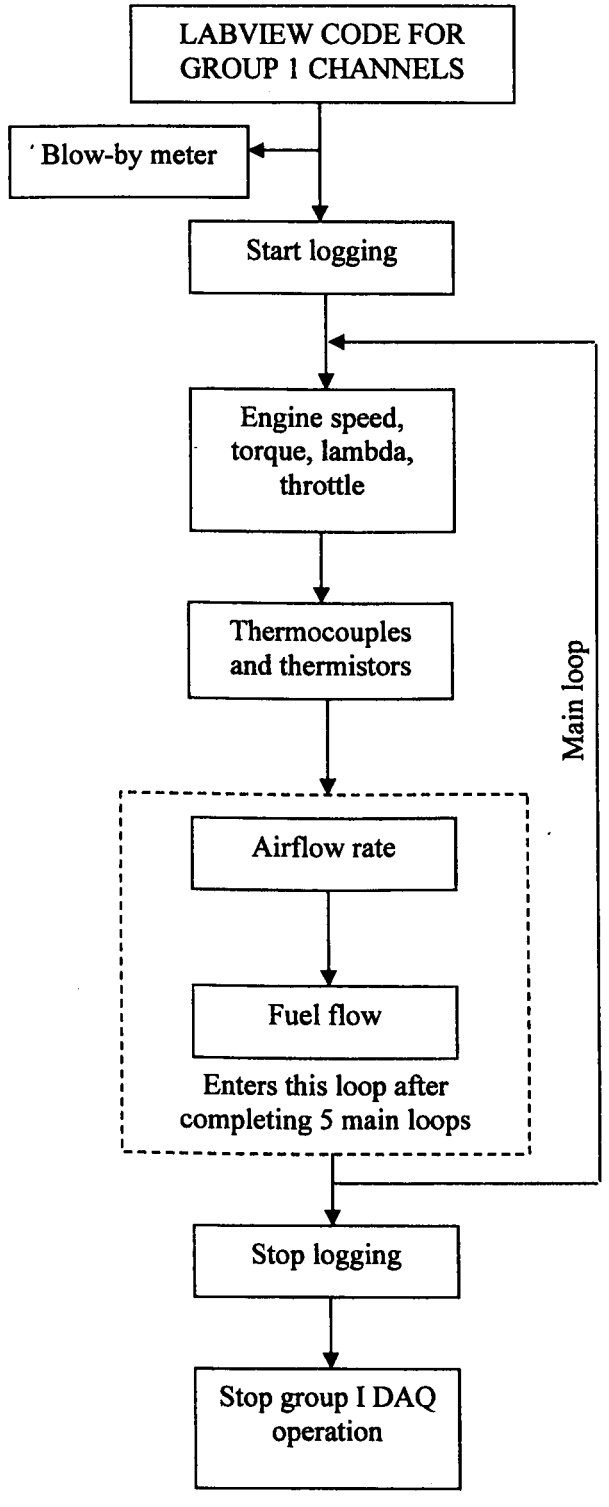

Figure 11.7. Group 1 channels Labview code flow chart.

- Sequence 2: Twenty two thermocouples plus cold junction and four thermistors sampled at a scan rate of 300 samples per second.
- Sequence 3: The airflow rate was scanned at a rate, dependent on the engine speed. This channel was scanned after every 5 main loops.
- Sequence 4: The counter/timer calculated the fuel flow rate and the information was forwarded. This channel was also scanned after every 5 main loops.

- All the above channels data were then analysed, processed and displayed. Depending on the data recording time interval, the information was also stored on the hard disk of the personal computer.

- The loop started again from Sequence 1. This main loop continued until the user stopped the DAQ operation.

11.5.2 LABVIEW CODE FOR GROUP 2 CHANNELS

The scanning of the group 2 channels is quite straightforward. As mentioned earlier the optical encoder incremental signal was used as a sampling clock for logging these channels.

- On executing the Labview program all the group 2 channels on both the PCI-6110E boards along with the optical encoder pulse period were simultaneously and instantaneously sampled at a rate dependent on the engine speed.

- After the scanning was completed the data was transferred from the system memory onto the hard disk.

- The data was logged on the hard disk in the ASCII format, which could then be imported into spreadsheets or other programs for further analysis.

After collecting and logging the above data, a separate post-processing program called "Read and rec valve-piston-bearing powerloss.vi" (working file given in Appendix V) was used to calculate and log the following information:

- Instantaneous piston assembly friction force.
- Inlet and exhaust camshaft friction torque over cam profile period only.
- Inlet and exhaust camshaft friction torque over complete cam cycle.
- bmep (break mean effective pressure).
- pmep (pumping mean effective pressure).
- Total friction fmep (friction mean effective pressure).
- imep (indicated mean effective pressure).
- Piston assembly friction power loss.
- Valve train friction power loss.
- Engine bearing friction power loss.
- Total engine friction power loss.
- Pumping power loss.
- Brake power.
- Indicated power.

11.6 CONCLUSIONS

To measure the engine power loss at component level, a high-speed synchronised simultaneous sampling data acquisition system has been developed. The channels were divided into two groups as a function of their sampling rate. Data from more than fifty different transducers were sampled and analysed using Labview software. The information from low speed group 1 channels was mostly used for the validation of FLAME engine friction model and the data from high-speed group 2 channels was purely used for measuring total and component engine friction.

For smooth operation of the DAQ system both National Instruments hardware and software was used for greater compatibility and programming flexibility.

Chapter twelve

CONCLUSIONS AND RECOMMENDATIONS FOR FURTHER WORK

12.1 CONCLUSIONS AND RECOMMENDATIONS

The main aim of this research project was to, for the very first time, measure frictional losses in all the three main tribological components of a fried engine and to use the findings to validate and specify areas for further improvement of the FLAME engine friction model. The model comprises three friction models addressing each of the tribological parts of the valve train, piston assembly and engine bearings. The experimental engine used for this project was a Ricardo Hydra single cylinder four-valve gasoline engine derived from a standard production, four-cylinder, GM 2.0 litre engine. The conclusions for each of the aims mentioned above and in section 1.2, quoted in italics below, are as follows,

12.1.1 ENGINE VALVE TRAIN FRICTION

Develop an experimental technique to measure camshaft friction torque and the findings to be used to validate the FLAME engine valve train friction model.

Experiments have been carried out on the Hydra engine to measure valve train friction loss under different engine operating conditions. The experiments were carried out under both motored and fired conditions and the effect of different lubricants on engine valve train was analysed. The outcome of the valve train friction research is as follows,

- A new experimental technique has been developed using a specially designed pulley torque transducer that allows instantaneous and mean camshaft friction torque to be measured. The technique was designed in such a way that no modification of engine valve train was required. The installation procedure of

the original engine cam drive pulley and the torque transducer was identical. The belt loading had no detrimental effect on the pulley torque transducer output signal.

- The technique has been successfully applied to the inlet and exhaust camshafts of a single cylinder engine with direct-acting overhead camshafts acting on flat faced, hydraulic lash adjusted bucket followers. As the technique was implemented on a single cylinder engine, for the very first time, detailed study of friction torque during valve opening and closing was possible on a real fired engine. The technique allowed valve train friction measurements not only under motored conditions but also under fired conditions, taking into consideration the engine speed variation throughout the complete engine cycle as the Hydra being a single cylinder engine.

- Engine valve train friction measurements were performed on four different lubricants: SAE 0W20 with and without organic friction modifier; SAE 10W40 and SAE 5W30 with friction modifier. It was concluded that the valve train friction torque decreased with increasing engine speed, in part due to the improved lubrication conditions at the cam/follower interface, caused by increase in entraining velocity, and also because of the load reduction at the cam nose region as the follower has a negative acceleration around this area. Regarding lubricant temperature, at low engine speeds the trend for all four lubricants was generally an increase in friction with increasing lubricant temperature. But at higher engine speeds, the fluid film lubrication contribution increased resulting in a reduction in friction at lower lubricant temperatures but a sharp increase was observed in friction at higher lubricant temperatures as the mixed to boundary lubrication becomes dominant. The results also showed a reduction in friction for lubricants containing friction modifier, particularly at higher lubricant temperatures.

- For the validation of the FLAME valve train friction model, the experimental results under motored conditions for SAE 0W20 with and without friction modifier were compared with the predicted results. It was concluded that at

engine speeds of 1500rpm and above, the model predicted friction of the same order as the experimental data. However, there was a much reduced sensitivity to engine speed and temperature in the predictions. This clearly showed that the model needs some modification through the application of EHL theory at the cam/follower interface. One of the areas that may improve the model is the introduction of the Roelands equation instead of Barus equation for the pressure-viscosity relationship as Barus relationship becomes inaccurate at high pressures. Also the variation of temperature is more likely to influence the limiting friction coefficient and thus the use of fixed limiting friction coefficient for given oil across all operating conditions needs some reconsideration. Also, the experimental instantaneous valve train friction revealed that at low engine speeds and high lubricant temperatures the camshaft bearings might encounter mixed lubrication, which is not taken into account in the model.

- Experiments were also carried out under fired conditions and was found that the valve train friction measurement under fired conditions was greater than under motored conditions. The difference was mainly due to cylinder gas force acting on the exhaust valve during valve opening. This results in the camshaft performing extra work to open the valve and thus increasing the load at the cam/follower interface, whereas no difference in drive torque was found for inlet camshaft. The experimental results indicate that the difference between motored and fired valve train friction increases as engine speed and load increases. The FLAME valve train friction model is insensitive to cylinder pressures, which the experiments, as mentioned above, showed affects the exhaust camshaft drive torque and thus the valve train friction.

12.1.2 ENGINE PISTON ASSEMBLY FRICTION

Experimentally measuring piston assembly friction under fired conditions using advanced data acquisition system and to use the results to validate the FLAME piston assembly friction model.

- The IMEP method was chosen for application to the Hydra engine to measure piston assembly friction, as no major engine modification was required. The forces acting on the piston assembly were carefully measured by monitoring the cylinder pressure, crankshaft angular velocity and strain on the connecting rod. A water-cooled piezo-electric pressure transducer was used to measure relative pressures in the cylinder and a miniature resistive absolute pressure transducer, fitted in the cylinder liner, was used to peg the cylinder pressure data to determine absolute cylinder pressure values. A 24-wire grasshopper linkage guided the signal wires at from the engine crankcase. The experiments were carried out under different engine operating conditions and the performance of different lubricants was analysed. Both mean and instantaneous piston assembly friction was measured under motored as well as fired conditions. As the method was applied on a single cylinder engine, the effect of crankshaft angular acceleration on the piston assembly inertial force was taken into account. Because of the complex nature of this technique, an advance data acquisition system was designed/developed, giving special attention to the synchronisation and simultaneous sampling of analogue and digital channels.

- Piston assembly friction was measured for two different lubricants: SAE 5W30 with friction modifier and SAE 0W20 without fiction modifier. For both the lubricants it was concluded that at low lubricant inlet temperatures hydrodynamic lubrication was dominant whereas at higher inlet lubricant temperatures mixed to boundary became more influential. At any engine speed the averaged piston assembly friction data correlated very well with the Stribeck curve, a decrease and then increase in friction as lubricant temperature changed from low to higher values. A rapid change of lubrication regime from boundary to hydrodynamic was clearly seen in each piston stroke due to the change in piston velocity. During mid-stokes, hydrodynamic lubrication contribution was higher whereas near the piston dead centres, boundary to mixed lubrication became more dominant. At low lubricant inlet temperatures the average piston assembly friction for SAE 5W30 with friction modifier was higher than for SAE 0W20 without friction modifier due to higher shear losses. However a completely opposite effect was seen at higher lubricant temperatures indicating

the benefit of friction modifier and the higher viscosity lubricant SAE 5W30, when the contribution of mixed to boundary lubrication is higher.

- For the validation of the FLAME piston assembly friction model the experimental results for SAE 0W20 without friction modifier were compared with the predicted results. It was concluded that the predicted results correlated very well with the measured results, especially at higher lubricant inlet temperatures. The predicted friction loss from compression rings increased as lubricant inlet temperature increased at any engine speed, whereas no effect of lubricant viscosity was seen on the performance of oil control ring as FLAME assumes it operates under boundary lubrication regime, which may not be the case. The analysis of this ring can be improved by including it within the more developed compression ring analysis. The piston skirt friction was predicted using both a concentric piston/liner (FLAME) and the more realistic method (Leeds Piston Skirt Lubrication and Dynamics Analysis model) incorporating piston secondary motion. The results clearly indicates that the former method over-predicts friction loss due to high shear loss whereas the later more realistic method showed better correlation with the measured data and should be incorporated directly into the FLAME piston assembly friction model.

- Piston assembly friction measurements were also carried out under motored conditions and were found to be lower than under fired conditions. The difference in results was mainly due to the effect of combustion pressure and temperature on the piston assembly and was most clearly seen during the power stroke.

12.1.3 ENGINE BEARING FRICTION

Determine engine bearing friction and to use the experimental data to validate the FLAME engine bearing friction model.

- An innovative experimental technique has been developed that allows for the very first time, the evaluation of engine crankshaft bearing friction under fired

conditions without any major engine modification. The PV-diagram was used to measure total engine friction and by determining piston assembly friction using IMEP method and valve train friction using specially designed pulley torque transducers, engine bearing friction was determined by subtraction.

- Two different lubricants, an SAE 0W20 without friction modifier and SAE 5W30 with friction modifier, were used to evaluate engine bearing friction under different engine operating conditions. The results clearly showed for both the lubricants, a decrease in engine bearing friction with increase in lubricant temperature at any engine speed, indicating that the engine bearings operate mostly under hydrodynamic lubrication conditions. A sharp decrease in friction was seen at higher lubricant inlet temperature. The lubricant with higher viscosity, SAE 5W30 generated higher bearing friction than the lower viscosity lubricant, SAE 0W20, clearly showing the benefit of low viscosity lubricant for engine bearing performance.

- The bearing friction results for SAE 0W20 without friction modifier were used for the validation of the FLAME engine bearing fiction model. The results obtained from three different engine bearing friction models (short bearing theory, finite width method and Petroff zero eccentricity method) were compared with the experimental results. It was concluded that the theoretical results obtained via the short bearing for the π film case were very close to the measured values.

- For the engine bearing friction experiments lubricant temperature was measured at two different locations: at inlet to the engine crankcase, assumed to be equal to the main bearing inlet lubricant temperature, and the big end bearing upper cup near surface temperature, assumed to be equal to the lubricant inlet temperature for the big end bearing. For very accurate bearing friction analysis it is vital to measure true bearing lubricant temperatures by having thermocouples placed very close to the bearing surface. The FLAME engine bearing friction model can be further improved by taking into account some of the parameters that can effect engine crankshaft bearing performance, such as

elastic deformation of bearing, piezo-viscous effects and the friction contribution from the crankcase bearing seals.

The engine component friction results clearly indicate that the friction contribution from the engine bearings was the highest, compared to the valve train and piston assembly at low lubricant inlet temperatures, whereas the piston assembly contributed the most at higher lubricant temperatures. The effect of two different lubricants, an SAE 0W20 without friction modifier and SAE 5W30 with friction modifier, on the percentage contribution of the friction loss from each component was also analysed in detail. Overall the benefit of the higher viscosity lubricant was clearly observed at high lubricant temperatures and the advantage of friction modifier at high lubricant temperature was clearly experienced on the valve train friction.

Overall the predicted total engine power loss results generated using the FLAME engine friction model, showed a good correlation with the experimental results especially at high lubricant inlet temperature and engine speed. It is concluded that the predicted results are in good agreement with the experimental results and the comparison validated the FLAME engine friction model.

12.2 NOVEL ASPECTS OF THE PROJECT

For the very first time;

- An experimental system has been developed to measure simultaneously the friction losses in all the three main tribological components of a real engine under fired conditions.
- The percentage frictional power loss contribution of piston assembly, valve train and engine bearing of a fired engine was analysed, examining the effect of speed and lubricant temperature on the friction distribution.
- Instantaneous measurement of valve train friction allowed detailed power loss analysis of both the inlet and exhaust camshaft friction, allowing detailed study of the difference in friction under motored and fired engine conditions without any modification to the engine valve train layout.
- Engine bearing friction was determined in a real fired engine under fired conditions without any major engine modification.

- Experiments were carried out under different engine operating conditions and the data was generated during the tests for the total engine and component friction. This data along with the detailed input engine data collected for the FLAME engine friction model is of immense importance to the automotive and lubricant industries and engine component manufactures, including the sponsored companies, allowing to validate and improve their own engine friction models.

12.3 FURTHER RECOMENDATIONS

- To improve the performance of the engine and to screen lubricants, one of the areas that may need attention is the accurate control of the lubricant temperatures on the Ricardo Hydra engine. The Hydra engine has an external sump and lubricant cooling/heating system. This single cylinder Hydra engine is relatively more exposed to environment (atmospheric temperature) than a multi-cylinder engine fitted in the vehicle and to keep the lubricant and coolant temperature stable for such an engine is relatively difficult. In the present system the lubricant temperature is controlled by an external oil bath monitoring the bath temperature only and with such a system, measurement of engine component friction under very similar lubricant temperature for different lubricants is relatively very difficult. Thus it is important to have a very stable and accurate lubricant and coolant heating/cooling system using advanced PID (proportional, integral and derivative) controllers and/or to have the engine fitted in a climate controlled test cell.

- The present experimental system can be used to investigate the power loss at component level at various engine speeds and loads. The analysis of cold start conditions and wear studies at component level could be carried out using this system. Such data would be of great value to the various stakeholders in engine friction.

- For the detailed validation of the FLAME engine bearing friction model and to analyse the influence of different lubricants on each of the engine bearings measurement of friction loss generated in each engine bearing independently would be a very powerful tool. A very novel experimental technique has been developed to determine small end and big end bearing friction indirectly by measuring the bending of the connecting rod, as all the other forces acting on the connecting rod are known. A pair of strain gauges were fitted parallel to the neutral axis of the connecting rod to measure only bending of the connecting rod, figure 12.1. Jaguar Cars Ltd carried out a finite element analysis on the connecting rod to determine the most appropriate place for fitting bending strain gauges, figure 12.2. The connecting rod was calibrated for bending by Federal Mogul Technology for the range 0-100 Nm. But during the experiments it was found that for the engine speed range of 800rpm to 2000rpm the bending moment varied between 2 to 3 Nm. Although the output signal was relatively clean, little confidence would be placed in the calibration at such low bending moments. Recalibration was thus necessary but due to time limitations of this research project, this task was left for future study. Using this technique instantaneous and mean big end and small end bearing friction can be determined. Knowing the friction contribution from these two bearings and the total engine bearing fiction (Chapters eight and nine), average main bearing friction can be determined. Knowing all the forces acting on the connecting rod, the instantaneous main bearing friction can also be calculated.

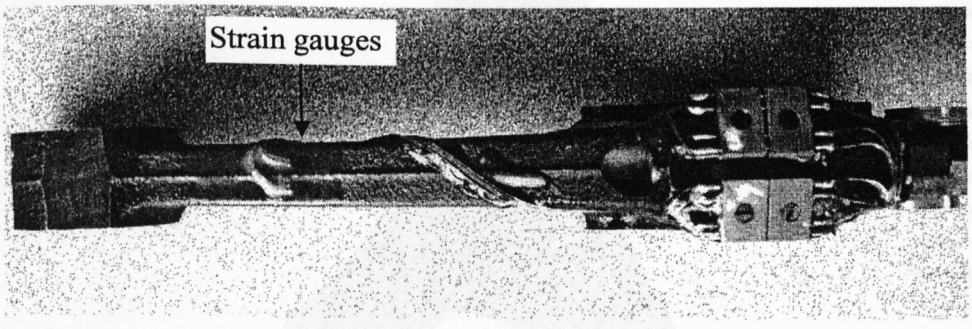

Figure 12.1. Instrumented connecting rod for bending moment measurements.

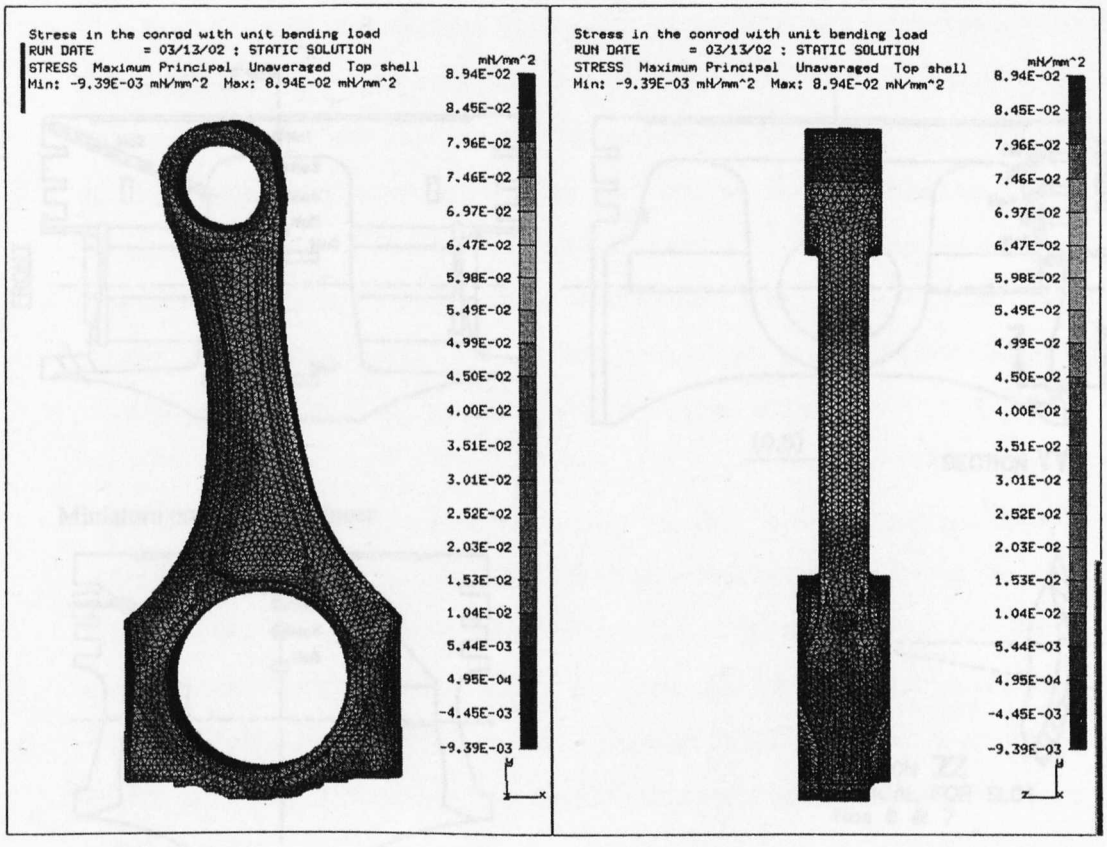

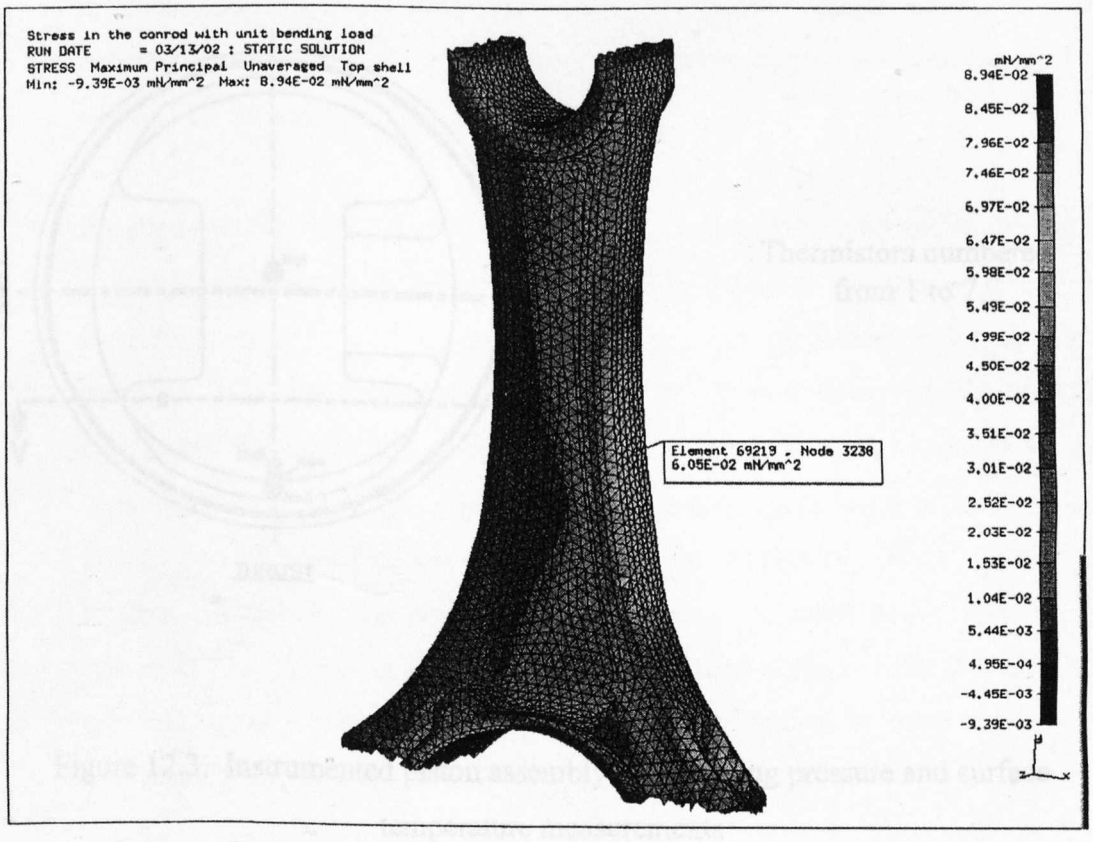

Figure 12.2. Connecting rod stress analysis under bending load.

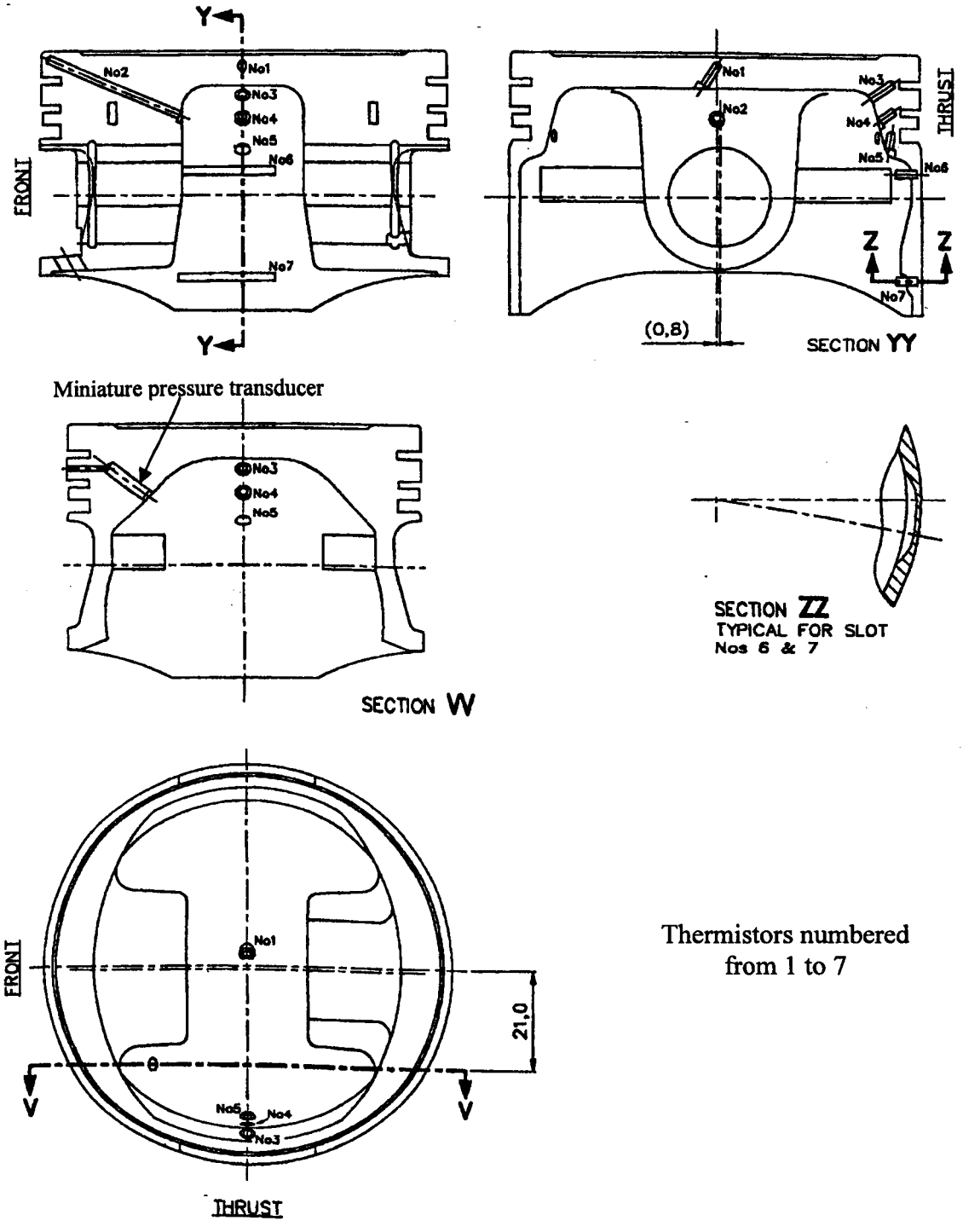

Figure 12.3. Instrumented piston assembly for inter ring pressure and surface temperature measurements

- A piston was also instrumented during this research project for the validation of the piston assembly inter-ring gas pressure model, described in chapter five. A miniature resistive absolute pressure transducer (Kulite XCE-152) was mounted in the piston land between the first and second ring to measure inter-ring absolute pressures. The piston assembly was also instrumented with seven thermistors to measure temperatures at different locations, figure 12.3. Federal Mogul Technology carried out the instrumentation work. Again due to time constraints this part of the research is left for future studies.

- The present grasshopper linkage system can be used to measure the piston eccentricity by using miniature inductive gap measuring sensors on the top and bottom edge of the piston skirt, monitoring the eccentricity and thus the clearance between the piston/liner. The data can then be used to validate the Leeds Piston Skirt Lubrication and Dynamics Analysis model for calculating piston skirt friction loss, keeping in mind that the piston/liner clearance can be affected by piston skirt elastic deformation and bore distortion. The same instrumented piston, mentioned above, and grasshopper linkage arrangement can be used to connect the wires from the sensors to the signal conditioning and data acquisition system.

- Average lubricant film thickness in the big end bearing can be measured by using the capacitance technique by electrically isolating the bearing shell from the bearing cup. Using the same miniature pressure transducer as for the piston assembly inter-ring gas pressure, but with a higher pressure range, the lubricant film pressure at a certain point in the big eng bearing can be measured. The same connecting rod grasshopper linkage arrangement used in this research project can be used to draw out wires from the crankcase. Thus knowing the bearing friction via the bending strain gauges mentioned above, the average lubricant film thickness using the capacitance technique and the lubricant film pressure using a miniature pressure transducer, advanced in-depth study of big end bearing lubrication analysis could be carried out.

- The present friction measurement system can be used as a powerful tool for screening different engine lubricants, studying the effect of different additives on each of the three main components. The system can be used to improve lubricant formulations and to analyse the performance of different engine component design, materials and coatings. This system was developed using more than fifty different sensors and using advanced high-speed simultaneous sampling synchronised data acquisition system. The instrumentation used in this system can be fitted to a multi-cylinder engine and significant analysis work can be carried out on modern production engines, including diesel engines.

REFERENCES

Amstrong, W.B., Buck, B.A., 1981, "Valve Gear Energy Consumption: Effect of Design and Operation Parameters", SAE Paper 810787.

Ball, W.F., Jackson, N.S., Pilley, A.D., and Porter, B.C., 1986, "The Friction of a 1.6 Litre Automotive Engine Gasoline and Diesel", SAE Paper 860418.

Ball, A.D., 1988, "A Tribological Study of the Design and Performance of Automotive Cams", Ph.D. Thesis, Dept. of Mechanical Engineering, University of Leeds, UK, pgs. 250.

Baniasad, M.S., and Emes, M.R., 1998, "Design and Development of Method of Valve-Train Friction Measurement", SAE Paper 980572.

Bates, T.W., and Benwell, S., 1988, "Effect of oil Rheology on journal bearing performance Part 3 – Newtonian oils in the connecting rod bearing of an operating engine", SAE Paper 880679.

Bates, T.W., and Evans P.G., 1985, "Effect of oil Rheology on journal bearing performance: Part 1 – Instrumentation of the big-end bearing of a fired engine", Proc. J.S.L.E. International Tribology Conference., Vol. 2, pp 445-450.

Bates, T.W., Fantino, B., Launay, L., and Frene, J., 1990, "Oil film thickness in an elastic connecting rod bearing: Comparison between theory and experiment", STLE, Vol. 33, pp. 254-266.

Bates, T.W., Willamson, J.A., Spearot, J.A., and Murphy, C.K., 1986, "A correlation between engine oil Rheology and oil film thickness in engine journal bearing", SAE Paper 860376.

Booker, J.F. 1965, "A table of the journal bearing integral", Journal of basic engineering., Trans. ASME, Series D, Vol. 187, pp 533-535

Booker, J.F. 1965, "Dynamically loaded journal bearings: Mobility method of solution", Journal of basic engineering., Trans. ASME, Series D, Vol. 187, pp 537-546

Booker, J.F. 1971, "Dynamically loaded journal bearings: Numerical application of the Mobility method", J.Lub.Tech., Trans. ASME, Series F, Vol. 93-94, pp 168-176

Brown, S.R. and Hamilton, G.M., 1978, "Negative pressures under a lubricated piston ring", J. Mech. Eng. Sci., Vol. 20, No. 1, pp 49-57.

Brown, W.L., 1967, "Methods for Evaluating Requirements and Errors in Cylinder Pressure Measurement", SAE Paper 670008.

Brunt, M.F.J., Emtage, A.L., 1996, "Evaluation of IMEP Routines and Analysis Errors", SAE Paper 960609.

Cameron, A., 1981, "Basic lubrication theory", 3rd edition, Ellis Horwood series in engineering science.

Cerrato, R., Gozzelino, R. and Ricci, R., 1984, "A single cylinder engine for crankshaft bearings and piston friction losses measurement", SAE Paper 841295.

Cho, M.R., Han, D.C. and Choi, J.K., 1999, "Oil film thickness in engine connecting-rod bearing with consideration of thermal effects: Comparison between theory and experiment", J.Trib., ASME, Vol. 121, pp 901-907.

Cho, S., Choi, S. and Bae, C., 2000, "Frictional modes of barrel shaped piston rings under flooded lubrication", Tribology International 33, pp 545-551.

Choi, J.K, Lee, J.H., and Han, D.C., 1992, "Oil film thickness in engine main bearings: Comparison between calculation and experiment by total capacitance method", SAE Paper 922345.

Choi, J.K, Min, B.S., and Han, D.C., 1993, "Effect of oil aeration rate on the minimum oil film thickness and reliability of engine bearing", SAE Paper 932785.

Choi, J.K, Min, B.S. and Oh, D.Y., 1995, "A study on the friction characteristics of engine bearing and cam/tappet contacts from the measurement of temperature and oil film thickness", SAE Paper 952472.

Craig, R.C., King, W.H., and Appeldoorn, J.K., 1982, "Oil film thickness in bearing of a fired engine, Part II: The bearing as a capacitor", SAE Paper 821250.

Crane, M.E., and Meyer, R.C., 1990, "A Process to Predict Friction in an Automotive Valve Train", SAE Paper 901728.

Dickenson, A.N., 2000, "Engine Friction Modelling Considering Lubricant Tribological Characteristics", Ph.D. Thesis, School of Mechanical Engineering, University of Leeds, UK, pgs. 232.

Dowson, D., and Higginson, G.R., 1977, "Elastrohydrodynamic Lubrication", SI Edition, Pergamon Press, Oxford.

Dowson, D., and Toyoda, S., 1979, "A Central Film Thickness Formula for Elastrohydrodynamic Line Contacts", Elastohydrodynamics and Related Topics, Proc. 5th Leeds-Lyon Symposium on Tribology, Mechanical Engineering Publications, London, pp. 60-65.

Dowson, D., Harrison, P., and Taylor, C.M., 1986, "The Lubrication of Automotive Cams and Followers", Mechanisms and Surface Distress, Proc. 12th Leeds-Lyon Symposium on Tribology, Butterworths, London, pp. 305-322.

Dowson, D., Taylor, C.M., and Zhu, G., 1989, "An Experimental Study of the Tribology of a Cam and Flat-faced follower", 2nd Int. Conf., Combustion Engines - Reduction of Friction and Wear, Instn. Mech. Engrs. Conf. Pub., London, Paper C375/025, pp. 97-108.

Dursunkaya, Z., Keribar, R. and Ganapathy, V., 1994, "A model of piston secondary motion and elastohydrodynamic skirt lubrication", Jnl. Tribology. Trans. ASME., Vol. 116. pp 777-785.

Dyson, A., and Naylor, H., 1960, "Application of the Flash Temperature Concept to Cam and Tappet Wear Problems", Proc. Instn. Mech. Engrs., Automotive Div., Paper No. 8, pp. 255-280.

Eriksson, L., 1998, "Requirements for and a Systematic Method for Identifying Heat Release Model Parameters", SAE Paper 980626.

Eweis, M., 1935, "Reibungs und Undichtigkeitsverluste an Kolbenringen", Forschungshefte des Vereins Deutscher Ingenieure, No. 371

Filowitz, M.S., King, W.H., and Appeldoorn, J. K., 1982, "Oil film thickness in a bearing of a fired engine", SAE Paper 820511.

Forbes, J.E. and Taylor, E.S., 1943, "A Method of studying piston friction", NACA Wartime Report, March 1943.

Frene, J., Nicolas, D., Degueurce, B., Berthe, D. and Godet, M., 1997, "Hydrodynamic lubrication, bearing and thrust bearings", Elsevier Science Publishers, ISBN: 0-444-82366-2.

Furuhama, S. and Takiguchi, M., 1979, "Measurement of piston frictional force in actual operating diesel engine", SAE Paper 790855.

Goenka, P.K., 1984, "Dynamically loaded journal bearings: Finite element method analysis", J.Trib., Trans. ASME, Vol. 106, No.1 pp 429-439.

Gulwadi, S.D., and Shrimpling, G., 2003, "Journal bearing analysis in engines using simulation techniques", SAE Paper 2003-01-0245.

Harrison, P., 1985, "A study of the Lubrication of Automotive Cams", Ph.D. Thesis, School of Mechanical Engineering, University of Leeds.

van Helden, A.K., van der-Meer, R.J., van Sfaaden, J.J., and van Geldereren, E., 1985, "Dynamic friction in cam/tappet lubrication", SAE Paper 850441.

Hertz, H., 1882, "On the contact of elastic solids", J. Reine und Angewandte Mathematik, 92, pp. 156-171.

HMSO, 1995, Transport statistics Great Britain, The Department of Transport, London, HMSO, pp 57-58.

Hoshi, M., 1984, "Reducing friction losses in automobile engines", Tribology International, Vol. 17, pp. 185-189.

Irani, K., Pekkari, M., and Angstrom, H.E., 1997, "Oil film thickness measurement in the middle main bearing of a six-cylinder supercharged 9 litre diesel engine using capacitive transducers", Wear, pp 29-33

Ito, A., Yang, L., and Negishi, H., 1998, "Study on cam wear mechanism with a newly developed friction measurement apparatus", SAE Paper 982663.

Kikuchi, T., Ito, S. and Nakayama, Y., 2003, "Piston friction analysis using a direct-injection single-cylinder gasoline engine", JSAE. pp53-58.

Kuo, T., Selinau, M., Theobald, M. and Jones, J., 1989, "Calculation of flow in the piston-cylinder-ring crevices of a homogeneous charge engine and comparison with experiment", SAE Paper 890838.

Lancaster, D.R., Krieger, R.B., and Lienesch, J.H., 1975, "Measurement and analysis of engine pressure data", SAE Paper 750026.

Leary, W.A. and Jovellanos, J.U., 1944, "A study of piston and ring friction", NACA Wartime Report, November 1944.

Livengood, J.C. and Wallour, C., 1944, "A study of piston ring friction", NACA Technical Note No. 1249, 1945.

Martin, F.A., 1985, "Friction in internal combustion engines", Proc. Instn. Mech. Engrs. Conf. on reduction of friction and wear in combustion engines, Paper C67/85, pp 1-17.

Masuda, T., 1992, "A measurement of oil film pressure distribution in connecting rod bearing with test rig", Tribology transactions, Vol. 35, No.1, pp. 71-76.

Mihara, Y., Hayashi, T., Nakamura, M. and Someya, T., 1995, "Development of measuring method for oil film pressure of engine main bearing by thin film sensor", JSAE. pp125-130.

Monteil, G., Lonchampt, J., Roques-carmes, C., Godet, M., 1987, "Interface composition in Hertzian contacts. Application to the cam-tappet system", 14th Leeds-Lyon Symposium on Tribology, pp. 355-365.

Monaghan, M.L., 1987, "Engine friction – A change in emphasis", Instn. Mech. Engrs. 2nd BP Tribology lecture.

Nakayama, K., Yasutake, Y., Takiguchi, M. and Furuhama, S., 1997, "Effect of piston motion on piston skirt friction of a gasoline engine", SAE Paper 970839.

NI, 2003, Measurement and automation, National Instruments 2003 catalogue.

Patterson, D.J., 1983, "Measurement of piston and ring assembly friction instantaneous IMEP method", SAE Paper 830416.

Parker, D.A., and Adams, D.R., 1982, "Friction losses in the Reciprocating Internal combustion Engine", Tribology - Key to the Efficient Engine, Instn. Mech. Engrs. Conf. Pub. 1982-1, London, Paper C5/82, pp. 31-39.

Parker, D.A., and Adams, D.R. and Donnison, G., 1989, "The measurement and reduction of piston assembly friction", 2nd Int. Conf. Combustion engines – Reduction of friction and wear, Instn. Mech. Engrs. Conf. Pub. 1989-9, Paper C375/017, pp. 27-34.

Pieprzak, J.M., and Willermet, P.A., Dailey, D.P., 1990, "Experimental Evaluation of Tappet/Bore and Cam/Tappet Friction for a Direct Acting Bucket Tappet Valvetrain", SAE Paper 902086.

Randolph, A.L., 1990, "Methods of processing cylinder-pressure transducer signals to maximise data accuracy", SAE Paper 900170.

Rezrka, S.F., and Henein, N.A., 1984, "A New Approach to Evaluate Instantaneous Friction and Its Components in Internal Combustion Engines", SAE Paper 840179.

Richez, M.F., Constans, B. and Winquist, K., 1982, "Theoretical and experimental study of ring-liner friction", 9th Leeds-Lyon Symposium, pp 122-131.

Rogowski, A.R., 1961, "Method of measuring the instantaneous friction of piston rings in a firing engine", MIT, SAE Paper 379F.

Ruddy, B.L., 1979, "The lubrication and dynamics of piston rings and the theoretical rediction of ring pack gas flow", PhD. Thesis, Dept. Mech. Eng., Leeds Univ.

Ruddy, B.L., Dowson, D. and Economou, P., 1981, "The prediction of gas pressure within the ring packs of large bore diesel engines", J. Mech. Eng. Sci., Vol. 23, No. 6, pp 295-304

Rycroft, J.E., Taylor, R.I. and Scales, L.E., 1997, "Elastohydrodynamic effects in piston ring lubrication in modern gasoline and diesel engines", Pro. 23rd Leeds-Lyon Symposium in Tribology, September 1996, Dowson et al(ed), Elsevier, 1997, pp 49-54.

Seki, T., Nakayama, K., Yamada, T., Yoshida, A. and Takiguchi, M., 2000, "A study on variation in oil film thickness of a piston ring package: variation of oil film thickness in piston sliding direction", JSAE 2000, pp 315-320.

Schilowitz, A.M. and Waters, J.L., 1986, "Oil film thickness in a bearing of a fired engine - Part IV: Measurements in a vehicle on the road", SAE Paper 861561.

Sherrington, I. and Smith, E.H., 1988, "The measurement of piston-ring friction by the floating liner method", IMechE., Experimental methods in engine research and development, pp 265.

Spearot, J.A., and Murphy, C.K., 1988, "A comparison of the total capacitance and total resistance techniques for measuring the thickness of journal bearing oil films in an operating engine", SAE Paper 880680.

Staron, J.T., and Willermet, P.A., 1983, "An Analysis of Valve Train Friction in Terms of Lubrication Principles", SAE Paper 830165.

Suzuki, S., Ozasa, T., Yamamoto, M., Nozawa, Y., Noda, T., and Ohori, M., 1995, "Temperature distribution and lubrication characteristics of connecting rod big end bearings", SAE Paper 953550.

Taylor, C.M., 1991, "Valve Train Lubrication Analysis", Vehicle Tribology, Proc. 17th Leeds-Lyon Symposium on Tribology, Elsevier, Amsterdam, pp. 119-131.

Taylor, C.M., 1993, "Engine tribology", Tribology series 26, Elsevier Science Publishers.

Teodorescu, M., Taraza, D., Henein, N.A., and Bryzik, W., 2002, "Experimental analysis of dynamics and friction in valve train systems", SAE Paper 2002-01-0484.

Thring, R.H., 1989, "Piston skirt friction in internal combustion engines", Proc. Instn. Mech. Engrs., Conf. on reduction of friction and wear on combustion engines, Paper C375/002, pp 7-11.

Ting, L.L and Mayer, J.E., 1974, "Piston ring lubrication and cylinder bore wear analysis, part I", J. Lub. Tech., Trans. ASME, Vol. 96, Ser. F, No. 3, pp. 258-266.

Ting, L.L and Mayer, J.E., 1974, "Piston ring lubrication and cylinder bore wear analysis, part II", J. Lub. Tech., Trans. ASME, Vol. 96, Ser. F, No. 2, pp. 258-266.

Uras, H.M. and Patterson, D.J., 1985, "Oil and ring effects on piston-ring assembly friction by the instantaneous IMEP method", SAE Paper 850440.

Vichard, J.P., and Godet, M., 1967, "Simultaneous Measurement of Load, Friction and Film Thickness in a Cam and Tappet System", Symposium on Experimental Methods in Tribology, Proc. IMechE., vol. 182, pt 3G, pp109-113

Wakuri, Y., Soejima, M., Ejima, Y., Hamatake, T., and Kitahara, T., 1995, "Studies on Friction Characteristics of Reciprocating Engines", SAE Paper 952471.

Yun, J.E. and Kim, S.S., 1992, "An improved approach to the instantaneous IMEP method for piston-ring assembly friction force measurement", JEME. series 2, vol. 35, No. 2, pp 310-318.

Yang, L.S., 1992, "Friction modelling for internal combustion engines", Ph.D. Thesis, Department of Mechanical Engineering, University of Leeds, UK, pgs. 230.

Zhu, G., 1988, "A Theoretical and Experimental Study of the Tribology of a Cam and Follower", Ph.D. Thesis, Department of Mechanical Engineering, University of Leeds, UK, pgs. 236.

Zhu, G., and Taylor, C.M., 2001, "Tribological Analysis and Design of a Modern Automobile Cam and Follower", Engineering Research Series 7, Instn. Mech. Engrs., Professional Engineering Publishing, London.

APPENDIX

The appendix is provided in the attached CD ROM and contains the following details:

APPENDIX I

- Engine data for the Ricardo Hydra gasoline engine.
- Flame valve train Ricardo Hydra input data
  - Exhaust valve train Ricardo Hydra input data
- Flame piston assembly Ricardo Hydra input data
- Flame engine bearing Ricardo Hydra input data

APPENDIX II

- Lubricants data

APPENDIX III

- Connecting rod thermistor curves

APPENDIX IV

Specifications:

- BNC 2110 (connector block)
- Encoder 755 series (British encoder)
- Fylde 379TA (instrument amplifier)
- Kistler 5011B (charge amplifier)
- Kistler 6067 (piezo-electric pressure transducer)
- Kulite XCE-152 (resistive pressure transducer)
- PCI 6071E (Data acquisition board)

- PCI 6110E (Data acquisition board)
- SCB 68 (connector block)
- SCXI 1000 (chassis)
- SCXI 1102 (thermocouple module)
- SCXI 1303 (thermocouple terminal block)

APPENDIX V

Data acquisition system working files:

- Engine friction measurement (Combine all 9 channels.vi)
- Engine friction measurement, post processing (Read and rec valve-piston-beaing powerloss.vi)
- Engine performance (DAQ Ricardo Hydra Engine, new.vi)

APPENDIX VI

Published papers:

- Mufti, R.A. and Priest, M, "Experimental and theoretical study of instantaneous engine valve train friction", Jour. Tribology, ASME 2003, vol 125(3), pp 628-637.

- Mufti, R.A. and Priest, M, "Experimental evaluation of engine valve train friction under motored and fired conditions", Tribological research and design for engineering systems, Proc. 29th Leeds-Lyon Symposium on Tribology 2002, Elsevier, Tribology series 41, pp 767-778.

Presentations:

- R.A. Mufti, "Experimental investigation of piston assembly, valve train and crankshaft bearing friction in a firing gasoline engine", Mission of Tribology Research 11, Institution of Mechanical Engineers, London, December 2002.

- R.A. Mufti, M. Priest and R.J. Chittenden, "Experimental and theoretical study of piston assembly friction in a fired gasoline engine", STLE annual

meeting, New York, April 2003. (The contents of this presentation to be submitted as a journal paper):